

<https://doi.org/10.15388/vu.thesis.741>
<https://orcid.org/0000-0001-7133-7864>

VILNIUS UNIVERSITY
CENTER FOR PHYSICAL SCIENCES AND TECHNOLOGY

Laurynas Bučinskas

Dynamics and Balance of Sulfur Compounds in Environmental Systems

DOCTORAL DISSERTATION

Natural sciences,
Physics (N 002)

VILNIUS 2025

The dissertation was prepared between 2020 and 2024 at the Center for Physical Sciences and Technology.

Academic Supervisor – Dr. Andrius Garbaras (Center for Physical Sciences and Technology, Natural Sciences, Physics, N 002).

Dissertation Defence Panel:

Chairman – Prof. Dr. Zigmas Balevičius (Center for Physical Sciences and Technology, Natural Sciences, Physics, N 002).

Members:

Dr. Vytautas Klimavičius (Vilnius University, Natural Sciences, Physics, N 002),

Dr. Galina Lujaniénė (Center for Physical Sciences and Technology, Natural sciences, Physics, N 002),

Habil. Dr. Andrzej Pelc (Maria Curie-Skłodowska University, Natural sciences, Physics, N 002),

Assoc. Prof. Dr. Vaida Šerevičienė (Vilnius Gediminas Technical University, Technological Sciences, Environmental Engineering – T 004).

The dissertation shall be defended at a public meeting of the Dissertation Defence Panel at 13:00 on 28th March, 2025 in meeting room A101 of the Center for Physical Sciences and Technology.

Address: Saulėtekio ave. 3, A101, Vilnius, Lithuania.

Tel.: +370 5 264 9211; e-mail: office@ftmc.lt

The text of this dissertation can be accessed at the libraries of Center for Physical Sciences and Technology and Vilnius University, as well as on the website of Vilnius University:

www.vu.lt/lt/naujienos/ivykiu-kalendorius

VILNIAUS UNIVERSITETAS
FIZINIŲ IR TECHNOLOGIJOS MOKSLŲ CENTRAS

Laurynas Bučinskas

Sieros junginių dinamika ir balansas aplinkos sanduose

DAKTARO DISERTACIJA

Gamtos mokslai,
Fizika (N 002)

VILNIUS 2025

Disertacija rengta 2020–2024 metais Fizinių ir technologijos mokslų centre.

Mokslinis vadovas – dr. Andrius Garbaras (Fizinių ir technologijos mokslų centras, gamtos mokslai, fizika, N 002).

Gynimo taryba:

Pirmininkas – prof. dr. Zigmas Balevičius (Fizinių ir technologijos mokslų centras, gamtos mokslai, fizika, N 002).

Nariai:

dr. Vytautas Klimavičius (Vilniaus universitetas, gamtos mokslai, fizika, N 002),

dr. Galina Lujanienė (Fizinių ir technologijos mokslų centras, gamtos mokslai, fizika, N 002),

habil. dr. Andrzej Pelc (Marijos Kiuri-Sklodovskos universitetas, gamtos mokslai, fizika, N 002),

doc. dr. Vaida Šerevičienė (Vilniaus Gedimino technikos universitetas, technologijos mokslai, aplinkos inžinerija – T 004).

Disertacija ginama viešame Gynimo tarybos posėdyje 2025 m. kovo mėn. 28 d. 13:00 val. Fizinių ir technologijos mokslų centro A101 auditorijoje.

Adresas: Saulėtekio al. 3, D401, Vilnius, Lietuva.

Tel.: +370 5 264 9211; el. paštas: office@ftmc.lt

Disertaciją galima peržiūrėti Fizinių ir technologijos mokslų centro ir Vilniaus universiteto bibliotekose ir VU interneto svetainėje adresu:

<https://www.vu.lt/naujienos/ivykiu-kalendorius>

ABBREVIATIONS

AMS	Accelerator mass spectrometer
EC	Elemental carbon
EA	Elemental analyzer
GHGs	Greenhouse gases
HFO	Heavy fuel oil
IRMS	Isotope ratio mass spectrometer
MCMC	Markov chain Monte Carlo
MDF	Mass-dependent fractionation
MIF	Mass-independent fractionation
OC	Organic carbon
PIT	Principle of identical treatment
PM₁	Particulate matter ($d < 1 \mu\text{m}$)
QC	Quality control
RM	Reference material
SIA	Stable isotope analysis
S/K	sulfur to potassium ratio
SOR	Sulfur oxidation ratio
TC	Total carbon
TMI	Transition metal ions
TPS	Thermal power station
VOC	Volatile organic compound
WSII	Water-soluble inorganic ions
$\delta^{13}\text{C}$	Stable isotope ratio values of carbon
$\delta^{34}\text{S}$	Stable isotope ratio values of sulfur

TABLE OF CONTENTS

ABBREVIATIONS.....	5
INTRODUCTION.....	8
1. LITERATURE OVERVIEW	13
1.1. Sulfate aerosol.....	13
1.2. Natural and anthropogenic sources of sulfur.....	16
1.3. Atmospheric sulfate production	18
1.4. Sulfur and carbon isotopes	23
1.5. Isotope fractionation	28
1.5.1. Equilibrium isotope effects	30
1.5.2. Kinetic isotope effects.....	33
1.5.3. Mass-dependent and mass-independent isotope effects.....	35
1.6. Isotope fractionation during sulfate production	36
1.7. Region-specific sources of atmospheric sulfur-containing species and carbonaceous PM ₁	38
1.7.1. Statistical Bayesian isotope mixing model for source apportionment of sulfur-containing species.....	39
1.7.2. Evaluation of sulfur source contributions	41
1.7.3. Evaluation of carbonaceous PM ₁ source contributions.....	42
2. RESEARCH OBJECT AND METHODOLOGY	44
2.1. Sample collection.....	44
2.2. Sample chemical preparation	46
2.3. Isotope ratio mass spectrometry.....	47
2.3.1. Stable isotope ratio measurement data corrections	50
2.3.2. Combined uncertainty evaluation	55
2.3.3. Isotope data quality assurance.....	56
2.4. Radiocarbon measurements	57
2.5. Ion concentration measurements.....	59
2.6. Air mass trajectories and meteorological parameters	59

2.7. Sulfur oxidation pathway contribution calculations.....	61
2.8. Event description.....	63
3. RESULTS	65
3.1. Results from the entire sampling period	65
3.2. The influence of long-range pollutant transport.....	71
3.3. Seasonality of concentrations and isotopic compositions	73
3.4. Apportionment of sulfur sources.....	76
3.5. Impacts of quarantine conditions on PM ₁ emissions.....	80
3.6. Impacts of heavy fuel oil usage.....	86
3.7. Factors influencing isotopic composition variations.....	92
CONCLUSIONS	98
REFERENCES	99
SUPPLEMENTARY MATERIALS	127
SANTRAUKA	130
ACKNOWLEDGEMENT.....	163
PUBLICATIONS AND CONFERENCES	164
CURRICULUM VITAE	168

INTRODUCTION

Aerosol particles or particulate matter, can have diverse compositions, including ions of sulfate (SO_4^{2-}), nitrate (NO_3^-), ammonium (NH_4^+), transition metal ions (TMIs), and other compounds such as organic compounds (OC), black carbon (BC) or elemental carbon (EC), which are typically found in fine particles (Pöschl, 2005; Seinfeld and Pandis, 2016). Sulfates, formed primarily through the oxidation of SO_2 in the atmosphere, are a particularly important component of atmospheric aerosols, accounting for 12 % to 44 % in particulate matter smaller than 1 μm in diameter or PM_1 (Bressi et al., 2021; Masalaite et al., 2022; Singh et al., 2019). Sulfur compounds play a crucial role in Earth's climate and can have detrimental effects on human health (Kiehl and Briegleb, 1993; Kreyling et al., 1999; Pope and Dockery, 2006). A key example of sulfur pollution impact is acid rain, which severely harmed natural ecosystems in Europe during the 1970s and 1980s (Menz and Seip, 2004; Worobiec et al., 2008). In addition, sulfate aerosols influence the balance of radiative forcing by cooling the climate, either directly by scattering incoming solar radiation or indirectly through various in-cloud processes that modify cloud albedo, their lifetimes, and other properties (Albrecht, 1989; Boucher and Lohmann, 1995; Kulmala et al., 2013; Solomon, S. et al., 2007; Ten Brink et al., 1997; Twomey, 1991). However, the magnitude of induced radiative forcing is still largely uncertain (Bellouin et al., 2020; Myhre et al., 2004; Solomon, S. et al., 2007). In urban environments, non-sea salt (nss) sulfate aerosols are predominantly produced as a secondary particles through gas-to-particle conversion of SO_2 (Tomasi and Lupi, 2016). Around 50 % of emitted SO_2 is oxidized to sulfate via various gas-phase or aqueous-phase reactions (Chin et al., 2000). The dominant SO_2 oxidation pathways are thought to be gas-phase oxidation by OH radicals and H_2O_2 , O₃, TMI catalysis of O₂ in the aqueous phase (Harris et al., 2012b; Herrmann et al., 2000; Tanaka et al., 1994). The partitioning of SO_2 oxidation pathways is crucial in determining the properties of the resulting sulfate, including its size distribution, optical characteristics, transport, and radiative forcing (both direct and indirect effects), making it a key problem in studying the sulfur cycle (Alexander et al., 2009; Harris et al., 2013b; Hegg et al., 2004). Therefore, a thorough understanding of sulfur emission sources and subsequent formation of sulfate aerosol mechanisms is essential, as these processes govern aerosol properties, which have significant impacts on environment and human health (Thiemens, 2006; Tomasi et al., 2017; Q. Zhang et al., 2023).

In this context, stable isotope analysis provides a robust signature-based method for the study of sulfur emission sources and the subsequent gas-to-particle transformation processes in the atmosphere (Dasari and Widory, 2024; Kawamura et al., 2001; Mukai et al., 2001). Recently, multiple studies have examined factors influencing the isotopic composition ($\delta^{34}\text{S}$) values of particulate sulfate, such as source signatures, sulfate production pathways, ambient temperature, and sulfur oxidation rates in polluted regions of China (Guo et al., 2019; Han et al., 2016; Li et al., 2020; Wei et al., 2018; Zhou et al., 2019), India (Dasari et al., 2022c; Dasari and Widory, 2024; Rastogi et al., 2020; Sawlani et al., 2021), and Korea (Kim et al., 2021; Lee et al., 2023). In contrast, isotope-based studies aimed at identifying pollution sources and the fate of sulfur compounds in the atmosphere are currently scarce and under-researched in Europe (Górka et al., 2017; Novák et al., 2001; Sinha et al., 2008). Thus, in this thesis, stable isotope analysis methods are employed to investigate the seasonal dynamics of sulfur emission sources and their transformation mechanisms in the atmosphere, with the aim of improving understanding of the causes and environmental impacts of atmospheric sulfur pollution. By integrating stable sulfur isotope analysis with complementary meteorological, water-soluble inorganic ion, and radiocarbon data, the study provides a comprehensive framework for identifying primary pollution sources, quantifying their respective contributions, and investigating atmospheric sulfate production mechanisms.

Objective and tasks of the work

The aim of this work is to investigate the long-term seasonal variation of sulfurous compounds in the atmosphere and evaluate their emission sources through the application of stable sulfur isotope analysis. For this purpose, the following tasks were outlined:

- To investigate the behavior of sulfur-containing species as atmospheric pollutants using a multiple isotope approach (^{34}S , ^{13}C , and ^{14}C).
- To determine factors influencing seasonal variations in the concentrations and isotopic compositions of SO_2 and PM_{l} -related SO_4^{2-} .
- To identify and quantify the seasonal sources of sulfur pollution affecting air quality in Vilnius, Lithuania, through a Bayesian statistical model integrated with region-specific isotope endmembers.
- To evaluate the relative contributions of the different oxidation pathways of SO_2 to the formation of PM_{l} -related SO_4^{2-} .
- To assess the impact of changing emission sources during specific periods (e.g., COVID-19 restrictions and increased heavy fuel oil emissions) on air quality and the isotopic compositions of PM_{l} .

Scientific novelty

The results obtained during this study showed reversed seasonal dynamic in the isotopic composition of sulfur compounds in the atmosphere, in contrast to most published data on this topic. The primary driver of the observed seasonal variation in isotopic compositions was attributed to changing contributions from local and remote pollution sources.

The combined application of multiple stable isotope (^{34}S and ^{13}C) and radiocarbon (^{14}C) analysis allowed for the first time, a comprehensive characterization of common anthropogenic sources contributing to sulfate and carbonaceous aerosols.

Isotopic composition data from synchronously collected SO_2 and sulfate aerosol samples enabled a quantitative assessment of the predominant atmospheric SO_2 oxidation pathways. This study confirmed that transition metal ion-catalyzed oxidation of SO_2 , previously estimated by atmospheric models as a significant contributor, was the predominant mechanism for the formation of SO_4^{2-} in the urban environment of Vilnius during winter.

Study relevance

Sulfur compounds play a crucial role in Earth's climate system and significantly affect air quality and human health. Sulfate aerosols are key atmospheric components that influence climate by cooling the atmosphere through scattering of solar radiation. The radiative forcing properties of sulfate aerosols depend on their formation pathways via the oxidation of SO₂. Therefore, precise apportionment of sulfur pollution sources and understanding atmospheric oxidation mechanisms are essential for evaluating their environmental and climatic impacts.

The findings in this dissertation provide a framework for characterizing anthropogenic emissions and their atmospheric fate through a combination of stable isotope (³⁴S and ¹³C) analyses and radiocarbon measurements. Long-term observations of atmospheric sulfur compound isotopic compositions could be applied in environmental monitoring, enabling the identification of seasonal pollution sources, differentiating between local and remote emission origins, and detecting anomalous pollution events. Apportionment of pollution sources could assist environmental agencies in developing targeted strategies for reducing emissions and effectively improving air quality. Evaluating SO₂ oxidation pathways could be adapted to improve climate models by allowing more accurate estimations of radiative forcing impacts of atmospheric sulfate.

Contribution of the author

Collection of weekly SO₂ and sulfate aerosol samples throughout the sampling campaign, from November 11, 2020 to June 30, 2023. Application and validation of chemical pre-treatment methods for sulfate extraction from SO₂ and aerosol samples. Sample preparation for isotope ratio, radiocarbon, and water-soluble inorganic ion concentration measurements. Participation in the preparation, implementation, and validation of methodologies for measuring stable isotope ratios of sulfur. Measurement of sulfur isotopic compositions by isotope ratio mass spectrometer. Data correction and normalization of stable isotope ratio results. Collection and adaptation of meteorological data and application of backward air mass trajectory models. Application of Bayesian statistical models. Interpretation and analysis of integrated data. Preparation of original manuscript drafts, including the descriptions of methodology, data analyses and calculations, interpretation of results, data visualization, and formulation of conclusions.

Statements of the defense

1. The isotopic composition of sulfur compounds shows strong seasonal variations, with higher $\delta^{34}\text{S}$ values in the summer months and lower $\delta^{34}\text{S}$ values in the winter months, driven by shifts in predominant pollution sources and oxidation pathways.
2. The main sources of sulfur pollution affecting the urban air quality in Vilnius are biomass burning, coal combustion emissions from neighboring countries, and, during the 2022 – 2023 heating season, emissions from heavy fuel oil, which became a significant contributor during this period.
3. During the period of increased emissions from heavy fuel oil combustion, the predominant pathway of sulfate formation was found to be oxidation of SO_2 by O_2 , catalyzed by transition metal ions, with lesser contributions from H_2O_2 and OH oxidation pathways.

1. LITERATURE OVERVIEW

The aim of this chapter is to provide a detailed and contextually relevant overview of the research object. It focuses on the key topics relevant to this study, with a particular emphasis on sulfur compound emission sources and their dynamics in the atmosphere. Isotope fractionation is described in more detail as a fundamental aspect of gas-to-particle conversion processes in the atmosphere. Additionally, the concept of stable isotope analysis of sulfur is introduced, explaining the notations used and giving a basic overview of isotopic effects, on which it is based. Finally, anthropogenic pollution sources relevant to Vilnius are detailed, and methods for evaluating their contributions is described.

1.1. Sulfate aerosol

Aerosols, suspended liquid or solid particles in air, are responsible for their detrimental effects on human health, global climate, and air quality (Kulmala et al., 2004; Landkocz et al., 2017; Moreno-Ríos et al., 2022). Aerosol pollution is linked to several detrimental effects to human health, including respiratory and cardiovascular problems, lung cancer, and premature mortality (Brook et al., 2010; Kreyling et al., 1999).

Submicron particles, with sizes smaller than $1.0 \mu\text{m}$, are especially important as air pollutants primarily released during incomplete combustion processes or formed as secondary aerosol in the atmosphere. Due to their small size, they have long atmospheric lifetimes, allowing them to travel over significant distances. Aerosols consist of various organic and inorganic compounds, with sulfates being a key component. Sulfate accounts for up to 44 % of PM_1 particles and play a crucial role in atmospheric chemistry (Bressi et al., 2021; Charlson et al., 1992; Kiehl and Briegleb, 1993; Singh et al., 2019; Zhou and Tazaki, 1996). Both organic compounds and sulfate in submicron aerosols can originate from secondary processes, condensing volatile organic compounds (VOCs) and sulfur dioxide (SO_2) onto existing particles through the oxidation of these compounds (Chin et al., 2000; Shrivastava et al., 2017).

In contrast to greenhouse gases (GHGs) and soot particles (black carbon, BC), sulfate aerosols scatter sunlight, thus producing a negative radiative forcing effect, consequently cooling the Earth's surface (Solomon, S. et al., 2007; Wofsy et al., 2007). This direct effect of sulfate aerosols has negated some of the warming caused by GHGs but the magnitude of radiative forcing is still largely uncertain (Bellouin et al., 2020; Myhre et al., 2004; Solomon,

S. et al., 2007). In Fig. 1.1, the significant radiative forcing impact of sulfate, and other aerosols alongside GHGs are pictured.

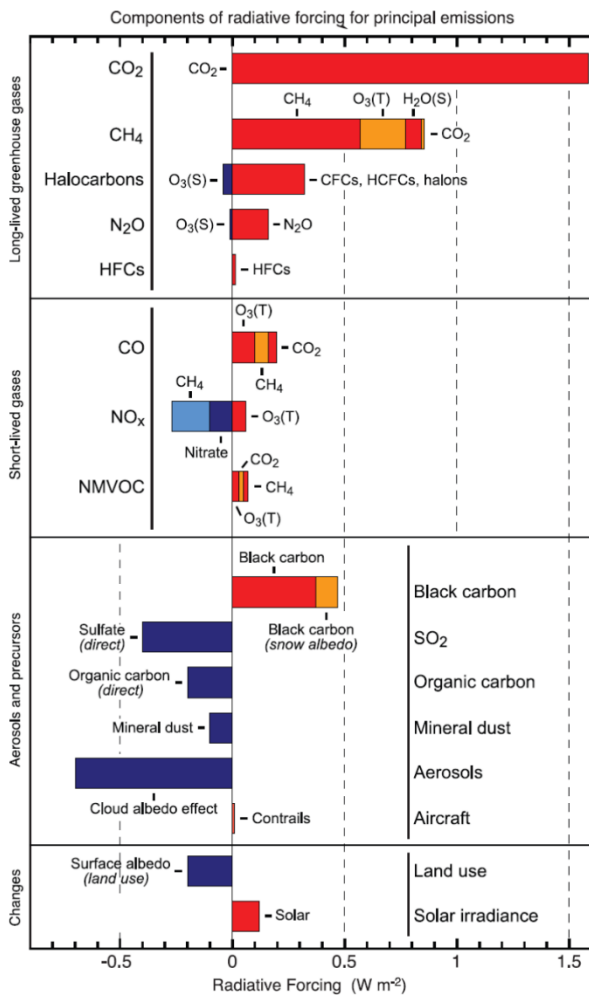


Fig. 1.1. Main atmospheric components responsible for radiative forcing. Adapted from Agostini et al. (2014).

Aerosols sizes ranging from around $0.4 \mu\text{m}$ to $1.0 \mu\text{m}$ are most effective for scattering of incident light as their sizes match the wavelengths of visible light spectrum (Ten Brink et al., 1997). Sulfates that form through heterogeneous reactions on existing particles change their size and chemical composition and are important for direct scattering of solar radiation (Hegg et al., 2004). Homogenous oxidation of SO_2 forms gaseous sulfuric acid (H_2SO_4), which adheres on particles or nucleate to create new ones. However, freshly created

particles are minuscule in the range of ~1 – 2 nm, which are too small for efficient light scattering. These particles can quickly grow by coagulation and condensation, with sulfuric acid playing a critical role in their formation (Kulmala et al., 2013). Sulfuric acid condenses onto clusters, which are then stabilized by ammonia, amines, and organic compounds. Sulfate particles can grow as they age in atmosphere, reaching sufficient sizes (up to 50 – 200 nm) to act as cloud condensation nuclei (CCN), thus affecting the lifetime and albedo of clouds (Boucher and Lohmann, 1995; Kulmala, 2003; Väkevä et al., 2000). The first indirect (Twomey) effect describes how increased CCNs from anthropogenic emissions enhance cloud albedo, leading to greater scattering of solar radiation (Lohmann and Feichter, 2004; Twomey, 1991). The second indirect effect, known as the Albrecht effect, describes how elevated CCN concentrations can increase liquid water content, cloud height, and cloud lifetime, thereby enhancing cooling (Albrecht, 1989; Tomasi et al., 2017). However, these cooling effects may be offset by factors like cloud heating from radiation-absorbing soot particles (Ackerman et al., 2000).

Radiative forcing effects are thus highly dependent on aerosol size and properties, which are determined by sulfate production mechanisms in the atmosphere. Once formed, sulfate retains its sulfur isotopic composition, preserving the original formation signature and making it an effective tracer for analyzing atmospheric sulfur sources and transformation processes by stable isotope analysis (SIA) methods (Górka et al., 2017; Tichomirowa et al., 2007). Additionally, directly comparing the isotopic compositions of SO₂ and sulfate can elucidate the contributions of different SO₂ oxidation pathways that determine the radiative forcing properties of produced sulfate.

A historic example of consequences of increased sulfur pollution levels is acid rain (or acidic deposition), which had significant detrimental effects on natural ecosystems in Europe during the 1970s and 1980s (Menz and Seip, 2004; Worobiec et al., 2008). Acidic deposition results from SO₂ and/or NO_x emissions, mainly from fossil fuel power stations, metal smelters, and vehicles, which can form sulfuric and/or nitric acids in aerosols and precipitation. Adverse impacts of acidic deposition included soil and water acidification, damages to forests and aquatic life, and deterioration of historic buildings and statues. In response to this, strict regulations were introduced after sulfur and nitrogen emissions peaked in the 1980s, resulting in a reduction of SO₂ emissions in Europe by over 70 % between 1980 and 2004 (Smith et al., 2011; Vestreng et al., 2007). Consequently, in Lithuania SO₂ emissions decreased by 95 % from 1981 to 2017, however, SO₄²⁻ concentrations only decreased by 79 % over the same period and have remained higher than SO₂ emission levels since 2008 (Davuliene et al., 2021).

Recent trends demonstrate that the complex dynamics of sulfur compounds in the atmosphere remains highly relevant in today's context, highlighted by recently observed warming effects associated with reduced shipping emissions of SO₂ (Gettelman et al., 2024). Under favorable conditions for low marine cloud formation, ship emissions of SO₂ result in visible ship tracks that scatter sunlight, contributing up to 40 % of total aerosol cooling through negative radiative forcing (Lauer et al., 2007). New shipping regulations instituted in 2020 (IMO2020) reduced allowed sulfur content in fuels by approximately 80 %, which resulted in a significant reduction of observed ship tracks (Gettelman et al., 2024; IMO, 2016). Early models indicate that the reduction of sulfur emissions may have caused an estimated net radiative forcing of 0.12 – 0.13 W/m², which could have contributed to observed significant temperature anomalies in the Northern Hemisphere during 2022 – 2023 (Gettelman et al., 2024; Yoshioka et al., 2024). However, more precise global warming impacts of the reduced SO₂ emissions in shipping are expected to emerge during the coming years.

1.2. Natural and anthropogenic sources of sulfur

The majority of natural sulfur released into the atmosphere is either emitted as SO₂ gases or formed through the oxidation of precursors such as hydrogen sulfide (H₂S), carbonyl sulfide (OCS), dimethyl sulfide (DMS), and others (Berresheim et al., 2002; Harris et al., 2013a; Seinfeld and Pandis, 2016; Singh, 1995). Hydrogen sulfide is regionally important source of natural sulfur emissions, emitted from anaerobic environments (such as wetlands and marshes) by sulfate-reducing bacteria as they break down organic matter. Once emitted in the atmosphere, H₂S is rapidly oxidized to SO₂. The major source of DMS is the emission from oceans, produced by phytoplankton species. When emitted from the ocean's surface, DMS also undergoes rapid oxidation, with approximately 27 % to 54 % converting to SO₂ (Seinfeld and Pandis, 2016; Yvon et al., 1996). In addition, oceans and seas emit large quantities of sea salt sulfate, generated by sea spray when wind or waves cause bubbles to burst (Tomasi et al., 2017). Size distribution of aerosols created by sea spray is bimodal, that is, particles formed from bursting bubble films belong to the first mode, centered around 0.1 µm, while those formed from water jets belong to the second mode, centered around 2.5 µm (Mårtensson et al., 2003). Particles in the second mode have short lifetimes and settle quickly, whereas first-mode particles are longer-lasting and can have impacts even on continental areas. Sulfate aerosol emitted in this way is referred to as primary sulfate, in contrast to secondary sulfate that is produced through gas-to-

particle conversion via different oxidation pathways of SO₂. Alongside DMS, oceans also directly release carbonyl sulfide, either directly or through conversion from DMS or carbon disulfide (CS₂). The OCS is notable for its low reactivity resulting in a long atmospheric lifetime, averaging 7 years. Biomass burning is also an important source of OCS, contributing up to 20 % of global budget (Seinfeld and Pandis, 2016). In addition, burning of vegetation (wildfires) release significant amounts of direct SO₂ emissions and vary seasonally, dependent on active fire seasons (Ricky et al., 2022). Volcanic emissions are also episodic, but release large quantities of SO₂, H₂S and particles into the troposphere or even directly to stratosphere. Volcanic SO₂ emissions are around 4.5 times more effective at producing particulate sulfate than anthropogenic sources because volcanic eruptions inject SO₂ to higher atmospheric altitudes, extending their atmospheric lifetime (Tomasi et al., 2017). In addition, mineral dust particles are a significant source of primary sulfate aerosols, particularly in arid regions. Mineral dust is produced by resuspension of soil particles or by anthropogenic sources, such as agricultural activities and road dust from traffic. Dust particles commonly exhibit short atmospheric lifetimes up to 3 days due to their larger sizes. The size distribution of dust particles peaks around 7 µm (Tomasi et al., 2017). A global budget summary of natural and anthropogenic pollution sources of sulfur are given in Table 1.1.

Table 1.1. The sulfate aerosol source emissions in Tg(S)/year (Andreae and Crutzen, 1997; Lee et al., 2011; Seinfeld and Pandis, 2016; Sofen et al., 2011; Tomasi et al., 2017).

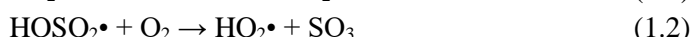
	H ₂ S	DMS	CS ₂	OCS	SO ₂	SO ₄ ²⁻	Total
Oceans	<0.3	15–25	0.08	0.08	-	40-320	15–25 (nss)
Wetlands	<1.1	<0.68	<0.06	-	-	-	0.01-2
Plants and soils	0.17–0.53	0.05–0.16	0.02–0.05	-	-	2-4	0.25–0.78 (-dust)
Volcanoes	0.5–1.5	-	-	0.01	6.6	2-4	9.3–11.8
Biomass burning	<0.01	-	<0.01	0.075	1.3	0.1	2.2–3
Fossil fuels		2.2			56.3	2.2	71–77
Total anthropogenic				0.08	72-80	2.3	73–80
Total natural (-nss;-dust)							25–40

On a global scale, approximately 80 % of all sulfur emissions originate from anthropogenic sources (Faloona, 2009). The majority of anthropogenic emissions are of SO_2 , which can then be oxidized to form new sulfuric acid particles or nucleate on existing ones as sulfate. However, industrial activities can also produce primary sulfate during combustion processes, releasing it to the atmosphere (Holt et al., 1982). The dominant anthropogenic sulfur sources are of liquid and gas fossil fuel combustion (transportation, electricity generation, shipping), solid fossil fuel (coal, lignite) combustion (thermal energy generation, domestic heating), industrial processes (oil refinery, chemical manufacturing), biomass burning (domestic heating, land clearing), landfills, and waste incineration (Smith et al., 2011; Tomasi et al., 2017).

1.3. Atmospheric sulfate production

In the atmosphere, the most abundant form of particulate matter sulfur is sulfate (Tomasi et al., 2017). In the atmosphere, sulfate is formed from gaseous precursors (secondary sulfate) through various oxidation reaction pathways in the atmosphere. Most sulfate is formed by oxidation of SO_2 , with approximately half of SO_2 in the troposphere being converted to sulfate, while the remainder is removed by wet or dry deposition onto surfaces such as ground or bodies of water (Chin et al., 2000, 1996; Kellogg et al., 1972). The atmospheric lifetime of SO_2 is short, from a few hours to 2 days, with an average of approximately 12 hours (Lee et al., 2011). In contrast, sulfate aerosol can remain in the atmosphere for several days or weeks (Bondietti and Papastefanou, 1993; Kristiansen et al., 2016).

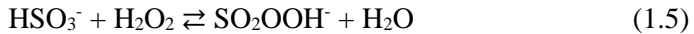
Sulfur dioxide gases are thermodynamically likely to react with oxygen (O_2) in the atmosphere to form sulfur trioxide (SO_3). However, under normal atmospheric conditions, this reaction is slow, and its contribution to the production of sulfate aerosol is inconsequential (Seinfeld and Pandis, 2016). Instead, the oxidation of SO_2 to SO_4^{2-} is predominant, and takes place through either gas-phase or aqueous-phase reactions. Aqueous-phase reactions modify the chemical composition of already-present particles, in contrast to gas-phase reactions that are likely to lead to formation of new particulates. In the gas phase, the predominant oxidation pathway is the reaction of SO_2 with hydroxyl radicals (OH), resulting in the form of sulfuric acid (Calvert and Stockwell, 1983):



Homogenous oxidation produces H_2SO_4 gases, which may then condensate on existing particles or nucleate to create new particulates (Kulmala et al., 2004; Tanaka et al., 1994). Oxidation of SO_2 by OH radicals significantly contributes to sulfate production and is estimated to account for up to 36 % of global sulfate formation (Berglen et al., 2004; Pozzoli et al., 2008). Although the highest OH concentrations are found in the tropics (Bahm and Khalil, 2004), and the oxidation rate by this pathway is lower in temperate climates. In addition, this SO_2 oxidation reaction occurs only during the day because OH radicals are produced by ozone (O_3) photolysis with ultraviolet radiation, followed by the reaction with oxygen atoms (O) and water vapor to produce OH radicals (Lelieveld et al., 2004; Seinfeld and Pandis, 2016). Therefore, contribution of this oxidation pathway to sulfate production is reduced during winter at higher latitudes, such as in Lithuania (~55° N).

In contrast to the homogeneous oxidation of SO_2 , the heterogeneous oxidation pathways do not produce new particles; instead, these reactions take place on existing particles such as sea salt, dust or within cloud droplets (Harris et al., 2013b). In the aqueous-phase, the oxidation of SO_2 occurs through following primary mechanisms (Ajdari et al., 2016; Lee and Schwartz, 1983; Seinfeld and Pandis, 2016; Tomasi et al., 2017):

1. Oxidation by hydrogen peroxide (H_2O_2):



H_2O_2 is a particularly significant oxidant of SO_2 due to its high solubility in aqueous solutions and its high concentrations when compared to other oxidants. Additionally, the oxidation rate of this pathway is relatively independent of pH over a wide range of values. The GEOS-Chem model simulated results estimate that approximately 43 % of all sulfate produced is attributed to the H_2O_2 oxidation pathway (Alexander et al., 2009; Park et al., 2004).

2. Oxidation by oxygen (O_2) catalyzed by transition metal ions:



Without a catalyst, the rate of this reaction is low, however, in the atmosphere, traces of transition metal ions are generally present (Huss et al., 1978; Tsunogai, 1971). The primary catalysts of this oxidation pathway are Fe^{3+} and Mn^{2+} ions, and the oxidation rate of this pathway is pH-dependent, with the reaction rate increasing at higher pH values. In addition, the reaction rate increases significantly when both Fe^{3+} and Mn^{2+} ions are present, up to 10 times faster than the sum of all ions reaction rates (Martin, 1984). However, laboratory results and real-world studies have shown that other ions present on aerosols, such Zn^{2+} , Ni^{2+} and Cu^{2+} , play a lesser role in the TMI-catalyzed oxidation (Grgić et al., 1991; Harris et al., 2013b).

The importance of TMI-catalyzed pathway was previously significantly underestimated, but recent studies have shown that the TMI-catalysis pathway's contribution to global SO_2 removal is approximately 10 times higher in magnitude than previously thought (Harris et al., 2013a). At higher latitudes (Fig. 1.2), where photochemical reactions decline during winter, TMI-catalyzed pathway is predicted to contribute between 7 % and 35 % (or more) of all SO_2 oxidation (Alexander et al., 2009; Harris et al., 2013a).

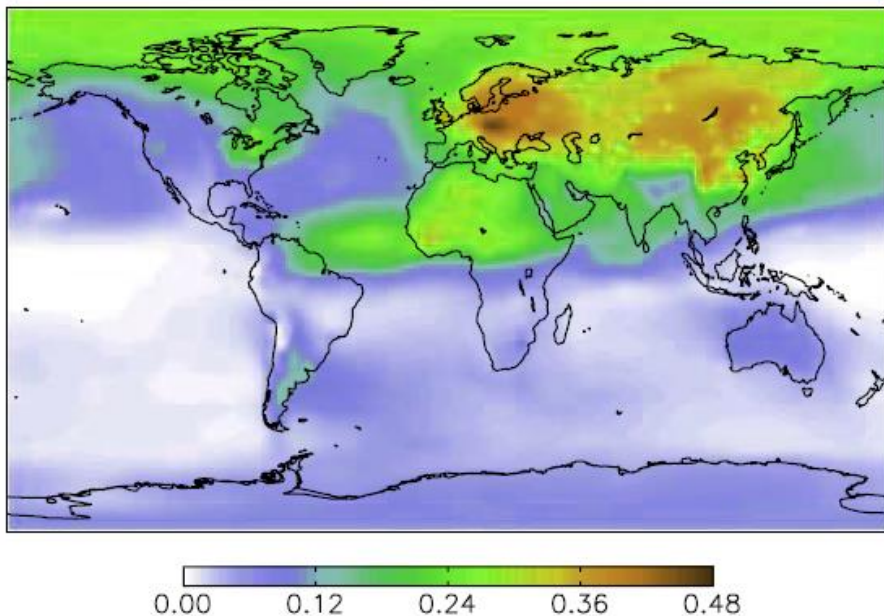


Fig. 1.2. The global contributions of TMI-catalysis oxidation pathway. The fraction of total sulfate produced annually by TMI pathway is denoted as a color gradient. Adapted from Alexander et al. (2009).

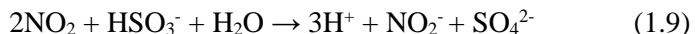
Previously, it was suggested that in Europe only the anthropogenic sources of TMIs are consequential as catalysts, as natural TMIs are characterized by low solubility (Alexander et al., 2009). However, other studies indicated that the uptake of acidic compounds onto aerosols might enhance natural TMI solubility, potentially making this the dominant oxidation pathway in the coarse aerosol mode ($>1\text{ }\mu\text{m}$) (Harris et al., 2013b). Whereas in the fine mode ($<1\text{ }\mu\text{m}$), TMIs of anthropogenic origin are expected to be the predominant source of Fe^{3+} and Mn^{2+} ions in the aerosols.

3. Oxidation by ozone (O_3):



This reaction also occurs in the gas phase although it is very slow. In the aqueous-phase, the rate of oxidation strongly depends on the pH and is generally only important at values greater than 4. As the rate of oxidation increases, the pH of the solution decreases as acidic solutions with sulfate are produced, which in turn slow down the reaction, making it a self-limiting reaction. Additionally, the solubility of ozone is several orders of magnitude lower than that of H_2O_2 , and as a result, typical concentrations of O_3 are usually insignificant. Thus, on a global scale, O_3 oxidation contributes minimally to sulfate production ($<4\text{ \%}$) and is less significant than aforementioned oxidation pathways of gas-phase OH and aqueous-phase H_2O_2 and TMI catalysis (Alexander et al., 2009; Barrie et al., 2001).

4. Oxidation by nitrogen dioxide (NO_2):



In urban environments with elevated NO_2 concentrations (e.g., in highly polluted urban areas of China and India), NO_2 can play an important role as an oxidant, contributing up to a third of the sulfate produced, especially under conditions of fog or haze (Au Yang et al., 2018; Fan et al., 2020; Jion et al., 2023). However, due to its low concentration in atmospheric aqueous solutions and limited water solubility, the contribution of NO_2 oxidation for sulfate production is less significant globally compared to the aforementioned pathways and is oftentimes neglected (Cheng et al., 2016; Herrmann et al., 2000).

The reaction rates of primary SO_2 oxidation pathways strongly depend on the concentration of oxidants and the pH of the aqueous solutions (Seinfeld

and Pandis, 2016). The dependence of the oxidation rates on pH for different pathways in the aqueous phase are summarized in Fig. 1.3.

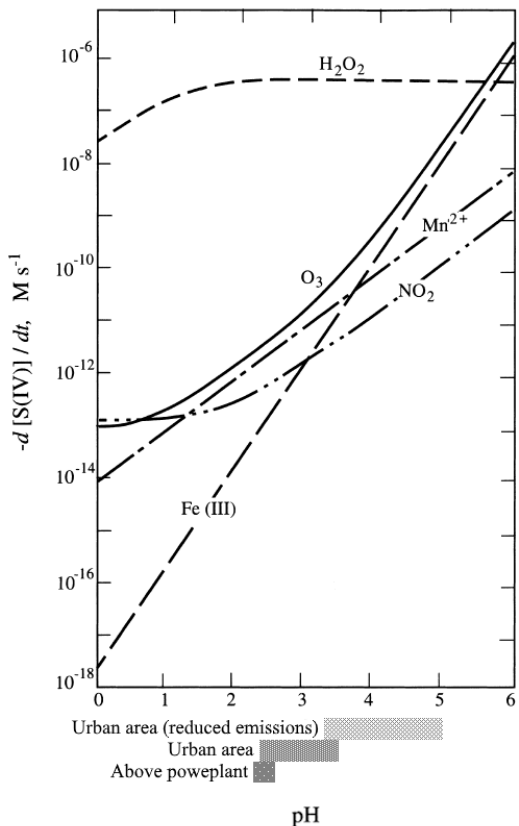


Fig. 1.3. A comparison of the conversion rates of SO_2 ($-d[\text{S(IV)}]/dt$, M/s) oxidation pathways based on their dependence on pH in the aqueous phase. Adapted from Au Yang et al. (2018) and Seinfeld and Pandis (2016). Below the graph are the pH ranges for distinct environments (Jaeschke, 1986). Oxidation rates represented for these conditions: SO_2 (g) – 5 ppb; NO_2 (g) – 1 ppb; H_2O_2 (g) – 1 ppb; O_3 (g) – 50 ppb; $\text{Fe}^{3+} = 0.3 \mu\text{M}$, $\text{Mn}^{2+} = 0.03 \mu\text{M}$.

As previously indicated, H_2O_2 is a key oxidant of SO_2 , especially in the lower pH ranges (below 5 pH), and it is the only pathway that is relatively independent of pH. At higher pH values (>5 pH), TMI, together with O_3 , can become the predominant oxidation pathways. In contrast, at low NO_2 concentrations (1 ppb), its contribution remains insubstantial across the typical pH ranges found in atmospheric aqueous solutions, such as in clouds and liquid aerosols.

Aforementioned reactions are not the only pathways of SO₂ oxidation; additional reactions involve interactions with OH, SO₅⁻, HSO₅⁻, CH₃OOH, HO₂, NO₃, HCHO, Cl⁻, and others (Pandis and Seinfeld, 1989). In addition, gas-phase SO₂ oxidation by Criegee intermediates has been reported to be a potentially significant contributor in regions with high volatile organic compound (VOC) emissions (Amiri et al., 2018). While these oxidation pathways are generally insignificant on a global scale, they can play an important role locally.

1.4. Sulfur and carbon isotopes

In nature, sulfur has four isotopes of ³²S, ³³S, ³⁴S, and ³⁶S that are stable, with natural abundances of 95.0 %, 0.8 %, 4.2 %, and 0.02 %, correspondingly (Thode et al., 1953). Stable isotope abundance measurements of sulfur are particularly valuable in environmental studies, as isotopes can be used as tracers of natural processes. Historically, stable isotope techniques were first employed in the sciences of geochemistry and geology. However, as these techniques have advanced, they have begun to be applied in many other fields, such as forensic sciences, hydrology, paleoclimatology, biology, ecology, archaeology, food authenticity research, and countless others (Fry, 2006; Lebedev, 2013; Meier-Augenstein, 2010). In atmospheric studies, stable isotope analysis of sulfur ($\delta^{34}\text{S}$) has often been applied to trace particulate sulfate pollution sources (Dasari and Widory, 2024; Guo et al., 2010; Han et al., 2016; Inomata et al., 2016; Mukai et al., 2001; Norman et al., 2006, 2004). Additionally, analysis of sulfur isotopic compositions is also used to investigate SO₂ oxidation pathways (Fan et al., 2020; Harris et al., 2013a; Li et al., 2020; Norman et al., 2006). However, due to innate difficulties concerning sample collection and their pretreatment, studies analyzing simultaneously collected SO₂ and sulfate aerosols are rare (Amiri et al., 2018; Kawamura et al., 2001; Lin et al., 2017; Mukai et al., 2001).

Stable isotope compositions in samples with natural abundances (without artificial enrichment) are typically expressed in the notation of δ values - the ratio of the element's heavy (^HX) and light (^LX) isotopes relative to reference materials. As differences in isotopic composition are minuscule, δ values are expressed in per mil (‰, parts per thousand):

$$\delta^{HX} = \left[\frac{\left(\frac{^{HX}}{^{LX}}\right)_{sample} - \left(\frac{^{HX}}{^{LX}}\right)_{standard}}{\left(\frac{^{HX}}{^{LX}}\right)_{standard}} \right] \cdot 1000\% \quad (1.10)$$

where δ^{HX} is isotopic composition of element of interest (e.g., $\delta^{34}S$, $\delta^{13}C$), $(^{HX}/^{LX})_{sample}$ and $(^{HX}/^{LX})_{standard}$ are the ratios of heavy and light isotope of the sample and reference material, correspondingly.

Positive $\delta^{34}S$ values indicate that the sample is enriched in heavy isotopes compared to the reference material used. Negative δ values indicate a reduced amount of the heavy isotope in comparison with the standard. Such measurements of differences in heavy and light isotope ratios provide far greater precision than using absolute ratio values of the samples. This is achieved by using multiple ion collectors to calculate ratios, which effectively cancel out the measurement fluctuations and inherent noise generated in the source and focusing components of the mass spectrometer (Fry, 2006).

In atmospheric studies, insights into the sources of sulfur pollution can be obtained through the analysis of isotopic compositions of sulfate aerosols. Emissions from different pollution sources are characterized by distinct stable sulfur isotope signatures, which can be traced through measurements of sulfate in particulate matter. A summary of different sulfur source $\delta^{34}S$ value ranges is given in Fig. 1.4.

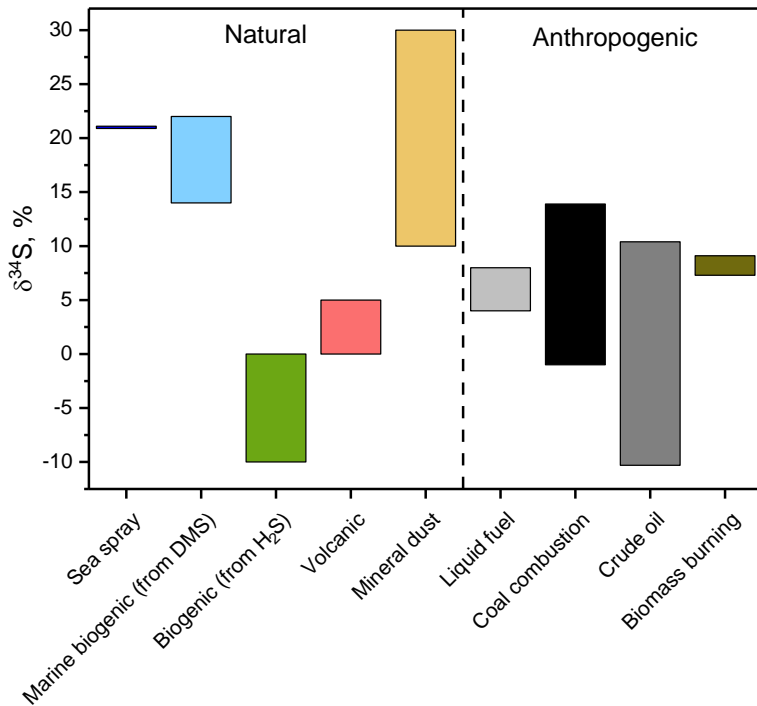


Fig. 1.4. Typical isotopic composition ($\delta^{34}\text{S}$) value ranges of atmospheric sulfur emission sources. Dashed line separates the natural and anthropogenic sources. The following literature sources were used: marine biogenic SO_2 emissions, from DMS oxidation (Calhoun et al., 1991; Sanusi et al., 2006); biogenic SO_2 , from H_2S oxidation (Norman et al., 2004); volcanic SO_2 (Liotta et al., 2012; Nguyen and Putaud, 1993); mineral dust sulfate (Strauss, 1997); liquid fuel SO_2 /sulfate (Norman et al., 2004); coal combustion SO_2 (Górka et al., 2017); crude oil SO_2 (Becker and Hirner, 1998; Dasari and Widory, 2024); biomass burning sulfate (Sawlani et al., 2019).

Although sulfur emissions from natural sources are characterized by well-defined isotopic composition ranges, anthropogenic sources display strong regional dependence. Significant variability in $\delta^{34}\text{S}$ values for anthropogenic sulfur sources, with overlapping ranges, complicates their differentiation. Thus, these source isotopic composition ranges must be constrained to region-specific isotopic endmembers that would allow identifying and quantitatively evaluating their contributions. The analysis of sulfur compounds with distinct regional isotopic compositions allows stable isotope analysis to be used as a signature-based method for tracing the origins of pollution sources (Dasari

and Widory, 2024; Guo et al., 2010; Han et al., 2017; Li et al., 2020). The $\delta^{34}\text{S}$ values of region-specific sources that could influence urban air quality levels in Vilnius are discussed in Chapter 1.7.

Similarly, to sulfur isotopes, stable isotope analysis of carbon ($\delta^{13}\text{C}$) allow for characterization of carbonaceous aerosol pollution sources, as their $\delta^{13}\text{C}$ values possess unique values for biomass, coal, or liquid fossil fuels. This approach has been applied in multitude of studies worldwide (Bikkina et al., 2016; Cachier et al., 1985; Dong et al., 2023; Fisseha et al., 2009; Górká et al., 2023; Kundu and Kawamura, 2014; Kunwar et al., 2016; Li et al., 2022; Masalaite et al., 2018, 2017; Vodička et al., 2019). A summary of $\delta^{13}\text{C}$ values for different carbon sources is presented in Fig. 1.5.

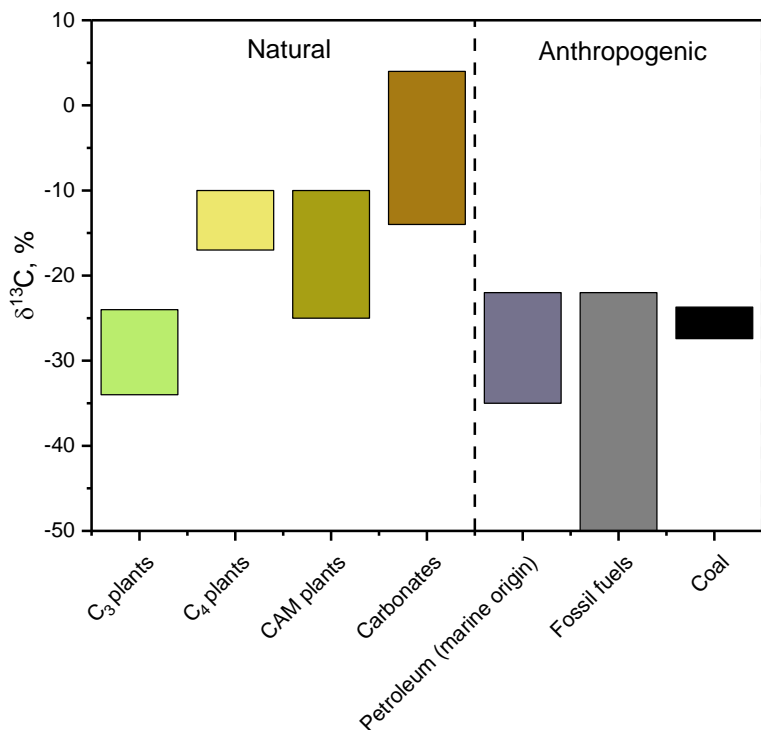


Fig. 1.5. Carbon isotopic composition value ($\delta^{13}\text{C}$) ranges of natural and anthropogenic sources (separated by a dashed line). Adapted from Meier-Augenstein (1999); Suto and Kawashima (2016).

Carbon has only two stable forms: the lighter ^{12}C (98.9 %) and the heavier ^{13}C (1.1 %) (Farquhar et al., 1989). However, radioactive isotope of carbon (^{14}C or radiocarbon) is of particular importance, with a half-life of 5730 ± 40 years (Hajdas et al., 2021; Stenström et al., 2011). The ^{14}C is a radioactive

cosmogenic isotope which forms in the upper layers of the troposphere and stratosphere when nitrogen (^{14}N) captures thermal neutrons. These thermal neutrons are produced through various nuclear reactions as cosmic radiation interacts with the atmosphere. The natural abundance of radiocarbon is very low and equal to only 1 ppt (10^{-12}). In the atmosphere, ^{14}C quickly oxidizes to ^{14}CO and later to $^{14}\text{CO}_2$, which then participates in the carbon cycle (Rom et al., 2000). $^{14}\text{CO}_2$ may then be incorporated into the food chain as plants absorb the radiocarbon from the atmosphere through photosynthesis, and these plants are then consumed by animals or humans. Following that, carnivorous animals consume herbivores and so acquire the same radiocarbon ratio. As a result, the ^{14}C concentration in the biosphere is in equilibrium with the atmosphere. When an organism dies, its exchange of ^{14}C with the atmosphere stops, and the amount of radiocarbon begins to decrease due to radioactive decay. This is the core principle of radiocarbon dating, where the remaining ^{14}C content in a sample is measured to estimate the time that has passed since the organism ceased exchanging ^{14}C with the atmosphere (Hajdas et al., 2021). In environmental studies, radiocarbon data is usually expressed in percent modern carbon (pMC):

$$pMC = \frac{A_{SN}}{A_{ON}} \times 100\% \quad (1.11)$$

where A_{SN} is the sample activity normalized for fractionation, A_{ON} is the absolute activity of an international reference material.

Percent modern carbon is used in radiocarbon dating and environmental studies to denote the relative amount of ^{14}C in a sample compared to a reference material. For example, 100 pMC is indicative of radiocarbon levels in atmosphere as of 1950, a year before widespread nuclear testing in the atmosphere. Values higher than 100 pMC are indicative of post-1950 samples affected by nuclear bomb tests, and samples lower than 100 pMC are older and depleted in ^{14}C . Radiocarbon analysis provides a robust approach for unambiguous distinction between fossil and non-fossil sources, and, in combination with stable isotope analyses of carbon, can provide a detailed characterization of particles formed during combustion processes (Dusek et al., 2017; Garbaras et al., 2018; Garbarienė et al., 2016; Kirillova et al., 2013; Ni et al., 2018). In this thesis, multiple isotope analysis (^{34}S , ^{13}C , and ^{14}C) was applied to examine common anthropogenic source origins of sulfate and carbonaceous aerosols. To our understanding, no previous studies have used such an approach to investigate the sources of aerosol pollution.

1.5. Isotope fractionation

Isotope fractionation refers to the process by which isotopes of a particular element are unequally distributed between different substances, causing an enrichment or depletion of heavier isotope (or lighter) in one phase relative to another. Isotope fractionation is responsible for the distinct isotopic compositions observed across different mediums. Fractionation occurs due to the chemical and physical differences in their properties that arise from the varying atomic masses of the different isotopes. The origin of isotope fractionation is in isotope effects that occur at an atomic level, where slight differences in atomic mass can lead to noticeable effects on the formation and breaking of chemical bonds. Generally speaking, isotope fractionation refers to the measurable differences between the isotopic compositions of reactants and their products, while isotope effects describe the physical processes responsible for the observed isotopic differences. Isotopic mass differences primarily influence the vibrational bond components (stretching or bending) of molecules, with minimal impact on their rotational and translational motions for most molecules (Hoefs, 2021). To illustrate the fractionation mechanism, it is convenient to consider a simple molecule, such as X-H (e.g., H₂S), where X is some compound or atom and H is the hydrogen atom (¹H or ²H). Fig. 1.6 presents a potential energy curve (for an anharmonic oscillator) of the molecule X-H, illustrating the vibrational energy levels for both the lighter isotope ¹H and its isotopologue, the heavier deuterium ²H.

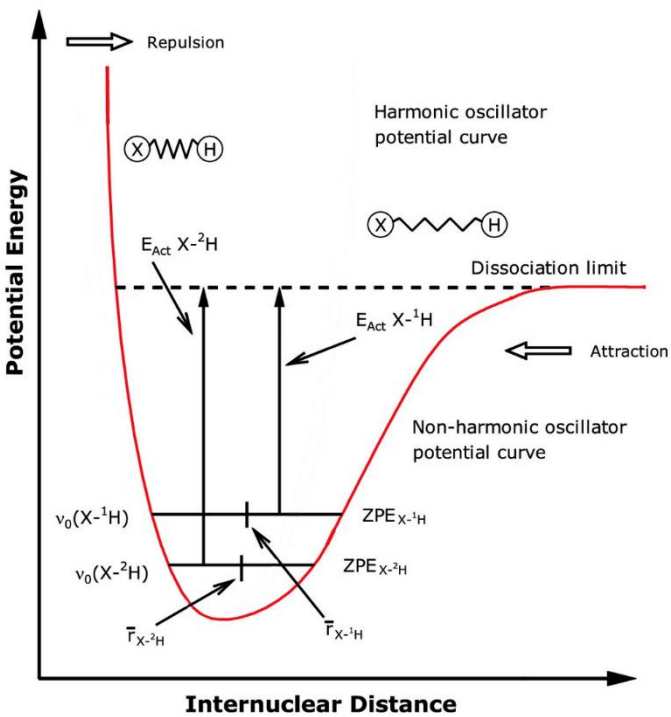


Fig. 1.6. Potential energy diagram of diatomic molecule of hydrogen and any X atom. The terms $ZPE_{X^{-1}H}$ and $ZPE_{X^{-2}H}$ represent zero point energies of 1H and 2H , with corresponding vibrational levels of $v_0(X^{-1}H)$ and $v_0(X^{-2}H)$. The terms $E_{Act}(X^{-1}H)$ and $E_{Act}(X^{-2}H)$ refer to the activation energies required to break the bonds of the molecules $X^{-1}H$ and $X^{-2}H$, respectively. Adapted from (Werner and Cormier, 2022).

By solving the Schrödinger equation for such system (Fig. 1.6), we find the quantum energies associated with vibrational modes (Gulbinas V, 2008):

$$E_n = \left(n + \frac{1}{2} \right) h\nu \quad (1.12)$$

where n is the quantum number, h is the Planck constant, ν is the vibrational frequency. Vibrational frequency is expressed as:

$$\nu = \frac{1}{2\pi} \sqrt{\frac{k}{\mu}} \quad (1.13)$$

where k is the force constant and μ is the reduced mass of the molecule:

$$\mu = \frac{m_1 \times m_2}{m_1 + m_2} \quad (1.14)$$

where m_1 and m_2 are the masses of corresponding atoms.

As we can see from Eq. 1.13, the vibrational frequencies depend on the reduced mass of the molecule constituents. It follows that a molecule with a heavier isotope, in this example ^2H , reduces the vibrational frequency of the bond and the vibrational levels of isotopically heavier molecules sit lower in the potential well ($\text{ZPE}_{\text{X}-2\text{H}} < \text{ZPE}_{\text{X}-1\text{H}}$). Thus, the bonds of isotopically lighter molecules are easier to break ($E_{\text{Act}}(\text{X}-^1\text{H}) < E_{\text{Act}}(\text{X}-^2\text{H})$). Additionally, the average bond lengths of molecules involving lighter isotopes are slightly longer than those involving heavier isotopes, as depicted by the horizontal black lines indicating the differing intramolecular bond lengths in Fig. 1.6 (Vogel and Houk, 2018). The consequence of these mass-dependent differences is that the bond involving the heavier isotope is harder to break, as such molecules have lower potential energy and require more energy to dissociate. Thus, when energy is added to a system containing both isotopically light and heavy molecules, the bonds in the lighter molecules are more likely to break, leading to discrimination against the heavier isotopes. This process results in isotope fractionation. However, the formation of new bonds is not simply a reverse of the previously described process. The isotopically heavier atoms need higher activation energy to form bonds. Consequently, the reaction rates for both bond cleavage and formation are generally slower for heavier isotopes.

During various kinetic and chemical equilibrium reactions, the reaction rates vary for isotopes of different masses, leading to varying degrees of enrichment or depletion of isotopes. Isotope fractionation primarily arises from two fundamental mechanisms: equilibrium isotope effects (EIE), also referred to as thermodynamic isotope effects or isotope exchange processes, and kinetic isotope effects (KIE). These mechanisms will be examined in greater detail in the subsequent chapters.

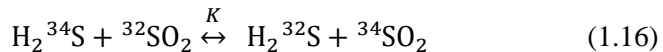
1.5.1. Equilibrium isotope effects

During isotope exchange processes, heavy isotopes tend to concentrate in compounds where the bonds are strongest, as these isotopically heavy molecules require higher activation energies to break bonds (Bigeleisen, 1965). During isotope exchange reactions, the chemical reactions do not go to completion; instead, isotopes are unevenly distributed between different

phases or molecules. General isotope exchange reactions are expressed as (Hoefs, 2009):



where light and heavy isotopes are denoted with subscripts (L and H, respectively) on the elements A and B involved. K is the equilibrium constant. For example, equilibrium reaction for hydrogen sulfide and sulfur dioxide is written as (Thode, 1991):



For this reaction, equilibrium constant K can be expressed as either ratio of concentrations or partition functions Q :

$$K = \frac{[^{34}SO_2]/[^{32}SO_2]}{[H_2^{34}S]/[H_2^{32}S]} = \frac{Q^{34}SO_2/Q^{32}SO_2}{QH_2^{34}S/QH_2^{32}S} \quad (1.17)$$

Partition function is the summation of all possible energy levels E_i of the system and describes the probability of a system being at a state i :

$$Q = \sum_i g_i e^{-E_i/kT} \quad (1.18)$$

where g_i is the degree of degeneracy of the i state and describes whether a specific energy level has more than one energetically equivalent quantum states, k is the Boltzmann constant and T is the temperature of the system.

In isotope studies, a reduced partition function is often employed, expressed as the ratio of partition functions of heavy and light isotopes, Q_H/Q_L (Hoefs, 2021; Urey, 1947). The partition function of a specific molecule can be divided into components of vibrational, rotational, or translational energy levels. However, as mentioned previously, rotational and translational energy differences are consistent between isotopologues, with vibrational energy differences being the main cause of fractionation effects (Hoefs, 2009). An exception is hydrogen, where rotational energy differences also need to be considered between isotopologues, due to large atomic mass differences. Therefore, in Eq. 1.17, for most cases, only the vibrational energy states need to be considered for calculating equilibrium constants.

The equilibrium constant K is used to assess the extent of equilibrium isotope effects; if K differs from 1, it indicates that the isotope ratios, such as $^{34}\text{S}/^{32}\text{S}$, will vary between the equilibrated phases. In environmental studies, the constant K is usually replaced by fractionation factor α (Werner and Cormier, 2022):

$$\alpha = \frac{R_A}{R_B} \quad (1.19)$$

where R_A and R_B are isotope ratios for compound A or compound B, correspondingly. Fractionation factor values of $\alpha > 1$ denote an enrichment of the heavy isotope in compound A, while values lower than 1 signify a depletion of the heavy isotope. The relation between fractionation factor and equilibrium constant K is given as:

$$\alpha = K^{1/N} \quad (1.20)$$

where N is the exchanged atom number during the reaction. An alternative way of expressing fractionation factor α is through a more convenient ε notation, typically expressed in parts per thousand (‰):

$$\varepsilon = (\alpha - 1) \times 1000 \text{ ‰} \quad (1.21)$$

The ε notation is also referred to as the fractionation factor or, occasionally, as the isotopic enrichment factor. In practice, isotope fractionation can be conveniently approximated by measuring the $\delta^{34}\text{S}$ values of the reactant (or compound A) and the product (compound B) given in Eq. 1.22, which is related to other notations by Eq. 1.23.

$$\Delta^{34}\text{S} = \delta^{34}\text{S}_A - \delta^{34}\text{S}_B \quad (1.22)$$

$$\Delta^{34}\text{S} \approx \varepsilon = \alpha \quad (1.23)$$

For differences of less than 10 ‰ between reactant and product, this approximation agrees very well with the “real” fractionation values of α . The distinction between these notations becomes negligible, considering that uncertainties of $\delta^{34}\text{S}$ (or other isotopic elements) measurements often exceed 0.1 ‰ (Hoefs, 2021).

An example of equilibrium isotope effects is given in Fig. 1.7, which displays the reaction of H₂S and SO₂ as they reach isotopic equilibrium at 800 K in the aqueous phase.

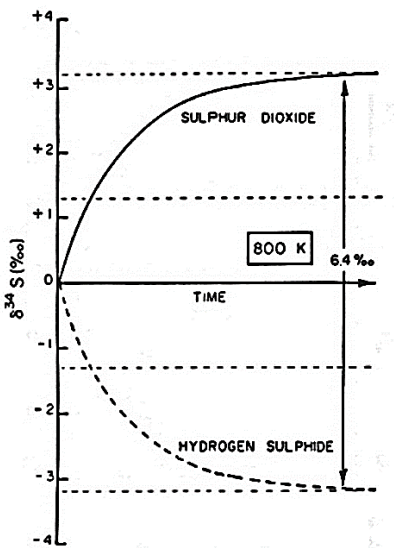


Fig. 1.7. Isotope equilibrium effects (EIE) visualized through changes in $\delta^{34}\text{S}$ values as equilibrium between H₂S and SO₂ is reached. Adapted from Thode (1991).

As equilibrium is reached ($K = 1.0064$), sulfur dioxide is enriched with heavy isotope and is 6.4 % heavier than hydrogen sulfide. The largest differences in isotope ratios are typically observed between the species with the greatest differences in oxidation states, such as between H₂S (with sulfur in the -2 oxidation state) and SO₄²⁻ (with an oxidation state of +6), with $K = 1.074$ (Thode, 1991). The ³⁴S is bound more strongly in the more oxidized species, in this case, to SO₄²⁻. In the atmosphere, equilibrium isotope effects are significant in various heterogeneous oxidation reactions of SO₂ (Eriksen et al., 1972a) and will be examined further in Chapter 1.6.

1.5.2. Kinetic isotope effects

Kinetic isotope effects (KIE) can be considered a unidirectional form of equilibrium isotope effects, where the reactions are irreversible. In this case, fractionation arises from the different reaction rates between the isotopically heavier and lighter compounds. Additional examples of KIE include

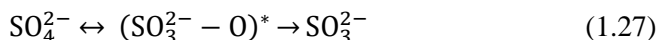
evaporation, condensation, dissociation, and diffusion. If we consider the reduction of sulfate to hydrogen sulfide for ^{34}S and ^{32}S isotopes:



The k_{32}/k_{34} ratio is equal to 1.022 at 20 °C, meaning that the lighter isotope reacts at a faster rate and the produced H_2S is ~22 ‰ depleted in ^{34}S when compared to the reactant sulfate. Similarly to the EIE constant K , the k_{32}/k_{34} ratio can be expressed as the ratio of two partition functions (Hoefs, 2021; Thode, 1991):

$$\frac{k_{32}}{k_{34}} = \left[\frac{Q^{34}\text{SO}_4^{2-}/Q^{32}\text{SO}_4^{2-}}{(Q^{34}\text{SO}_4^{2-})^*/(Q^{32}\text{SO}_4^{2-})^*} \right] v_{32} \quad (1.26)$$

Here, $(Q^{34}\text{SO}_4^{2-})^*$ and $(Q^{32}\text{SO}_4^{2-})^*$ represent the reactant partition functions of the transition state, which refers to the molecular configuration at an intermediate reaction step between the reactants and the products. Energy (E_{Act}) must be added to the reactants to reach activated transition state, which is in equilibrium with the ground state of the reactants. Once the reaction proceeds to form products, it becomes irreversible (Werner and Cormier, 2022). For isotopically heavier molecules with lower vibrational frequencies, higher activation energy E_{Act} is required to reach the transition state, causing isotopically lighter molecules to react more quickly. The factor v_{32}/v_{34} refers to mass term ratio of the ^{32}S and ^{34}S isotopes and is related to the vibrational frequencies of the activated state. An example of such a reaction is the reduction of SO_4^{2-} to SO_3^{2-} , which involves an intermediate step where the S-O bond is broken:



Such kinetic isotope effects usually occurs during homogenous gas-phase oxidation reactions in the atmosphere (Leung et al., 2001; Tanaka et al., 1994).

1.5.3. Mass-dependent and mass-independent isotope effects

Mass-dependent fractionation (MDF) effects occur when isotopic fractionation is proportional to the isotope mass differences, leading to predictable isotopic enrichment or depletion patterns between different isotopes of the same element. Thus, during MDF processes, the magnitude of fractionation is directly related to the relative mass differences between isotopes. These MDF effects are commonly observed in most natural processes and apply to equilibrium and kinetic processes. In practice, it is convenient to display mass-dependent fractionation as a single linear slope of a three-isotope plot, such as $\delta^{33}\text{S}$ vs $\delta^{34}\text{S}$ or $\delta^{36}\text{S}$ vs $\delta^{34}\text{S}$ (Hoefs, 2021; Thiemens, 2006). For example, the three-isotope plot of $\delta^{33}\text{S}$ vs $\delta^{34}\text{S}$ has a slope of 0.515, and α_{34} is about twice larger than α_{33} (Hulston and Thode, 1965). This also holds true for other elements, such as oxygen. Any sufficiently large deviations from this slope are considered as mass-independent isotope effects.

Mass-independent fractionation (MIF) occurs when fractionation differences between different isotopes are not related by their relative masses and deviations from the MDF slope in three-isotope plot are observed. The mechanism responsible for mass-independent isotope effects is complex and many processes involving MIF are still largely uncertain (Hoefs, 2021; Thiemens, 2006). An example of MIF in sulfur isotopes is observed when sulfur dioxide (SO_2) undergoes photodissociation by ultraviolet (UV) radiation (190 – 220 nm) (Farquhar et al., 2001), which produces isotopic anomalies ($\Delta^{33}\text{S} \neq 0$ or $\Delta^{36}\text{S} \neq 0$), expressed as:

$$\Delta^x\text{S} = \delta^x\text{S} - 1000 \times \left(\left[1 + \left[\frac{\delta^{34}\text{S}}{1000} \right] \right]^{\beta_x} - 1 \right) \quad (1.28)$$

where $\Delta^x\text{S}$ is the deviation from MDF for sulfur isotope X (e.g. ^{33}S , ^{36}S), $\delta^x\text{S}$ δ value of ^xS isotope, β_x is the relation between isotope ^xS and ^{34}S (e.g. 0.515 for ^{33}S , 1.889 for ^{36}S).

Deviations in $\Delta^{33}\text{S}$ up to 0.2 ‰ may result from MDF, while anomalies exceeding 0.2 ‰ are generally considered indicative of mass-independent processes (Farquhar and Wing, 2003; Harris et al., 2013a). Of particular relevance are volcanic eruptions, as emitted SO_2 can reach the stratosphere, where SO_2 photolysis and oxidation by OH radicals produce sulfate aerosols with pronounced MIF (Endo et al., 2022; Savarino et al., 2003). Naturally, this

can only occur at altitudes higher than 20 km, above the ozone layer. Aerosols formed in this way possess distinct MIF signatures, and they can be deposited onto polar snow, allowing multiple sulfur isotope analysis to trace the origins of past volcanic eruptions (distinguishing between tropospheric and stratospheric injections) or to track past ozone depletion events (Dasari et al., 2022b; Savarino et al., 2003). Moreover, detection of isotope anomalies in ambient particulate matter samples may be indicative of air mass transport between the stratosphere and troposphere (Han et al., 2017; Romero and Thiemens, 2003). In general, in the troposphere, major SO₂ oxidation pathways of OH, H₂O₂, and TMI catalysis cause limited MIF, with $\Delta^{33}\text{S}$ ranging from -0.15 ‰ to 0.20 ‰ (Harris et al., 2013a, 2012b). On the other hand, the O₃ oxidation pathway is unlikely to result in any measurable MIF (Harris et al., 2012b, 2012d). However, the $\Delta^{33}\text{S}$ values of different SO₂ oxidation pathways vary seasonally, with $\Delta^{33}\text{S}$ values fluctuating in opposition to each other, resulting in a net $\Delta^{33}\text{S}$ value of approximately 0 when averaged over the entire duration of the year (Harris et al., 2013a). Nevertheless, significant isotope anomalies ($\Delta^{33}\text{S} = \pm 0.5$) are sometimes detected in aerosols from urban environments, which could be indicative of a new sulfate production mechanisms currently not accounted for in atmospheric models and are yet to be sufficiently explained (Au Yang et al., 2018; Guo et al., 2010; Han et al., 2017; Romero and Thiemens, 2003; Shaheen et al., 2014).

1.6. Isotope fractionation during sulfate production

The predominant production mechanism of sulfate aerosol is the oxidation of gaseous SO₂ emissions. The differences between $\delta^{34}\text{S}$ values of gaseous SO₂ and particulate SO₄²⁻ reflect distinct isotope fractionation processes, and previous studies have shown that these differences are influenced by shifts in dominant SO₂ oxidation pathways. (Kawamura et al., 2001; Saltzman et al., 1983). Different oxidation pathways can either lead to depletion of the heavy isotope ³⁴S or to an enrichment of it. Homogeneous oxidation by OH radicals was initially reported to cause depletion in the production of sulfate (-9.0 ‰ at 25 °C) (Eriksen et al., 1972a, 1972b; Saltzman et al., 1983; Tanaka et al., 1994). However, later empirical studies found that oxidation by hydroxyl radicals leads to an enrichment of 10.5 ‰ at a temperature of 25 °C (Harris et al., 2013a, 2012b). At the same time, previous studies reported that heterogeneous SO₂ oxidation pathways result in a fractionation of 16.5 ‰ at 25 °C (Eriksen et al., 1972a, 1972b). However, there are at least three major aqueous-phase oxidation pathways: H₂O₂, O₃, and transition metal ion-

catalyzed oxidation by O_2 (Alexander et al., 2009; Liu et al., 2021; Shao et al., 2019). Precise laboratory measurements of fractionation factors were conducted by Harris et al. (2013a, 2012b) for the dominant SO_2 oxidation pathways. The following temperature-dependent relationships were reported:

$$\varepsilon_{OH} = (10.60 \pm 0.73) - (0.004 \pm 0.015) \times T \quad (1.29)$$

$$\varepsilon_{H_2O_2} = (16.51 \pm 0.15) - (0.085 \pm 0.004) \times T \quad (1.30)$$

$$\varepsilon_{TMI} = (-5.039 \pm 0.044) - (0.237 \pm 0.004) \times T \quad (1.31)$$

where ε_{OH} , ε_{TMI} and $\varepsilon_{H_2O_2}$ are the fractionation factors for OH, TMI, and H_2O_2 oxidation pathways, respectively. Whereas, T is the temperature in $^{\circ}C$. A summary of sulfate production mechanisms through various SO_2 oxidation pathways and their associated induced isotopic fractionation factors is provided in Fig. 1.8.

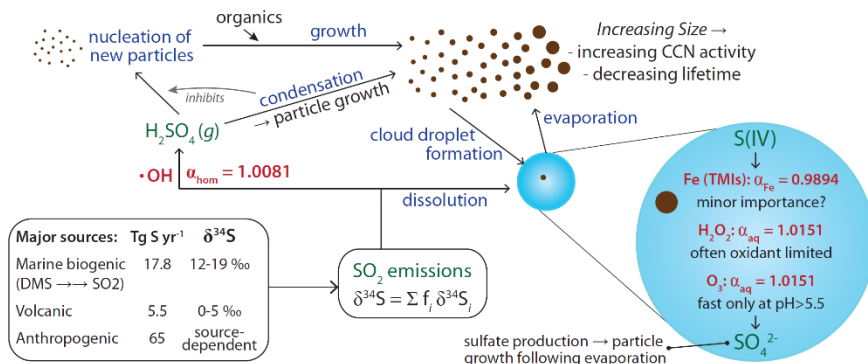


Fig. 1.8. Sulfur emission sources and their fate in the atmosphere. Adapted from Harris et al. (2012b). All fractionation factors (α) are calculated for 19 $^{\circ}C$.

Both H_2O_2 pathways yield similar heavy isotope enrichment in the product and are sometimes reported as a combined contribution of both pathways (Fan et al., 2020; Li et al., 2020). However, the fractionation factor of the H_2O_2 pathway decreases modestly with rising temperatures. In contrast, SO_2 oxidation by OH produces a lower in magnitude enrichment of ^{34}S with minimal temperature dependence. While oxidation by either OH, H_2O_2 , or O_3

leads to a $\delta^{34}\text{S}$ enrichment in the product, only transition metal ion catalysis produces sulfate that is depleted in $\delta^{34}\text{S}$ (Harris et al., 2013b, 2012a). The above-mentioned fractionation factors, in tandem with measurements of sulfate $\delta^{34}\text{S}$ values, provide a basis for evaluating the relative contributions of distinct SO_2 oxidation pathways, which will be discussed further in Chapter 2.7.

1.7. Region-specific sources of atmospheric sulfur-containing species and carbonaceous PM_{1}

According to national air pollution emission inventories, Lithuania emits 11.3 Gg of SO_2 annually (European Environment Agency, 2023). The primary anthropogenic sources of SO_2 are fuel processing and production, with the Mažeikiai oil refinery contributing 7.1 Gg of sulfur dioxide annually, and fertilizer production facilities in Kėdainiai accounting for 2.2 Gg of SO_2 emissions per year. Other important sources of sulfur pollution include residential emissions (domestic heating), which contribute 1.2 Gg of SO_2 , and electricity/heat generation, responsible for 0.7 Gg of SO_2 emissions annually. The oil refinery in Mažeikiai previously relied heavily on Russian crude oil; however, following Russia's invasion of Ukraine in 2022, the refinery began phasing out Russian oil, shifting to imports of Saudi Arabian origin (LRT, 2022; PKN ORLEN, 2023). Both the oil refinery and fertilizer production facilities are located at a considerable distance northwest of the sampling site, at distances of 270 km and 100 km, respectively. Thus, in Vilnius, local sulfur emissions from the thermal power station (TPS) and domestic heating are expected to contribute more to the observed pollution levels. The Vilnius TPS typically utilizes biomass and natural gas for electricity and heat generation, but during the 2022 – 2023 heating season, it temporarily switched to using low-sulfur heavy fuel oil (HFO) of non-Russian origin due to the reduced availability of natural gas supplies (LRT, 2023). The exact origin of the HFO utilized in Vilnius TPS during this experiment is not publicly disclosed, however, the $\delta^{34}\text{S}$ analysis conducted in this study (see Chapter 3.6) strongly suggests that it may have originated from Saudi Arabia or the United Arab Emirates.

Other possible local sulfur pollution sources include biomass (wood chips or pellets), natural gas and to lesser degree, coal utilized for domestic heating purposes in private houses during the cold season. Although, natural gas contains only trace amounts of sulfur (Brown et al., 2015). The widespread use of biomass for heating is expected to have a notable effect on the sulfur concentrations and isotopic composition at the sampling site. However,

biomass contains only up to 0.2 % sulfur (Demirbas, 2004). Additionally, sulfur emissions from traffic are expected to be negligible due to stringent European Union regulations on sulfur content in fuels (< 10 ppm S) (EU directive 2003/6/EC, 2003).

Sulfur pollution levels in Lithuania have historically been strongly influenced by emissions from neighboring countries such as Poland and Germany, underscoring the significant role of long-range pollutant transport from these regions (Davulienė et al., 2021). In the aforementioned countries, coal combustion has been a primary driver of emissions, with SO₂ emissions in 2021 totaling 392.4 Gg for Poland and 254.5 Gg for Germany (European Environment Agency, 2023; Likus-Cieślik et al., 2020). Coal is significant contributor of sulfur pollution due to its high sulfur content (< 4 %) (Calkins, 1994; Chmielewski et al., 2002). The $\delta^{34}\text{S}$ values of coal are region-specific and depend on the relative proportions of its primary sulfur species: organic sulfur, pyrite and sulfate (Chmielewski et al., 2002; Derda et al., 2007, 2006). Gaseous SO₂ emissions from high-temperature coal combustion reflect the $\delta^{34}\text{S}$ values of its source, but flue gas desulfurization process used to reduce SO₂ emissions in power plants, may deplete the emitted SO₂ $\delta^{34}\text{S}$ values by 6 ‰ (Derda et al., 2007, 2006; Górką et al., 2017). However, coal use in Lithuania is minimal (International Energy Agency, 2022; Konstantinaviciute et al., 2014). Additionally, Russia and Belarus may also significantly contribute to Lithuania's SO₂ levels, as they heavily rely on heavy fuel oil for energy production, oil refining, and industrial processes (Fioletov et al., 2016; United Nations Economic Commission for Europe, 2016).

Biogenic emissions are present during summer months, characterized by $\delta^{34}\text{S}$ values ranging from -10 ‰ to 0 ‰, their contribution is expected to be minimal relative to anthropogenic emissions (Górką et al., 2017; Sinha et al., 2008). Similarly, sea spray emissions are expected to have negligible impact in Vilnius year-round due to the city's considerable distance from the coast (~250 km) (Lim et al., 2014; Tichomirowa et al., 2007). Additionally, terrigenous primary sulfate from resuspended soil dust particles typically makes a minor contribution in the PM₁ fraction and was not therefore not considered in this current study (Hien et al., 2021).

1.7.1. Statistical Bayesian isotope mixing model for source apportionment of sulfur-containing species

In this thesis, statistical Bayesian mixing model FRUITS (Food Reconstruction Using Isotopic Transferred Signals) was applied for

evaluating mixing equations and quantifying the relative contributions of various sources with improved accuracy (Fernandes et al., 2014). Although, the FRUITS model was originally developed for the human and animal diet studies (Fernandes et al., 2014), this tool and other Bayesian statistical models can be applied to various other isotope mixing problems (Dasari et al., 2022a, 2020; Dasari and Widory, 2024; Lee et al., 2002). The FRUITS model provides a quantitative estimate of source contributions by calculating the most probable outputs of distinct sources that equate to the signal of the measured target, even in undetermined systems. Endmember (source $\delta^{34}\text{S}$ values) uncertainties are far larger than measurement uncertainties, and in order to accurately estimate source contributions, source $\delta^{34}\text{S}$ value variation must be accounted for. Thus, the simulations account for associated uncertainties of both the measured data and source signals and are derived from Markov Chain Monte Carlo (MCMC) algorithms. MCMC methods approximate complex posterior distributions of source contributions by generating samples through a Markov chain, where each step depends only on the previous one, ultimately converging to the target posterior distribution. The FRUITS model also allows accounting for isotopic fractionation. The model is formulated by the following equation:

$$H_k = \frac{\sum_j (W_{jk} \sum_i \alpha_i C_{ij} [I_{ijk} + T_k])}{\sum_j (W_{jk} \sum_i \alpha_i C_{ij})} \quad (1.32)$$

where:

- H_k is the measured isotopic signal ($\delta^{34}\text{S}$) in the k^{th} level (e.g. PM₁ sulfate), based normal distribution of signal $H_k \sim N(\mu_{H,k}, \delta_{H,k}^2)$ and $\mu_{H,k}$ represents the average measured value and the uncertainty of it - $\delta_{H,k}^2$.
- α_i is the unknown contribution of i^{th} level source (e.g. sources of biomass, coal, HFO), where $0 \leq \alpha_i \leq 1$ and $\sum_{i=1}^n \alpha_i = 1$.
- I_{ijk} is the source isotopic signal, associated with i^{th} level source and k^{th} level measured values. Modeled by normal distribution to account for source value uncertainties, $I_{ijk} \sim N(\mu_{I,ijk}, \delta_{I,ijk}^2)$.
- T_k is the isotopic fractionation offset for the k^{th} level isotopic signal, $T_k \sim N(\mu_T, \delta_{T,k}^2)$. It is only considered when evaluating PM₁ sulfate contributions.
- W_{jk} is the weighed contribution of j^{th} source fraction, to account for preferential inputs to the measured signal. For example, if some sources do not contribute to the measured $\delta^{34}\text{S}$ values, or contribute less. In our case, all defined sources contributed equitably to the

- measured signal values, that is, only SO_2 emissions contribute to measured PM_{1} sulfate signal. Thus, $W_{jk} = 1$.
- C_{ij} is the concentration of the j^{th} fraction of the i^{th} level sources, which were unknown.

The model, through application of MCMC simulations, yields probability distributions and boxplots for each source, an example of which are given in Fig. S1. In total, 10 000 runs were made for each sample, 5 000 of which were discarded after reaching convergence. For the isotopic mixing equations in this thesis, the uncertainties of calculated contributions were within 15 %.

1.7.2. Evaluation of sulfur source contributions

In order to quantitatively evaluate the influence of individual sulfur pollution sources, appropriate isotopic source endmembers must be chosen. The following sources of sulfur pollution were considered appropriate for Vilnius: biomass combustion, coal combustion of Polish (PL) origin, HFO emissions of Saudi Arabian (SA)/United Arab Emirate (UAE) origin and crude oil emissions of Russian (RU) origin. A comprehensive summary of potential sulfur pollution sources with their corresponding $\delta^{34}\text{S}$ values used in this study is provided in Table 1.2.

Table 1.2. The $\delta^{34}\text{S}$ values of distinct sulfur pollution source emissions relevant for Vilnius. Brackets indicate the origin of pollution source fuels: coal of Polish origin (PL), heavy fuel oil of Saudi Arabian or United Arab Emirate origin (SA + UAE), crude oil of Russian origin (RU).

Sulfur pollution sources	Emission $\delta^{34}\text{S}$ values, ‰
Biomass burning	7.3 – 9.1 ‰ ^a
Coal combustion (PL)	-1 – 4.4 ‰ ^b
Heavy fuel oil emissions (SA + UAE)	-10.3 – 0.7 ‰ ^c
Crude oil emissions (RU)	Evolved emissions: ~1.1 ‰ ^d Liquid crude oil: 2.7 – 5.3 ‰ ^e

^a(Sawlani et al., 2019); ^b(Górka et al., 2017); ^c(Becker and Hirner, 1998; Dasari and Widory, 2024); ^d(Maruyama et al., 2000); ^e(Becker and Hirner, 1998).

It is important to note that heavy fuel oil of Russian origin may have been used in Lithuania or neighboring countries during the entire sampling periods. However, its $\delta^{34}\text{S}$ values overlap with those of coal combustion, therefore, crude oil inputs of Russian origin will not be analyzed separately but rather considered as a combined contributor in the analysis.

The fractional contributions of SO₂ and sulfate aerosol sources were determined using a mixing equation approach:

$$\delta^{34}\text{S} = \delta^{34}\text{S}_{\text{Coal,Oil}} f_{\text{Coal,Oil}} + \delta^{34}\text{S}_{\text{Biomass}} f_{\text{Biomass}} + \delta^{34}\text{S}_{\text{HFO}} f_{\text{HFO}} \quad (1.33)$$

where $f_{\text{Coal,Oil}}$ is the relative source contribution of coal combustion + fuel oil (RU) emissions, f_{Biomass} is the contribution of biomass burning, f_{HFO} is contribution of HFO (SA + UAE) emissions. The sum of the fractions $f_{\text{Coal,Oil}}$, f_{Biomass} and f_{HFO} equals 1. The $\delta^{34}\text{S}_{\text{Coal,Oil}}$, $\delta^{34}\text{S}_{\text{Biomass}}$, $\delta^{34}\text{S}_{\text{HFO}}$ values are their respective isotopic compositions of evolved source emissions.

1.7.3. Evaluation of carbonaceous PM₁ source contributions

Isotope mixing equations were also applied to calculate the source contributions of carbonaceous particulate matter for selected periods:

- From January 11, 2020 to March 16, 2021. Discussed in Chapter 3.5.
- from December 10, 2021 to February 18, 2022. Discussed in Chapter 3.6.
- from October 17, 2022 to March 10, 2023. Discussed in Chapter 3.6.

Three primary sources of carbonaceous PM pollution: biomass burning, coal combustion, and other fossil fuel emissions, were identified as relevant to this study, based on prior source apportionment research conducted in Lithuania (Garbarienė et al., 2016; Mašlaitė et al., 2012). Their source values are provided in Table 1.3.

Table 1.3. The δ¹³S values of distinct carbon pollution sources relevant for Vilnius.

	Emission δ ¹³ C values, ‰
Biomass burning	-27 – -26 ‰ ^a
Coal combustion	-24.5 ± 0.8 ‰ ^b
Liquid fossil fuel emissions	-29 – -28 ‰ ^c

^a(Garbaras et al., 2015; Garbarienė et al., 2016); ^b(Górka et al., 2014; Widory, 2006; Yao et al., 2022);

^c(Garbarienė et al., 2016; Mašlaitė et al., 2012; Widory, 2006).

The apportionment of carbonaceous PM samples is conducted in analogous way to sulfur with mass-balance calculations:

$$\delta^{13}\text{C} = \delta^{13}\text{C}_{\text{Biomass}} f_{\text{Biomass}} + \delta^{13}\text{C}_{\text{Coal}} f_{\text{Coal}} + \delta^{13}\text{C}_{\text{Fossil}} f_{\text{Fossil}} \quad (1.34)$$

where f_{Biomass} represents the fraction of biomass burning, f_{Coal} corresponds to the contribution of coal combustion and f_{Fossil} denotes the fraction attributed to other fossil fuel (liquid) emissions. The sum f_{Biomass} , f_{Coal} and f_{Fossil} equals 1. The $\delta^{34}\text{S}_{\text{Coal,Oil}}$, $\delta^{34}\text{S}_{\text{Biomass}}$, $\delta^{34}\text{S}_{\text{HFO}}$ values are their corresponding isotopic compositions of particulate matter source emissions.

However, source apportionment of total carbon in particulate matter is challenging due to its diverse composition, which includes an isotopically stable elemental carbon (EC) fraction and a varied organic carbon (OC) fraction, which consists of a multitude of organic compounds. Therefore, in contrast to the sulfur source apportionment, the contribution to carbonaceous PM₁ from fossil fuels emissions (both coal and liquid fuels) was assessed separately using radiocarbon measurements. Considering that fossil fuel sources have no radiocarbon in them, the fraction modern value (f_M) is then equal to 0. On the other hand, the f_M value of biomass sources is estimated to be equal to 1.02 (Heal et al., 2011; Niu et al., 2021; Romano et al., 2022), if the biomass used for domestic heating purposes is sourced from present-day materials rather than biomass aged 50 years or more (Garbariené et al., 2016; Levin and Hesshaimer, 2000). In this way, fraction of non-fossil (f_{nf}) sources can be estimated by:

$$f_{\text{nf}} = \frac{f_M}{1.02} \quad (1.35)$$

The fraction of fossil fuel sources (f_f) is then calculated as:

$$f_f = 1 - f_{\text{nf}} \quad (1.36)$$

Application of radiocarbon measurements enables the unambiguous determination of the fossil fuel contribution to carbonaceous PM₁, thereby simplifying the mixing model in Eq. 1.34.

2. RESEARCH OBJECT AND METHODOLOGY

This chapter provides an overview of sampling procedures, sample pre-treatment and measurement techniques, a description of anomalous events, and other contextually relevant details essential to the study. Details on sample collection and subsequent pretreatment procedures are presented first. Following this, the methods for stable isotope, radiocarbon, and ion concentration measurements are described. Finally, key concepts for interpreting the results are discussed, including air mass transport modeling and calculations of SO₂ oxidation pathway distributions.

2.1. Sample collection

The PM₁ particle samples (92 in total) were collected over a period from November 11, 2020 until June 30, 2023 in Vilnius, Lithuania. Gaseous SO₂ samples (48 in total) were also collected together with PM₁ samples from December 10, 2021 until June 30, 2023. These samples were collected atop a four-story building of Center for Physical Sciences and Technology (Fig. 2.1). The site serves as an example of an urban background location in Lithuania. Situated amidst a blend of private and residential dwellings, the sampling site possesses a relatively low traffic volume compared to other parts of the city. The nearest high-traffic street lies approximately 1 kilometer away, with two other major streets exhibiting lower traffic volumes.

The PM₁ samples were obtained utilizing pre-heated (500°C for 8 hours) quartz fiber filters with a diameter of 150 millimeters (Whatman QM-A). The samples were collected employing a high-volume aerosol sampler (DIGITEL HVS DH-77) operating at 500 L/min (Fig. 2.2). Average sampling duration per filter was 191 hours.

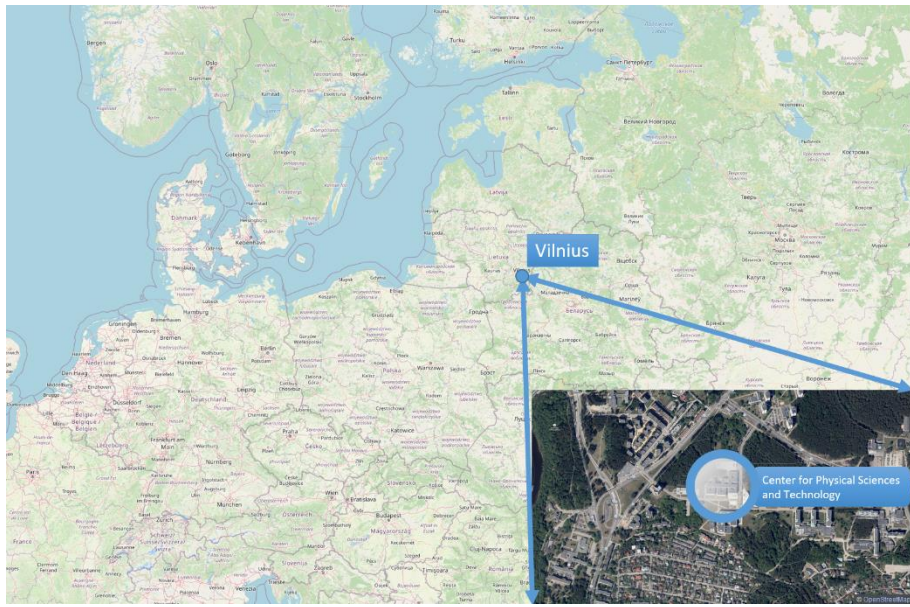


Fig. 2.1. The sampling site located at the Center for Physical Sciences and Technology, Vilnius, Lithuania. (54.72°N, 25.32°E, 158 meters above mean sea level).

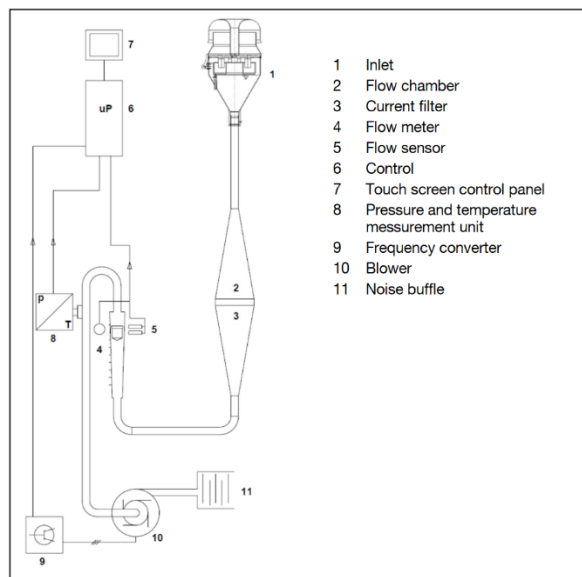


Fig. 2.2. Operational flowchart of the Digitel DH-77. Adapted from DIGITEL Aerosol Sampler DH-77 (2015).

Additionally, collection of SO₂ samples was performed on glass fiber filters (Munktell and Filtrak, Gf-Microfilter) pretreated with potassium carbonate (K₂CO₃) in glycerol solution (Amiri et al., 2018). The potassium carbonate serves as a capturing agent for SO₂ by forming potassium sulfite (K₂SO₃) when it reacts with SO₂ and is retained on the filter material as a stable compound (Huygen, 1963). Glycerol acts as a stabilizing agent on SO₂ and is also hygroscopic. The PM₁ and SO₂ filters were setup in tandem, with first quartz filter used to collect particulate matter, and subsequent K₂CO₃-impregnated glass fiber filter for the collection of SO₂ gases. This method of simultaneous collection of PM₁ and SO₂ is advantageous because of the consistent sampling conditions and allows for integrated analysis and interpretation of the data. Following the sampling procedures, the filters were enveloped in pre-heated aluminum foil, sealed within zip lock bags, and stored at -20°C until subsequent analyses.

2.2. Sample chemical preparation

Before isotopic composition measurements, sulfur has to be extracted from the collected filter materials. In this chemical pretreatment procedure, the water-soluble SO₄²⁻ is precipitated as barium sulfate (BaSO₄) by adding BaCl₂. This method is advantageous because it does not produce noticeable fractionation (Claypool et al., 1980; Fan et al., 2020). The chemical preparation procedure applied in this thesis is widely used in stable isotope studies of atmospheric sulfur compounds (Mayer and Krouse, 2004; Mukai et al., 2001; Zhang et al., 2010).

First, half of the 150 mm quartz fiber filter is shredded and immersed in 100 mL of ultrapure water, followed by ultrasonication for 30 minutes. The following day, samples are filtered using 0.22 µm syringe filters and the resulting solution is acidified with HCl to pH of 2 – 3. The values of pH lower than 4 are necessary for dissolved carbonates to be converted to CO₂ instead of CO₃²⁻, which are typically present in basic solutions and would react with added BaCl₂ to precipitate as BaCO₃. In addition, pH values lower than 2 are to be avoided, because HSO₄⁻ will be the primary sulfate species and will slow down the precipitation of BaSO₄. Next, 5 mL of 1 mol/l BaCl₂ is added in excess, resulting in the precipitation of sulfate ions as BaSO₄. The solution undergoes an additional overnight incubation period to ensure the precipitation of sulfate (including those present as bisulfate ions, HSO₄⁻) as BaSO₄. Subsequently, the precipitate is collected onto 0.2 µm cellulose acetate filters (Sartorius CA Membrane Filters). The filters are then thoroughly washed with 150 ml ultrapure water to eliminate residual chloride ions (Cl⁻).

Following this rinsing step, the samples are dried at 60°C for a duration of 6 hours and, subsequently, the cellulose acetate filters are combusted at 500°C so only the BaSO₄ precipitate is left. By empirical experiments in the laboratory, the 500°C temperature was chosen as optimal for the complete combustion of cellulose acetate filters, with no apparent fractionation measured in $\delta^{34}\text{S}$ values of BaSO₄.

Similarly, for extraction of impregnated SO₂ filters, the procedure is nearly identical, but with an additional prerequisite step. The filters must be treated with 1 ml of 30% w/w hydrogen peroxide to oxidize the captured SO₂ to SO₄²⁻ before the subsequent steps as described previously: sonication, filtration, acidification, addition of barium sulfate, and collection of the precipitate.

2.3. Isotope ratio mass spectrometry

Carbon and sulfur isotopic compositions were determined using a combination of an elemental analyzer (EA) and a stable isotope ratio mass spectrometer (IRMS), presented in Fig. 2.3. The IRMS instruments are designed for precise measurements of minute differences in the proportions of isotopes of light elements, such as ³⁴S/³²S and ¹³C/¹²C, as used in this work. Other major IRMS applications are of ¹⁵N/¹⁴N, ¹⁸O/¹⁶O, and ²H/¹H. Before the IRMS analysis, samples are transformed into simple gases in the elemental analyzer to sulfur dioxide, carbon dioxide, nitrogen, or others, depending on the material's composition and the isotopes under investigation. The mass spectrometer is then used to measure the ratio of ions corresponding to the various isotopic forms of these gases.

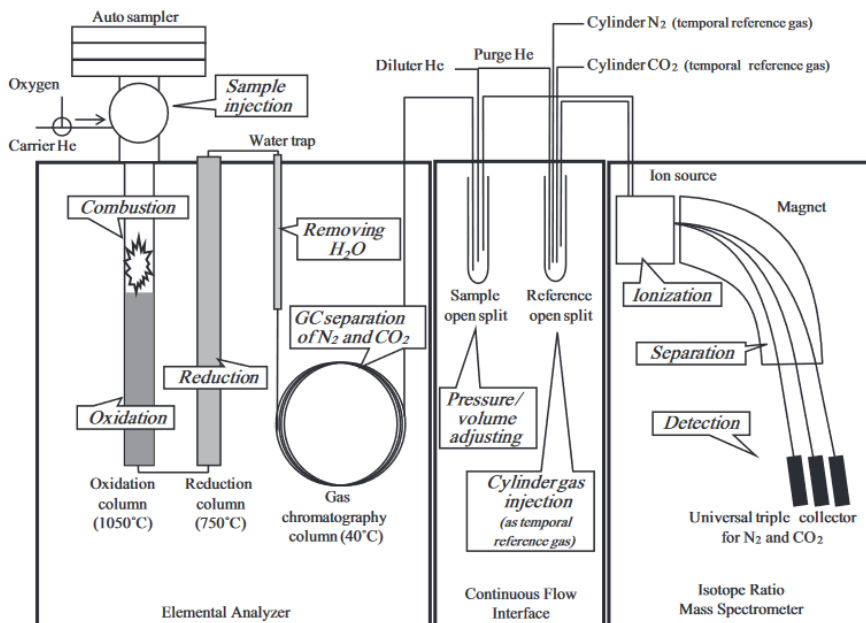


Fig. 2.3. Elemental analyzer – continuous flow interface – isotope ratio mass spectrometer system in carbon and nitrogen measurement configuration. The layout is analogous for sulfur measurement configuration, although typically, only one column is used in elemental analyzer for both combustion and reduction. Adapted from Ogawa et al. (2010).

The system (manufacturer: Thermo Fisher Scientific) used in this work was a Flash EA1112 elemental analyzer connected to a Delta V Advantage mass spectrometer via a continuous flow interface ConFlow III. Within the system (configured for sulfur measurements), samples enclosed in tin capsules undergo combustion in a single oxidation/reduction column of EA, heated to 1050 °C. For sulfur measurements of BaSO₄, approximately 0.50 mg sample material is encapsulated in tin capsules together with vanadium pentoxide (V₂O₅) powder. The tin capsule promotes a violent reaction and local temperature reaches 1800 °C for a few seconds, which is termed as flash combustion. In such a way, the BaSO₄ powder is thermally decomposed to SO₂ gases (Bailey and Smith, 1972). Better results are achieved when using additional O₂ stream and V₂O₅, which promote oxidation (Dunn and Carter, 2018). The oxidation/reduction column is filled with tungsten oxide (used to promote combustion) and copper wires, which reduce SO₃ to SO₂ gases. Immediately after exiting the column, water vapor is removed from the effluent stream through a water trap column filled with magnesium perchlorate (Mg(ClO₄)₂). Magnesium perchlorate is a hygroscopic substance

which is widely used because of its efficient water removal and ease of use (Santos et al., 2004). Subsequently, combustion gases (SO_2 , CO_2 , and N_2) are separated using a gas chromatographic column (Sercon SC2003, PTFE, 2 m), which are then detected through a thermal conductivity detector (TCD). The TCD provides data for calculating the elemental content of the sample by measuring the thermal conductivity of passing gases.

The resulting effluents from the elemental analyzer are then introduced into the continuous-flow interface ConFlo III, through which effluents are directed to the ion source for mass spectrometry analysis via a capillary leak. The ConFlo III facilitates the connection between the EA and the IRMS. Establishing this connection via an open split arrangement is required due to the differences in gas flow through the EA and IRMS (Fig. 2.4). The IRMS operates with a helium flow of around 0.3 ml/min, whereas the EA operates with a helium flow ranging from 80 to 120 ml/min. Thus, the key concept behind the open split arrangement is to reduce this gas flow. This is achieved through the limited size of the IRMS capillary, which limits the gas flow up to 0.3 ml/min. There is also a reference section, required for the reference gas introduction into the IRMS.

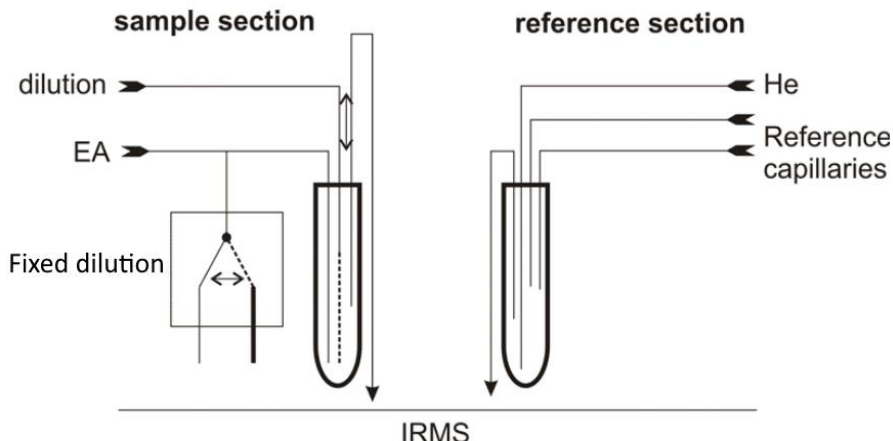


Fig. 2.4. Schematic representation of ConFlo III sections and principle parts. Adapted from Werner et al. (1999).

In the mass spectrometer the diluted effluent is then introduced into the ion source where the gas molecules are ionized with the use of electron ionization method, where gas molecules are bombarded by electrons to produce positive ions. Ionization energies from 70 eV and up to 124 eV are commonly used for this purpose (Dunn and Carter, 2018). Ions are accelerated out of the source with extraction plates and diverted thought system of different lenses,

focusing the ion beam, which is then accelerated via high voltage (around 3 KV). In the mass spectrometer, ions traverse a magnetic field in the sector magnet before reaching the Faraday collectors, which are used to measure the intensity of the specific ion beams. The trajectories of ions and their respective entry into specific Faraday collectors are determined by the strength of the magnetic field and the accelerating voltage. Three Faraday collectors are used as a universal triple collector configuration, which are applied to simultaneously measure mass to charge ratio (m/z) of the desired ions. However, in the case of sulfur measurements, only two detectors are used for m/z ratios of 66 and 64 for SO_2 gases, corresponding to $^{34}\text{S}^{16}\text{O}_2$ and $^{32}\text{S}^{16}\text{O}_2$. For carbon measurements, all three detectors are used for m/z : 44, 45 and 46, corresponding to $^{12}\text{C}^{16}\text{O}_2$, $^{13}\text{C}^{16}\text{O}_2$ and $^{13}\text{C}^{17}\text{O}^{16}\text{O}$. In this case, the m/z of 46 is used to account for the influence of undesired isotopes of oxygen (^{17}O), contributing to the same m/z as ^{13}C isotope. This is termed as the ^{17}O correction and is done automatically by the IRMS software according to predefined algorithms (Assonov and Brenninkmeijer, 2003; Brand et al., 2010). Each collector is connected to an amplifier with its gain calibrated by a precise, high-ohm resistor. Signals from each amplifier are simultaneously recorded approximately every tenth of a second, digitized, and stored by the IRMS data system. This process generates a chromatogram, plotting intensity against time for ions with specific m/z values, with intensity proportional to the number of ions detected (Dunn and Carter, 2018). The IRMS software then integrates the Faraday collector signals of the sample along with single or multiple peaks of the working gas (e.g., SO_2 , CO_2 other gases). The resulting ion current signals are then converted to raw $\delta^{34}\text{S}$ values, referenced against the monitoring gas.

2.3.1. Stable isotope ratio measurement data corrections

Initially, IRMS measurements only provide raw isotope ratios that are in reference to the monitoring gases of known isotopic composition. An example of $\delta^{34}\text{S}$ measurement window is displayed in Fig. 2.5.

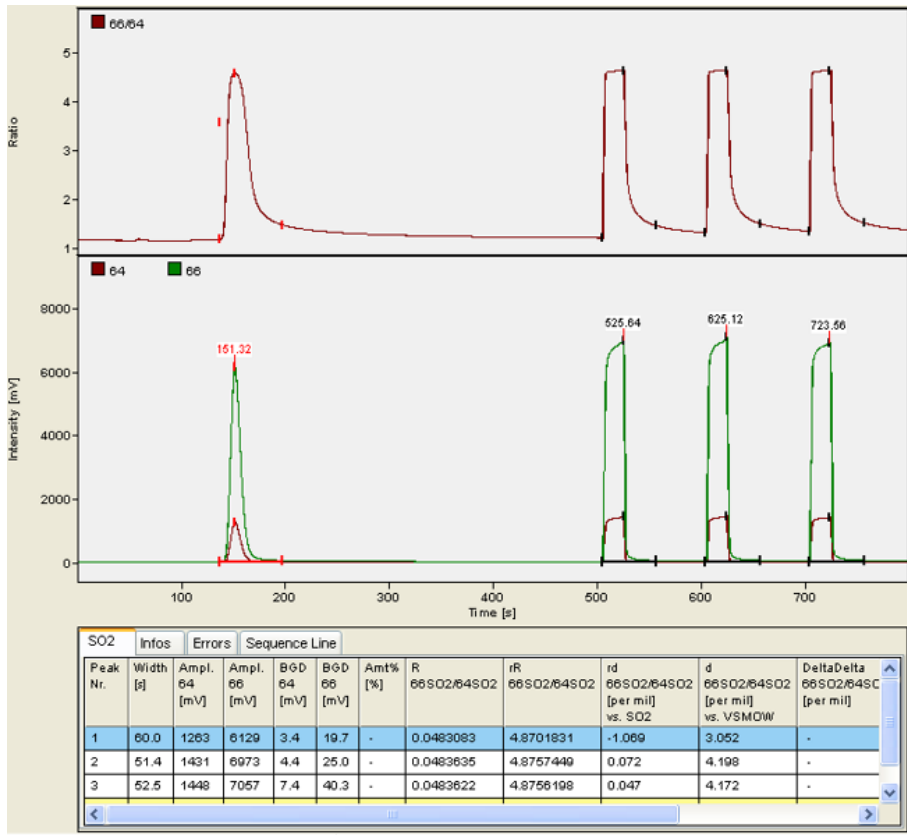


Fig. 2.5. In-program view of $\delta^{34}\text{S}$ measurements in Isodat 2.0. The top window displays mass spectrometry data of m/z ratios (66/64), while the bottom window presents a TCD chromatogram. The first peak on the left corresponds to SO_2 gases derived from the combusted sample material. The following three peaks are monitoring gases, which are used for the initial calculation of raw $\delta^{34}\text{S}$ values.

To ensure result comparability between laboratories, the measured δ values must be linked to international reporting scales (V-CDT for $\delta^{34}\text{S}$ or V-PDB for $\delta^{13}\text{C}$) through the scale calibration (normalization) process. The first reference material (RM) used in sulfur isotope scale realization was iron sulfide (FeS) from the Canyon Diablo meteorite troilite (CDT) found in Arizona, with a ratio of $^{34}\text{S}/^{32}\text{S}$ corresponding to 1/22.22, which has been used since 1962. It is believed that the $^{34}\text{S}/^{32}\text{S}$ ratio in this standard reflects the primordial isotopic values of the solar system, as well as those of Earth's mantle and crust (Thode, 1991). Therefore, this standard value is considered the baseline $\delta^{34}\text{S}$ value, against which contemporary environmental samples

are compared. However, as the supply of the reference material dwindled, and it was further observed that CDT was not sufficiently homogeneous (variability of 0.4 %) to serve as a primary reference standard, the need for a new standard material became evident (Krouse and Coplen, 1997; Werner and Brand, 2001). Consequently, in 1993, the International Atomic Energy Agency (IAEA) proposed a revised V-CDT scale (Vienna-CDT) and developed a new primary reference material IAEA-S-1 for scale realization. The IAEA-S-1 is derived from silver sulfide (Ag_2S) of sphalerite material, with a $\delta^{34}\text{S}$ value of -0.30 ‰ (de Groot, 2004). All modern sulfur isotope compositions are reported as $\delta^{34}\text{S}$ in accordance to V-CDT (Ding et al., 2001).

Historically, isotopic compositions of carbon ($\delta^{13}\text{C}$) were reported in accordance to Pee Dee Belemnite (PDB), a calcium carbonate (CaCO_3) with a $^{13}\text{C}/^{12}\text{C}$ ratio of 0.0112372. The PDB standard was derived from a marine fossil found in the Pee Dee Formation in South Carolina, USA. However, this reference material has since been depleted, leading to the adoption of other standards based on the revised Vienna-PDB (V-PDB) scale. The primary standard became the carbonate NBS-19, with a value of 1.95 ‰. This, too, has been exhausted and is currently replaced by the carbonate IAEA-603, with a value of 2.46 ± 0.01 ‰ (Assonov et al., 2020). However, caution must be exercised when reporting $\delta^{13}\text{C}$ values, because, as of 2024, two scales exist: the V-PDB scale anchored by single primary RM (IAEA-603), and the V-PDB – LSVEC scale, anchored by two RMs (additional LSVEC RM) (Assonov, 2018). In the current study, all $\delta^{13}\text{C}$ values are reported in reference to V-PDB scale.

The normalization process involves measuring reference materials within the same analytical sequence as the samples, using RMs that ideally should span the expected $\delta^{34}\text{S}$ range. Reference materials used are either primary standards (e.g., IAEA-S-1, IAEA-603) or secondary materials calibrated against these primary standards. Primary standards are directly linked to zero-point scale materials (e.g., V-CDT, V-PDB), but their use in routine laboratory measurements is discouraged due to their limited availability (Dunn and Carter, 2018). Instead, the use of secondary (or tertiary) reference materials that are linked to primary RMs is more appropriate. Alternatively, it is common practice in laboratories to use in-house reference materials that are sufficiently homogenous and are carefully calibrated against primary or secondary RMs. All reference materials used should be matrix-matched to the samples, in accordance to principle of identical treatment (PIT), to ensure any bias effects from gas combustion or transfer are equivalent and would cancel out (Carter and Fry, 2013; Dunn and Carter, 2018). In this thesis, SO_2 and particulate sulfate samples were precipitated as BaSO_4 powder and later

analyzed collectively with secondary RMs of IAEA-SO-5 ($\delta^{34}\text{S} = 0.5 \pm 0.2\text{‰}$) and NBS-127 ($\delta^{34}\text{S} = 20.3 \pm 0.4\text{‰}$) reference materials and laboratory working standards, which are also in BaSO₄ form. For $\delta^{13}\text{C}$ measurements, IAEA-600 ($\delta^{13}\text{C} = -27.771 \pm 0.043\text{‰}$) and USGS24 ($\delta^{13}\text{C} = -16.05 \pm 0.04\text{‰}$) RMs were used. By measuring samples and two RMs in one sequence, the following equation of “two-point linear normalization” can be applied for δ scale realization (Dunn and Carter, 2018):

$$\delta_{\text{true(S)}} = \delta_{\text{true(R1)}} + \left([\delta_{\text{raw(S)}} - \delta_{\text{raw(R1)}}] \times \left[\frac{\delta_{\text{true(R1)}} - \delta_{\text{true(R2)}}}{\delta_{\text{raw(R1)}} - \delta_{\text{raw(R2)}}} \right] \right) \quad (2.1)$$

where $\delta_{\text{true(S)}}$ is the normalized value of the sample, $\delta_{\text{true(S)}}$ is the measured value, $\delta_{\text{true(R1)}}$ and $\delta_{\text{true(R2)}}$ are certified isotopic compositions of reference materials 1 and 2, $\delta_{\text{raw(R1)}}$ and $\delta_{\text{raw(R2)}}$ are measured values of the 1 and 2 RMs.

Such conversion of measured δ values to international RM scales allows for intercomparison of the results between different laboratories, which has become a standard practice for more than 30 years now (Dunn and Carter, 2018; Sharp, 2017). In a more general case, multi-point linear normalization is applied by finding the best fit across multiple reference materials (RMs). This approach is represented by the following simple linear regression:

$$\delta_{\text{true(S)}} = m \times \delta_{\text{raw(S)}} + b \quad (2.2)$$

where m is the slope of regression, termed as expansion or stretch factor, and b is the intercept, or the shift factor.

Aside from normalization, other corrections may be necessary, if the measurement sequence displays high blank signals, data drift, poor linearity or memory effects. These corrections are made before normalization and must be consistently applied across the entire sample sequence, according to PIT (Carter and Fry, 2013). Blank correction is performed by the following equation:

$$\delta_{\text{corr(blank)}} = \frac{\delta_{\text{meas}} \times \text{Area}_{\text{meas}} - \delta_{\text{blank}} \times \text{Area}_{\text{blank}}}{\text{Area}_{\text{meas}} - \text{Area}_{\text{blank}}} \quad (2.3)$$

where $\delta_{\text{corr(blank)}}$ is the blank corrected δ value, δ_{meas} is the raw measurement value, δ_{blank} is the δ value of the blank, $\text{Area}_{\text{meas}}$ is the area of measured sample signal, $\text{Area}_{\text{blank}}$ is the area of the blank signal.

Due to small signal peaks, δ_{blank} and $\text{Area}_{\text{blank}}$ are calculated as the average of multiple measurements. In this work, to assess the influence of signals created by blanks, empty tin foil capsules were combusted. However, the resulting signal peaks were negligible and blank correction was unnecessary.

Drift correction is applied to the results if noticeable shift in δ values of RMs over time is observed. Common causes of drift include system leaks, changes in the monitoring gas, efficiency variation of oxidation/reduction column materials, or variations in the ion source. Drift can be corrected by recurring measurements of QC or other RMs, using the following equation (Carter and Fry, 2013):

$$\delta_{\text{corr(drift)}} = \delta_{\text{meas}} - m \times \text{Pos} \quad (2.4)$$

where $\delta_{\text{corr(drift)}}$ is drift corrected δ value, m is the slope of drift curve regression and Pos is the sample number in the sequence.

In the current study, a slight drift in $\delta^{34}\text{S}$ values was observed. To account for this, RMs were measured at regular intervals throughout the sequence, specifically every three to six samples.

Linearity correction must be applied if sample sizes vary greatly, resulting in signal peaks outside the linearity range of the system. Linearity of the instrument is corrected in a similar way to drift, by the following equation:

$$\delta_{\text{corr(linear)}} = \delta_{\text{meas}} - m \times \text{Area} \quad (2.5)$$

where $\delta_{\text{corr(linear)}}$ is linearity corrected δ value, m is the slope of the linearity correction curve and Area is the area of the sample signal peak.

For very small sample sizes, with signal amplitude (at $\text{m/z} = 64$) below 500 mV or an area of $\sim 8 \text{ mV}\cdot\text{s}$, linearity correction was performed. A set of RMs were measured at different weights to plot the linearity correction curve. Alternatively, system linearity can be assessed by introducing monitoring gases of different heights (Dunn and Carter, 2018).

Memory effects are observed when preceding sample residuals affect the subsequent measurement, altering its δ values. This is caused by incomplete removal of preceding sample gases or remaining sample materials. Memory effects are more challenging to correct and require multiple consecutive analyses of the same sample, by discarding the initial measurements.

However, in some applications (e.g. in high conversion temperature IRMS for O and H measurements), the memory effects can influence up to 10 measurements, making aforementioned correction method inadequate (Gröning, 2018). However, there are several methods to apply memory correction as described by Gröning (2018, 2011). One of which, is to calculate correction factor between consecutive sample pairs and to presume that in all subsequent measurements memory effects decrease by the same factor. This factor is further adjusted to account for residual contributions from earlier samples. The final memory correction factor is obtained as the average of all valid factors across the measurement sequence, providing the best estimate of memory effects. However, in this study, continuous-flow EA-IRMS is used, and memory effects were found to have negligible effect, confirmed by consecutive measurement of RMs and working standards. A more detailed description of memory correction methods are provided in a Technical Note on SICalib program by Gröning (2018).

2.3.2. Combined uncertainty evaluation

Corrections, described in the previous chapter, introduce additional sources of uncertainty, alongside the IRMS measurement uncertainties. It is recommended to account for these uncertainties in accordance with International Organization for Standardization Geneva ISBN (2008) guidelines. However, proper analytical conditions, such as using reference materials with the same chemical composition as the samples, helps to minimize the introduction of these new sources of uncertainties (Dunn and Carter, 2018).

The combined δ value standard uncertainty (1σ) for two-point linear normalization are evaluated by the use of partial derivatives, as described by Gröning (2011):

$$u(\delta^{34}S_{\text{sample}}) = \sqrt{\left(\frac{\partial f}{\partial \delta^{34}S_{\text{ref1}}} \right)^2 u(\delta^{34}S_{\text{ref1}})^2 + \left(\frac{\partial f}{\partial \delta^{34}S_{\text{ref2}}} \right)^2 u(\delta^{34}S_{\text{ref2}})^2 + \left(\frac{\partial f}{\partial \delta^{34}S_{\text{m ref1}}} \right)^2 u(\delta^{34}S_{\text{m ref1}})^2 + \left(\frac{\partial f}{\partial \delta^{34}S_{\text{m ref2}}} \right)^2 u(\delta^{34}S_{\text{m ref2}})^2 + \left(\frac{\partial f}{\partial \delta^{34}S_{\text{m sample}}} \right)^2 u(\delta^{34}S_{\text{m sample}})^2} \quad (2.6)$$

where:

- $\left(\frac{\partial f}{\partial \delta^{34}S_{\text{ref1}}} \right)^2 u(\delta^{34}S_{\text{ref1}})^2$ – true (certified) uncertainty of the first reference material;

- $\left(\frac{\partial f}{\partial \delta^{34}S_{\text{ref2}}}\right)^2 u(\delta^{34}S_{\text{ref2}})^2$ – true (certified) uncertainty of the second reference material;
- $\left(\frac{\partial f}{\partial \delta^{34}S_{\text{m ref1}}}\right)^2 u(\delta^{34}S_{\text{w ref1}})^2$ – measuring uncertainty of the first reference material;
- $\left(\frac{\partial f}{\partial \delta^{34}S_{\text{m ref2}}}\right)^2 u(\delta^{34}S_{\text{w ref2}})^2$ – measuring uncertainty of the second reference material;
- $\left(\frac{\partial f}{\partial \delta^{34}S_{\text{m sample}}}\right)^2 u(\delta^{34}S_{\text{w sample}})^2$ – measuring uncertainty of the sample material.

However, such an approach is cumbersome and use of Excel-based Kragten spreadsheets is often more straightforward as it simplifies the calculations. The Kragten spreadsheet method, used for estimating uncertainties arising from normalization, is described in detail by Dunn et al. (2015). This method, allows for easy addition of uncertainties associated with other corrections, as described in Chapter 2.3.1, including drift and linearity corrections that were applied in this work.

2.3.3. Isotope data quality assurance

Quality control (QC) is an essential procedure of stable isotope measurements and is used for assuring optimal IRMS operation of daily measurements and long-term monitoring of the device parameters (Dunn and Carter, 2018). It is performed by measuring quality control reference materials in the same sequence as other RMs and samples. One such application is evaluating the accuracy of the applied normalization by including QC RMs into the sequence that are not used in the scale (in this case, V-CDT or V-PDB) calibration. Successful normalization procedure should yield δ values for the QC materials that match with their true values. In current work, sample matrix-matched material (BaSO_4 powder) was used as an in-house QC material to monitor performance of the IRMS, with its known $\delta^{34}\text{S}$ value ($11.1 \pm 0.5 \text{ ‰}$) validated through previous measurements. Daily measurements of QC materials are evaluated against the mean value within acceptable limits ($< \pm 2\sigma$) after applying all required corrections and normalization steps. Larger deviations indicate faulty measurements and/or applied corrections. Such failures should be investigated to determine if they are random or systematic, according to Westgard rules (Thompson and Wood, 1995). If the measurement sequence passes QC tests, the normalized δ values can be used for further data analysis.

In addition to routine QC RM measurements, participation in interlaboratory comparison exercises is imperative as it ensures the reliability and quality of the δ value measurements and is helpful to track long-term reproducibility of the results.

2.4. Radiocarbon measurements

The samples must undergo a graphitization process before radiocarbon measurements. Graphitization is performed using an Automated Graphitization Equipment (AGE 3, Ionplus AG) connected to a Vario Isotope Select (Elementar Analysensysteme GmbH) EA system. This setup enables the graphitization of samples with low carbon contents ($>40 \mu\text{g}$), employing a punch (0.39 cm^2) of filter material, following a methodology outlined by Butkus et al. (2022). In this approach, PM₁ filter graphitization involves sample dilution, incorporating a mass balance equation to estimate ^{14}C values. The EA-AGE 3 system facilitates separate combustion of multiple punches from a single sample, capturing all released CO₂ in a zeolite trap before transferring it into a single reactor. This methodology allowed for the combustion of one punch of samples containing approximately $100 \mu\text{g}$, with the additional carbon needed for graphitization supplemented from ^{14}C -free phthalic anhydride (PhA). The ^{14}C values are then calculated utilizing a mass balance equation, expressed in percent Modern Carbon (pMC):

$$\text{pMC}_{(\text{mixture})} = \text{pMC}_{(s)} n_{(s)} + \text{pMC}_{(\text{PhA})} n_{(\text{PhA})} \quad (2.6)$$

$$\text{pMC}_{(s)} = \frac{\text{pMC}_{(\text{mixture})} - \text{pMC}_{(\text{PhA})} n_{(\text{PhA})}}{n_{(s)}} \quad (2.7)$$

where pMC_(mixture) represents the measured pMC of the mixture, pMC_(s) denotes the pMC of the reference material with n_s as its partial contribution; and pMC_(PhA) corresponds to the pMC of phthalic anhydride, with $n_{(\text{PhA})}$ as its partial contribution.

Radiocarbon measurements were conducted utilizing a single-stage accelerator mass spectrometer (Fig. 2.6, SSAMS, National Electrostatics Corp.). The phthalic anhydride was employed to estimate the background of measurements, yielding an f_M (fraction of modern carbon, see Eq. 2.8) background value of 2.45×10^{-3} , and NIST OXII served as the reference material. The accuracy of the $^{14}\text{C}/^{12}\text{C}$ ratio measurements was better than 0.3%. The ratio of ^{13}C to ^{12}C plays a crucial role in correcting isotopic

fractionation occurring during the graphite is bombarded with cesium ions, used for AMS analysis of pMC. Subsequently, a normalization is performed, wherein the $\delta^{13}\text{C}$ value is adjusted to -25.0‰, to ensure the accuracy of the final ^{14}C concentration measurements.

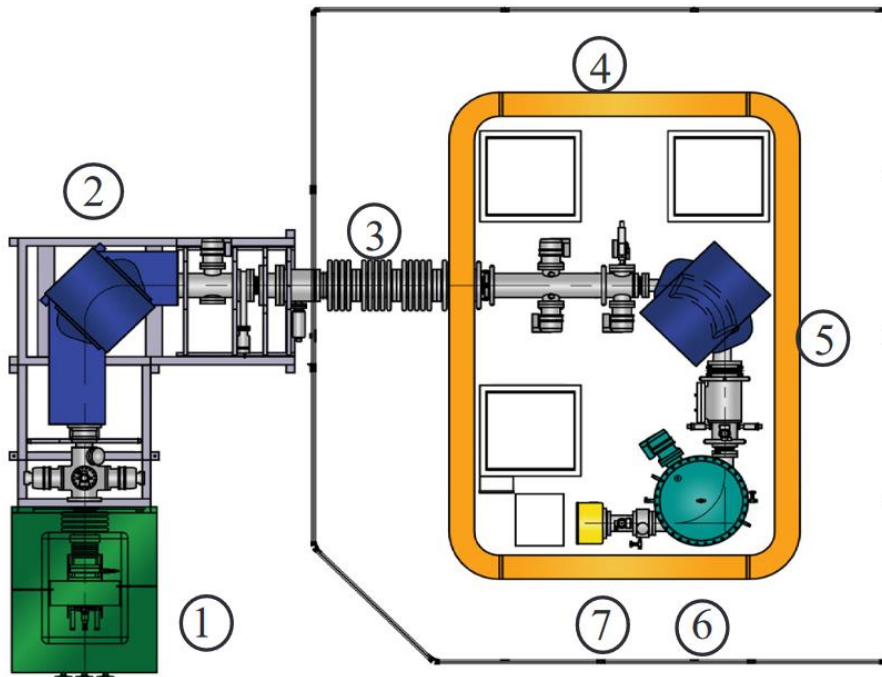


Fig. 2.6. Single-stage accelerator mass spectrometer schematic. Number explanations: 1 – 39 sample capacity ion source, 2 – 90° deflecting magnet, 3 – 250 kV acceleration stage, 4 – isolated deck, 5 – 90° deflecting analysis magnet, 6 – 90° deflecting electrostatic spherical analyzer, 7 – semiconductor ^{14}C detector. Adapted from Single Stage Accelerator Mass Spectrometry (2018).

In environmental studies, the f_M notation is commonly used and is defined as (Stuiver and Polach, 1977):

$$f_M = \frac{(^{14}\text{C}/^{12}\text{C})_{\text{Sample}}}{0.749(^{14}\text{C}/^{12}\text{C})_{\text{OxII}}} \quad (2.8)$$

where $(^{14}\text{C}/^{12}\text{C})_{\text{Sample}}$ is the $^{14}\text{C}/^{12}\text{C}$ ratio of the sample and $(^{14}\text{C}/^{12}\text{C})_{\text{OxII}}$ is the isotope ratio of the OxII reference material.

2.5. Ion concentration measurements

The water-soluble sulfate ion concentrations of PM₁ samples were quantified using an ion chromatograph system (Dionex 2010i), which includes a high-pressure pump, liquid eluent, sample injector, guard and separator columns, chemical suppressor, and conductivity detector. Before sample analysis, the system has to be calibrated against a reference solution. By comparing the data obtained from the sample with that of known standard, the ions in the sample can be identified and quantified. This is done via chromatography software, that generates a chromatogram of the sample. The software then allows separate peaks in the chromatogram to be translated to concentration of specific compounds of interest and produces a printed report of the findings.

The chromatograph system used in this work utilized an Ion Pac AS4A-SC column for inorganic anion separation. During the analysis process, 1.8 mM Na₂CO₃ and 1.7 mM NaHCO₃ was employed as an eluent, while 20 mM H₂SO₄ served as a regenerant. During selected periods, concentrations of SO₄²⁻, NO₃⁻, NH₄⁺, Ca²⁺, Na⁺, K⁺, Mg²⁺, and Cl⁻ were also measured.

2.6. Air mass trajectories and meteorological parameters

Backward air mass trajectories for individual sampling periods were generated using hybrid single particle HYSPLIT model provided by National Oceanic and Atmospheric Administration (NOAA) (Stein et al., 2015). The following parameters were used: each trajectory was modeled for 48 hours, with new trajectories initiated approximately every 8 hours, at heights of 50, 500, and 1500 meters above ground level (AGL). Examples of typical trajectories for various directions are shown in Fig. 2.7.

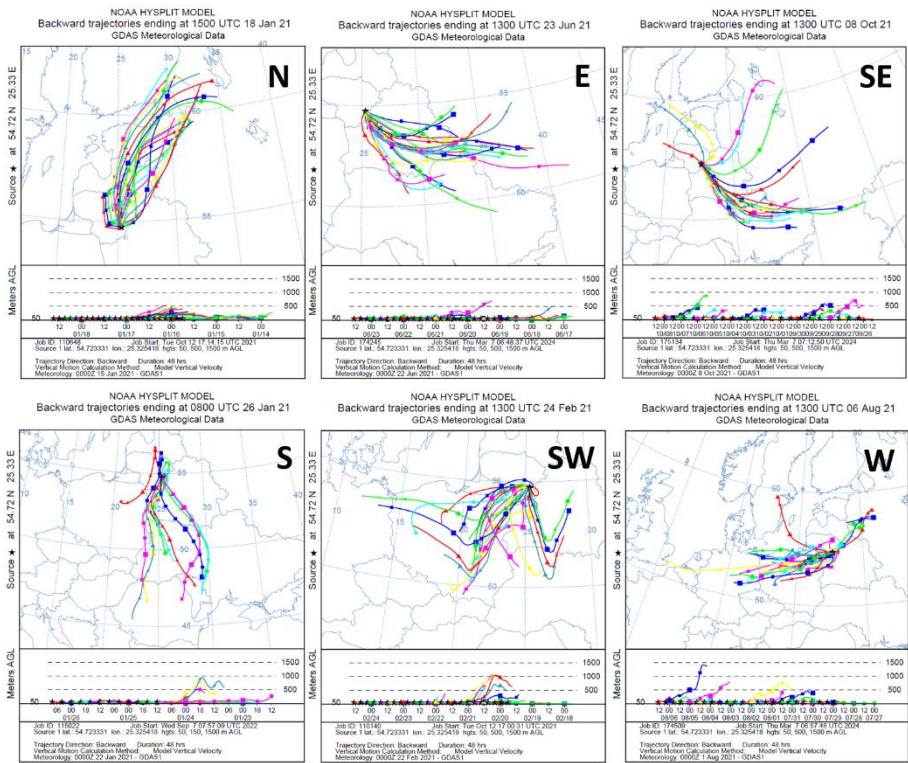


Figure 2.7. Examples of typical backward air mass trajectories of different origins (indicated in top right corner) generated by NOAA HYSPLIT modeling system (Stein et al., 2015).

Air masses from different directions exhibit varying levels of pollution, characterized by Davuliene et al. (2021). Northwestern air masses, primarily from Scandinavian countries, are labeled as clean. In contrast, air masses of western origin (Northern Poland, Germany), are considered somewhat polluted, whilst southwestern (Southern Poland) and southern directions (Belarus, Ukraine) are treated as more polluted. Air masses of northern (Latvia, Estonia) and eastern (Belarus, Russia) origin are considered moderately polluted.

Meteorological parameters, including mixed layer depth, wind speed, relative humidity and ambient temperature were also taken from NOAA's database ("NOAA Climate Data Online (CDO)," 2021).

2.7. Sulfur oxidation pathway contribution calculations

The SO₂ oxidation rate depends on various factors, including oxidant and catalyst concentrations, aerosol acidity and liquid water content (Harris et al., 2013b). As a result, assessing the contributions of different oxidation mechanisms through traditional chemical kinetic reaction rate calculations is challenging due to the varying conditions present during in situ measurements (Fan et al., 2020). Advantageously, stable isotope analysis provides a practical method to evaluate SO₂ oxidation pathway contributions through measurements of synchronously collected PM₁ and SO₂ samples. Collected gaseous SO₂ provides the δ³⁴S values of source emissions, while comparing these values with δ³⁴S of sulfate, reveals the extent of fractionation caused by gas-to-particle conversion. The contributions of distinct SO₂ oxidation pathways can be evaluated by analyzing the fractionation effects caused by oxidation, as distinct pathways result in different δ³⁴S signatures in sulfate. However, the fractionation factors depend on the extent of the reaction (Hoefs, 2021). Thus, it is crucial to evaluate the SO₂ to sulfate conversion rate or sulfur oxidation ratio (SOR), denoting the fraction of SO₂ oxidized to SO₄²⁻ (Mukai et al., 2001):

$$SOR = \frac{[SO_4^{2-}]}{[SO_4^{2-}] + [SO_2]} \quad (2.9)$$

where [SO₄²⁻] is the molar concentration of sulfate and [SO₂] is the molar concentration of sulfur dioxide.

For the estimation of the contributions of different SO₂ oxidation pathways, Rayleigh fractionation equations are used, describing how the isotopic compositions of product and reactants change in relation to the fractionation factors (Harris et al., 2013a; Mariotti et al., 1981; Rayleigh, 1896). Firstly, the δ³⁴S_{emission} value must be determined, which represents the δ³⁴S values of SO₂ from the local pollution sources, at the point of their emission. It is the value the measured SO₂ values would have if there was no production of sulfate (SOR = 0). We used our measured δ³⁴S_{SO2} values at the sampling site, to assess the δ³⁴S_{emission} values, by using the following Rayleigh fractionation equations (Fan et al., 2020; Li et al., 2020):

$$\delta^{34}S_{\text{emission}} = \delta^{34}S_{\text{SO}_2} \times (1 - SOR) + \delta^{34}S_{\text{PM}_1} \times SOR \quad (2.10)$$

where $\delta^{34}\text{S}_{\text{SO}_2}$ and $\delta^{34}\text{S}_{\text{PM}_1}$ are the measured isotopic composition values of collected gaseous SO_2 and PM_1 sulfate values.

Next, we calculated the fractionation factor $\varepsilon_{\text{g} \rightarrow \text{p}}$, which represents the overall isotopic fractionation during the gas-to-particle conversion:

$$\delta^{34}\text{S}_{\text{SO}_2} = \delta^{34}\text{S}_{\text{emission}} + \ln(1 - \text{SOR}) \times \varepsilon_{\text{g} \rightarrow \text{p}} \quad (2.11)$$

Finally, to estimate the contributions of different oxidation pathways, we applied the following mixing equation:

$$\varepsilon_{\text{g} \rightarrow \text{p}} = \varepsilon_{\text{OH}} \times f_{\text{OH}} + \varepsilon_{\text{TMI}} \times f_{\text{TMI}} + \varepsilon_{\text{H}_2\text{O}_2} \times f_{\text{H}_2\text{O}_2} \quad (2.12)$$

where $\varepsilon_{\text{g} \rightarrow \text{p}}$ represents the fractionation factor (per mil notation) for gas-to-particle conversion, while ε_{OH} , ε_{TMI} and $\varepsilon_{\text{H}_2\text{O}_2}$ are the fractionation factors for OH, TMI, and H_2O_2 oxidation pathways, respectively. Additionally, f_{OH} , f_{TMI} , and $f_{\text{H}_2\text{O}_2}$ denote the contributions of the OH, TMI, and H_2O_2 oxidation pathways.

Homogenous and heterogeneous oxidation processes involve both kinetic and equilibrium isotope effects, and can cause either an enrichment or depletion of ^{34}S in the product (SO_4^{2-}) (Harris et al., 2012b; Saltzman et al., 1983). Aforementioned ε_{OH} , ε_{TMI} , and $\varepsilon_{\text{H}_2\text{O}_2}$ fractionation factors are temperature-dependent and were calculated using linear regressions for the average temperature (T) for individual sampling periods by Eq. 1.29 – 1.31, given in Section 1.6. However, f_{OH} fraction was evaluated separately, by the following equation (Harris et al., 2013a):

$$f_{\text{OH}} = \text{SOR} \times 0.27 \times \frac{[\text{OH}]}{[\text{OH}]_m} \times \frac{24}{HL} \quad (2.13)$$

where 0.27 is the fraction of average sulfate produced specifically by OH oxidation pathway annually (Sofen et al., 2011). The OH concentrations fluctuate both diurnally and seasonally, as OH is produced only during the daylight hours. The $[\text{OH}]/[\text{OH}]_m$ term describes seasonal OH concentration variation, based on global tropospheric OH concentration distribution model ACM (Global Change Research Program Atmospheric Chemistry Model (Bahm and Khalil, 2004)). Average [OH] concentrations of a specific months were considered, ranging from 0.1 mol/cm³ to 2.1 mol/cm³, which is then

divided by the average monthly concentration of $[\text{OH}]_m$ ($3.1 \times 10^5 \text{ mol/cm}^3$), fit for the latitude of Lithuania (~55 °N) (Bahm and Khalil, 2004). This is then multiplied by the ratio of 24/HL, representing available daylight hours (HL) as a fraction. Thus, calculated the contribution of OH oxidation pathway can be eliminated from combined $\varepsilon_{g \rightarrow p}$ factor (Eq. 2.12) by subtracting the $\varepsilon_{\text{OH}} \times f_{\text{OH}}$ component.

2.8. Event description

The sampling campaign covered few notable events which could have had an appreciable effect on local air pollution in Vilnius. The first event was the outbreak of coronavirus disease (COVID-19). The initial outbreak of the disease occurred in December during the year 2019 in China and rapidly spread worldwide afterwards (Ciotti et al., 2020). To contain the swift transmission of the disease, numerous governments worldwide imposed restrictions or stringent measures. Throughout the COVID-19 lockdowns, there were notable shifts in aerosol concentrations and the contributions of various emission sources that had significant and unexpected impacts on the atmosphere and the environment (Rodríguez-Urrego and Rodríguez-Urrego, 2020). These effects were largely due to reduced human activities, particularly transportation, industry, and energy use. The first documented instance of coronavirus disease in Lithuania was officially recorded on February 28, 2020. Subsequently, in response to a rapid escalation in case numbers, the first lockdown was decreed on March 16, 2020 and lasted until June 17, 2020. Following a resurgence of new cases in the summer, a subsequent lockdown was implemented on November 4, 2020. Throughout the duration of the second lockdown in Lithuania, a multitude of measures were instituted to mitigate the propagation of the virus. Strict restrictions were enforced, including the closure of public venues (e.g., restaurants, cafes, bars), a ban on most public gatherings, and advisories discouraging non-essential travel. With cases steadily decreasing, the lockdown was ended on July 1, 2021. Globally, particulate concentrations and pollution sources were drastically affected by the COVID-19 lockdowns, though the extent of these changes varied by region (Rodríguez-Urrego and Rodríguez-Urrego, 2020).

The second notable event was the introduction of low-sulfur (0.9 %) heavy fuel oil (or mazut) at the Vilnius thermal power station during the cold season of 2022–2023, in contrast to previous years when only natural gas and biomass fuels were mainly used. Heavy fuel oil is a type of heavy, low-quality fuel oil derived from the distillation of crude oil. It is commonly used in industrial applications, such as heating large buildings, generating steam, or fueling

industrial boilers and furnaces. HFO is characterized by its high viscosity, density, and sulfur content, making it less desirable for the use in vehicles or smaller-scale heating systems compared to lighter grades of fuel oil. The heavy fuel oil was utilized from November 9, 2022, until the end of March 2023, largely supplanting the regularly employed fuels (biomass and natural gas). The shift to usage of HFO was prompted to mitigate the European gas crisis, caused by the consequences of Russian invasion of Ukraine in February of 2022 (Celasun et al., 2022). In the 2022–2023 period, HFO accounted for 36 % of the fuel used at Vilnius TPS, while biomass, natural gas, and diesel contributed 56 %, 7 %, and 1 %, respectively (AB Vilniaus šilumos tinklai, 2023). In comparison, during the previous period of 2021 – 2022, the fuel mix consisted of only biomass (61 %) and natural gas (39 %) (AB Vilniaus šilumos tinklai, 2021).

3. RESULTS

In this chapter, the results of the thesis are presented. First, the findings from the entire sampling period are discussed, covering data collected over more than 31 months, from November 11, 2020, to the end of sampling on June 30, 2023. The results include sulfur compound concentrations, isotopic composition measurements, meteorological parameter data and overview of predominant backward air mass trajectories. Next, key periods of interest are discussed in detail. First, the period from November 11, 2020, to March 16, 2021, is analyzed, focusing on changes in pollution sources induced by the COVID-19 lockdown, using stable carbon and sulfur isotopes alongside radiocarbon measurements of PM₁ samples, as presented in Bučinskas et al. (2024c). This is followed by a discussion of a unique period of increased sulfur pollution due to the use of heavy fuel oil in local thermal power station of Vilnius, with a comparison of the heating seasons of 2022–2023 and 2021–2022, when HFO was not utilized. Stable carbon, sulfur, and radiocarbon analyses were employed for comparison, and the results were published in Bučinskas et al. (2024b). Lastly, seasonal dynamics of sulfur compounds during a period of more than two years, from March 16, 2021, to June 30, 2023, is examined through stable sulfur isotope analysis of PM₁ sulfate and SO₂ gas emissions and seasonal sulfur concentration changes. Additionally, the apportionment of predominant sulfur pollution sources is presented, and prevailing SO₂ oxidation pathways are calculated by comparing $\delta^{34}\text{S}$ values of SO₂ gases and PM₁ sulfate. This work was published in Bučinskas et al. (2024a).

3.1. Results from the entire sampling period

Seasonal variation of weekly average SO₂ and sulfate ion concentrations is shown in Fig. 3.1(a) covering the entire sampling period of 2020 – 2023. In Fig. 3.1(a) sulfur oxidation ratio is also displayed, which indicates the oxidation rate of SO₂ (Chapter 2.7). Weekly averages of wind speed (WS) are shown in Fig. 3.1(b), mixed layer depth (MLD) in Fig. 3.1(c) and relative humidity in Fig. 3.1(d). Table 3.1 presents the calculated correlation coefficients between meteorological parameters and sulfur compound concentrations, as well as SOR.

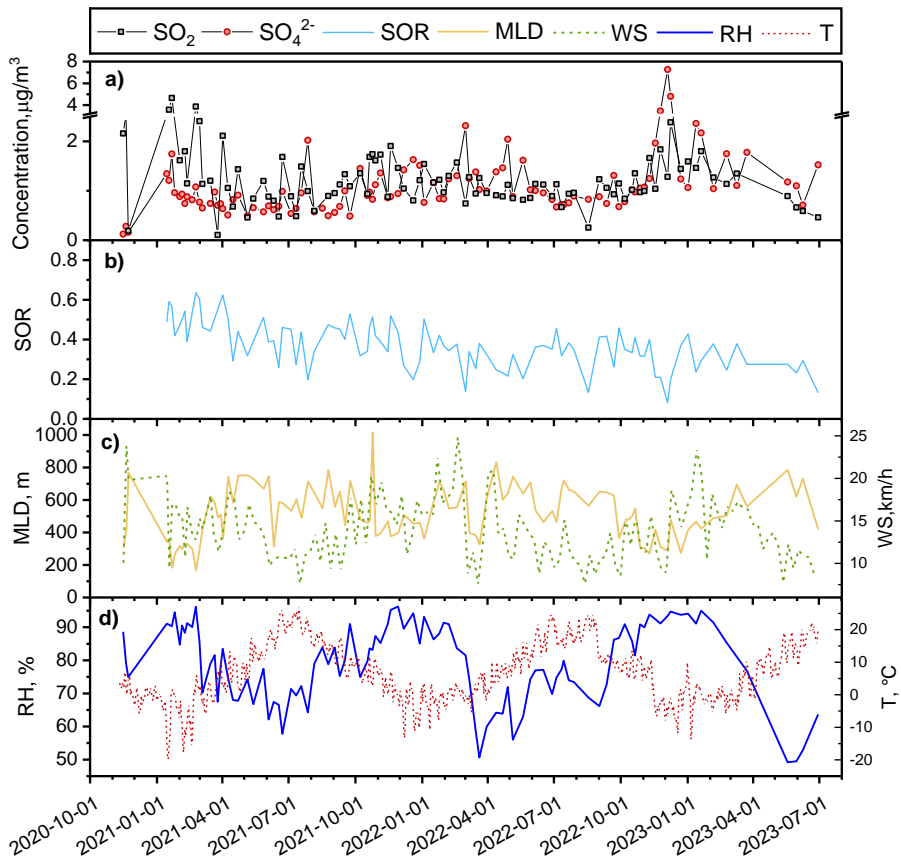


Fig. 3.1. Measured concentrations and weekly averages of monitoring data of the period from 11 November 2020 to 30 June 2023: a) SO_2 and SO_4^{2-} concentrations and sulfur oxidation ratio; b) wind speed; c) mixed layer depth; d) relative humidity. A break is applied on the Y-axis in (a) to highlight the seasonal variations of SO_2 and SO_4^{2-} concentrations.

Table 3.1. Correlation coefficients of SO_2 , SO_4^{2-} concentrations and SOR with meteorological parameters: of temperature, wind speed, mixed layer depth, and relative humidity. The p-values were lower than 0.05 in all cases.

	$\text{SO}_2, \mu\text{g}/\text{m}^3$	$\text{SO}_4^{2-}, \mu\text{g}/\text{m}^3$	SOR
$T, ^\circ\text{C}$	$r = -0.29$	$r = -0.46$	$r = -0.11$
$WS, \text{km}/\text{h}$	$r = 0.07$	$r = 0.22$	$r = 0.09$
MLD, m	$r = -0.22$	$r = -0.52$	$r = -0.17$
$RH, \%$	$r = 0.23$	$r = 0.45$	$r = 0.25$

During the whole measurement period, SO_2 concentrations varied in a range from 0.49 to 7.27 $\mu\text{g}/\text{m}^3$ with an average value of $1.16 \pm 0.85 \mu\text{g}/\text{m}^3$. Concurrently, SO_4^{2-} concentrations varied from 0.11 to 2.39 $\mu\text{g}/\text{m}^3$, averaging $1.19 \pm 0.52 \mu\text{g}/\text{m}^3$. Weak correlation between SO_2 and SO_4^{2-} ($r = 0.25$, $p < 0.05$), reflects that SO_4^{2-} concentration variation cannot be solely explained by changes in SO_2 levels. This indicates differing atmospheric sources for SO_2 and sulfate, highlighting the need for stable isotope analysis to distinguish between these sources.

The SO_4^{2-} concentrations displayed moderate correlation with temperature (Table 3.1, $r = -0.46$, $p < 0.05$) during the entire sampling duration indicating possible chemical reaction rate dependence on temperature or emission variations of dominant sources. During the entire sampling period, wind speeds ranged from 7.5 km/h to 24.8 km/h, averaging 14.0 km/h. Wind speeds were generally higher in the winter months, averaging 16.6 km/h, and lower in summer, averaging 11.1 km/h. Changes in wind speed can result in either the accumulation or dilution of pollutant concentrations. Low wind speeds create stagnant atmospheric conditions, which lead to the accumulation of pollutants and higher concentrations, while higher wind speeds promote dispersion and dilution, reducing pollutant levels. However, changes in wind speed did not lead to corresponding changes in SO_2 or SO_4^{2-} concentrations during this experiment (Table 3.1). Equivalently, decreased mixed layer depth can lead to an increase of gaseous and particulate matter pollutant concentrations, especially in urban environments (Chou et al., 2007; Salvador et al., 2020). During this study, MLD varied from 167.2 m to a recorded maximum of 1015.2 m, with a mean value of 519.5 m. The MLD displayed low correlation (but statistically significant) with concentrations of SO_2 ($r = -0.22$, $p < 0.05$), while SO_4^{2-} concentrations featured a stronger dependence with MLD ($r = -0.52$, $p < 0.05$), indicating a greater influence of MLD on accumulation of particulate matter. Relative humidity displayed a moderate correlation with SO_4^{2-} concentrations ($r = 0.45$, $p < 0.05$), as higher RH values are expected to promote secondary aerosol formation, enhance the hygroscopic growth of particles, and increase aqueous-phase reaction rates.

The variation in $\delta^{34}\text{S}$ values of SO_2 and PM_1 sulfate is shown in Fig. 3.2, along with daily temperature averages.

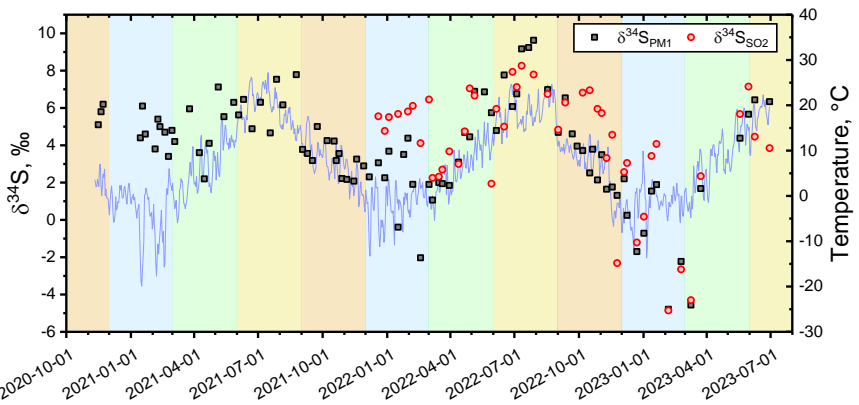


Fig. 3.2. The measured $\delta^{34}\text{S}$ values of SO_2 gases ($\delta^{34}\text{S}_{\text{SO}_2}$) and PM_1 sulfate ($\delta^{34}\text{S}_{\text{PM}1}$) recorded throughout the sampling period from November 11, 2020 to June 30, 2023. Daily average temperature is represented as a blue continuous line. The data is presented across different calendar seasons, with blue section representing winter, green for spring, yellow for summer, and brown for autumn. In total, 91 PM_1 and 47 SO_2 weekly samples were analyzed and included in this graph.

The $\delta^{34}\text{S}$ values of SO_2 varied in a wide range from -4.85 ‰ to 9.41 ‰ , with an average of $4.38 \pm 3.12\text{ ‰}$. At the same time, $\delta^{34}\text{S}$ values of PM_1 sulfate ranged from -4.79 ‰ to 9.63 ‰ , with an average of $3.88 \pm 2.62\text{ ‰}$. Measured extremum $\delta^{34}\text{S}$ values of SO_2 and sulfate are very close and fall within the range of typical measurement precision of $\delta^{34}\text{S}$ measurements ($<0.10\text{ ‰}$), suggesting that these maximum values reflect the influence of different dominant sulfur pollution sources during winter and summer. Although the $\delta^{34}\text{S}$ value ranges were similar for both SO_2 and sulfate, the average $\delta^{34}\text{S}_{\text{PM}1}$ value was 0.50 ‰ lower than that of $\delta^{34}\text{S}_{\text{SO}_2}$ (with the median $\delta^{34}\text{S}_{\text{PM}1}$ lower by 0.90 ‰) throughout the whole measurement period, indicative of different source contributions and/or sulfate production fractionation effects. In addition, the $\delta^{34}\text{S}$ values between SO_2 and $\text{PM}_1 \text{SO}_4^{2-}$ demonstrate a significant positive correlation ($r = 0.77$, $p < 0.05$), reaffirming that SO_2 emissions and subsequent sulfate formation are interrelated.

To determine the influence of meteorological conditions on the measured $\delta^{34}\text{S}$ values of SO_2 and sulfate, the relationships between $\delta^{34}\text{S}$ values and corresponding concentrations, wind speed, mixed layer depth, and relative humidity were analyzed and correlation coefficients are given in Table 3.2.

Table 3.2. Correlation coefficients of $\delta^{34}\text{S}$ values of SO_2 and sulfate with their respective concentrations, SOR and meteorological parameters: temperature (T), wind speed (WS), mixed layer depth (MLD), and relative humidity (RH). The p-values were lower than 0.05 for all cases.

	$\delta^{34}\text{S}_{\text{SO}_2}$, ‰	$\delta^{34}\text{S}_{\text{PM}1}$, ‰
SO_2 , $\mu\text{g}/\text{m}^3$	r = -0.26	r = -0.32
SO_4^{2-} , $\mu\text{g}/\text{m}^3$	r = -0.41	r = -0.30
SOR	r = 0.06	r = 0.08
T, °C	r = 0.57	r = 0.51
WS, km/h	r = -0.21	r = -0.36
MLD, m	r = 0.26	r = 0.26
RH, %	r = -0.21	r = -0.41

The low $\delta^{34}\text{S}$ value correlations (but statistically significant) observed with many meteorological parameters (Table 3.2) suggest a complex nature of atmospheric sulfur compounds, displaying a moderately high positive correlation only with temperature. The concentrations of SO_2 and SO_4^{2-} , along with SOR, showed negligible to low correlations, suggesting that local pollution sources had a lesser impact on the measured $\delta^{34}\text{S}$ values, which were likely more influenced by remote pollution sources from neighboring countries. Other meteorological parameters, such as wind speed and mixed layer depth, exhibited low correlation coefficients with $\delta^{34}\text{S}$ values. However, relative humidity had stronger effect on $\delta^{34}\text{S}_{\text{PM}1}$ values, highlighting the importance of aqueous-phase sulfate production in aerosols. Considering, the $\delta^{34}\text{S}$ value dependence on temperature, an increased correlation ($r = 0.68$, $p < 0.05$) is observed when two distinct periods are excluded. In Fig. 3.3 $\delta^{34}\text{S}_{\text{PM}1}$ value relationship with ambient temperatures is presented, highlighting two periods with contrasting trends. Green triangle data points indicate the trend observed during the 2020 – 2021 period, where $\delta^{34}\text{S}_{\text{PM}1}$ values exhibit an opposite pattern, becoming more positive with decreasing temperatures. Additionally, another period, during the years 2022 – 2023, is notable, due to very negative $\delta^{34}\text{S}_{\text{PM}1}$ values of PM_1 sulfate observed. Aforementioned periods will be analyzed in greater detail in the Chapters 3.5 – 3.6.

$r = 0.68, p < 0.05$ (excluding 2020-2021, 2022-2023 HFO periods)

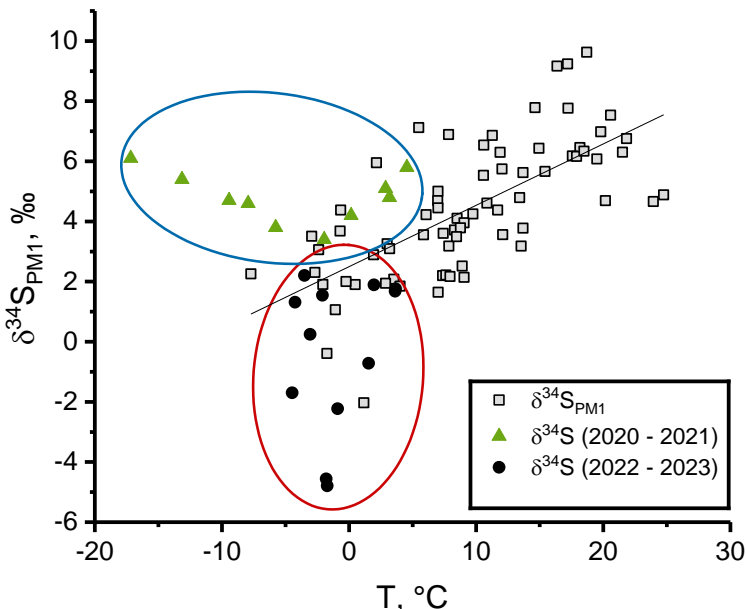


Fig. 3.3. The variation of $\delta^{34}\text{S}_{\text{PM}1}$ values with temperature presented for three distinct periods: 2020 – 2021 (indicated by green triangles, discussed in Chapter 3.5), 2022 – 2023 (indicated by black dots), and the remainder of the sampling campaign (indicated by gray squares, discussed in Chapter 3.6).

Overall, temperature may influence $\delta^{34}\text{S}$ values indirectly or directly. An indirect effect of temperature variation is the seasonal shift in contributions from sulfur pollution sources, such as increased emissions from biomass combustion during colder periods (heating season), driven by its use as a fuel for domestic heating. Source contributions will be later discussed in Chapter 3.4. Seasonal changes in SO_2 oxidation pathways can also play a significant role, particularly through homogeneous SO_2 oxidation by OH radicals, which strongly depends on atmospheric OH concentrations. The OH production decreases significantly during the winter season due to reduced photochemical reactions, particularly in the Northern Hemisphere (Harris et al., 2013a). A direct effect is the temperature-dependent fractionation of different SO_2 oxidation pathways, which can be significant in some cases (Harris et al., 2012b; Novák et al., 2001).

3.2. The influence of long-range pollutant transport

Since 1980s, SO₂ concentrations in Lithuania have been steadily declining, and by the year 2008, ambient atmospheric PM SO₄²⁻ concentrations surpassed SO₂ emission levels, indicating a growing influence of remote sulfur pollution sources (Davuliene et al., 2021). Therefore, it is essential to assess the impact of long-range transport of sulfur pollutants, primarily present as sulfate aerosol, which may affect air quality in Vilnius.

The impact of long-range air mass transport on fluctuations in SO₂ and SO₄²⁻ concentrations is given in Fig. 3.4(a,b). Samples collected during the heavy fuel oil usage period were excluded from the air mass analysis due to plausible increased emissions from local sources, which could skew the results related to prevailing air mass trajectories. However, HFO usage period will be analyzed thoroughly in Chapter 3.6. Over the duration of this study, SO₂ concentrations across the different air mass directions remained relatively stable, ranging from $0.87 \pm 0.07 \mu\text{g}/\text{m}^3$ to $1.08 \pm 0.42 \mu\text{g}/\text{m}^3$ (Fig. 3.4(a)). While the overall variation in SO₂ concentrations across different air mass directions was minimal, distinct trends were observed in the northeastern, southeastern, and northwestern directions with higher spread of recorded concentrations. Additionally, air masses coming from the east consistently showed lower SO₂ concentrations throughout the measurement period. Notably, no significant increase of SO₂ concentrations is observed from northwestern direction, where Lithuania's primary sulfur pollution sources are located, including a fertilizer production facility in Kėdainiai (located ~100 km away) and crude oil refinery Mažeikiai (~270 km away) (European Environment Agency, 2023). Additionally, air masses from the northwest accounted only for approximately 12 % of the total air masses reaching Vilnius during the entire sampling campaign. Furthermore, considering the short atmospheric lifetime of SO₂ gases (approximately 12 hours) (Lee et al., 2011), it is reasonable to conclude that emissions from the northwest had minimal impact, and the SO₂ samples collected in Vilnius primarily represented the emissions of local sources.

Concurrently, SO₄²⁻ concentrations fluctuated in a wider range, between $0.86 \pm 0.32 \mu\text{g}/\text{m}^3$ and $1.53 \pm 0.63 \mu\text{g}/\text{m}^3$, with peak concentrations noted in southwestern direction (Fig. 3.4(b)). Air masses originating from the southwest often traverse more polluted areas in Central and Eastern Europe, including southern Poland, where coal is commonly used for domestic heating and energy production (Bertelsen and Mathiesen, 2020; Igliński et al., 2015). Similarly to SO₂ concentrations, no increase in SO₄²⁻ concentrations was observed from the northwestern direction, suggesting that sulfur emissions,

whether in gaseous or particulate form, from these industrial sources have a minor impact on air quality in Vilnius.

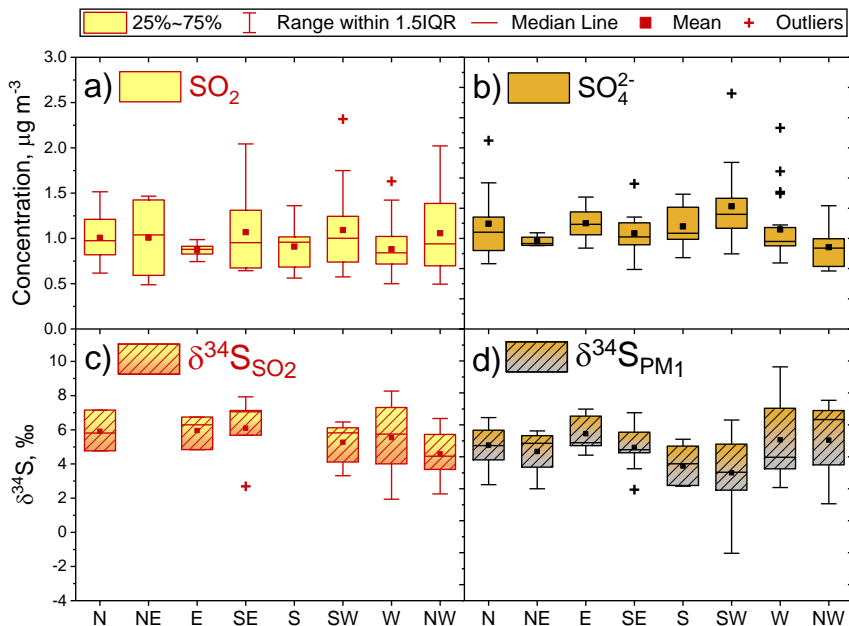


Fig. 3.4. Distribution of: SO_2 (a) and SO_4^{2-} (b) concentrations across different air mass origins, along with corresponding distributions of $\delta^{34}\text{S}_{\text{SO}_2}$ (c) and $\delta^{34}\text{S}_{\text{PM}1}$ (d) values. The northeastern and southern directions contained fewer than three data points per boxplot and were therefore excluded from the figure.

Direction-averaged $\delta^{34}\text{S}_{\text{SO}_2}$ values fluctuated within a range from $3.5 \pm 1.2 \text{ ‰}$ to $6.1 \pm 1.7 \text{ ‰}$ (Fig. 3.4(c)). Overall, $\delta^{34}\text{S}_{\text{SO}_2}$ did not demonstrate a clear correlation with the direction of air masses. This observation aligns with the notion that collected SO_2 sampled are more representative of emissions from local pollution sources, given the rapid oxidation of SO_2 in the atmosphere. In contrast, Fig. 3.4(d) presents an increased variability of $\delta^{34}\text{S}_{\text{PM}1}$ values across different air mass origins, with direction-averaged $\delta^{34}\text{S}_{\text{PM}1}$ values ranging from $3.0 \pm 2.2 \text{ ‰}$ to $5.4 \pm 1.0 \text{ ‰}$. The most pronounced trends were found in the southern and southwestern directions, with the lowest average $\delta^{34}\text{S}_{\text{PM}1}$ values recorded at $3.4 \pm 1.1 \text{ ‰}$ and $3.0 \pm 2.2 \text{ ‰}$, respectively. The southwestern direction showed the lowest $\delta^{34}\text{S}_{\text{PM}1}$ values during this study, which may indicate the influence of air masses coming from polluted regions in southern Poland. Consequently, excluding the periods when heavy fuel oil

is used, the measured $\delta^{34}\text{S}_{\text{SO}_2}$ values are likely indicative of local pollution sources of gaseous SO_2 , whereas $\delta^{34}\text{S}_{\text{PM}1}$ values are more closely associated with long-range transport of particulate sulfate.

3.3. Seasonality of concentrations and isotopic compositions

Seasonal SO_2 and SO_4^{2-} concentrations variation with respective $\delta^{34}\text{S}_{\text{SO}_2}$ and $\delta^{34}\text{S}_{\text{PM}1}$ values is represented in Fig. 3.5. The sampling period was divided into four segments, each corresponding to the full calendar seasons of spring, summer, autumn, and winter. The first segment in Fig. 3.5(a), spans the years 2020 – 2021 but includes only autumn and winter seasons. During this period, the second national lockdown in Lithuania was decreed from November 7, 2020. The subsequent period, covering the years 2021 – 2022 (Fig. 3.5(b)), saw a gradual easing of the lockdown restrictions, which were fully lifted by July 1, 2021. Next, is the period of the years 2022 – 2023 (Fig. 3.5(c)), which is notable for the use of heavy fuel oil in Vilnius TPS during the heating season. The HFO was used from November 9, 2022 to March 31, 2023. Thus, the final segment during the year 2023 in Fig. 3.5(d) represents the conclusion of HFO usage at Vilnius TPS.

During the entire sampling period, notable trends were observed, with both SO_2 and SO_4^{2-} concentrations exhibiting low-amplitude seasonal variations, with lower concentrations more frequently observed during the summer months (June, July, August), averaging $0.83 \pm 0.33 \mu\text{g}/\text{m}^3$ for SO_2 and $0.89 \pm 0.33 \mu\text{g}/\text{m}^3$ for SO_4^{2-} . In comparison, during the winter months (December, January, February) concentrations are usually higher, with an average of $1.35 \pm 0.80 \mu\text{g}/\text{m}^3$ for SO_2 and $1.50 \pm 0.65 \mu\text{g}/\text{m}^3$ for SO_4^{2-} . Seasonal fluctuations in sulfur pollutant concentrations may have been driven by shifts in the relative contributions of pollution sources as well as changes in meteorological conditions as discussed in a study by Davulienė et al. (2021). The following paragraphs will discuss concentration variations of sulfur compounds observed during different periods.

Throughout the 2020 – 2021 period (Fig. 3.5(a)), SO_2 concentrations remained consistent between autumn and winter, averaging $1.03 \mu\text{g}/\text{m}^3$ for both seasons. In contrast, SO_4^{2-} concentrations were markedly higher, averaging $1.31 \mu\text{g}/\text{m}^3$ in the autumn and rising to a high value of $1.68 \mu\text{g}/\text{m}^3$ during the winter.

During subsequent period of 2021 – 2022 (Fig. 3.5(b)), SO_2 concentrations were measured at $0.72 \mu\text{g}/\text{m}^3$ in spring, $0.73 \mu\text{g}/\text{m}^3$ in summer, $0.96 \mu\text{g}/\text{m}^3$ in autumn, and $1.30 \mu\text{g}/\text{m}^3$ in winter. During the same timeframe, SO_4^{2-} concentrations were generally higher than SO_2 concentrations, averaging

0.96 $\mu\text{g}/\text{m}^3$ in spring, 0.85 $\mu\text{g}/\text{m}^3$ in summer, 1.40 $\mu\text{g}/\text{m}^3$ in autumn. Although, during the winter, SO_4^{2-} concentrations were consistently lower, with an average of 1.16 $\mu\text{g}/\text{m}^3$. With the exception of the aforementioned season, both 2020 – 2021 and 2021 – 2022 periods exhibited a general trend of $\text{PM}_1 \text{SO}_4^{2-}$ pollution levels generally exceeding SO_2 emission levels, suggesting that the SO_2 emissions from local sulfur pollution sources were low in comparison. Previous research by Davulienė et al. (2021) showed that particulate sulfur concentrations in Lithuania exceed those of SO_2 gases, which is attributed to a relative increase in the influence of long-range PM_1 sulfate transport from neighboring countries, due to diminished emissions of SO_2 gases from local sources.

During the 2022 – 2023 period (Fig. 3.5(c)), the trend reversed, with SO_2 concentrations increasing significantly in autumn (average of 1.80 $\mu\text{g}/\text{m}^3$) and winter (average of 2.06 $\mu\text{g}/\text{m}^3$) seasons, thus generally surpassing SO_4^{2-} concentrations, which equaled to 1.18 $\mu\text{g}/\text{m}^3$ in autumn and 1.59 $\mu\text{g}/\text{m}^3$ in winter. Although SO_4^{2-} concentrations were lower than SO_2 levels, they demonstrated a 37 % increase in winter when compared to the previous winter of 2021 – 2022. The rise in sulfur pollution levels was likely driven by the increase in SO_2 emissions resulting from the use of HFO at Vilnius thermal power station.

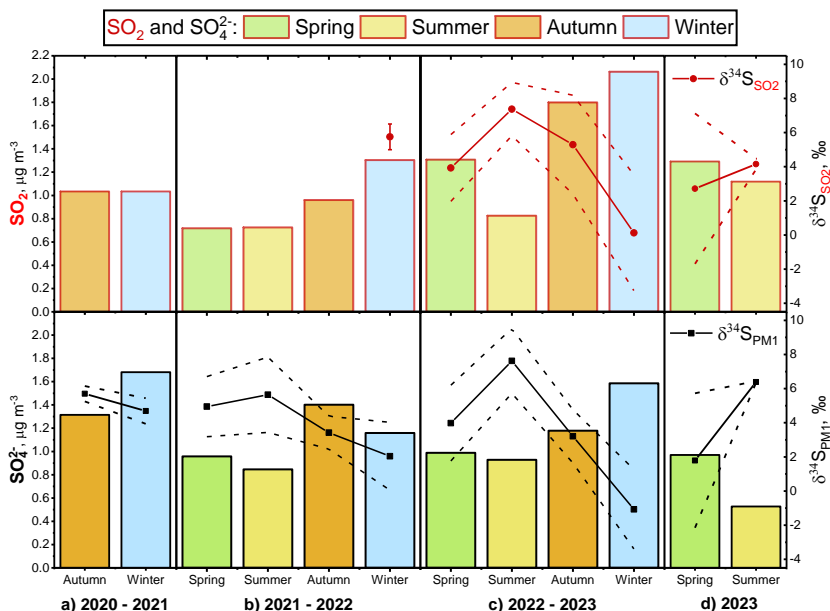


Fig. 3.5. Seasonal variation of SO_2 , SO_4^{2-} concentrations and $\delta^{34}\text{S}_{\text{SO}2}$, $\delta^{34}\text{S}_{\text{PM}1}$ values during periods: a) 2020 – 2021; b) 2021 – 2022; c) 2022 – 2023 and d) 2023.

The isotopic compositions of SO₂ and PM₁ sulfate also displayed pronounced seasonal patterns (Fig. 3.5), with moderate positive correlations with ambient temperature (Table 3.2: r = 0.57 for SO₂, r = 0.51 for SO₄²⁻). Notably, the δ³⁴S values of SO₂ changed with different seasons, confirming that source contributions change throughout the year. However, δ³⁴S values of sulfate can further be affected by partitioning SO₂ oxidation pathways (Harris et al., 2013a; Mukai et al., 2001; Novák et al., 2001), temperature-dependent fractionation factors (Caron et al., 1986; Harris et al., 2013a), and by pollutant transport from remote sources (as discussed in Chapter 3.2). In current study, the observed seasonal variations of δ³⁴S values are in opposition to other regions, including East Asia (Han et al., 2016; Kawamura et al., 2001; Lin et al., 2022; Mukai et al., 2001), North America (Nriagu and Coker, 1978; Saltzman et al., 1983) and Europe (Mayer et al., 1995), where an inverse relationship is generally recorded, with high δ³⁴S values recorded during the winter and low values during the summer. In the current study, sulfur compounds were more isotopically enriched during the summer months ($\delta^{34}\text{S}_{\text{SO}_2} = 6.5 \pm 1.7 \text{ ‰}$; $\delta^{34}\text{S}_{\text{PM}_1} = 6.5 \pm 1.5 \text{ ‰}$), whereas isotopically lighter fractions were found during the winter months ($\delta^{34}\text{S}_{\text{SO}_2} = 3.1 \pm 3.4 \text{ ‰}$; $\delta^{34}\text{S}_{\text{PM}_1} = 2.3 \pm 2.7 \text{ ‰}$). During winter, considerably greater variability in δ³⁴S was observed that could be indicative on complex interplay between multiple pollution sources of local and remote origins. In contrast, during summer, a reduced variability was observed, which could suggest an influence of a predominant, stable emission source(s). Based on current literature, similar seasonal patterns (low δ³⁴S in winter, high δ³⁴S in summer) were previously reported only in Czechia (Novák et al., 2001). Recorded seasonal patterns allude to the complex dynamics of atmospheric sulfur compounds in the urban environment of Vilnius, influenced by isotope fractionation during SO₂ oxidation and the presence of region-specific sulfur pollution sources, with varying relative contributions throughout the year. In the following paragraphs, δ³⁴S value variations during separate periods will be discussed.

The isotopic compositions of PM₁ sulfate during the autumn and winter of 2020 – 2021 (Fig. 3.5(a)) displayed relatively high δ³⁴S_{PM1} values compared to all other periods, averaging 5.7 ‰ in autumn and 4.7 ‰ in winter. In the subsequent period of 2021 – 2022 (Fig. 3.5(b)), δ³⁴S_{PM1} values featured moderate fluctuations, with an average of 4.5 ‰ in spring, the highest average of 5.4 ‰ in summer, autumn averaging 3.3 ‰, and winter possessing the isotopically lightest sulfur with an average of 2.1 ‰. Furthermore, during the winter of 2021 – 2022, δ³⁴S_{SO2} values averaged 5.5 ‰, indicating differing source contributions for SO₂ and PM₁ sulfate, or the influence of significant isotopic effects during sulfate production.

During the 2022 – 2023 period, $\delta^{34}\text{S}_{\text{PM}1}$ values averaged 3.9 ‰ and $\delta^{34}\text{S}_{\text{SO}_2}$ averaged 3.8 ‰ in spring, while in autumn, $\delta^{34}\text{S}_{\text{PM}1}$ values averaged 3.1 ‰ and $\delta^{34}\text{S}_{\text{SO}_2}$ values averaged 5.1 ‰. The 2022 – 2023 period featured increased variability of $\delta^{34}\text{S}_{\text{PM}1}$ values, with high isotopic composition values averaging 7.2 ‰ during the summer, contrasted by notable negative values averaging -0.8 ‰ in the winter. Similarly, the isotopic compositions of SO_2 reflected similar trends, with high $\delta^{34}\text{S}_{\text{SO}_2}$ values in summer, averaging 7.0 ‰, and low average $\delta^{34}\text{S}_{\text{SO}_2}$ values of 0.3 ‰ in winter. The average winter $\delta^{34}\text{S}_{\text{PM}1}$ values are 2.9 ‰ lower compared to the period of 2021 – 2022, whereas $\delta^{34}\text{S}_{\text{SO}_2}$ values are even lower, by 5.2 ‰ compared to the previous period. The significantly negative average isotopic composition values for SO_2 and sulfate – reaching as low as -4.85 ‰ for $\delta^{34}\text{S}_{\text{SO}_2}$ and -4.79 ‰ for $\delta^{34}\text{S}_{\text{PM}1}$ for the period from January 20, 2023 to February 6, 2023 – indicates the impact of a prominent new sulfur pollution source. The recorded low values fall outside the interval of the predominant source $\delta^{34}\text{S}$ values in Lithuania: biomass burning and coal combustion. The shift to negative values suggests that the new source is likely significantly depleted in the heavy ^{34}S isotope. Based on established $\delta^{34}\text{S}$ values of various natural and anthropogenic sources (Fig. 1.4), only anthropogenic SO_2 emissions from crude oil combustion are likely contributors, as biogenic sources are inhibited during winter. Specifically, heavy fuel oil could have been used, that was sourced from Saudi Arabia ($\delta^{34}\text{S}_{\text{SO}_2}$ ranging from -8.8 to -0.7 ‰) or the United Arab Emirates ($\delta^{34}\text{S}_{\text{SO}_2}$ ranging from -10.3 to -4.3 ‰). The low $\delta^{34}\text{S}_{\text{SO}_2}$ and $\delta^{34}\text{S}_{\text{PM}1}$ values measured during the winter of 2022 – 2023 (Fig. 3.5(c)), together with the significant increase in SO_2 and SO_4^{2-} concentrations, point to an increased influence of local emissions, with heavy fuel oil emissions likely outweighing the influence of long-range transport of coal combustion emissions.

3.4. Apportionment of sulfur sources

To evaluate the influence of changing sulfur pollution sources, relative contributions to both SO_2 and PM_1 sulfate were quantitatively calculated using Bayesian statistical model FRUITS as described in Chapter 1.7.1. Seasonal contributions of the entire sampling period are presented in Fig. 3.6.

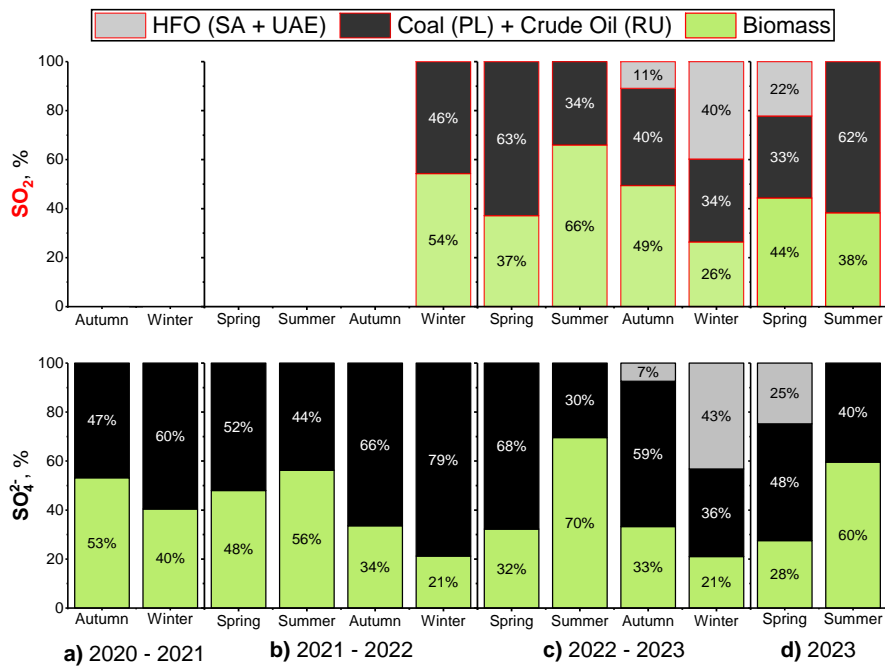


Fig. 3.6. Seasonal variation of SO₂ and PM₁ SO₄²⁻ pollution source contributions during: a) 2020 – 2021; b) 2021 – 2022; c) 2022 – 2023 and d) 2023. Green columns denote biomass burning contribution, black columns represent the combined contributions of coal combustion of Polish origin (PL) and crude oil emissions of Russian origin (RU), and gray columns symbolize the contributions of heavy fuel oil emissions of Saudi Arabian (SA) or/and United Arabian (UAE) origin.

Source contributions to both gaseous SO₂ and particulate sulfate exhibited similar seasonal trends, with biomass burning emissions contributing less during winter (averaging $28 \pm 14\%$) and coal combustion products contributing more (averaging $61 \pm 20\%$). During the heating season, both biomass burning emissions from domestic heating and power generation emissions rise due to increased demand for heating and electricity. This leads to higher SO₂ releases in winter compared to summer, which are evidenced by the higher atmospheric sulfur compounds concentrations commonly observed during the winter months (Fig. 3.5). However, during the winter in Vilnius, long-range transport of coal combustion emissions generally outweigh emissions from local biomass burning sources and, contributed with oil (RU) emissions an average of $61 \pm 20\%$. This is largely due to substantial sulfur emissions from coal used in energy production and residential heating in

neighboring countries like Poland, which emitted approximately 35 times more SO₂ than Lithuania in 2021 (European Environment Agency, 2023). During the summer months, when total emissions of sulfur compounds decrease, emissions from biomass combustion become the predominant fraction, averaging $63 \pm 16\%$, while emissions from coal + oil combustion contribute a decreased fraction of $37 \pm 16\%$. While emissions from residential heating decrease in summer, other sources like agricultural burning and wildfires become more prominent (Ricky et al., 2022), which is likely due to relative increase in contributions from biomass burning emissions. In Lithuania, SO₂ emissions from the energy production are largely attributed to the use of biomass fuels (Ren et al., 2021). The Vilnius TPS continues to utilize biomass even during the summer months, thereby maintaining a stable biomass burning emission background year-round (Vilniaus šilumos tinklai, 2021; Vilniaus šilumos tinklai, 2022). Throughout the sampling period, contributions from biomass burning emissions were generally higher in the gaseous SO₂ fraction, averaging 11% more than in the particulate SO₄²⁻, indicating the influence of local pollution sources.

During the winter of 2020 – 2021 period (Fig. 3.6(a)) coal combustion products contributed an average of $60 \pm 8\%$ to PM₁ sulfate, while biomass burning emissions accounted for $40 \pm 8\%$, marking the largest biomass burning emission contribution observed throughout the winter periods of the entire sampling campaign. The biomass burning emission contribution was twice as high as those recorded in 2021 – 2022 (Fig. 3.6(b)) and 2022 – 2023 (Fig. 3.6(c)). This period will be analyzed in more detail in the following Chapter 3.5, with additional measurements of δ¹³C and δ¹⁴C of carbonaceous aerosol.

During the period of 2021 – 2022 (Fig. 3.6(b)), coal combustion + oil emission input to particulate sulfate was notably large during the winter, averaging $79 \pm 15\%$, while only contributing $46 \pm 8\%$ in the SO₂ fraction. This period was notable for the high frequency (26 %) of air masses originating from the southwest, in addition to the lowest δ³⁴S_{PM1} values (-0.4 ‰ and -2.0 ‰, Fig. 3.4) measured during this period. Thus, during the winter period of 2021 – 2022, local pollution sources had a greater influence on the gaseous SO₂ fraction, while the PM₁ sulfate fraction was influenced more by air mass transport from remote pollution sources.

In the subsequent period of 2022 – 2023 (Fig. 3.6(c)), biomass burning emissions in summer contributed on average 4 % less to the SO₂ fraction (averaging $66 \pm 16\%$) compared to sulfate (averaging $70 \pm 18\%$), suggesting an increase in the influence of long-range pollutant transport. This period is notable due to the exceptionally severe wildfire season in Europe during the

summer of 2022, which saw a total of approximately 130,000 hectares burned in the European Union in July alone (San-Miguel-Ayanz et al., 2023). Additionally, extensive fires in agricultural areas of Ukraine were also widespread during this period. Until the year 2022, biomass burning and coal combustion + crude oil emissions were the predominant contributors to sulfur pollution in Vilnius during the winter months, accounting for $30 \pm 16\%$ and $70 \pm 16\%$, respectively. However, from November 9, 2022 heavy fuel oil was introduced to local Vilnius thermal power station as a substitute for reduced fuel supplies of natural gas. During the winter of 2022 – 2023, HFO emissions significantly affected the urban air quality in Vilnius, and constituted $40 \pm 17\%$ to SO₂ fraction and $40 \pm 13\%$ to PM₁ sulfate. As a result, relative contributions of coal + oil emission sources reduced to $34 \pm 6\%$ of SO₂ emissions and $36 \pm 8\%$ of particulate sulfate, owing to increased local sulfur emissions from HFO. It is evident that local emissions were the dominant contributors to both gaseous and particulate sulfur pollution in Vilnius during this period. Consequently, this anomalous phase will be analyzed separately in Chapter 3.6.

Lastly, during the period 2023 (Fig. 3.6(d)), HFO combustion remained a major source of sulfur pollution, contributing approximately half of the total SO₂ and PM₁ sulfate observed in March. However, with the conclusion of the heating season in Vilnius, HFO use ceased on March 31, 2023.

Overall, the urban environment of Vilnius exhibits a notably high proportion of sulfur compounds originating from biomass burning compared to other studies. In more polluted areas, biomass burning contributions are largely outweighed by fossil fuel emissions, such as those from coal and oil combustion, for instance, even during summertime, fossil fuel sources contribute for over 90 % of PM₁₀ in Delhi, India and more than 65 % of total suspended particles in Beijing, China throughout the year (Dasari and Widory, 2024; Han et al., 2016). In aforementioned regions, relative biomass burning contributions to both SO₂ and PM show a decreasing trend (Dasari and Widory, 2024; Ren et al., 2021). In contrast, biomass burning contributions in Europe have been rising, accounting for a larger 9.9 % fraction (less than 1 % in China; 2.7 % in India) of all SO₂ sources (Ren et al., 2021). In neighbouring Poland, sulfur emissions from traffic and domestic heating contributed from approximately 60 % (heating season) and 80 % (other periods) to sulfate in precipitation, however biomass burning contributions were not evaluated separately (Górka et al., 2017).

3.5. Impacts of quarantine conditions on PM₁ emissions

The period of 2020 – 2021, is notable due to unique conditions present in Lithuania at that time. This chapter provides in-depth dual-carbon (¹³C and ¹⁴C) and sulfur isotopic analysis (³⁴S) of PM₁ samples collected from January 11, 2020 to March 16, 2021, during the second coronavirus (COVID-19) quarantine, revealing its impact and providing insights into observed urban pollution shifts.

During the 2020 – 2021 period, total carbon (TC) and SO₄²⁻ concentrations were measured and are given in Fig. 3.7, together with temperature and wind speed averages of each sample. TC concentrations varied in a large interval of 2.4 µg/m³ – 12.4 µg/m³, with a mean of $5.7 \pm 3.0 \mu\text{g}/\text{m}^3$. A study from the years 2014 – 2015 in Vilnius, reported slightly lower TC concentrations, averaging 4.5 µg/m³ (Garbarienė et al., 2016). Similarly, Rodríguez-Urrego and Rodríguez-Urrego, (2020) reported PM_{2.5} concentration levels changed insignificantly before and during quarantine in Vilnius. Additionally, an inverse relationship was recorded between TC concentrations and ambient temperature ($r = -0.60$, $p < 0.05$). Increased electricity demand and heightened domestic heating emissions may have offset the impact of reduced transport and movement during the pandemic.

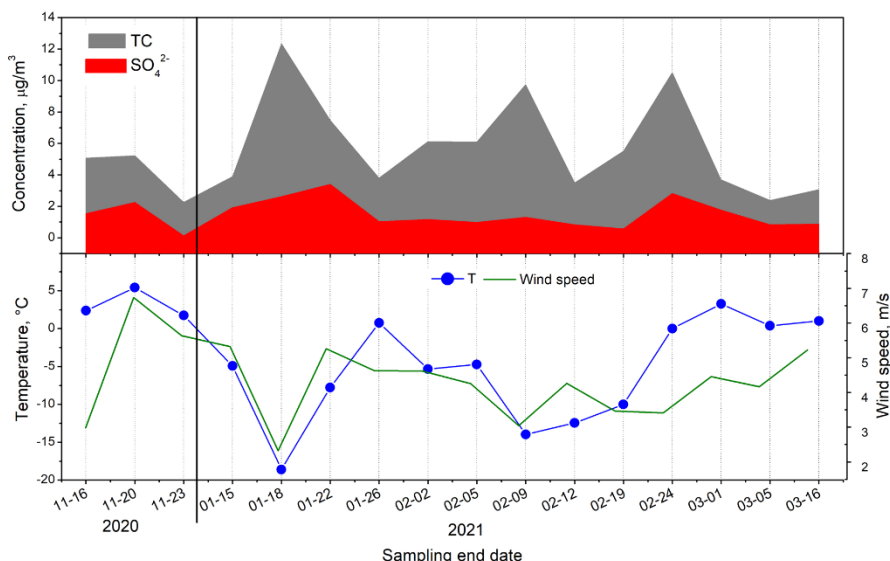


Fig. 3.7. Total carbon (gray filled area) and SO₄²⁻ (red area) concentrations in PM₁ particles collected between November 11, 2020 and March 16, 2021. Average temperatures (blue line) and wind speeds (green line) are also represented.

Concurrently, SO_4^{2-} concentrations ranged in an interval of $0.1 \mu\text{g}/\text{m}^3$ – $3.4 \mu\text{g}/\text{m}^3$ (Fig. 3.7) with a mean value of $1.5 \pm 0.9 \mu\text{g}/\text{m}^3$. The low correlation between SO_4^{2-} levels and temperature ($r = -0.12$, $p < 0.05$) indicates a minimal contribution from local sources like domestic heating to the PM_1 sulfate. However, a higher correlation between total carbon and SO_4^{2-} concentrations was observed ($r = 0.66$, $p < 0.05$), indicating that both carbonaceous and sulfate fractions are likely linked to shared anthropogenic sources. Throughout the study period, TC concentrations remained relatively stable across different air mass origins (Fig. S2(a)), indicating a stronger influence from local pollution sources rather than long-range transport. By contrast, sulfate ion concentrations varied significantly in reference to air mass origins (Fig. S2(b)), with the highest levels occurring when air masses originated from the southwest, particularly from southern Poland, an area with numerous coal-fired power plants and wide use of coal for residential heating (Bertelsen and Mathiesen, 2020). Additionally, the period from January 15 to January 18 is notable, due to increased concentrations of both TC and SO_4^{2-} , despite air masses originating primarily from north, which are considered less polluted than western or southwestern directions (Davuliene et al., 2021). This period was notable for the lowest recorded mean temperature of -17.2°C during the entire study, combined with low wind speeds (2.6 m/s) and a low mixed layer depth (352 m). Thus, it is likely that the increase in emissions from domestic heating during the period of extremely low temperatures, combined with stagnant atmospheric conditions, contributed to the accumulation of PM_1 components, resulting in elevated concentrations of both TC and SO_4^{2-} .

Strong correlation found between TC and SO_4^{2-} in concentrations, warrants a combined $\delta^{13}\text{C}$ and $\delta^{34}\text{S}$ analysis of these fractions. During the 2020 – 2021 period, total carbon isotopic composition values of carbonaceous aerosol fell within a relatively narrow range of one per mill, and varied from $-26.7\text{\textperthousand}$ to $-25.7\text{\textperthousand}$, averaging $-26.2 \pm 0.2\text{\textperthousand}$. The $\delta^{13}\text{C}$ values displayed weak correlation with TC concentrations ($r = 0.34$, $p < 0.05$). At the same time, $\delta^{34}\text{S}$ values of PM_1 sulfate ranged from $3.4\text{\textperthousand}$ to $6.1\text{\textperthousand}$, with a mean value of $4.8 \pm 0.8\text{\textperthousand}$. The $\delta^{34}\text{S}$ values exhibited negligible correlation with SO_4^{2-} concentration levels ($r = 0.13$, $p < 0.05$). The weak correlations between isotopic compositions and concentrations suggests that multiple sources with distinct isotopic signatures are contributing, leading to a more complex influence on the composition and concentration of particulate matter. Sulfur pollution sources vary significantly in the sulfur content (Chapter 1.7.2), thus an increased influence from low-sulfur sources (like biomass burning) may not necessarily raise SO_4^{2-} levels but can cause a shift in measured $\delta^{34}\text{S}$ values. For instance, higher biomass inputs would result in more positive $\delta^{34}\text{S}$ values.

In Fig. 3.8 variance of total carbon $\delta^{13}\text{C}$ values, sulfate $\delta^{34}\text{S}$ values and the fractions of non-fossil (or contemporary) carbon (f_{nf}) are presented in accordance to air mass origins.

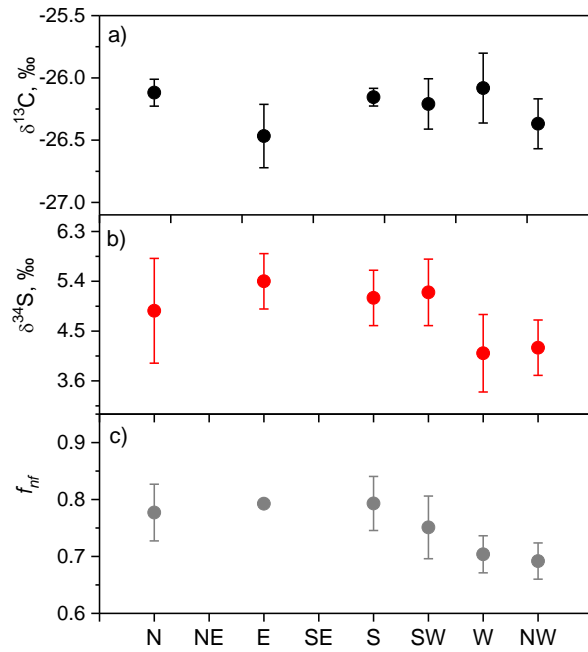


Fig. 3.8. PM_1 TC $\delta^{13}\text{C}$ (a), sulfate $\delta^{34}\text{S}$ (b) value and TC f_{nf} dependence on modeled backward air mass trajectories.

As shown in the figure, there is no clear relationship between $\delta^{13}\text{C}$ values and air mass origins, consistent with the TC concentrations reported in Fig. S2(a). This suggests that local pollution sources were the primary contributors to carbonaceous aerosols. Although, the lowest measure $\delta^{13}\text{C}$ value (-26.72 ‰) occurred in the eastern air direction (moderately polluted regions), where biomass fuels are often used for domestic heating activities in Belarus and Russia (Huang et al., 2020; Popovicheva et al., 2022; Qi and Wang, 2019). On the contrary, $\delta^{34}\text{S}$ values possessed stronger dependence on air mass origins, with lower values for westerly (4.1 ± 0.7 ‰) and northwesterly (4.2 ‰) air masses, likely reflecting coal combustion or crude oil emissions from these regions. By comparison, northern (5 ± 0.9 ‰), southern (5.1 ‰), and southwestern directions (5.2 ± 0.6 ‰) displayed relatively higher values, although only one data point was available for the southern direction. Similar dependence is observed for f_{nf} , with lower values for PM_1 originating from

westerly (0.70 ± 0.03) and northwesterly (0.69) air masses compared to other directions (f_{nf} (N+E+S+SW) = 0.78 ± 0.02).

Next, by applying radiocarbon measurements of TC in aerosols, we can unambiguously determine the contributions of fossil and non-fossil sources, during this period (Fig. 3.9).

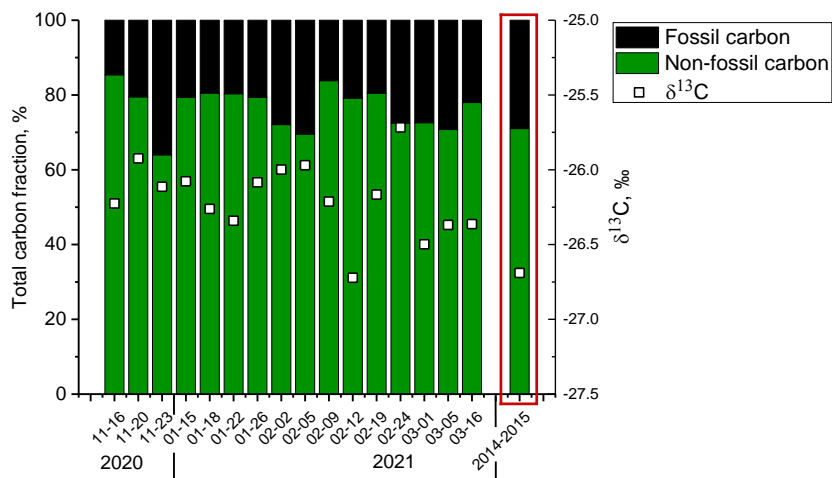


Fig. 3.9. Fossil and non-fossil source contributions to the carbonaceous aerosol throughout 2020 – 2021 period. This period is compared to the years of 2014 – 2015 (Garbarienė et al., 2016). Additionally, measured $\delta^{13}\text{C}$ values are reported for individual sampling periods, denoted as square data points.

During the 2020 – 2021 period, non-fossil sources were the dominant contributors of carbonaceous PM₁, likely due to local domestic heating emissions, specifically biomass fuels, such as firewood, wood pellets and briquettes (Lithuania's National Inventory Report, 2021). Contemporary emission contributions varied from 64 % to 85 % (average 77 ± 6 %), while fossil fuels contributed from 15 % to 36 % (mean 23 ± 6 %). During 2020 – 2021 period, fossil fuel contribution was noticeably lower than reported previously, when compared to the years of 2014 – 2015 from a study by Garbarienė et al. 2016), where fossil fuel contributions averaged 30 %. This reduction likely reflects decreased traffic-related emissions during COVID-19 lockdowns, while biomass burning emissions increased as more individuals were quarantined in their private dwellings. The $\delta^{13}\text{C}$ values in current study (-26.2 ± 0.2 ‰) were more positive than those reported during 2014 – 2015 (-26.7 ± 0.4 ‰), reaffirming that traffic-related emissions decreased during the

quarantine, with $\delta^{13}\text{C}$ values of particulate matter in Lithuania typically ranging from -29 ‰ to -28 ‰ (Chapter 1.7.3.).

In contrast, particulate matter sulfate sources showed a dominant coal combustion emissions contributing on average $60 \pm 10\%$ and ranging from 40 % to 80 % throughout the 2020 – 2021 period (Fig. 3.10).

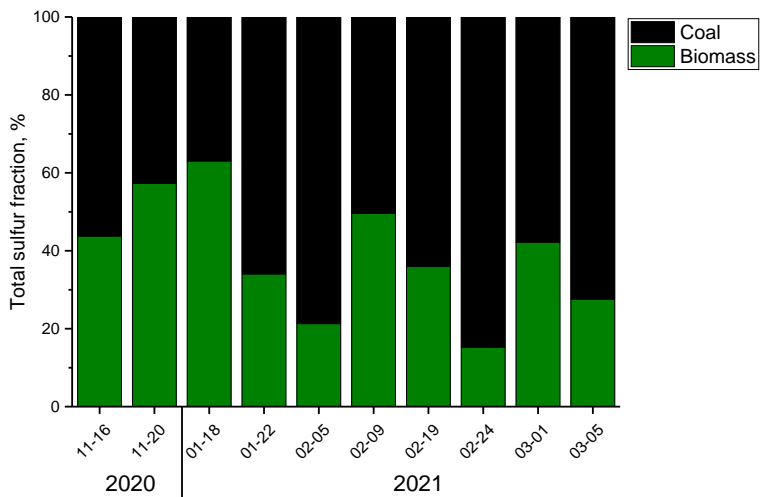


Fig. 3.10. Coal and biomass contributions to total PM₁ sulfate fraction during the 2020 – 2021 period.

Biomass burning emission contribution in the sulfate fraction was much reduced in comparison, ranging from 20 % to 60 %, with a mean value of $40 \pm 10\%$. However, biomass burning emission contributions were significantly greater during this period compared to the subsequent periods of 2021 – 2022 and 2022 – 2023, during which biomass burning emissions contributed 21 % in each period (Fig. 3.6). Additionally, higher coal fractions ($70 \pm 10\%$) were observed in reference to western and northwestern air masses, while other directions (N + S + SW) averaged $60 \pm 10\%$. The lowest coal fraction of 40 % occurred on a previously discussed period from January 15 to January 18, 2021, with air masses coming from the northern regions. Overall, the periods characterized by low temperatures combined with unfavorable conditions for atmospheric mixing, can lead to a prevailing influence of local pollution sources during some periods. This is further evidenced by the $\delta^{34}\text{S}$ value dependence on temperatures in Fig. 3.11.

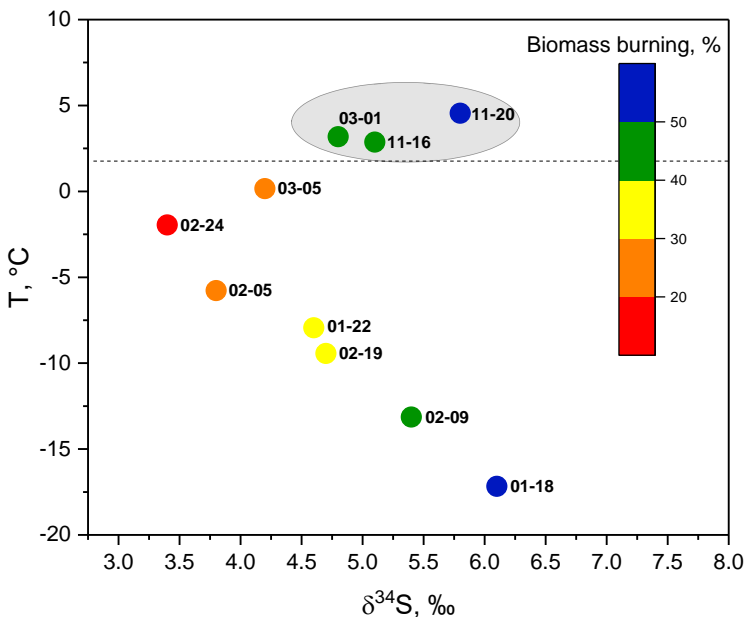


Fig. 3.11. $\delta^{34}\text{S}$ value dependence on average temperatures during individual sampling periods, with their end dates written near the data points. Calculated biomass burning contributions are denoted as color gradient. A threshold at 2.9 °C is marked by a dashed line, below which, $\delta^{34}\text{S}$ values exhibit strong inverse linearity with recorded temperatures.

During the 2020 – 2021 period, $\delta^{34}\text{S}$ values of PM_1 sulfate displayed a strong correlation with temperature ($r = -0.90$, $p < 0.05$), below a threshold of approximately 2.9 °C. As temperatures decreased below this point, biomass burning contribution grew from 20 % to a maximum of 60 %. Although, temperature-related variations in sulfate $\delta^{34}\text{S}$ values may be linked to shifting SO_2 oxidation pathways or changes in gas-to-particle fractionation coefficients, the observed $\delta^{34}\text{S}$ value variation during this period likely reflects changing contributions from different sulfur pollution sources. Furthermore, during the periods when air masses originated from less polluted northern and northwestern sectors, where SO_4^{2-} concentrations are typically low (Davuliene et al., 2021), biomass burning fraction can reach up to 60 %, with local sources predominating over remote ones. Thus, PM_1 samples collected during 01-18, 02-05, 02-09, and 02-19, could be representative of periods with prevailing local source emissions. Over the 2.9 °C mark, sulfate $\delta^{34}\text{S}$ values revert back to the “normal” dependence on temperature, observed during other periods in this study (Fig. 3.3).

Overall, the period of 2020 – 2021 was significant due to rare events which affected the pollutant source distributions, notably the quarantine restrictions in place and, during some intervals, severe atmospheric conditions. However, the study found that traffic mobility restrictions did not affect winter TC concentrations in Vilnius, Lithuania, likely due to increased electricity production emissions and domestic heating activities during the heating season. Overall, contemporary sources ($77 \pm 6\%$) dominated over fossil fuel emissions ($23 \pm 6\%$), with fossil fuel emissions contributing on average 1.3 less than in 2014 – 2015, attributed to confinement conditions. In addition, during the pandemic restrictions, TC $\delta^{13}\text{C}$ values were somewhat enriched ($-26.2 \pm 0.2\text{‰}$) compared to previous measurements ($-26.7 \pm 0.4\text{‰}$), due to reduction in transport emissions. Thus, although total carbon concentrations in PM₁ did not significantly change during the quarantine conditions, notable shifts in $\delta^{13}\text{C}$ values and changes in the pollution sources of carbonaceous aerosol were observed. At the same time, PM₁-related sulfate was primarily attributed to coal combustion ($60 \pm 10\%$) and biomass burning ($40 \pm 10\%$) sources. During the heating season, as ambient temperatures decreased from 0.2 °C to -17.2 °C, $\delta^{34}\text{S}$ values of sulfate increased, indicating a rising influence of biomass burning sources, reaching a maximum of 60 %.

3.6. Impacts of heavy fuel oil usage

To assess the impacts of heavy fuel oil usage, a comparative analysis was performed between two wintertime periods, the conventional heating (CH) period and the period when heavy fuel oil was utilized. For this purpose, CH and HFO periods were compared by analysis of their wintertime concentration levels of water-soluble inorganic ions in PM₁. These periods were further analyzed by combining $\delta^{34}\text{S}$ measurements of atmospheric sulfur compounds with $\delta^{13}\text{C}$ and ^{14}C measurements of the elemental carbon fraction in carbonaceous aerosol. A combined multiple isotope approach of sulfur compounds and EC in PM₁, allows for a detailed description of dominant pollution sources and will help to elucidate changes caused by the use of heavy fuel oil in Vilnius TPS during this time.

The two heating seasons are defined as follows: the CH period (2021 – 2022) is characterized by biomass and natural gas use in Vilnius TPS, and the HFO usage period (2022 – 2023), when low sulfur (0.9 %) heavy fuel oil mostly replaced natural gas in Vilnius TPS. The heavy fuel oil was utilized from November 9, 2022, until the end of March 2023, exclusively. The meteorological conditions during both CH and HFO usage periods were similar. During the CH period, the average temperature was $0.6 \pm 2.8\text{ °C}$, with

a relative humidity of $82 \pm 14\%$, a mixed layer depth of 503 ± 124 m, and an average wind speed of 16.1 ± 4.4 km/h. The air masses from northwestern, western and southwestern directions were prevalent during the CH period. In comparison, during the HFO period, the average temperature was equal to -0.3 ± 3.4 °C, with a relative humidity of $90 \pm 5\%$, a mixed layer depth of 430 ± 118 m, and an average wind speed of 15.4 ± 3.5 km/h. The prevailing air mass directions were of western, southwestern and southeastern origins.

For CH and HFO usage periods, water-soluble inorganic ion concentrations of SO_4^{2-} , NO_3^- , NH_4^+ , Ca^{2+} , Na^+ , K^+ , Mg^{2+} , and Cl^- were measured in the PM_1 fraction (Fig. 3.12). The monitoring data of SO_2 concentrations are also given. The most abundant ions were SO_4^{2-} , K^+ and NO_3^- , consisting approximately 70 % of all measured WSII during both CH and HFO periods. During the CH period (Fig. 3.12(a)), total WSII concentrations ranged from $3.17 \mu\text{g}/\text{m}^3$ to $6.42 \mu\text{g}/\text{m}^3$, with a mean value of $5.12 \mu\text{g}/\text{m}^3$. Average concentrations of SO_4^{2-} were equal to $1.16 \pm 0.31 \mu\text{g}/\text{m}^3$, K^+ equal to $1.61 \pm 0.48 \mu\text{g}/\text{m}^3$ and NO_3^- equal to $1.05 \pm 0.44 \mu\text{g}/\text{m}^3$. Measured concentrations of potassium were the highest, contributing 27 % to total WSII, which is indicative of significant influence of biomass burning emissions (Urban et al., 2012).

During the HFO usage period (Fig. 3.12(b)), total WSII concentrations varied between $2.79 \mu\text{g}/\text{m}^3$ and $7.21 \mu\text{g}/\text{m}^3$, with a mean value of $4.03 \mu\text{g}/\text{m}^3$. This period, saw an increase in the SO_4^{2-} fraction leading to a 37 % contribution, a 15 % increase compared to the CH period. Concentrations of SO_4^{2-} increased by a factor of 1.3, to an average value of $1.53 \pm 0.38 \mu\text{g}/\text{m}^3$. However, the concentrations of potassium ($1.04 \pm 0.58 \mu\text{g}/\text{m}^3$) and nitrate ions ($0.47 \pm 0.37 \mu\text{g}/\text{m}^3$) decreased. In addition, significant rise in monitored SO_2 concentrations was recorded during the HFO usage period, with a mean of $2.54 \pm 2.13 \mu\text{g}/\text{m}^3$, nearly double the level observed during the CH period ($1.30 \pm 0.39 \mu\text{g}/\text{m}^3$).

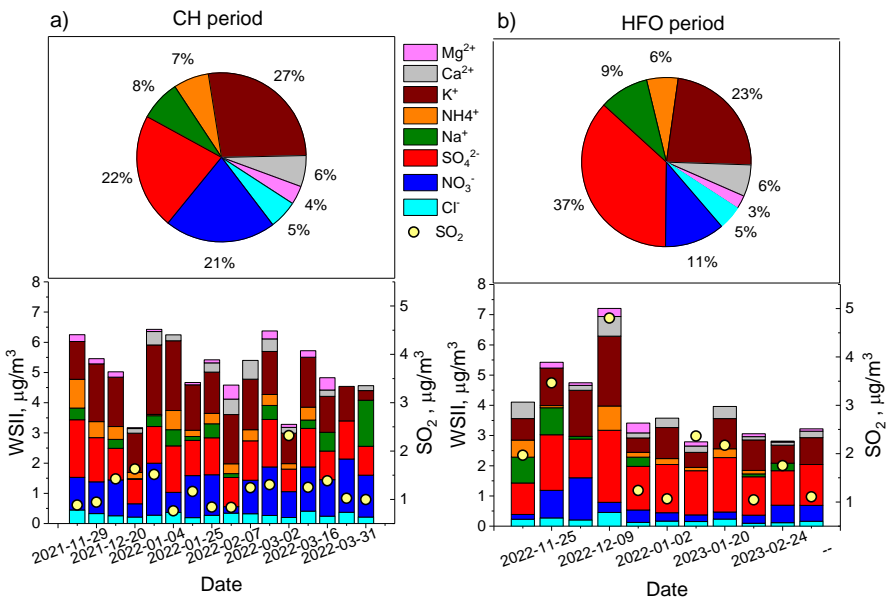


Fig. 3.12. Mass concentration distributions of WSII in PM₁ during individual periods, together with relative contributions to total WSII and SO₂ during CH period (a) and HFO usage period (b).

During the conventional heating period, SO₄²⁻ concentrations (1.16 µg/m³) were comparable to SO₂ levels (1.3 µg/m³), possibly due to the absence of significant local sulfur emission sources. During the CH period, a moderate negative correlation was observed between SO₄²⁻ and SO₂ ($r = -0.55$, $p < 0.05$), indicating contributions of remote sulfur pollution sources to SO₄²⁻ concentrations in Vilnius. Sulfate ion concentrations also displayed a strong positive correlation with ammonium ($r = 0.77$, $p < 0.05$), indicating that (NH₄)₂SO₄ was likely the main species of sulfate in the PM₁.

The atmospheric balance between ammonium sulfate and ammonium nitrate depends on the relative concentrations of SO₄²⁻, NO₃⁻ and NH₄⁺ available at the atmosphere. The higher observed NO₃⁻ concentrations during the CH period are not solely linked to increased emission levels but are influenced by a combination of factors, such as thermodynamic equilibrium between gaseous and particulate phases, and gaseous precursor concentrations (SO₂, NO_x and NH₃) (Harrison et al., 2013; Tsimpidi et al., 2007). In the aqueous phase, atmospheric ammonia neutralizes sulfuric acid, leading to the production of particulate ammonium sulfate, which is a faster reaction than the formation of ammonium nitrate. As a result, ammonium nitrate can only

be produced when there is an excess of ammonium available after neutralization of sulfuric acid (Pathak et al., 2004; Seinfeld and Pandis, 2016). The elevated $[NH_4^+]/[SO_4^{2-}]$ molar ratio (1.6 ± 0.5) and NO_3^-/SO_4^{2-} ratio (0.90 ± 0.78) concentrations, pictured in Fig. 3.13(a,b), imply that decreased SO_4^{2-} levels during the CH period lead to higher nitrate formation.

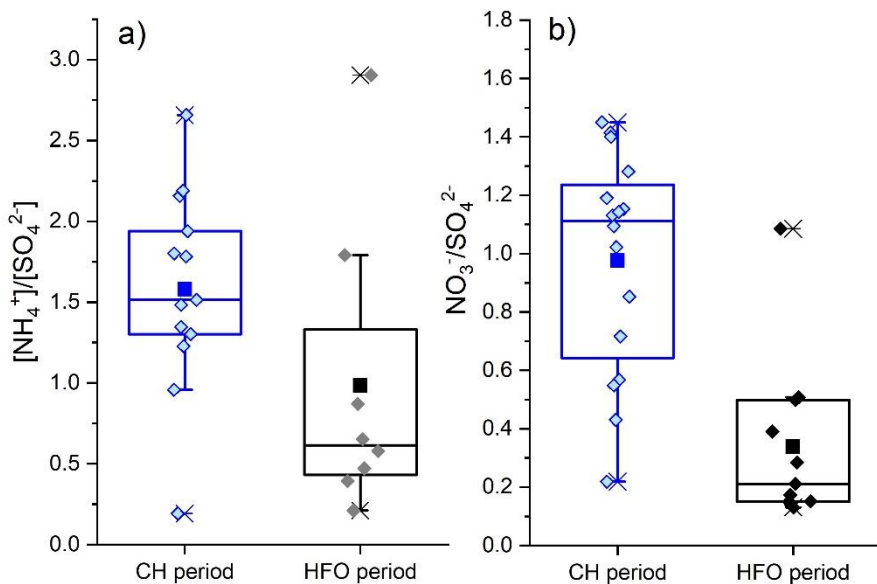


Fig. 3.13. (a) Molar concentration ratios of $[NH_4^+]/[SO_4^{2-}]$ during CH and HFO period. (b) Concentration ratios of NO_3^-/SO_4^{2-} during CH (2021 – 2022) and HFO periods (2022 – 2023).

In comparison, during the HFO period, increased SO_4^{2-} levels lead to a decrease in $[NH_4^+]/[SO_4^{2-}]$ ratio to 0.98 ± 0.52 (Fig. 3.13(a)). Consequently, the NO_3^-/SO_4^{2-} ratio decreases to 0.34 ± 0.31 , reflecting a reduced formation of ammonium nitrate. In addition to these results, during the HFO period, a strong dependence was observed between SO_4^{2-} and K^+ ions (Fig. S3(b), $r = 0.72$, $p < 0.05$). This indicates that sulfate was mainly present as a particulate K_2SO_4 , which is common in environments with elevated biomass burning emissions (Li et al., 2003; Niemi et al., 2004; Viana et al., 2013). Furthermore, sulfur-to-potassium ratio (S/K), often used as an indicator of sulfur accumulation in aerosols of biomass burning origin, was equal to 0.6 (Niemi et al., 2004). This value is similar to those typically found near biomass burning sources (around 0.5) and tends to increase (up to 8) with distance from the source due to aerosol aging (Christensen et al., 1998; Li et al., 2003; Liu

et al., 2000; Viana et al., 2013). Thus, the S/K ratio indicates that collected PM₁ sulfate during the HFO period primarily originated from local sources.

Next, for both the increased HFO usage period and the CH period, we conducted multiple isotope analyses (¹³C, ¹⁴C, and ³⁴S), as shown in Fig. 3.14. The pre-HFO period (Fig. 3.14(b)), for reference, is identified as the time just before the use of HFO, spanning from October 17, 2022, to the start of HFO usage on November 9, 2022.

During the CH period (Fig. 3.14(a)), $\delta^{34}\text{S}_{\text{SO}_2}$ values remained relatively stable, ranging from 4.8 ‰ to 6.1 ‰, averaging 5.4 ± 0.6 ‰. These consistent values suggest that local sources provided a steady background, while remote sources had a lesser influence during this period. This is evidenced by the significant biomass contribution of 54 %, as shown in Fig. 3.14. In contrast, $\delta^{34}\text{S}_{\text{PM}1}$ sulfate values were markedly more variable, ranging from -2.0 ‰ to 4.4 ‰, and averaging 2.0 ± 2.1 ‰, indicating a varying influence of more remote sulfur sources. This is evidenced by the largest coal combustion contribution observed during the whole study, when during the winter of 2021 – 2022, it constituted a contribution of 79 %. In, addition, lowest $\delta^{34}\text{S}_{\text{PM}1}$ values were recorded when air masses originated from the southwest. Overall, $\delta^{34}\text{S}_{\text{SO}_2}$ values were more indicative of the influence of local source emissions, while $\delta^{34}\text{S}_{\text{PM}1}$ values reflected the dominant contribution from remote sources.

During the CH period, PM₁ elemental carbon $\delta^{13}\text{C}_{\text{EC}}$ values varied from -29.3 ‰ to -27.4 ‰, averaging -28.4 ± 0.6 ‰. Although the $\delta^{13}\text{C}_{\text{EC}}$ signatures of regional pollution sources in Lithuania are unknown, a comparative assessment can be made by referencing known source ranges from the literature. The measured values align well with biomass burning source, with $\delta^{13}\text{C}_{\text{EC}}$ values ranging from -29.9 ‰ to -25.4 ‰ (Aguilera and Whigham, 2018; Liu et al., 2014; C. Zhang et al., 2023), and are near of traffic emission values in TC fraction, varying from -31.6 to -29.9 ‰ (Garbaras et al., 2023). However, measured values fall outside the typical range for coal combustion emissions in EC fraction, ranging from -24.7 to -23.3 ‰ (Kawashima and Haneishi, 2012; Yao et al., 2022; C. Zhang et al., 2023).

Simultaneously, radiocarbon analysis showed, that the non-fossil fuel (mainly biomass burning) fraction f_{nf} was equal to 15 ± 6 %, consistent with previous studies (Bernardoni et al., 2013; Dusek et al., 2017; Genberg et al., 2011; Szidat et al., 2004). At the same time, the fossil fuel fraction was the dominant fraction in EC, ranging from 76 to 91 %, with an average of 85 ± 6 %.

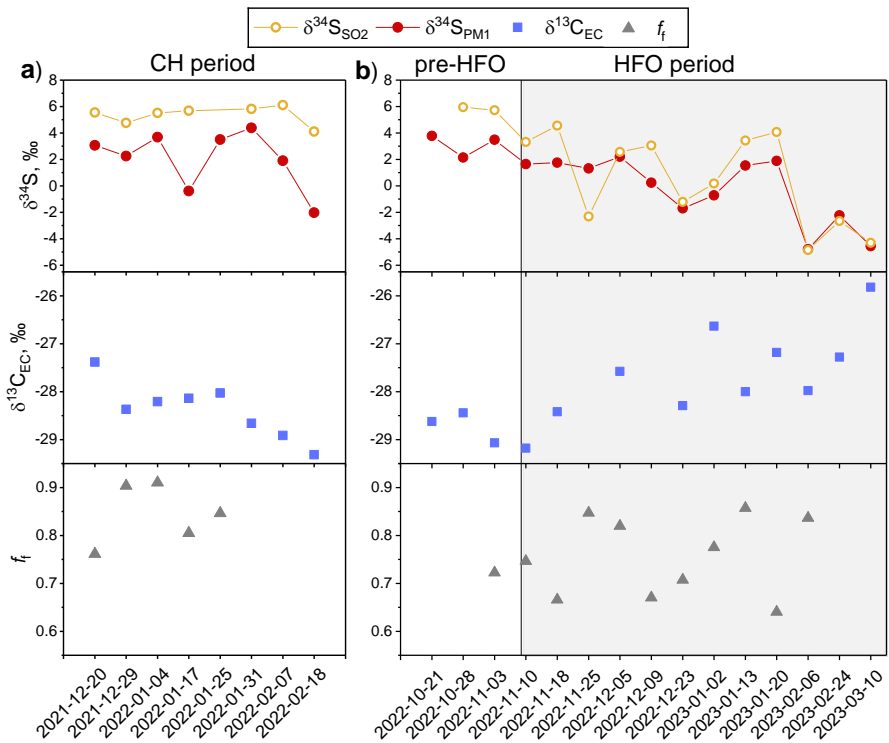


Figure 3.14. The $\delta^{34}\text{S}_{\text{SO}_2}$, $\delta^{34}\text{S}_{\text{PM}1}$, $\delta^{13}\text{C}_{\text{EC}}$ and f_f values for the period from December 10, 2021 to February 18, 2022 (b) considered as a conventional heating (CH) period. In comparison, measurements from October 17, 2022 to March 10, 2023 (b) are given with the interval when heavy fuel oil (HFO) was used marked by gray shading. Measurements taken in 2022, prior to the use of HFO (before November 9, 2022), are classified as the pre-HFO period.

During the HFO period (Fig. 3.14(b)), significant shifts in both $\delta^{34}\text{S}$ values of SO_2 and SO_4^{2-} , and $\delta^{13}\text{C}$ of EC were observed. During this period, the stable SO_2 concentrations and isotopic composition values from the CH period were disrupted, particularly with $\delta^{34}\text{S}_{\text{SO}_2}$ values showing increased variability. The isotopic composition values of SO_2 became more negative, averaging of $0.4 \pm 3.2 \text{ ‰}$, and reaching a minimum $\delta^{34}\text{S}_{\text{SO}_2}$ value of -4.9 ‰ . At the same time, $\delta^{34}\text{S}_{\text{PM}1}$ values averaged $-0.3 \pm 2.4 \text{ ‰}$, and reached a minimum of -4.8 ‰ . As described in Chapter 3.3, these observed low $\delta^{34}\text{S}$ values are indicative of the influence of a new source, likely from HFO combustion with a Middle Eastern origin.

As $\delta^{34}\text{S}$ values became more negative during the HFO usage period, the isotopic composition of PM_1 EC showed an opposite trend, with $\delta^{13}\text{C}_{\text{EC}}$ values

becoming more positive. During pre-HFO period, $\delta^{13}\text{C}_{\text{EC}}$ values averaged $-28.8 \pm 0.3 \text{ ‰}$. After the start of HFO usage, the values increased to an average of $-27.5 \pm 0.8 \text{ ‰}$, reaching a peak of -25.8 ‰ , which is close to reported values of fuel oil ($\sim -26.0 \text{ -- } -25.5 \text{ ‰}$ in combustion particles) by Widory (2006). However, it should be emphasized that the recorded enrichment in ^{13}C could also be influenced by increased emissions from coal combustion or biomass burning. Nonetheless, the observed simultaneous trend of more negative $\delta^{34}\text{S}_{\text{SO}_2}$ and $\delta^{34}\text{S}_{\text{PM}1}$ values, along with the positive shift in $\delta^{13}\text{C}_{\text{EC}}$ values, indicates a common source of pollution. This is further supported by a significant negative correlation between $\delta^{34}\text{S}_{\text{PM}1}$ and $\delta^{13}\text{C}_{\text{EC}}$ (Fig. S4, $r = -0.6$, $p < 0.05$).

The fossil fuel emission f_f fraction of EC varied greatly from 64 % to 86 % during the HFO usage period (Fig. 3.14(b)). However, compared to the CH period, average f_f decreased insignificantly, equaling $75 \pm 7\%$. A comparison between the CH and HFO usage periods is provided in Fig. S5. The decline in the fossil fuel fraction could be attributed to elevated biomass burning emissions.

In summary, the use of HFO in Vilnius TPS had significant impacts on local pollution levels and the source contributions, as reflected in changes to $\delta^{34}\text{S}$ values and concentrations of SO_2 and PM_1 sulfate. The usage of HFO led to almost two-fold increase in ambient SO_2 concentrations and led to a 30% rise in PM_1 sulfate, making SO_4^{2-} the dominant water-soluble inorganic ion, accounting for a 37 % of total WSII. During the CH period (2021 – 2022), when HFO was not used in local TPS, $\delta^{34}\text{S}_{\text{SO}_2}$ values remained stable ($5.4 \pm 0.6 \text{ ‰}$), reflecting the elevated contribution of local biomass burning emissions. Concurrently, $\delta^{34}\text{S}_{\text{PM}1}$ displayed greater variability ($2.0 \pm 2.1 \text{ ‰}$), indicating the prevailing influence of remote pollution sources during this period. In contrast, during the HFO usage period (2022 – 2023), both $\delta^{34}\text{S}_{\text{SO}_2}$ and $\delta^{34}\text{S}_{\text{PM}1}$ shifted to more negative values (mean $\delta^{34}\text{S}_{\text{SO}_2} = 0.4 \pm 3.2 \text{ ‰}$, mean $\delta^{34}\text{S}_{\text{PM}1} = -0.3 \pm 2.4 \text{ ‰}$), highlighting the dominant HFO emission effect on local emission levels. However, total fossil fuel fraction to EC slightly decreased during the HFO period (mean $75 \pm 7\%$), while $\delta^{13}\text{C}_{\text{EC}}$ values became more positive, suggesting ^{13}C enriched emissions of fossil fuel sources, possibly from HFO combustion.

3.7. Factors influencing isotopic composition variations

Seasonal variation in $\delta^{34}\text{S}_{\text{PM}1}$ and $\delta^{34}\text{S}_{\text{SO}_2}$ values, in addition to previously analyzed shifts in source contributions (Chapter 3.4), are also impacted by changes in SO_2 oxidation pathways and temperature-driven isotope

fractionation effects. The synchronous sampling of SO₂ and SO₄²⁻ compounds can provide insights into the factors affecting the isotopic differences between them ($\delta^{34}\text{S}_{\text{PM}1} - \delta^{34}\text{S}_{\text{SO}_2}$), allowing to isolate the influence of SO₂ emission source variation. Here, we will compare isotopic differences during the periods dominated by fluctuating contributions from local and remote sources, and the HFO period, when local emission sources were prevalent.

In Fig. 3.15 isotopic differences between $\delta^{34}\text{S}_{\text{PM}1}$ and $\delta^{34}\text{S}_{\text{SO}_2}$ values are given, for the periods when both SO₂ and PM₁ SO₄²⁻ samples were collected in tandem. Negative $\delta^{34}\text{S}_{\text{PM}1} - \delta^{34}\text{S}_{\text{SO}_2}$ values were observed during winter (mean $-2.0 \pm 1.7 \text{ ‰}$), spring (mean $-0.5 \pm 1.4 \text{ ‰}$) and autumn (mean $-1.6 \pm 2.3 \text{ ‰}$) seasons. However, during the summer, sulfate particles were more isotopically enriched in ³⁴S, averaging $\delta^{34}\text{S}_{\text{PM}1} - \delta^{34}\text{S}_{\text{SO}_2} = 0.4 \pm 1.3 \text{ ‰}$. Spring and winter $\delta^{34}\text{S}_{\text{PM}1} - \delta^{34}\text{S}_{\text{SO}_2}$ differences were similarly small in magnitude, however the HFO period skewed the results as an obvious shift towards zero can be seen during this period. If the winter of 2021 – 2022 is analyzed separately, the largest $\delta^{34}\text{S}_{\text{PM}1} - \delta^{34}\text{S}_{\text{SO}_2}$ differences are observed, averaging $-3.6 \pm 1.7 \text{ ‰}$. This winter season, detailed in Chapter 3.6 as the conventional heating (CH) period, revealed that $\delta^{34}\text{S}_{\text{SO}_2}$ values primarily reflected the influence of local biomass burning sources, while the more negative $\delta^{34}\text{S}_{\text{PM}1}$ values indicated the influence of remote sources, mainly coal combustion. In addition to this, the largest $\delta^{34}\text{S}_{\text{PM}1} - \delta^{34}\text{S}_{\text{SO}_2}$ differences were marked, when air masses originated from southern - southwestern directions (average of $-5.2 \pm 0.9 \text{ ‰}$), highlighting the distinct differences in ³⁴S signatures of local SO₂ and remote sulfate sources.

The observed $\delta^{34}\text{S}_{\text{PM}1} - \delta^{34}\text{S}_{\text{SO}_2}$ value variations during the conventional periods (excluding HFO period) contrast with the modeled isotopic composition seasonality reported by Harris et al. (2013a). In their study, the seasonal variation of $\delta^{34}\text{S}_{\text{PM}1} - \delta^{34}\text{S}_{\text{SO}_2}$ difference was modeled solely based on changing oxidation pathway contributions and the fractionation factor dependence on temperature and lower $\delta^{34}\text{S}_{\text{PM}1} - \delta^{34}\text{S}_{\text{SO}_2}$ differences were reported in summer, and higher in winter, displaying good agreement with real observations made by Novák et al. (2001). However, in the model, SO₂ emission fluxes were assumed to be constant. In contrast, real observations made in the relatively clean environment of Vilnius are heavily influenced by remote pollution sources (evidenced in Chapters 3.2 and 3.4) and changing SO₂ emissions levels (Chapter 3.3), which likely account for the observed discrepancy when compared to the modeled results. In addition, TMI catalysis pathway was possibly underestimated in the model (Harris et al., 2013a), contributing 35 % of annual SO₂ oxidation.

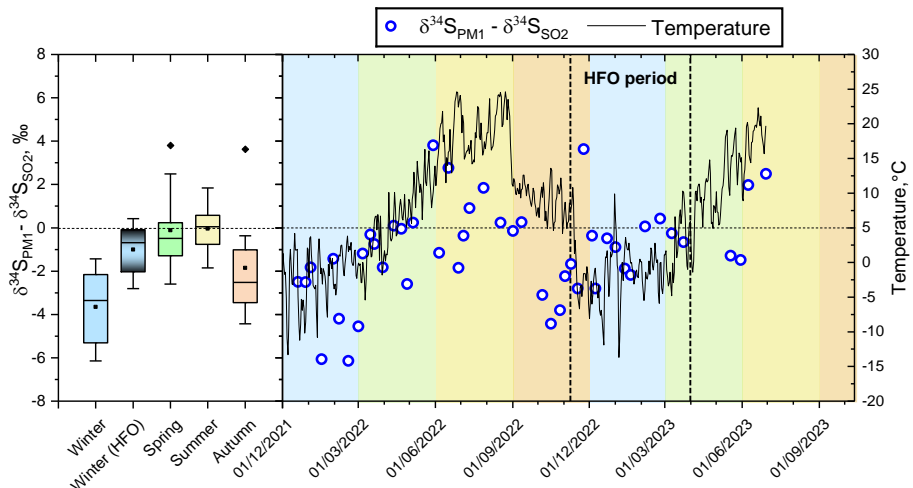


Fig. 3.15. The isotopic differences between $\delta^{34}\text{S}$ values of SO_2 and PM_1 sulfate ($\delta^{34}\text{S}_{\text{PM}1} - \delta^{34}\text{S}_{\text{SO}2}$) are presented on the right side for the period from December 10, 2021 up until June 30, 2023, with HFO period marked by dashed lines. Colored shading separates distinct seasons: blue for winter, green for spring, yellow for summer, and orange for autumn. On the left, boxplots of $\delta^{34}\text{S}_{\text{PM}1} - \delta^{34}\text{S}_{\text{SO}2}$ for corresponding seasons are given, with HFO period discerned by black gradient.

However, in contrast to the winter of 2021 – 2022, during the HFO usage period (Fig. 3.15), $\delta^{34}\text{S}_{\text{PM}1} - \delta^{34}\text{S}_{\text{SO}2}$ difference became far less pronounced, averaging at $-0.7 \pm 1.7 \text{ ‰}$. During the HFO usage period, a significantly stronger correlation between $\delta^{34}\text{S}_{\text{PM}1}$ and $\delta^{34}\text{S}_{\text{SO}2}$ values was observed (Fig. S6, $r = 0.86$, $p = 0.05$), compared to all other periods ($r = 0.47$, $p < 0.05$). High relative humidity levels observed during this period averaging $90 \pm 5 \text{ %}$ also could have created favorable conditions for efficient sulfate production. Furthermore, $\delta^{34}\text{S}_{\text{PM}1}$ displayed strong correlation with SOR ($r = -0.69$, $p = 0.05$), in contrast to the very low dependency observed during all other periods ($r = -0.06$, $p < 0.05$). These relations, point to an increased influence of local SO_2 pollution sources that directly contribute to the subsequent PM_1 sulfate production through gas-to-particle conversion processes in the atmosphere. Thus, during HFO usage period, measured $\delta^{34}\text{S}_{\text{PM}1}$ values are likely to be representative of local pollution sources and thus are well-constrained. Furthermore, it is both feasible and appropriate to examine the fractionation

effects of SO₂ oxidation reactions, and to evaluate the contributions of distinct oxidation pathways, during this period.

Due to aforementioned increased influence of local pollution sources during the HFO usage period from November 9, 2022, to March 31, 2023, different SO₂ oxidation pathway contributions were calculated exclusively for this timeframe. During this period, the observed $\delta^{34}\text{S}_{\text{PM}1}$ - $\delta^{34}\text{S}_{\text{SO}_2}$ values are more closely linked to gas-to-particle fractionation effects, rather than reflecting the differences between remote and local pollution sources. Considering that, HFO emissions in Vilnius occurred exclusively during the cold season, the oxidation contribution from OH radicals was expected to be minimal due to the low concentrations of hydroxyl radicals in winter (Harris et al., 2013a). The fractional inputs from OH oxidation was evaluated separately based on data from previous studies (Harris et al., 2013a; Sofen et al., 2011), by taking into account diurnal variations in mean OH concentrations, daily hours of sunlight, and calculated SOR values for individual sampling periods (Chapter 2.7). Furthermore, SO₂ oxidation by O₃ was not evaluated separately due to its minor annual contributions and its similar fractionation factor to that of H₂O₂. Additionally, oxidation by O₃ is slow at pH values below 5.5, and the reaction is self-limiting as the production of sulfate acidifies the aqueous solution (Seinfeld and Pandis, 2016). Consequently, the contributions of these oxidants are typically treated as a combined total (Fan et al., 2020; Li et al., 2020). In addition, the contribution of NO₂ pathway was also not considered due to negligible regional concentrations and small fractionation effects at low temperatures (below ~8 °C) (Au Yang et al., 2018). Thus, we focused on three main oxidation pathways relevant to the environment of Vilnius: OH, H₂O₂, and O₂ in the presence of TMIs. Relative contributions were calculated using Eq. 2.10 – Eq. 2.13.

During the HFO period, average $\delta^{34}\text{S}_{\text{emission}}$ value (Eq. 2.10), representing the isotopic composition of SO₂ at emission, was equal to $0.2 \pm 2.9\text{‰}$. The factor $\varepsilon_{g \rightarrow p}$ (Eq. 2.11) of the overall fractionation of gas-to-particle conversion, averaged $-0.6 \pm 1.5\text{‰}$, indicating changing contributions of several oxidation pathways. In this period, average ambient temperature varied between -4.5 °C and 3.7 °C, corresponding to ε_{OH} factor ranging 10.59 ‰ to 10.62 % (mean $10.60 \pm 0.01\text{‰}$), $\varepsilon_{\text{H}_2\text{O}_2}$ varying from 16.20 ‰ to 16.87 ‰ (mean $16.59 \pm 0.24\text{‰}$) and ε_{TMI} fluctuating between -4.36 ‰ and -3.14 ‰ (mean $-3.69 \pm 0.35\text{‰}$). Thus, fractionation factor dependence on temperature was low during this period.

The fractionation factors depend on the reaction extent, and were represented in Fig. 3.16(a) for the average $\delta^{34}\text{S}_{\text{emission}}$ value, together with

measured $\delta^{34}\text{S}_{\text{PM}1}$ data points. From the figure, it is evident that evaluation of different SO_2 oxidation pathway contributions is only reasonable for lower SOR ranges, where relative differences between fractionation factors is the greatest. During the HFO period, results fall in this lower SOR value region and apportionment of oxidation pathways was performed as was described in Chapter 2.7.

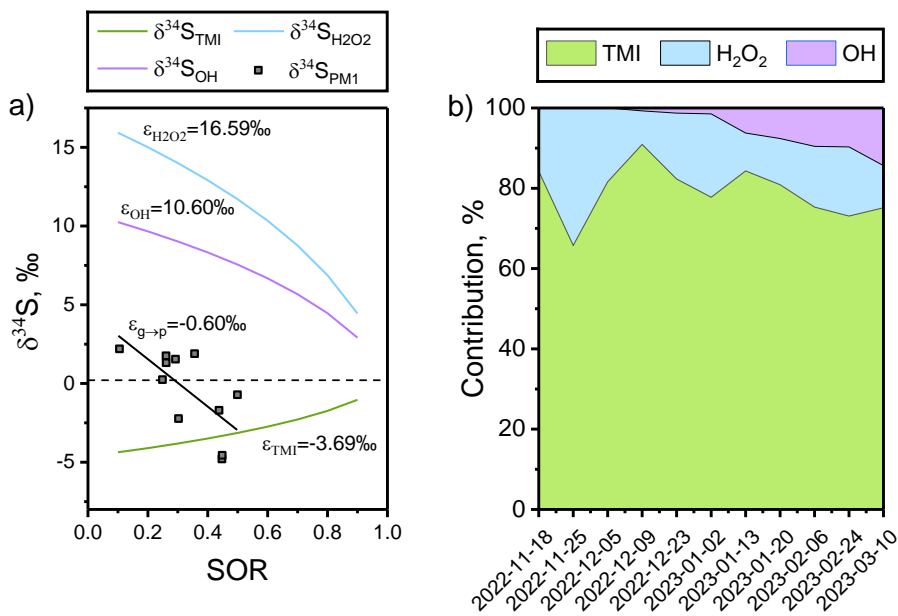


Fig. 3.16. (a) Relationship between measured $\delta^{34}\text{S}_{\text{PM}1}$ values and sulfur oxidation ratio (SOR) during HFO period, with the black line representing fitted $\delta^{34}\text{S}_{\text{PM}1}$ values ($r = -0.69$, $p < 0.05$, $N = 11$). For reference, theoretical $\delta^{34}\text{S}_{\text{PM}1}$ value curves were calculated for each SO_2 oxidation pathway, based on average $\delta^{34}\text{S}_{\text{emission}}$ value of 0.2 % (marked by a dashed line). The blue line represents theoretical $\delta^{34}\text{S}_{\text{PM}1}$ values for oxidation only by H_2O_2 , the purple line corresponds to oxidation by OH radicals, and green line reflects the TMI oxidation pathway. (b) Variation of evaluated contributions of different SO_2 oxidation pathways (TMI, H_2O_2 and OH) during the HFO usage period. The uncertainties of estimated SO_2 oxidation contributions were generally below 10 % (1σ).

In Fig. 3.16(b), the dominant contribution of TMI oxidation pathway is notable, which ranged from 66 % to 91 %, averaging 79 ± 7 % during this period (Fig. 3.16(b)). The contribution of the H_2O_2 pathway ranged from 8 % to 34 %, with an average of 16 ± 7 %. The OH pathway, though consistently

low, gradually increased from a negligible fraction of nearly 0 % in November to 14 % in March, averaging 5 ± 5 %. It has been previously estimated that TMI-catalyzed O₂ oxidation of SO₂ accounted for up to 17 % of global sulfate production (Alexander et al., 2009). However, current studies suggest this has been significantly underestimated and regionally could contribute more than 35 % (Harris et al., 2013a, 2013b). Some previous field studies have identified SO₂ oxidation by TMI catalysis to be significant contributor (Amiri et al., 2018; Harris et al., 2013b), especially during winter (Jacob and Hoffmann, 1983; McCabe et al., 2006). At an arctic environment in Alert, Canada, during corresponding months as this study (November to March), the TMI pathway accounted for an average of approximately 45 %, with a maximum of 60 % during January, which is still considerably lower than in this study (Alexander et al., 2009). In more polluted regions, such as urban environments in China, TMI oxidation contributed 24 % of sulfate formation during relatively clean periods in wintertime but could rise to as much as 49 ± 10 % during haze episodes (Fan et al., 2020; Li et al., 2020). In urban locations, the influence of TMI oxidation rises during winter due to increased anthropogenic emissions from energy generation (primarily coal combustion (Luo et al., 2008)). Considering that coal combustion is a major source of Fe and Mn ions, TMI catalysis likely plays a key role in SO₂ oxidation in Central and Eastern European regions, if we consider modeled results reported by Alexander et al. (2009). During the colder months, the OH oxidation pathways is inhibited, further elevating the relative contribution of TMI oxidation (Harris et al., 2013a). In addition, heavy fuel oil is rich in metal ions like Fe ions (~34% in PM) (Allouis et al., 2003), which likely also increased atmospheric TMI concentrations during HFO usage. Therefore, increased metal ion emissions from coal combustion and heavy fuel oil usage at the local TPS in Vilnius, likely enhanced the dominant fraction of TMI oxidation pathway observed during the winter of 2022 – 2023.

CONCLUSIONS

1. Over the course of more than two years, clear seasonal patterns in both SO_2 and sulfate isotopic compositions were observed, with isotopically enriched sulfur species occurring during the summer months ($\delta^{34}\text{S}_{\text{SO}_2} = 6.5 \pm 1.7 \text{ ‰}$; $\delta^{34}\text{S}_{\text{PM}_1} = 6.5 \pm 1.5 \text{ ‰}$), whereas isotopically lighter fractions were found during the winter months ($\delta^{34}\text{S}_{\text{SO}_2} = 3.1 \pm 3.4 \text{ ‰}$; $\delta^{34}\text{S}_{\text{PM}_1} = 2.3 \pm 2.7 \text{ ‰}$). The seasonal variations of $\delta^{34}\text{S}_{\text{SO}_2}$ and $\delta^{34}\text{S}_{\text{PM}_1}$ were primarily driven by changes in sulfur pollution source contributions and the partitioning between different SO_2 oxidation pathways, with temperature-dependent fractionation playing a minor role.
2. From 2020 to 2022, local biomass burning sources and long-range transport of coal combustion emissions from neighboring countries were the predominant contributors to sulfur pollution in Vilnius during the winter months, accounting for $30 \pm 16 \text{ %}$ and $70 \pm 16 \text{ %}$, respectively. Throughout the summer months of the entire sampling period, reduced emissions from coal and oil combustion made biomass burning the prevalent source of sulfur, contributing $60 \pm 18 \text{ %}$ to SO_2 and $63 \pm 16 \text{ %}$ PM_1 fractions.
3. During the winter of 2022 – 2023, the introduction of heavy fuel oil at the local thermal power station led to significant shifts in the measured isotopic compositions of sulfur compounds and carbonaceous PM_1 , evidenced by highly negative $\delta^{34}\text{S}$ values ($\delta^{34}\text{S}_{\text{SO}_2} = 0.4 \text{ ‰}$, $\delta^{34}\text{S}_{\text{PM}_1} = -0.3 \text{ ‰}$) and more positive $\delta^{13}\text{C}$ values ($-27.5 \pm 0.8 \text{ ‰}$). During this period, heavy fuel oil emissions contributed approximately 40 % to both SO_2 and sulfate fractions, while coal combustion emissions contributions decreased to $34 \pm 6 \text{ %}$ for SO_2 and $36 + 8 \text{ %}$ for sulfate.
4. When heavy fuel oil was used in Vilnius thermal power station, sulfur emissions from local pollution sources outweighed those from remote sources. This allowed the assessment of gas-to-particle fractionation factors and the calculation of the relative contributions from different SO_2 oxidation pathways. The predominant SO_2 oxidation pathway was determined to be catalysis by transition metal ions, which contributed $79 \pm 7 \text{ %}$ to total sulfate production in PM_1 . Other oxidants were less effective: H_2O_2 and OH contributed $16 \pm 7 \text{ %}$ and $5 \pm 5 \text{ %}$, respectively.

REFERENCES

- Ackerman, A.S., Toon, O.B., Stevens, D.E., Heymsfield, A.J., Ramanathan, V., Welton, E.J., 2000. Reduction of tropical cloudiness by soot. *Science* (1979) 288. <https://doi.org/10.1126/science.288.5468.1042>
- Agostini, A., Giuntoli, J., Boulamanti, A., 2014. Carbon accounting of forest bioenergy critical literature review. EC JRC Scietific and policy reports. Rep EUR 25354
- Aguilera, J., Whigham, L.D., 2018. Using the $^{13}\text{C}/^{12}\text{C}$ carbon isotope ratio to characterise the emission sources of airborne particulate matter: a review of literature. *Isotopes Environ Health Stud.* <https://doi.org/10.1080/10256016.2018.1531854>
- Ajdari, S., Normann, F., Andersson, K., Johnsson, F., 2016. Reduced Mechanism for Nitrogen and Sulfur Chemistry in Pressurized Flue Gas Systems. *Ind Eng Chem Res* 55. <https://doi.org/10.1021/acs.iecr.5b04670>
- Albrecht, B.A., 1989. Aerosols, cloud microphysics, and fractional cloudiness. *Science* (1979) 245. <https://doi.org/10.1126/science.245.4923.1227>
- Alexander, B., Park, R.J., Jacob, D.J., Gong, S., 2009. Transition metal-catalyzed oxidation of atmospheric sulfur: Global implications for the sulfur budget. *Journal of Geophysical Research Atmospheres* 114. <https://doi.org/10.1029/2008JD010486>
- Allouis, C., Beretta, F., D'Alessio, A., 2003. Structure of inorganic and carbonaceous particles emitted from heavy oil combustion, in: *Chemosphere*. [https://doi.org/10.1016/S0045-6535\(02\)00714-2](https://doi.org/10.1016/S0045-6535(02)00714-2)
- Amiri, N., Ghahremaninezhad, R., Rempillo, O., Tokarek, T.W., Odame-Ankrah, C.A., Osthoff, H.D., Norman, A.L., 2018. Stable sulfur isotope measurements to trace the fate of SO₂ in the Athabasca oil sands region. *Atmos Chem Phys* 18. <https://doi.org/10.5194/acp-18-7757-2018>
- Andreae, M.O., Crutzen, P.J., 1997. Atmospheric aerosols: Biogeochemical sources and role in atmospheric chemistry. *Science* (1979) 276. <https://doi.org/10.1126/science.276.5315.1052>
- Assonov, S., 2018. Summary and recommendations from the International Atomic Energy Agency Technical Meeting on the Development of Stable Isotope Reference Products (21–25 November 2016), in: *Rapid Communications in Mass Spectrometry*. <https://doi.org/10.1002/rcm.8102>
- Assonov, S., Groening, M., Fajgelj, A., Hélie, J.F., Hillaire-Marcel, C., 2020. Preparation and characterisation of IAEA-603, a new primary reference

- material aimed at the VPDB scale realisation for $\delta^{13}\text{C}$ and $\delta^{18}\text{O}$ determination. *Rapid Communications in Mass Spectrometry* 34, e8867. <https://doi.org/10.1002/RCM.8867>
- Assonov, S.S., Brenninkmeijer, C.A.M., 2003. On the ^{17}O correction for CO_2 mass spectrometric isotopic analysis. *Rapid Communications in Mass Spectrometry* 17. <https://doi.org/10.1002/rcm.1012>
- Au Yang, D., Bardoux, G., Assayag, N., Laskar, C., Widory, D., Cartigny, P., 2018. Atmospheric SO_2 oxidation by NO_2 plays no role in the mass independent sulfur isotope fractionation of urban aerosols. *Atmos Environ* 193. <https://doi.org/10.1016/j.atmosenv.2018.09.007>
- Bahm, K., Khalil, M.A.K., 2004. A new model of tropospheric hydroxyl radical concentrations. *Chemosphere* 54. <https://doi.org/10.1016/j.chemosphere.2003.08.006>
- Bailey, S.A., Smith, J.W., 1972. Improved Method for the Preparation of Sulfur Dioxide from Barium Sulfate for Isotope Ratio Studies. *Anal Chem* 44. <https://doi.org/10.1021/ac60316a034>
- Barrie, L.A., Yi, Y., Leaitch, W.R., Lohmann, U., Kasibhatla, P., Roelofs, G.J., Wilson, J., McGovern, F., Benkovitz, C., Mélières, M.A., Law, K., Prospero, J., Kritz, M., Bergmann, D., Bridgeman, C., Chin, M., Christensen, J., Easter, R., Feichter, J., Land, C., Jeuken, A., Kjellström, E., Koch, D., Rasch, P., 2001. A comparison of large-scale atmospheric sulphate aerosol models (COSAM): Overview and highlights. *Tellus B Chem Phys Meteorol* 53. <https://doi.org/10.3402/tellusb.v53i5.16642>
- Becker, S., Hirner, A. V., 1998. Characterisation of Crude Oils by Carbon and Sulphur Isotope Ratio Measurements as a Tool for Pollution Control. *Isotopes Environ Health Stud* 34, 255–264. <https://doi.org/10.1080/10256019808234058>
- Bellouin, N., Quaas, J., Gryspeerd, E., Kinne, S., Stier, P., Watson-Parris, D., Boucher, O., Carslaw, K.S., Christensen, M., Daniau, A.L., Dufresne, J.L., Feingold, G., Fiedler, S., Forster, P., Gettelman, A., Haywood, J.M., Lohmann, U., Malavelle, F., Mauritzen, T., McCoy, D.T., Myhre, G., Mülmenstädt, J., Neubauer, D., Possner, A., Rugenstein, M., Sato, Y., Schulz, M., Schwartz, S.E., Sourdeval, O., Storelvmo, T., Toll, V., Winker, D., Stevens, B., 2020. Bounding Global Aerosol Radiative Forcing of Climate Change. *Reviews of Geophysics*. <https://doi.org/10.1029/2019RG000660>
- Berglen, T.F., Berntsen, T.K., Isaksen, I.S.A., Sundet, J.K., 2004. A global model of the coupled sulfur/oxidant chemistry in the troposphere: The sulfur cycle. *Journal of Geophysical Research D: Atmospheres* 109. <https://doi.org/10.1029/2003JD003948>

- Bernardoni, V., Calzolai, G., Chiari, M., Fedi, M., Lucarelli, F., Nava, S., Piazzalunga, A., Riccobono, F., Taccetti, F., Valli, G., Vecchi, R., 2013. Radiocarbon analysis on organic and elemental carbon in aerosol samples and source apportionment at an urban site in Northern Italy. *J Aerosol Sci* 56. <https://doi.org/10.1016/j.jaerosci.2012.06.001>
- Berresheim, H., Elste, T., Tremmel, H.G., Allen, A.G., Hansson, H.C., Rosman, K., Dal Maso, M., Mäkelä, J.M., Kulmala, M., O'Dowd, C.D., 2002. Gas-aerosol relationships of H₂SO₄, MSA, and OH: Observations in the coastal marine boundary layer at Mace Head, Ireland. *Journal of Geophysical Research Atmospheres* 107. <https://doi.org/10.1029/2000JD000229>
- Bertelsen, N., Mathiesen, B.V., 2020. EU-28 residential heat supply and consumption: Historical development and status. *Energies (Basel)* 13. <https://doi.org/10.3390/en13081894>
- Bigeleisen, J., 1965. Chemistry of isotopes. *Science (1979)* 147. <https://doi.org/10.1126/science.147.3657.463>
- Bikkina, S., Kawamura, K., Sarin, M., 2016. Stable carbon and nitrogen isotopic composition of fine mode aerosols (PM2.5) over the Bay of Bengal: Impact of continental sources. *Tellus B Chem Phys Meteorol* 68. <https://doi.org/10.3402/tellusb.v68.31518>
- Bondietti, E.A., Papastefanou, C., 1993. Estimates of residence times of sulfate aerosols in ambient air. *Science of the Total Environment, The* 136. [https://doi.org/10.1016/0048-9697\(93\)90294-G](https://doi.org/10.1016/0048-9697(93)90294-G)
- Boucher, O., Lohmann, U., 1995. The sulfate-CCN-cloud albedo effect: a sensitivity study with two general circulation models. *Tellus, Series B* 47 B. <https://doi.org/10.3402/tellusb.v47i3.16048>
- Brand, W.A., Assonov, S.S., Coplen, T.B., 2010. Correction for the ¹⁷O interference in $\delta(13\text{C})$ measurements when analyzing CO₂ with stable isotope mass spectrometry (IUPAC Technical Report). *Pure and Applied Chemistry* 82. <https://doi.org/10.1351/PAC-REP-09-01-05>
- Bressi, M., Cavalli, F., Putaud, J.P., Fröhlich, R., Petit, J.E., Aas, W., Äijälä, M., Alastuey, A., Allan, J.D., Aurela, M., Berico, M., Bougiatioti, A., Bukowiecki, N., Canonaco, F., Crenn, V., Dusanter, S., Ehn, M., Elsasser, M., Flentje, H., Graf, P., Green, D.C., Heikkinen, L., Hermann, H., Holzinger, R., Hueglin, C., Keernik, H., Kiendler-Scharr, A., Kubelová, L., Lunder, C., Maasikmets, M., Makeš, O., Malaguti, A., Mihalopoulos, N., Nicolas, J.B., O'Dowd, C., Ovadnevaite, J., Petralia, E., Poulain, L., Priestman, M., Riffault, V., Ripoll, A., Schlag, P., Schwarz, J., Sciare, J., Slowik, J., Sosedova, Y., Stavroulas, I., Teinemaa, E., Via, M., Vodička, P., Williams, P.I., Wiedensohler, A.,

- Young, D.E., Zhang, S., Favez, O., Minguillón, M.C., Prevot, A.S.H., 2021. A European aerosol phenomenology - 7: High-time resolution chemical characteristics of submicron particulate matter across Europe. *Atmos Environ X* 10. <https://doi.org/10.1016/j.aeaoa.2021.100108>
- Brook, R.D., Rajagopalan, S., Pope, C.A., Brook, J.R., Bhatnagar, A., Diez-Roux, A. V., Holguin, F., Hong, Y., Luepker, R. V., Mittleman, M.A., Peters, A., Siscovich, D., Smith, S.C., Whitsel, L., Kaufman, J.D., 2010. Particulate matter air pollution and cardiovascular disease: An update to the scientific statement from the american heart association. *Circulation*. <https://doi.org/10.1161/CIR.0b013e3181dbece1>
- Brown, A.S., van der Veen, A.M.H., Arrhenius, K., Murugan, A., Culleton, L.P., Ziel, P.R., Li, J., 2015. Sampling of gaseous sulfur-containing compounds at low concentrations with a review of best-practice methods for biogas and natural gas applications. *TrAC - Trends in Analytical Chemistry*. <https://doi.org/10.1016/j.trac.2014.08.012>
- Bučinskas, L., Garbarienė, I., Mašalaitė, A., Jasinevičienė, D., Remeikis, V., Garbaras, A., 2024a. Variability in Stable Sulfur Isotope Composition of PM1 and SO₂: Insights from a 2-year Investigation into Seasonal Dynamics. *Aerosol Air Qual Res* 24, 240142. <https://doi.org/10.4209/AAQR.240142>
- Bučinskas, L., Garbarienė, I., Mašalaitė, A., Šapolaitė, J., Ežerinskis, Ž., Jasinevičienė, D., Garbaras, A., 2024b. Evaluating the Impact of Increased Heavy Oil Consumption on Urban Pollution Levels through Isotope ($\delta^{13}\text{C}$, $\delta^{34}\text{S}$, ^{14}C) Composition. *Atmosphere (Basel)* 15. <https://doi.org/10.3390/ATMOS15080883>
- Bučinskas, L., Garbarienė, I., Mašalaitė, A., Šapolaitė, J., Ežerinskis, Ž., Jasinevičienė, D., Remeikis, V., Garbaras, A., 2024c. Dual carbon and sulfur isotopes as tracers of PM1 pollution sources after COVID-19 confinement in Vilnius, Lithuania. *Urban Clim* 55. <https://doi.org/10.1016/j.uclim.2024.101894>
- Butkus, L., Šapolaitė, J., Garbarienė, I., Garbaras, A., Bučinskas, L., Pabedinskas, A., Remeikis, V., Ežerinskis, Ž., 2022. Development of graphitization method for low carbon aerosol filter samples with Automated Graphitization System AGE-3. *Applied Radiation and Isotopes* 190. <https://doi.org/10.1016/j.apradiso.2022.110461>
- Cachier, H., Buat-Menard, P., Fontugne, M., Rancher, J., 1985. Source terms and source strengths of the carbonaceous aerosol in the tropics. *J Atmos Chem*. <https://doi.org/10.1007/BF00053872>

- Calhoun, J.A., Bates, T.S., Charlson, R.J., 1991. Sulfur isotope measurements of submicrometer sulfate aerosol particles over the Pacific Ocean. *Geophys Res Lett.* <https://doi.org/10.1029/91GL02304>
- Calkins, W.H., 1994. The chemical forms of sulfur in coal: a review. *Fuel.* [https://doi.org/10.1016/0016-2361\(94\)90028-0](https://doi.org/10.1016/0016-2361(94)90028-0)
- Calvert, J.G., Stockwell, W.R., 1983. Acid generation in the troposphere by gas-phase chemistry. *Environ Sci Technol* 17. <https://doi.org/10.1021/es00115a002>
- Caron, F., Tessier, A., Kramer, J.R., Schwarcz, H.P., Rees, C.E., 1986. Sulfur and oxygen isotopes of sulfate in precipitation and lakewater, Quebec, Canada. *Applied Geochemistry* 1. [https://doi.org/10.1016/0883-2927\(86\)90067-3](https://doi.org/10.1016/0883-2927(86)90067-3)
- Carter, J.F., Fry, B., 2013. Ensuring the reliability of stable isotope ratio data - Beyond the principle of identical treatment. *Anal Bioanal Chem.* <https://doi.org/10.1007/s00216-012-6551-0>
- Celasun, O., Mineshima, A., Arregui, N., Mylonas, V., Ari, A., Teodoru, I., Black, S., Zhunussova, K., Iakova, D., Parry, I., 2022. Surging Energy Prices in Europe in the Aftermath of the War: How to Support the Vulnerable and Speed up the Transition Away from Fossil Fuels. IMF Working Papers 2022. <https://doi.org/10.5089/9798400214592.001>
- Charlson, R.J., Schwartz, S.E., Hales, J.M., Cess, R.D., Coakley, J.A., Hansen, J.E., Hofmann, D.J., 1992. Climate forcing by anthropogenic aerosols. *Science* (1979) 255. <https://doi.org/10.1126/science.255.5043.423>
- CHC, 2023. PEOPLE CREATE HEAT 2022. Available online: <https://chc.lt/lt> (accessed 6.20.24)
- CHC, 2022. PEOPLE CREATE HEAT 2021. Available online: <https://chc.lt/lt> (accessed 6.26.24)
- Cheng, Y., Zheng, G., Wei, C., Mu, Q., Zheng, B., Wang, Z., Gao, M., Zhang, Q., He, K., Carmichael, G., Pöschl, U., Su, H., 2016. Reactive nitrogen chemistry in aerosol water as a source of sulfate during haze events in China. *Sci Adv* 2. <https://doi.org/10.1126/sciadv.1601530>
- Chin, M., Jacob, D.J., Gardner, G.M., Foreman-Fowler, M.S., Spiro, P.A., Savoie, D.L., 1996. A global three-dimensional model of tropospheric sulfate. *Journal of Geophysical Research Atmospheres*. <https://doi.org/10.1029/96jd01221>
- Chin, M., Rood, R.B., Lin, S.J., Müller, J.F., Thompson, A.M., 2000. Atmospheric sulfur cycle simulated in the global model GOCART: Model description and global properties. *Journal of Geophysical Research Atmospheres* 105. <https://doi.org/10.1029/2000JD900384>

- Chmielewski, A.G., Wierzchnicki, R., Derda, M., Mikołajczuk, A., 2002. Sulfur isotope composition of selected Polish coals, in: Nukleonika.
- Chou, C.C.K., Lee, C.T., Chen, W.N., Chang, S.Y., Chen, T.K., Lin, C.Y., Chen, J.P., 2007. Lidar observations of the diurnal variations in the depth of urban mixing layer: A case study on the air quality deterioration in Taipei, Taiwan. *Science of the Total Environment* 374. <https://doi.org/10.1016/j.scitotenv.2006.11.049>
- Christensen, K.A., Stenholm, M., Livbjerg, H., 1998. The formation of submicron aerosol particles, HCl and SO₂ in straw-fired boilers. *J Aerosol Sci* 29. [https://doi.org/10.1016/S0021-8502\(98\)00013-5](https://doi.org/10.1016/S0021-8502(98)00013-5)
- Ciotti, M., Ciccozzi, M., Terrinoni, A., Jiang, W.C., Wang, C. Bin, Bernardini, S., 2020. The COVID-19 pandemic. *Crit Rev Clin Lab Sci*. <https://doi.org/10.1080/10408363.2020.1783198>
- Dasari, S., Andersson, A., Popa, M.E., Röckmann, T., Holmstrand, H., Budhavant, K., Gustafsson, Ö., 2022a. Observational Evidence of Large Contribution from Primary Sources for Carbon Monoxide in the South Asian Outflow. *Environ Sci Technol* 56. <https://doi.org/10.1021/acs.est.1c05486>
- Dasari, S., Andersson, A., Stohl, A., Evangelou, N., Holmstrand, H., Budhavant, K., Salam, A., Gustafsson, Ö., 2020. Source Quantification of South Asian Black Carbon Aerosols with Isotopes and Modeling. *Environ Sci Technol* 54. <https://doi.org/10.1021/acs.est.0c02193>
- Dasari, S., Paris, G., Charreau, J., Savarino, J., 2022b. Sulfur-isotope anomalies recorded in Antarctic ice cores as a potential proxy for tracing past ozone layer depletion events. *PNAS Nexus* 1. <https://doi.org/10.1093/pnasnexus/pgac170>
- Dasari, S., Paris, G., Saar, B., Pei, Q., Cong, Z., Widory, D., 2022c. Sulfur Isotope Anomalies ($\Delta^{33}\text{S}$) in Urban Air Pollution Linked to Mineral-Dust-Associated Sulfate. *Environ Sci Technol Lett* 9. <https://doi.org/10.1021/acs.estlett.2c00312>
- Dasari, S., Widory, D., 2024. Retrospective Isotopic Analysis of Summertime Urban Atmospheric Sulfate in South Asia Using Improved Source Constraints. *ACS ES&T Air* 1. <https://doi.org/10.1021/acsestair.3c00060>
- Davuliene, L., Jasineviciene, D., Garbariene, I., Andriejauskienė, J., Ulevicius, V., Bycenkiene, S., 2021. Long-term air pollution trend analysis in the South-eastern Baltic region, 1981–2017. *Atmos Res* 247. <https://doi.org/10.1016/j.atmosres.2020.105191>
- de Groot, P.A., 2004. Handbook of Stable Isotope Analytical Techniques, *Handbook of Stable Isotope Analytical Techniques*.

- Demirbas, A., 2004. Combustion characteristics of different biomass fuels. *Prog Energy Combust Sci.* <https://doi.org/10.1016/j.pecs.2003.10.004>
- Derda, M., Chmielewski, A.G., Licki, J., 2007. Sulphur isotope compositions of components of coal and S-isotope fractionation during its combustion and flue gas desulphurization. *Isotopes Environ Health Stud* 43. <https://doi.org/10.1080/10256010601153827>
- Derda, M., Chmielewski, A.G., Licki, J., 2006. Stable isotopes of sulphur in investigating pollution sources. *Environment Protection Engineering* 32.
- DIGITEL, 2019. Aerosol Sampler DH-77. Available online: <http://www.digitel-ag.com/de/en/products/high-volume-sampler-en/dh-77/> (accessed 6.2.19).
- Ding, T., Valkiers, S., Kipphardt, H., De Bièvre, P., Taylor, P.D.P., Gonfiantini, R., Krouse, R., 2001. Calibrated sulfur isotope abundance ratios three IAEA sulfur isotope reference materials and V-CDT with a reassessment of the atomic weight of sulfur. *Geochim Cosmochim Acta* 65. [https://doi.org/10.1016/S0016-7037\(01\)00611-1](https://doi.org/10.1016/S0016-7037(01)00611-1)
- Dong, Z., Pavuluri, C.M., Xu, Z., Wang, Y., Li, P., Fu, P., Liu, C.Q., 2023. Measurement report: Chemical components and ^{13}C and ^{15}N isotope ratios of fine aerosols over Tianjin, North China: year-round observations. *Atmos Chem Phys* 23. <https://doi.org/10.5194/acp-23-2119-2023>
- Dunn, P.J.H., Carter, J.F., 2018. FIRMS good practice guide for isotope ratio mass spectrometry, *Isotopes in Environmental and Health Studies*.
- Dunn, P.J.H., Hai, L., Malinovsky, D., Goenaga-Infante, H., 2015. Simple spreadsheet templates for the determination of the measurement uncertainty of stable isotope ratio delta values. *Rapid Communications in Mass Spectrometry*. <https://doi.org/10.1002/rcm.7376>
- Dusek, U., Hitzenberger, R., Kasper-Giebl, A., Kistler, M., Meijer, H.A.J., Szidat, S., Wacker, L., Holzinger, R., Röckmann, T., 2017. Sources and formation mechanisms of carbonaceous aerosol at a regional background site in the Netherlands: Insights from a year-long radiocarbon study. *Atmos Chem Phys* 17. <https://doi.org/10.5194/acp-17-3233-2017>
- Endo, Y., Sekine, Y., Ueno, Y., 2022. Sulfur mass-independent fractionation during SO_2 photolysis in low-temperature/pressure atmospheres. *Chem Geol* 609. <https://doi.org/10.1016/j.chemgeo.2022.121064>
- Eriksen, T.E., Thieden, H.I.D., Dich, J., Nilsson, K., Nimmich, W., 1972a. Sulfur Isotope Effects. III. Enrichment of ^{34}S by Chemical Exchange Between SO_2g and Aqueous Solutions of SO_2 . *Acta Chem Scand* 26. <https://doi.org/10.3891/acta.chem.scand.26-0975>

- Eriksen, T.E., Vikane, O., Swahn, C.-G., Larsson, R., Nordén, B., Sundbom, M., 1972b. Sulfur Isotope Effects. I. The Isotopic Exchange Coefficient for the Sulfur Isotopes 34S-32S in the System SO₂g-HSO₃-aq at 25, 35, and 45 degrees C. *Acta Chem Scand* 26. <https://doi.org/10.3891/acta.chem.scand.26-0573>
- EU directive 2003/6/EC, 2003. Amendment Directive 98/70/EC Relating to the Quality of Petrol and Diesel Fuels. Official Journal of the European Union 10–19.
- European Environment Agency, 2023. Lithuania – air pollution country fact sheet. Available online: <https://www.eea.europa.eu/themes/air/country-fact-sheets/2023-country-fact-sheets/lithuania-air-pollution-country> (accessed 9.8.24).
- European Environment Agency, 2023. Air pollution country fact sheets 2023. Available online: <https://www.eea.europa.eu/themes/air/country-fact-sheets/2023-country-fact-sheets> (accessed 9.10.24).
- Faloona, I., 2009. Sulfur processing in the marine atmospheric boundary layer: A review and critical assessment of modeling uncertainties. *Atmos Environ.* <https://doi.org/10.1016/j.atmosenv.2009.02.043>
- Fan, M.Y., Zhang, Y.L., Lin, Y.C., Li, J., Cheng, H., An, N., Sun, Y., Qiu, Y., Cao, F., Fu, P., 2020. Roles of Sulfur Oxidation Pathways in the Variability in Stable Sulfur Isotopic Composition of Sulfate Aerosols at an Urban Site in Beijing, China. *Environ Sci Technol Lett* 7. <https://doi.org/10.1021/acs.estlett.0c00623>
- Farquhar, G.D., Ehleringer, J.R., Hubick, K.T., 1989. Carbon Isotope Discrimination and Photosynthesis. *Annu Rev Plant Physiol Plant Mol Biol.* <https://doi.org/10.1146/annurev.pp.40.060189.002443>
- Farquhar, J., Savarino, J., Airieau, S., Thiemens, M.H., 2001. Observation of wavelength-sensitive mass-independent sulfur isotope effects during SO₂ photolysis: Implications for the early atmosphere. *J Geophys Res Planets* 106. <https://doi.org/10.1029/2000JE001437>
- Farquhar, J., Wing, B.A., 2003. Multiple sulfur isotopes and the evolution of the atmosphere. *Earth Planet Sci Lett* 213. [https://doi.org/10.1016/S0012-821X\(03\)00296-6](https://doi.org/10.1016/S0012-821X(03)00296-6)
- Fernandes, R., Millard, A.R., Brabec, M., Nadeau, M.J., Grootes, P., 2014. Food Reconstruction Using Isotopic Transferred Signals (FRUITS): A Bayesian Model for Diet Reconstruction. *PLoS One* 9, e87436. <https://doi.org/10.1371/JOURNAL.PONE.0087436>
- Fioletov, V.E., McLinden, C.A., Krotkov, N., Li, C., Joiner, J., Theys, N., Carn, S., Moran, M.D., 2016. A global catalogue of large SO₂ sources

- and emissions derived from the Ozone Monitoring Instrument. *Atmos Chem Phys* 16. <https://doi.org/10.5194/acp-16-11497-2016>
- Fisseha, R., Saurer, M., Jäggi, M., Siegwolf, R.T.W., Dommen, J., Szidat, S., Samburova, V., Baltensperger, U., 2009. Determination of primary and secondary sources of organic acids and carbonaceous aerosols using stable carbon isotopes. *Atmos Environ* 43. <https://doi.org/10.1016/j.atmosenv.2008.08.041>
- Fry, B., 2006. Stable isotope ecology, *Stable Isotope Ecology*. <https://doi.org/10.1007-0-387-33745-8>
- Garbaras, A., Garbarienė, I., Bučinskas, L., Šapolaitė, J., Ežerinskis, Ž., Matijošius, J., Rimkus, A., Remeikis, V., 2023. Characterization of particulate matter emissions from internal combustion engines using $\delta^{13}\text{C}$ values: Impact of engine operation conditions and fuel type on PM10 isotopic composition. *Atmos Pollut Res* 14. <https://doi.org/10.1016/j.apr.2023.101868>
- Garbaras, A., Masalaite, A., Garbariene, I., Ceburnis, D., Krugly, E., Remeikis, V., Puida, E., Kvietkus, K., Martuzevicius, D., 2015. Stable carbon fractionation in size-segregated aerosol particles produced by controlled biomass burning. *J Aerosol Sci.* <https://doi.org/10.1016/j.jaerosci.2014.10.005>
- Garbaras, A., Šapolaitė, J., Garbarienė, I., Ežerinskis, Ž., Mašalaitė-Nalivaikė, A., Skipitytė, R., Plukis, A., Remeikis, V., 2018. Aerosol source (biomass, traffic and coal emission) apportionment in Lithuania using stable carbon and radiocarbon analysis*. *Isotopes Environ Health Stud* 54. <https://doi.org/10.1080/10256016.2018.1509074>
- Garbarienė, I., Šapolaitė, J., Garbaras, A., Ežerinskis, Ž., Pocevičius, M., Krikščikas, L., Plukis, A., Remeikis, V., 2016. Origin identification of carbonaceous aerosol particles by carbon isotope ratio analysis. *Aerosol Air Qual Res.* <https://doi.org/10.4209/aaqr.2015.07.0443>
- Genberg, J., Hyder, M., Stenström, K., Bergström, R., Simpson, D., Fors, E.O., Jönsson, J.A., Swietlicki, E., 2011. Source apportionment of carbonaceous aerosol in southern Sweden. *Atmos Chem Phys* 11. <https://doi.org/10.5194/acp-11-11387-2011>
- Gettelman, A., Christensen, M.W., Diamond, M.S., Gryspeerd, E., Manshausen, P., Stier, P., Watson-Parris, D., Yang, M., Yoshioka, M., Yuan, T., 2024. Has Reducing Ship Emissions Brought Forward Global Warming? *Geophys Res Lett* 51, e2024GL109077. <https://doi.org/10.1029/2024GL109077>
- Górka, M., Rybicki, M., Simoneit, B.R.T., Marynowski, L., 2014. Determination of multiple organic matter sources in aerosol PM10 from

- Wrocław, Poland using molecular and stable carbon isotope compositions. *Atmos Environ* 89. <https://doi.org/10.1016/j.atmosenv.2014.02.064>
- Górka, M., Skrzypek, G., Hałas, S., Jędrysek, M.O., Strąpoć, D., 2017. Multi-seasonal pattern in 5-year record of stable H, O and S isotope compositions of precipitation (Wrocław, SW Poland). *Atmos Environ.* <https://doi.org/10.1016/j.atmosenv.2017.03.033>
- Górka, M., Trzyna, A., Lewandowska, A., Drzeniecka-Osiadacz, A., Miazga, B., Rybak, J., Widory, D., 2023. The impact of seasonality and meteorological conditions on PM2.5 carbonaceous fractions coupled with carbon isotope analysis: Advantages, weaknesses and interpretation pitfalls. *Atmos Res* 290. <https://doi.org/10.1016/j.atmosres.2023.106800>
- Grgić, I., Hudnik, V., Bizjak, M., Levec, J., 1991. Aqueous S(IV) oxidation—I. Catalytic effects of some metal ions. *Atmospheric Environment. Part A. General Topics* 25, 1591–1597. [https://doi.org/10.1016/0960-1686\(91\)90017-2](https://doi.org/10.1016/0960-1686(91)90017-2)
- Gröning, M., 2018. SICalib User Manual (Stable Isotope Calibration for routine δ -scale measurements) Ver 2.16j SICalib User Manual (Stable Isotope Calibration for routine δ -scale measurements) Version 2.16j.
- Gröning, M., 2011. Improved water $\delta^{2}\text{H}$ and $\delta^{18}\text{O}$ calibration and calculation of measurement uncertainty using a simple software tool, in: *Rapid Communications in Mass Spectrometry*. <https://doi.org/10.1002/rcm.5074>
- Gulbinas V, 2008. Šviesos sukelti molekuliniai vyksmai ir jų lazerinė spektroskopija. Leidykla TEV, Vilnius.
- Guo, Ziyang, Guo, Q., Chen, S., Zhu, B., Zhang, Y., Yu, J., Guo, Zhaobing, 2019. Study on pollution behavior and sulfate formation during the typical haze event in Nanjing with water soluble inorganic ions and sulfur isotopes. *Atmos Res* 217. <https://doi.org/10.1016/j.atmosres.2018.11.009>
- Guo, Z., Li, Z., Farquhar, J., Kaufman, A.J., Wu, N., Li, C., Dickerson, R.R., Wang, P., 2010. Identification of sources and formation processes of atmospheric sulfate by sulfur isotope and scanning electron microscope measurements. *J Geophys Res.* <https://doi.org/10.1029/2009jd012893>
- Hajdas, I., Ascough, P., Garnett, M.H., Fallon, S.J., Pearson, C.L., Quarta, G., Spalding, K.L., Yamaguchi, H., Yoneda, M., 2021. Radiocarbon dating. *Nature Reviews Methods Primers* 2021 1:1 1, 1–26. <https://doi.org/10.1038/s43586-021-00058-7>
- Han, X., Guo, Q., Liu, C., Fu, P., Strauss, H., Yang, J., Hu, J., Wei, L., Ren, H., Peters, M., Wei, R., Tian, L., 2016. Using stable isotopes to trace

- sources and formation processes of sulfate aerosols from Beijing, China. *Sci Rep* 6. <https://doi.org/10.1038/srep29958>
- Han, X., Guo, Q., Strauss, H., Liu, C., Hu, J., Guo, Z., Wei, R., Peters, M., Tian, L., Kong, J., 2017. Multiple Sulfur Isotope Constraints on Sources and Formation Processes of Sulfate in Beijing PM2.5 Aerosol. *Environ Sci Technol* 51. <https://doi.org/10.1021/acs.est.7b00280>
- Harris, E., Sinha, B., Foley, S., Crowley, J.N., Borrmann, S., Hoppe, P., 2012a. Sulfur isotope fractionation during heterogeneous oxidation of SO₂ on mineral dust. *Atmos Chem Phys*. <https://doi.org/10.5194/acp-12-4867-2012>
- Harris, E., Sinha, B., Hoppe, P., Crowley, J.N., Ono, S., Foley, S., 2012b. Sulfur isotope fractionation during oxidation of sulfur dioxide: Gas-phase oxidation by OH radicals and aqueous oxidation by H₂O₂, O₃ and iron catalysis. *Atmos Chem Phys* 12. <https://doi.org/10.5194/acp-12-407-2012>
- Harris, E., Sinha, B., Hoppe, P., Crowley, J.N., Ono, S., Foley, S., 2012c. Sulfur isotope fractionation during oxidation of sulfur dioxide: Gas-phase oxidation by OH radicals and aqueous oxidation by H₂O₂, O₃ and iron catalysis. *Atmos Chem Phys*. <https://doi.org/10.5194/acp-12-407-2012>
- Harris, E., Sinha, B., Hoppe, P., Foley, S., Borrmann, S., 2012d. Fractionation of sulfur isotopes during heterogeneous oxidation of SO₂ on sea salt aerosol: A new tool to investigate non-sea salt sulfate production in the marine boundary layer. *Atmos Chem Phys* 12. <https://doi.org/10.5194/acp-12-4619-2012>
- Harris, E., Sinha, B., Hoppe, P., Ono, S., 2013a. High-precision measurements of ³³S and ³⁴S fractionation during SO₂ oxidation reveal causes of seasonality in SO₂ and sulfate isotopic composition. *Environ Sci Technol* 47. <https://doi.org/10.1021/es402824c>
- Harris, E., Sinha, B., Van Pinxteren, D., Tilgner, A., Fomba, K.W., Schneider, J., Roth, A., Gnauk, T., Fahlbusch, B., Mertes, S., Lee, T., Collett, J., Foley, S., Borrmann, S., Hoppe, P., Herrmann, H., 2013b. Enhanced role of transition metal ion catalysis during in-cloud oxidation of SO₂. *Science* (1979) 340. <https://doi.org/10.1126/science.1230911>
- Harrison, R.M., Jones, A.M., Beddows, D.C.S., Derwent, R.G., 2013. The effect of varying primary emissions on the concentrations of inorganic aerosols predicted by the enhanced UK Photochemical Trajectory Model. *Atmos Environ* 69. <https://doi.org/10.1016/j.atmosenv.2012.12.016>

- Heal, M.R., Naysmith, P., Cook, G.T., Xu, S., Duran, T.R., Harrison, R.M., 2011. Application of ^{14}C analyses to source apportionment of carbonaceous PM_{2.5} in the UK. *Atmos Environ* 45. <https://doi.org/10.1016/j.atmosenv.2011.02.029>
- Hegg, D.A., Covert, D.S., Jonsson, H., Khelif, D., Friehe, C.A., 2004. Observations of the impact of cloud processing on aerosol light-scattering efficiency. *Tellus B Chem Phys Meteorol* 56. <https://doi.org/10.1111/j.1600-0889.2004.00099.x>
- Herrmann, H., Ervens, B., Jacobi, H.W., Wolke, R., Nowacki, P., Zellner, R., 2000. CAPRAM2.3: A chemical aqueous phase radical mechanism for tropospheric chemistry. *J Atmos Chem* 36. <https://doi.org/10.1023/A:1006318622743>
- Hien, P.D., Bac, V.T., Thinh, N.T.H., Anh, H.L., Thang, D.D., Nghia, N.T., 2021. A Comparison Study of Chemical Compositions and Sources of PM_{1.0} and PM_{2.5} in Hanoi. *Aerosol Air Qual Res* 21, 210056. <https://doi.org/10.4209/AAQR.210056>
- Hoefs, J., 2021. Stable Isotope Geochemistry. Springer Textbooks in Earth Sciences, Geography and Environment. <https://doi.org/10.1007/978-3-030-77692-3>
- Hoefs, J., 2009. Stable isotope geochemistry: Sixth edition, Stable Isotope Geochemistry: Sixth Edition. <https://doi.org/10.1007/978-3-540-70708-0>
- Holt, B.D., Kumar, R., Cunningham, P.T., 1982. Primary sulfates in atmospheric sulfates: Estimation by oxygen isotope ratio measurements. *Science* (1979) 217. <https://doi.org/10.1126/science.217.4554.51>
- Huang, B., Gan, T., Pei, C., Li, M., Cheng, P., Chen, D., Cai, R., Wang, Y., Li, L., Huang, Z., Gao, W., Fu, Z., Zhou, Z., 2020. Size-segregated characteristics and formation mechanisms of water-soluble inorganic ions during different seasons in heshan of Guangdong, China. *Aerosol Air Qual Res* 20. <https://doi.org/10.4209/aaqr.2019.11.0582>
- Hulston, J.R., Thode, H.G., 1965. Variations in the S₃₃, S₃₄, and S₃₆ contents of meteorites and their relation to chemical and nuclear effects. *J Geophys Res* 70. <https://doi.org/10.1029/jz070i014p03475>
- Huss, A., Lim, P.K., Eckert, C.A., 1978. On the “Uncatalyzed” Oxidation of Sulfur(IV) in Aqueous Solutions. *J Am Chem Soc.* <https://doi.org/10.1021/ja00487a059>
- Huygen, C., 1963. The sampling of sulfur dioxide in air with impregnated filter paper. *Anal Chim Acta* 28. [https://doi.org/10.1016/S0003-2670\(00\)87244-X](https://doi.org/10.1016/S0003-2670(00)87244-X)

- IEA, 2024. Coal supply in Lithuania. Available online <https://origin.iea.org/countries/lithuania/coal> (accessed 9.9.24).
- Igliński, B., Piechota, G., Buczkowski, R., 2015. Development of biomass in polish energy sector: An overview. *Clean Technol Environ Policy.* <https://doi.org/10.1007/s10098-014-0820-x>
- IMO, 2016. The 2020 global sulphur limit. International Maritime Organization.
- Inomata, Y., Ohizumi, T., Take, N., Sato, K., Nishikawa, M., 2016. Transboundary transport of anthropogenic sulfur in PM_{2.5} at a coastal site in the sea of japan as studied by sulfur isotopic ratio measurement. *Science of the Total Environment* 553. <https://doi.org/10.1016/j.scitotenv.2016.02.139>
- Jacob, D.J., Hoffmann, M.R., 1983. A dynamic model for the production of H⁺, NO₃⁻, and SO₄²⁻ in urban fog. *J Geophys Res* 88. <https://doi.org/10.1029/JC088iC11p06611>
- Jaeschke, W., 1986. Multiphase Atmospheric Chemistry, in: Chemistry of Multiphase Atmospheric Systems. https://doi.org/10.1007/978-3-642-70627-1_1
- Jion, M.M.M.F., Jannat, J.N., Mia, M.Y., Ali, M.A., Islam, M.S., Ibrahim, S.M., Pal, S.C., Islam, A., Sarker, A., Malafaia, G., Bilal, M., Islam, A.R.M.T., 2023. A critical review and prospect of NO₂ and SO₂ pollution over Asia: Hotspots, trends, and sources. *Science of The Total Environment* 876, 162851. <https://doi.org/10.1016/J.SCITOTENV.2023.162851>
- Joint Committee For Guides In, 2008. Evaluation of measurement data — Guide to the expression of uncertainty in measurement. International Organization for Standardization Geneva ISBN 50.
- Kawamura, H., Matsuoka, N., Tawaki, S., Momoshima, N., 2001. Sulfur isotope variations in atmospheric sulfur oxides, particulate matter and deposits collected at Kyushu Island, Japan. *Water Air Soil Pollut.* <https://doi.org/10.1023/A:1013932724433>
- Kawashima, H., Haneishi, Y., 2012. Effects of combustion emissions from the Eurasian continent in winter on seasonal δ¹³C of elemental carbon in aerosols in Japan. *Atmos Environ* 46. <https://doi.org/10.1016/j.atmosenv.2011.05.015>
- Kellogg, W.W., Cadle, R.D., Allen, E.R., Lazarus, A.L., Martell, E.A., 1972. The sulfur cycle. *Science* (1979) 175. <https://doi.org/10.1126/science.175.4022.587>

- Kiehl, J.T., Briegleb, B.P., 1993. The relative roles of sulfate aerosols and greenhouse gases in climate forcing. *Science* (1979) 260. <https://doi.org/10.1126/science.260.5106.311>
- Kim, Y., Lee, I., Farquhar, J., Kang, J., Villa, I.M., Kim, H., 2021. Multi isotope systematics of precipitation to trace the sources of air pollutants in Seoul, Korea. *Environmental Pollution* 286. <https://doi.org/10.1016/j.envpol.2021.117548>
- Kirillova, E.N., Andersson, A., Sheesley, R.J., Kruså, M., Praveen, P.S., Budhavant, K., Safai, P.D., Rao, P.S.P., Gustafsson, Ö., 2013. 13C- And 14C-based study of sources and atmospheric processing of water-soluble organic carbon (WSOC) in South Asian aerosols. *Journal of Geophysical Research Atmospheres* 118. <https://doi.org/10.1002/jgrd.50130>
- Konstantinaviciute, I., Miskinis, V., Norvaiša, E., Bobinaite, V., 2014. Assessment of national carbon dioxide emission factors for the Lithuanian fuel combustion sector. *Greenhouse Gas Measurement and Management* 4. <https://doi.org/10.1080/20430779.2014.905243>
- Kreyling, W.G., Dirscherl, P., Ferron, G.A., Heilmann, P., Josten, M., Miaskowski, U., Neuner, M., Reitmeir, P., Ruprecht, L., Schumann, G., Takenaka, S., Ziesenis, A., Heyder, J., 1999. Health effects of sulfur-related environmental air pollution. III. Nonspecific respiratory defense capacities. *Inhal Toxicol* 11. <https://doi.org/10.1080/089583799197069>
- Kristiansen, N.I., Stohl, A., Olivé, D.J.L., Croft, B., Søvde, O.A., Klein, H., Christoudias, T., Kunkel, D., Leadbetter, S.J., Lee, Y.H., Zhang, K., Tsigaridis, K., Bergman, T., Evangelou, N., Wang, H., Ma, P.L., Easter, R.C., Rasch, P.J., Liu, X., Pitari, G., Di Genova, G., Zhao, S.Y., Balkanski, Y., Bauer, S.E., Faluvegi, G.S., Kokkola, H., Martin, R. V., Pierce, J.R., Schulz, M., Shindell, D., Tost, H., Zhang, H., 2016. Evaluation of observed and modelled aerosol lifetimes using radioactive tracers of opportunity and an ensemble of 19 global models. *Atmos Chem Phys* 16. <https://doi.org/10.5194/acp-16-3525-2016>
- Krouse, H.R., Coplen, T.B., 1997. Reporting of relative sulfur isotope-ratio data. *Pure and Applied Chemistry* 69. <https://doi.org/10.1351/pac199769020293>
- Kulmala, M., 2003. How Particles Nucleate and Grow. *Science* (1979). <https://doi.org/10.1126/science.1090848>
- Kulmala, M., Kontkanen, J., Junninen, H., Lehtipalo, K., Manninen, H.E., Nieminen, T., Petäjä, T., Sipilä, M., Schobesberger, S., Rantala, P., Franchin, A., Jokinen, T., Järvinen, E., Äijälä, M., Kangasluoma, J., Hakala, J., Aalto, P.P., Paasonen, P., Mikkilä, J., Vanhanen, J., Aalto, J., Hakola, H., Makkonen, U., Ruuskanen, T., Mauldin, R.L., Duplissy, J.,

- Vehkamäki, H., Bäck, J., Kortelainen, A., Riipinen, I., Kurtén, T., Johnston, M. V., Smith, J.N., Ehn, M., Mentel, T.F., Lehtinen, K.E.J., Laaksonen, A., Kerminen, V.M., Worsnop, D.R., 2013. Direct observations of atmospheric aerosol nucleation. *Science* (1979) 339. <https://doi.org/10.1126/science.1227385>
- Kulmala, M., Riipinen, I., Sipilä, M., Manninen, H.E., Petäjä, T., Junninen, H., Dal Maso, M., Mordas, G., Mirme, A., Vana, M., Hirsikko, A., Laakso, L., Harrison, R.M., Hanson, I., Leung, C., Lehtinen, K.E.J., Kerminen, V.M., 2007. Toward direct measurement of atmospheric nucleation. *Science* (1979) 318. <https://doi.org/10.1126/science.1144124>
- Kulmala, M., Vehkamäki, H., Petäjä, T., Dal Maso, M., Lauri, A., Kerminen, V.M., Birmili, W., McMurry, P.H., 2004. Formation and growth rates of ultrafine atmospheric particles: A review of observations. *J Aerosol Sci* 35. <https://doi.org/10.1016/j.jaerosci.2003.10.003>
- Kundu, S., Kawamura, K., 2014. Seasonal variations of stable carbon isotopic composition of bulk aerosol carbon from Gosan site, Jeju Island in the East China Sea. *Atmos Environ* 94. <https://doi.org/10.1016/j.atmosenv.2014.05.045>
- Kunwar, B., Kawamura, K., Zhu, C., 2016. Stable carbon and nitrogen isotopic compositions of ambient aerosols collected from Okinawa Island in the western North Pacific Rim, an outflow region of Asian dusts and pollutants. *Atmos Environ* 131. <https://doi.org/10.1016/j.atmosenv.2016.01.035>
- Landkocz, Y., Ledoux, F., André, V., Cazier, F., Genevray, P., Dewaele, D., Martin, P.J., Lepers, C., Verdin, A., Courcot, L., Boushina, S., Sichel, F., Gualtieri, M., Shirali, P., Courcot, D., Billet, S., 2017. Fine and ultrafine atmospheric particulate matter at a multi-influenced urban site: Physicochemical characterization, mutagenicity and cytotoxicity. *Environmental Pollution* 221. <https://doi.org/10.1016/j.envpol.2016.11.054>
- Lauer, A., Eyring, V., Hendricks, J., Jöckel, P., Lohmann, U., 2007. Global model simulations of the impact of ocean-going ships on aerosols, clouds, and the radiation budget. *Atmos Chem Phys* 7. <https://doi.org/10.5194/acp-7-5061-2007>
- Lebedev, A.T., 2013. Environmental Mass Spectrometry. *Annual Review of Analytical Chemistry*. <https://doi.org/10.1146/annurev-anchem-062012-092604>
- Lee, C.C.W., Savarino, J.H., Cachier, H., Thiemens, M.H., 2002. Sulfur (32S,33S, 34S,36S) and oxygen (16O, 17O, 18O) isotopic ratios of

- primary sulfate produced from combustion processes. *Tellus B Chem Phys Meteorol* 54. <https://doi.org/10.1034/j.1600-0889.2002.01384.x>
- Lee, C., Martin, R. V., Van Donkelaar, A., Lee, H., Dickerson, R.R., Hains, J.C., Krotkov, N., Richter, A., Vinnikov, K., Schwab, J.J., 2011. SO₂ emissions and lifetimes: Estimates from inverse modeling using in situ and global, space-based (SCIAMACHY and OMI) observations. *Journal of Geophysical Research Atmospheres* 116. <https://doi.org/10.1029/2010JD014758>
- Lee, G., Ahn, J., Park, S.M., Moon, J., Park, R., Sim, M.S., Choi, H., Park, J., Ahn, J.Y., 2023. Sulfur isotope-based source apportionment and control mechanisms of PM2.5 sulfate in Seoul, South Korea during winter and early spring (2017–2020). *Science of the Total Environment* 905. <https://doi.org/10.1016/j.scitotenv.2023.167112>
- Lee, Y.N., Schwartz, S.E., 1983. Kinetics of oxidation of aqueous sulfur(iv) by nitrogen dioxide.
- Lelieveld, J., Dentener, F.J., Peters, W., Krol, M.C., 2004. On the role of hydroxyl radicals in the self-cleansing capacity of the troposphere. *Atmos Chem Phys* 4. <https://doi.org/10.5194/acp-4-2337-2004>
- Leung, F.Y., Colussi, A.J., Hoffmann, M.R., 2001. Sulfur isotopic fractionation in the gas-phase oxidation of sulfur dioxide initiated by hydroxyl radicals. *Journal of Physical Chemistry A* 105. <https://doi.org/10.1021/jp011014+>
- Levin, I., Hesshaimer, V., 2000. Radiocarbon - A unique tracer of global carbon cycle dynamics. *Radiocarbon*. <https://doi.org/10.1017/S0033822200053066>
- Li, J., Pósfai, M., Hobbs, P. V., Buseck, P.R., 2003. Individual aerosol particles from biomass burning in southern Africa: 2. Compositions and aging of inorganic particles. *Journal of Geophysical Research: Atmospheres* 108. <https://doi.org/10.1029/2002jd002310>
- Li, J., Zhang, Y.L., Cao, F., Zhang, W., Fan, M., Lee, X., Michalski, G., 2020. Stable Sulfur Isotopes Revealed a Major Role of Transition-Metal Ion-Catalyzed SO₂ Oxidation in Haze Episodes. *Environ Sci Technol* 54. <https://doi.org/10.1021/acs.est.9b07150>
- Likus-Cieślik, J., Socha, J., Gruba, P., Pietrzykowski, M., 2020. The current state of environmental pollution with sulfur dioxide (SO₂) in Poland based on sulfur concentration in Scots pine needles. *Environmental Pollution* 258, 113559. <https://doi.org/10.1016/J.ENVPOL.2019.113559>
- Lim, C., Jang, J., Lee, I., Kim, G., Lee, S.M., Kim, Y., Kim, H., Kaufman, A.J., 2014. Sulfur isotope and chemical compositions of the wet

- precipitation in two major urban areas, Seoul and Busan, Korea. J Asian Earth Sci. <https://doi.org/10.1016/j.jseaes.2013.09.013>
- Li, M., Hu, M., Walker, J., Gao, P., Fang, X., Xu, N., Qin, Y., Zhou, L., Liu, K., Czimczik, C.I., Xu, X., 2022. Source apportionment of carbonaceous aerosols in diverse atmospheric environments of China by dual-carbon isotope method. Science of the Total Environment 806. <https://doi.org/10.1016/j.scitotenv.2021.150654>
- Lin, M., Biglari, S., Thiemen, M.H., 2017. Quantification of Gas-to-Particle Conversion Rates of Sulfur in the Terrestrial Atmosphere Using High-Sensitivity Measurements of Cosmogenic ^{35}S . ACS Earth Space Chem 1. <https://doi.org/10.1021/acsearthspacechem.7b00047>
- Lin, Y.C., Yu, M., Xie, F., Zhang, Y., 2022. Anthropogenic Emission Sources of Sulfate Aerosols in Hangzhou, East China: Insights from Isotope Techniques with Consideration of Fractionation Effects between Gas-to-Particle Transformations. Environ Sci Technol 56. <https://doi.org/10.1021/acs.est.1c05823>
- Lithuania's national inventory report 2021, 2021. Available online: https://am.lrv.lt/uploads/am/documents/files/Klimato_kaita/NIR_2021%2003%2015.pdf.
- Liu, G., Li, J., Xu, H., Wu, D., Liu, Y., Yang, H., 2014. Isotopic compositions of elemental carbon in smoke and ash derived from crop straw combustion. Atmos Environ 92. <https://doi.org/10.1016/j.atmosenv.2014.04.042>
- Liu, T., Chan, A.W.H., Abbatt, J.P.D., 2021. Multiphase Oxidation of Sulfur Dioxide in Aerosol Particles: Implications for Sulfate Formation in Polluted Environments. Environ Sci Technol <https://doi.org/10.1021/acs.est.0c06496>
- Liu, X., Van Espen, P., Adams, F., Cafmeyer, J., Maenhaut, W., 2000. Biomass burning in southern Africa: Individual particle characterization of atmospheric aerosols and savanna fire samples. J Atmos Chem 36. <https://doi.org/10.1023/A:1006387031927>
- Lohmann, U., Feichter, J., 2004. Global indirect aerosol effects: a review. Atmospheric Chemistry and Physics Discussions 4, 7561–7614. <https://doi.org/10.5194/acpd-4-7561-2004>
- LRT, 2023. „Vilniaus šilumos tinklai“ paneigė, kad šildymui naudojamas mazutas gali būti kilę iš Rusijos. Available online: <https://www.lrt.lt/naujienos/verslas/4/1871641/vilniaus-silumos-tinklai-paneige-kad-sildymui-naudojamas-mazutas-gali-buti-kiles-is-rusijos> (accessed 10.11.24).

- LRT, 2022. Oil refinery in Lithuania to only import Saudi crude – minister. Available online: <https://www.lrt.lt/en/news-in-english/19/1654425/oil-refinery-in-lithuania-to-only-import-saudi-crude-minister> (accessed 9.8.24).
- Luo, C., Mahowald, N., Bond, T., Chuang, P.Y., Artaxo, P., Siefert, R., Chen, Y., Schauer, J., 2008. Combustion iron distribution and deposition. Global Biogeochem Cycles 22. <https://doi.org/10.1029/2007GB002964>
- Mariotti, A., Germon, J.C., Hubert, P., Kaiser, P., Letolle, R., Tardieu, A., Tardieu, P., 1981. Experimental determination of nitrogen kinetic isotope fractionation: Some principles; illustration for the denitrification and nitrification processes. Plant Soil 62. <https://doi.org/10.1007/BF02374138>
- Mårtensson, E.M., Nilsson, E.D., de Leeuw, G., Cohen, L.H., Hansson, H.C., 2003. Laboratory simulations and parameterization of the primary marine aerosol production. Journal of Geophysical Research D: Atmospheres. <https://doi.org/10.1029/2002jd002263>
- Martin, L.R., 1984. KINETIC STUDIES OF SULFITE OXIDATION IN AQUEOUS SOLUTION.
- Maruyama, T., Ohizumi, T., Taneoka, Y., Minami, N., Fukuzaki, N., Murai, H., Murano, K., Kusakabe, M., 2000. Sulfur isotope ratios of coals and oils used in China and Japan. Nippon Kagaku Kaishi / Chemical Society of Japan - Chemistry and Industrial Chemistry Journal 2000, 45–52. <https://doi.org/10.1246/NIKKASHI.2000.45>
- Masalaite, A., Byčenkiė, S., Pauraitė, J., Garbariene, I., Haddad, I. el, Bozzetti, C., Jaffrezo, J.L., Besombes, J.L., Plauškaitė-Šukienė, K., Garbaras, A., Šapolaitė, J., Ežerinskis, Dudoitidis, V., Bariseviciute, R., Ulevičius, V., Prevot, A.S.H., Remeikis, V., 2022. Seasonal observation and source apportionment of carbonaceous aerosol from forested rural site (Lithuania). Atmos Environ 272. <https://doi.org/10.1016/j.atmosenv.2021.118934>
- Mašalaitė, A., Garbaras, A., Remeikis, V., 2012. Stable isotopes in environmental investigations. Lithuanian Journal of Physics 52, 261–268. <https://doi.org/10.3952/lithjphys.52314>
- Masalaite, A., Holzinger, R., Ceburnis, D., Remeikis, V., Ulevičius, V., Röckmann, T., Dusek, U., 2018. Sources and atmospheric processing of size segregated aerosol particles revealed by stable carbon isotope ratios and chemical speciation. Environmental Pollution 240. <https://doi.org/10.1016/j.envpol.2018.04.073>
- Masalaite, A., Holzinger, R., Remeikis, V., Röckmann, T., Dusek, U., 2017. Characteristics, sources and evolution of fine aerosol (PM1) at urban,

- coastal and forest background sites in Lithuania. *Atmos Environ.* <https://doi.org/10.1016/j.atmosenv.2016.10.038>
- Mayer, B., Feger, K.H., Giesemann, A., Jäger, H.J., 1995. Interpretation of sulfur cycling in two catchments in the Black Forest (Germany) using stable sulfur and oxygen isotope data. *Biogeochemistry* 30. <https://doi.org/10.1007/BF02181039>
- Mayer, B., Krouse, H.R., 2004. Procedures for Sulfur Isotope Abundance Studies, in: *Handbook of Stable Isotope Analytical Techniques*. <https://doi.org/10.1016/B978-044451114-0/50028-4>
- McCabe, J.R., Savarino, J., Alexander, B., Gong, S., Thiemens, M.H., 2006. Isotopic constraints on non-photochemical sulfate production in the Arctic winter. *Geophys Res Lett* 33. <https://doi.org/10.1029/2005GL025164>
- Meier-Augenstein, W., 2010. Stable Isotope Forensics: An Introduction to the Forensic Application of Stable Isotope Analysis, *Stable Isotope Forensics: An Introduction to the Forensic Application of Stable Isotope Analysis*. <https://doi.org/10.1002/9780470688762>
- Meier-Augenstein, W., 1999. Applied gas chromatography coupled to isotope ratio mass spectrometry. *J Chromatogr A*. [https://doi.org/10.1016/S0021-9673\(98\)01057-7](https://doi.org/10.1016/S0021-9673(98)01057-7)
- Menz, F.C., Seip, H.M., 2004. Acid rain in Europe and the United States: An update. *Environ Sci Policy* 7. <https://doi.org/10.1016/j.envsci.2004.05.005>
- Moreno-Ríos, A.L., Tejeda-Benítez, L.P., Bustillo-Lecompte, C.F., 2022. Sources, characteristics, toxicity, and control of ultrafine particles: An overview. *Geoscience Frontiers* 13. <https://doi.org/10.1016/j.gsf.2021.101147>
- Mukai, H., Tanaka, A., Fujii, T., Zeng, Y., Hong, Y., Tang, J., Guo, S., Xue, H., Sun, Z., Zhou, J., Xue, D., Zhao, J., Zhai, G., Gu, J., Zhai, P., 2001. Regional characteristics of sulfur and lead isotope ratios in the atmosphere at several Chinese urban sites. *Environ Sci Technol* 35. <https://doi.org/10.1021/es001399u>
- Myhre, G., Stordal, F., Berglen, T.F., Sundet, J.K., Isaksen, I.S.A., 2004. Uncertainties in the radiative forcing due to sulfate aerosols. *J Atmos Sci* 61. [https://doi.org/10.1175/1520-0469\(2004\)061<0485:UITRFD>2.0.CO;2](https://doi.org/10.1175/1520-0469(2004)061<0485:UITRFD>2.0.CO;2)
- NEC, 2016. Single Stage Accelerator Mass Spectrometry (SSAMS). Available Online: <http://www.pelletron.com/wp-content/uploads/2016/09/SSAMS.pdf> (accessed 12.22.17).

- Nguyen, B.C., Putaud, J.P., 1993. Stable isotopes: Natural and anthropogenic sulphur in the environment. *Atmos Res* 29. [https://doi.org/10.1016/0169-8095\(93\)90011-c](https://doi.org/10.1016/0169-8095(93)90011-c)
- Niemi, J. V., Tervahattu, H., Vehkamäki, H., Kulmala, M., Koskentalo, T., Sillanpää, M., Rantamäki, M., 2004. Characterization and source identification of a fine particle episode in Finland. *Atmos Environ* 38. <https://doi.org/10.1016/j.atmosenv.2004.06.023>
- Ni, H., Huang, R.J., Cao, J., Liu, W., Zhang, T., Wang, M., Meijer, H.A.J., Dusek, U., 2018. Source apportionment of carbonaceous aerosols in Xi'an, China: Insights from a full year of measurements of radiocarbon and the stable isotope ^{13}C . *Atmos Chem Phys* 18. <https://doi.org/10.5194/acp-18-16363-2018>
- Niu, Z., Feng, X., Zhou, W., Wang, P., Liu, Y., Lu, X., Du, H., Fu, Y., Li, M., Mei, R., Li, Q., Cai, Q., 2021. Tree-ring $\Delta^{14}\text{C}$ time series from 1948 to 2018 at a regional background site, China: Influences of atmospheric nuclear weapons tests and fossil fuel emissions. *Atmos Environ* 246. <https://doi.org/10.1016/j.atmosenv.2020.118156>
- NOAA, 2021. Climate Data Online (CDO). Available online: <https://www.ncei.noaa.gov/cdo-web/>.
- Norman, A.L., Anlauf, K., Hayden, K., Thompson, B., Brook, J.R., Li, S.M., Bottenheim, J., 2006. Aerosol sulphate and its oxidation on the Pacific NW coast: S and O isotopes in PM_{2.5}. *Atmos Environ* 40. <https://doi.org/10.1016/j.atmosenv.2005.09.085>
- Norman, A.L., Belzer, W., Barrie, L., 2004. Insights into the biogenic contribution to total sulphate in aerosol and precipitation in the Fraser Valley afforded by isotopes of sulphur and oxygen. *Journal of Geophysical Research: Atmospheres* 109. <https://doi.org/10.1029/2002jd003072>
- Novák, M., Jačková, I., Přechová, E., 2001. Temporal trends in the isotope signature of air-borne sulfur in Central Europe. *Environ Sci Technol* 35. <https://doi.org/10.1021/es0000753>
- Nriagu, J.O., Coker, R.D., 1978. Isotopic composition of sulfur in precipitation within the Great Lakes Basin. *Tellus A: Dynamic Meteorology and Oceanography* 30. <https://doi.org/10.3402/tellusa.v30i4.10356>
- Ogawa, N.O., Nagata, T., Kitazato, H., Ohkouchi, N., 2010. Ultra-sensitive elemental analyzer/isotope ratio mass spectrometer for stable nitrogen and carbon isotope analyses. *Earth, Life, and Isotopes*.

- Pandis, S.N., Seinfeld, J.H., 1989. Sensitivity analysis of a chemical mechanism for aqueous-phase atmospheric chemistry. *J Geophys Res* 94. <https://doi.org/10.1029/JD094iD01p01105>
- Park, R.J., Jacob, D.J., Field, B.D., Yantosca, R.M., Chin, M., 2004. Natural and transboundary pollution influences on sulfate-nitrate-ammonium aerosols in the United States: Implications for policy. *Journal of Geophysical Research D: Atmospheres* 109. <https://doi.org/10.1029/2003JD00473>
- Pathak, R.K., Yao, X., Chan, C.K., 2004. Sampling Artifacts of Acidity and Ionic Species in PM_{2.5}. *Environ Sci Technol* 38. <https://doi.org/10.1021/es0342244>
- PKN ORLEN, 2023. PKN ORLEN secures crude oil supplies from non-Russian sources. Available online: <https://www.orlen.pl/en/about-the-company/media/press-releases/2023/february-2023/PKN-ORLEN-secures-crude-oil-supplies-from-non-Russian-sources> (accessed 9.8.24).
- Pope, C.A., Dockery, D.W., 2006. Health effects of fine particulate air pollution: Lines that connect. *J Air Waste Manage Assoc* 56. <https://doi.org/10.1080/10473289.2006.10464485>
- Popovicheva, O., Chichaeva, M., Kovach, R., Zhdanova, E., Kasimov, N., 2022. Seasonal, Weekly, and Diurnal Black Carbon in Moscow Megacity Background under Impact of Urban and Regional Sources. *Atmosphere (Basel)* 13. <https://doi.org/10.3390/atmos13040563>
- Pöschl, U., 2005. Atmospheric aerosols: Composition, transformation, climate and health effects. *Angewandte Chemie - International Edition*. <https://doi.org/10.1002/anie.200501122>
- Pozzoli, L., Bey, I., Rast, S., Schultz, M.G., Stier, P., Feichter, J., 2008. Trace gas and aerosol interactions in the fully coupled model of aerosol-chemistry-climate ECHAM5-HAMMOZ: 1. Model description and insights from the spring 2001 TRACE-P experiment. *Journal of Geophysical Research Atmospheres* 113. <https://doi.org/10.1029/2007JD009007>
- Qi, L., Wang, S., 2019. Fossil fuel combustion and biomass burning sources of global black carbon from GEOS-Chem simulation and carbon isotope measurements. *Atmos Chem Phys* 19. <https://doi.org/10.5194/acp-19-11545-2019>
- Rastogi, N., Agnihotri, R., Sawlani, R., Patel, A., Babu, S.S., Satish, R., 2020. Chemical and isotopic characteristics of PM₁₀ over the Bay of Bengal: Effects of continental outflow on a marine environment. *Science of the Total Environment* 726. <https://doi.org/10.1016/j.scitotenv.2020.138438>

- Rayleigh, Lord, 1896. L. Theoretical considerations respecting the separation of gases by diffusion and similar processes . The London, Edinburgh, and Dublin Philosophical Magazine and Journal of Science 42. <https://doi.org/10.1080/14786449608620944>
- Ren, Y., Shen, G., Shen, H., Zhong, Q., Xu, H., Meng, W., Zhang, W., Yu, X., Yun, X., Luo, Z., Chen, Y., Li, B., Cheng, H., Zhu, D., Tao, S., 2021. Contributions of biomass burning to global and regional SO₂ emissions. Atmos Res 260. <https://doi.org/10.1016/j.atmosres.2021.105709>
- Rickly, P.S., Guo, H., Campuzano-Jost, P., Jimenez, J.L., Wolfe, G.M., Bennett, R., Bourgeois, I., Crounse, J.D., Dibb, J.E., Digangi, J.P., Diskin, G.S., Dollner, M., Gargulinski, E.M., Hall, S.R., Halliday, H.S., Hanisco, T.F., Hannun, R.A., Liao, J., Moore, R., Nault, B.A., Nowak, J.B., Peischl, J., Robinson, C.E., Ryerson, T., Sanchez, K.J., Schöberl, M., Soja, A.J., St. Clair, J.M., Thornhill, K.L., Ullmann, K., Wennberg, P.O., Weinzierl, B., Wiggins, E.B., Winstead, E.L., Rollins, A.W., 2022. Emission factors and evolution of SO₂ measured from biomass burning in wildfires and agricultural fires. Atmos Chem Phys 22, 15603–15620. <https://doi.org/10.5194/ACP-22-15603-2022>
- Rodríguez-Urrego, D., Rodríguez-Urrego, L., 2020. Air quality during the COVID-19: PM_{2.5} analysis in the 50 most polluted capital cities in the world. Environmental Pollution. <https://doi.org/10.1016/j.envpol.2020.115042>
- Romano, S., Pichierri, S., Fragola, M., Buccolieri, A., Quarta, G., Calcagnile, L., 2022. Characterization of the PM_{2.5} aerosol fraction monitored at a suburban site in south-eastern Italy by integrating isotopic techniques and ion beam analysis. Front Environ Sci 10. <https://doi.org/10.3389/fenvs.2022.971204>
- Romero, A.B., Thiemens, M.H., 2003. Mass-independent sulfur isotopic compositions in present-day sulfate aerosols. Journal of Geophysical Research: Atmospheres 108. <https://doi.org/10.1029/2003jd003660>
- Rom, W., Brenninkmeijer, C.A.M., Bräunlich, M., Golser, R., Mandl, M., Kaiser, A., Kutschera, W., Priller, A., Puchegger, S., Röckmann, T., Steier, P., 2000. A detailed 2-year record of atmospheric ¹⁴CO in the temperate northern hemisphere. Nucl Instrum Methods Phys Res B 161–163. [https://doi.org/10.1016/S0168-583X\(99\)00707-7](https://doi.org/10.1016/S0168-583X(99)00707-7)
- Saltzman, E.S., Brass, G.W., Price, D.A., 1983. The mechanism of sulfate aerosol formation: Chemical and sulfur isotopic evidence. Geophys Res Lett 10. <https://doi.org/10.1029/GL010i007p00513>
- Salvador, P., Pandolfi, M., Tobías, A., Gómez-Moreno, F.J., Molero, F., Barreiro, M., Pérez, N., Revuelta, M.A., Marco, I.M., Querol, X.,

- Artíñano, B., 2020. Impact of mixing layer height variations on air pollutant concentrations and health in a European urban area: Madrid (Spain), a case study. *Environmental Science and Pollution Research* 27. <https://doi.org/10.1007/s11356-020-10146-y>
- San-Miguel-Ayanz, J., Durrant, T., Boca, R., Maianti, P., Liberta', G., Jacome, F.O.D., Branco, A., De, R.D., Suarez-Moreno, M., Ferrari, D., Roglia, E., Scionti, N., Broglia, M., Onida, M., Tistan, A., Loffler, P., 2023. Forest Fires in Europe, Middle East and North Africa 2022. <https://doi.org/10.2760/348120>
- Santos, G.M., Southon, J.R., Druffel-Rodriguez, K.C., Griffin, S., Mazon, M., 2004. Magnesium perchlorate as an alternative water trap in AMS graphite sample preparation: A report on sample preparation at KCCAMS at the University of California, Irvine, in: *Radiocarbon*. <https://doi.org/10.1017/S0033822200039485>
- Sanusi, A.A., Norman, A.L., Burridge, C., Wadleigh, M., Tang, W.W., 2006. Determination of the S isotope composition of methanesulfonic acid. *Anal Chem* 78. <https://doi.org/10.1021/ac0600048>
- Savarino, J., Romero, A., Cole-Dai, J., Bekki, S., Thiemens, M.H., 2003. UV induced mass-independent sulfur isotope fractionation in stratospheric volcanic sulfate. *Geophys Res Lett* 30. <https://doi.org/10.1029/2003GL018134>
- Sawlani, R., Agnihotri, R., Sharma, C., 2021. Chemical and isotopic characteristics of PM2.5 over New Delhi from September 2014 to May 2015: Evidences for synergy between air-pollution and meteorological changes. *Science of the Total Environment* 763. <https://doi.org/10.1016/j.scitotenv.2020.142966>
- Sawlani, R., Agnihotri, R., Sharma, C., Patra, P.K., Dimri, A.P., Ram, K., Verma, R.L., 2019. The severe Delhi SMOG of 2016: A case of delayed crop residue burning, coincident firecracker emissions, and atypical meteorology. *Atmos Pollut Res* 10. <https://doi.org/10.1016/j.apr.2018.12.015>
- Seinfeld, J.H., Pandis, S.N., 2016. *Atmospheric Chemistry and Physics: From Air Pollution to Climate Change*, Third Edition. ed.
- Shaheen, R., Abaunza, M.M., Jackson, T.L., McCabe, J., Savarino, J., Thiemens, M.H., 2014. Large sulfur-isotope anomaly in nonvolcanic sulfate aerosol and its implications for the Archean atmosphere. *Proc Natl Acad Sci U S A* 111. <https://doi.org/10.1073/pnas.1406315111>
- Shao, J., Chen, Q., Wang, Y., Lu, X., He, P., Sun, Y., Shah, V., Martin, R., Philip, S., Song, S., Zhao, Y., Xie, Z., Zhang, L., Alexander, B., 2019. Heterogeneous sulfate aerosol formation mechanisms during wintertime

- Chinese haze events: Air quality model assessment using observations of sulfate oxygen isotopes in Beijing. *Atmos Chem Phys* 19. <https://doi.org/10.5194/acp-19-6107-2019>
- Sharp, Z., 2017. Principles of Stable Isotope Geochemistry, 2nd edition. Principles of Stable Isotope Geochemistry, 2nd edition 136.
- Shrivastava, M., Cappa, C.D., Fan, J., Goldstein, A.H., Guenther, A.B., Jimenez, J.L., Kuang, C., Laskin, A., Martin, S.T., Ng, N.L., Petaja, T., Pierce, J.R., Rasch, P.J., Roldin, P., Seinfeld, J.H., Shilling, J., Smith, J.N., Thornton, J.A., Volkamer, R., Wang, J., Worsnop, D.R., Zaveri, R.A., Zelenyuk, A., Zhang, Q., 2017. Recent advances in understanding secondary organic aerosol: Implications for global climate forcing. *Reviews of Geophysics* 55. <https://doi.org/10.1002/2016RG000540>
- Singh, A., Satish, R.V., Rastogi, N., 2019. Characteristics and sources of fine organic aerosol over a big semi-arid urban city of western India using HR-ToF-AMS. *Atmos Environ* 208. <https://doi.org/10.1016/j.atmosenv.2019.04.009>
- Singh, H.G., 1995. Composition, chemistry, and climate of the atmosphere. Composition, chemistry, and climate of the atmosphere. [https://doi.org/10.1016/s1352-2310\(96\)00207-5](https://doi.org/10.1016/s1352-2310(96)00207-5)
- Sinha, B.W., Hoppe, P., Huth, J., Foley, S., Andreae, M.O., 2008. Sulfur isotope analyses of individual aerosol particles in the urban aerosol at a central European site (Mainz, Germany). *Atmos Chem Phys* 8, 7217–7238. <https://doi.org/10.5194/ACP-8-7217-2008>
- Smith, S.J., Van Aardenne, J., Klimont, Z., Andres, R.J., Volke, A., Delgado Arias, S., 2011. Anthropogenic sulfur dioxide emissions: 1850-2005. *Atmos Chem Phys* 11. <https://doi.org/10.5194/acp-11-1101-2011>
- Sofen, E.D., Alexander, B., Kunasek, S.A., 2011. The impact of anthropogenic emissions on atmospheric sulfate production pathways, oxidants, and ice core $\Delta^{17}\text{O}(\text{SO}_4^{2-})$. *Atmos Chem Phys* 11. <https://doi.org/10.5194/acp-11-3565-2011>
- Solomon, S., D., Qin, M., Manning, Z., Chen, M., Marquis, K.B., Averyt, M.T., Miller HL, Solomon, S., Qin, D., Manning, M., Chen, Z., Marquis, M., Averyt, K.B., Tignor, M., Miller, H.L., 2007. Summary for Policymakers. In: Climate Change 2007: The Physical Science Basis. Contribution of Working Group I to the Fourth Assessment Report of the Intergovernmental Panel on Climate Change. D Qin M Manning Z Chen M Marquis K Averyt M Tignor and HL Miller New York Cambridge University Press pp Geneva. <https://doi.org/10.1038/446727a>

- Stein, A.F., Draxler, R.R., Rolph, G.D., Stunder, B.J.B., Cohen, M.D., Ngan, F., 2015. NOAA's HYSPLIT atmospheric transport and dispersion modeling system. Bull Am Meteorol Soc. <https://doi.org/10.1175/BAMS-D-14-00110.1>
- Stenström, K.E., Skog, G., Georgiadou, E., Genberg, J., Johansson, A., 2011. A guide to radiocarbon units and calculations. Lund 6, 0–17.
- Strauss, H., 1997. The isotopic composition of sedimentary sulfur through time. Palaeogeogr Palaeoclimatol Palaeoecol 132. [https://doi.org/10.1016/S0031-0182\(97\)00067-9](https://doi.org/10.1016/S0031-0182(97)00067-9)
- Stuiver, M., Polach, H.A., 1977. Discussion Reporting of ^{14}C Data . Radiocarbon 19. <https://doi.org/10.1017/s0033822200003672>
- Suto, N., Kawashima, H., 2016. Global mapping of carbon isotope ratios in coal. J Geochem Explor 167. <https://doi.org/10.1016/j.gexplo.2016.05.001>
- Szidat, S., Jenk, T.M., Gäggeler, H.W., Synal, H.A., Fisseha, R., Baltensperger, U., Kalberer, M., Samburova, V., Wacker, L., Saurer, M., Schwikowski, M., Hajdas, I., 2004. Source apportionment of aerosols by ^{14}C measurements in different carbonaceous particle fractions, in: Radiocarbon. <https://doi.org/10.1017/S0033822200039783>
- Tanaka, N., Rye, D.M., Xiao, Y., Lasaga, A.C., 1994. Use of stable sulfur isotope systematics for evaluating oxidation reaction pathways and in-cloud-scavenging of sulfur dioxide in the atmosphere. Geophys Res Lett 21. <https://doi.org/10.1029/94GL00893>
- Ten Brink, H.M., Kruis, C., Kos, G.P.A., Berner, A., 1997. Composition/size of the light-scattering aerosol in the Netherlands. Atmos Environ 31. [https://doi.org/10.1016/S1352-2310\(97\)00232-X](https://doi.org/10.1016/S1352-2310(97)00232-X)
- Thiemens, M.H., 2006. History and applications of mass-independent isotope effects. Annu Rev Earth Planet Sci. <https://doi.org/10.1146/annurev.earth.34.031405.125026>
- Thode, H.G., 1991. Sulphur isotopes in nature and the environment: an overview. Stable isotopes: Natural and anthropogenic sulphur in the environment. [https://doi.org/10.1016/S0167-5273\(97\)00130-7](https://doi.org/10.1016/S0167-5273(97)00130-7)
- Thode, H.G., Macnamara, J., Fleming, W.H., 1953. Sulphur isotope fractionation in nature and geological and biological time scales. Geochim Cosmochim Acta 3. [https://doi.org/10.1016/0016-7037\(53\)90042-8](https://doi.org/10.1016/0016-7037(53)90042-8)
- Thompson, M., Wood, R., 1995. Harmonized guidelines for internal quality control in analytical chemistry laboratories (Technical Report). Pure and Applied Chemistry 67. <https://doi.org/10.1351/pac199567040649>

- Tichomirowa, M., Haubrich, F., Klemm, W., Matschullat, J., 2007. Regional and temporal (1992-2004) evolution of air-borne sulphur isotope composition in Saxony, southeastern Germany, central Europe, in: Isotopes in Environmental and Health Studies. <https://doi.org/10.1080/10256010701702499>
- Tomasi, C., Fuzzi, S., Kokhanovsky, A.A., 2017. Atmospheric aerosols : life cycles and effects on air quality and climate. Atmospheric aerosols : life cycles and effects on air quality and climate.
- Tomasi, C., Lupi, A., 2016. Primary and Secondary Sources of Atmospheric Aerosol, in: Atmospheric Aerosols. <https://doi.org/10.1002/9783527336449.ch1>
- Tsimpidi, A.P., Karydis, V.A., Pandis, S.N., 2007. Response of inorganic fine particulate matter to emission changes of sulfur dioxide and ammonia: The Eastern United States as a case study. J Air Waste Manage Assoc 57. <https://doi.org/10.3155/1047-3289.57.12.1489>
- Tsunogai, S., 1971. Oxidation rate of sulfite in water and its bearing on the origin of sulfate in meteoric precipitation. Geochem J 5. <https://doi.org/10.2343/geochemj.5.175>
- Twomey, S., 1991. Aerosols, clouds and radiation. Atmospheric Environment Part A, General Topics 25. [https://doi.org/10.1016/0960-1686\(91\)90159-5](https://doi.org/10.1016/0960-1686(91)90159-5)
- United Nations Economic Commission for Europe, 2016. Environmental Performance Reviews Belarus. Environmental Performance Reviews Series No. 44.
- Urban, R.C., Lima-Souza, M., Caetano-Silva, L., Queiroz, M.E.C., Nogueira, R.F.P., Allen, A.G., Cardoso, A.A., Held, G., Campos, M.L.A.M., 2012. Use of levoglucosan, potassium, and water-soluble organic carbon to characterize the origins of biomass-burning aerosols. Atmos Environ 61. <https://doi.org/10.1016/j.atmosenv.2012.07.082>
- Urey, H.C., 1947. The thermodynamic properties of isotopic substances. Journal of the Chemical Society (Resumed). <https://doi.org/10.1039/jr9470000562>
- Väkevä, M., Hämeri, K., Puhakka, T., Nilsson, E.D., Hohti, H., Mäkelä, J.M., 2000. Effects of meteorological processes on aerosol particle size distribution in an urban background area. Journal of Geophysical Research Atmospheres 105. <https://doi.org/10.1029/1999JD901143>
- Vestreng, V., Myhre, G., Fagerli, H., Reis, S., Tarrasón, L., 2007. Twenty-five years of continuous sulphur dioxide emission reduction in Europe. Atmos Chem Phys 7. <https://doi.org/10.5194/acp-7-3663-2007>

- Viana, M., Reche, C., Amato, F., Alastuey, A., Querol, X., Moreno, T., Lucarelli, F., Nava, S., Calzolai, G., Chiari, M., Rico, M., 2013. Evidence of biomass burning aerosols in the Barcelona urban environment during winter time. *Atmos Environ* 72. <https://doi.org/10.1016/j.atmosenv.2013.02.031>
- Vodička, P., Kawamura, K., Schwarz, J., Kunwar, B., Ždímal, V., 2019. Seasonal study of stable carbon and nitrogen isotopic composition in fine aerosols at a Central European rural background station. *Atmos Chem Phys* 19. <https://doi.org/10.5194/acp-19-3463-2019>
- Vogel, P., Houk, K.N., 2018. Organic chemistry: Theory, reactivity, mechanisms in modern synthesis. *Journal of Organic & Inorganic Chemistry* 04. <https://doi.org/10.21767/2472-1123-c5-015>
- Wei, L., Yue, S., Zhao, W., Yang, W., Zhang, Y., Ren, L., Han, X., Guo, Q., Sun, Y., Wang, Z., Fu, P., 2018. Stable sulfur isotope ratios and chemical compositions of fine aerosols (PM_{2.5}) in Beijing, China. *Science of the Total Environment* 633. <https://doi.org/10.1016/j.scitotenv.2018.03.153>
- Werner, R.A., Brand, W.A., 2001. Referencing strategies and techniques in stable isotope ratio analysis. *Rapid Communications in Mass Spectrometry*. <https://doi.org/10.1002/rcm.258>
- Werner, R.A., Bruch, B.A., Brand, W.A., 1999. ConFlo III - An interface for high precision $\delta^{13}\text{C}$ and $\delta^{15}\text{N}$ analysis with an extended dynamic range. *Rapid Communications in Mass Spectrometry* 13. [https://doi.org/10.1002/\(SICI\)1097-0231\(19990715\)13:13<1237::AID-RCM633>3.0.CO;2-C](https://doi.org/10.1002/(SICI)1097-0231(19990715)13:13<1237::AID-RCM633>3.0.CO;2-C)
- Werner, R.A., Cormier, M.-A., 2022. Isotopes—Terminology, Definitions and Properties. https://doi.org/10.1007/978-3-030-92698-4_8
- Widory, D., 2006. Combustibles, fuels and their combustion products: A view through carbon isotopes. *Combustion Theory and Modelling* 10, 831–841. <https://doi.org/10.1080/13647830600720264>
- Vilniaus šilumos tinklai, 2023. Available online: <https://chc.lt/lt/gn/44/vilniaus-silumos-tinklai-nuo-kovo-pabaigos-nebenaudos-mazasierio-mazuto-grizta-prie-atpigusių-gamtinių-duju:757> (accessed 5.12.24).
- Wofsy, S.C., Zhang, X., Qin, D., Manning, M., Chen, Z., Marquis, M., Averyt, K.B., 2007. Couplings Between Changes in the Climate System and Biogeochemistry. *Carbon N Y* 21.
- Worobiec, A., Zwozdziak, A., Sówka, I., Zwóździak, J., Stefaniak, E.A., Buczyńska, A., Krata, A., Van Meel, K., Van Grieken, R., Górką, M., Jędrysek, M.O., 2008. Historical changes in air pollution in the tri-border

region of Poland, Czech Republic and Germany. Environment Protection Engineering.

- Yao, P., Huang, R.J., Ni, H., Kairys, N., Yang, L., Meijer, H.A.J., Dusek, U., 2022. ^{13}C signatures of aerosol organic and elemental carbon from major combustion sources in China compared to worldwide estimates. *Science of the Total Environment* 810. <https://doi.org/10.1016/j.scitotenv.2021.151284>
- Yoshioka, M., Grosvenor, D.P., Booth, B.B.B., Morice, C.P., Carslaw, K.S., n.d. Warming effects of reduced sulfur emissions from shipping. <https://doi.org/10.5194/egusphere-2024-1428>
- Yvon, S.A., Saltzman, E.S., Cooper, D.J., Bates, T.S., Thompson, A.M., 1996. Atmospheric sulfur cycling in the tropical Pacific marine boundary layer (12°S , 135°W): A comparison of field data and model results 1. Dimethylsulfide. *Journal of Geophysical Research Atmospheres* 101. <https://doi.org/10.1029/95JD03356>
- Zhang, C., Liu, Y., Kang, S., Yan, F., Hu, Z., Chen, P., Huang, G., Li, C., Stubbins, A., 2023. Stable Carbon Isotope Signatures of Carbonaceous Aerosol Endmembers in the Tibetan Plateau. *Environ Sci Technol*. <https://doi.org/10.1021/acs.est.3c09357>
- Zhang, M.Y., Wang, S.J., Ma, G.Q., Zhou, H.Z., Fu, J., 2010. Sulfur isotopic composition and source identification of atmospheric environment in central Zhejiang, China. *Sci China Earth Sci*. <https://doi.org/10.1007/s11430-010-4017-9>
- Zhang, Q., Wang, Y., Liu, M., Zheng, M., Yuan, L., Liu, J., Tao, S., Wang, X., 2023. Wintertime Formation of Large Sulfate Particles in China and Implications for Human Health. *Environ Sci Technol* 57. <https://doi.org/10.1021/acs.est.3c05645>
- Zhou, G., Tazaki, K., 1996. Seasonal variation of gypsum in aerosol and its effect on the acidity of wet precipitation on the Japan Sea side of Japan. *Atmos Environ* 30. [https://doi.org/10.1016/1352-2310\(96\)00071-4](https://doi.org/10.1016/1352-2310(96)00071-4)
- Zhou, Y., Xiaodong, L., Shilu, W., Qinkai, L., Jun, H., Gaoyang, C., 2019. Aerosol pollution in a megacity of southwest China inferred from variation characteristics of sulfate- $\delta^{34}\text{S}$ and water-soluble inorganic compositions in TSP. *Particuology* 43. <https://doi.org/10.1016/j.partic.2018.03.009>

SUPPLEMENTARY MATERIALS

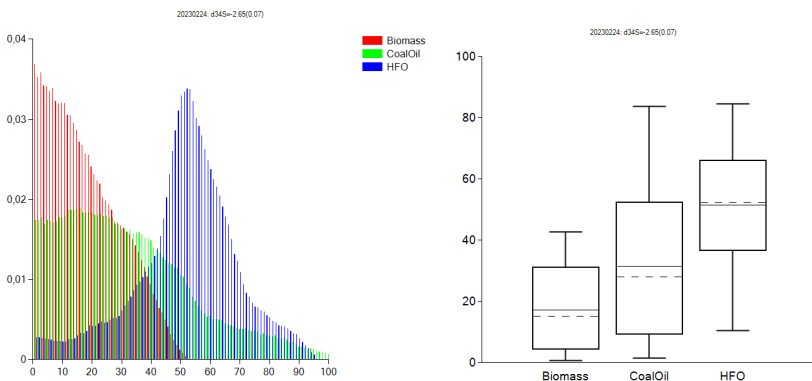


Figure S1. Example of FRUITS model outputs of evaluated source contributions for a SO_2 sample. The left side shows the probability distribution of the source contributions, while the right side presents the data in box plots. The box represents the 1σ interval, while the whiskers indicate the 2σ interval. Mean value is represented by the continuous line and dashed line is the calculated median.

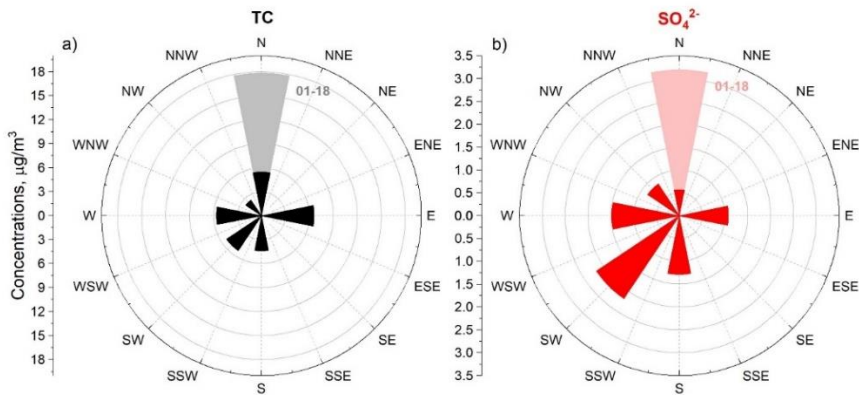


Fig. S2. Total carbon (a) and sulfate (b) concentration dependence on air mass origin. The period from January 15 to January 18, 2020, is highlighted as shaded sections due to the notably high concentrations recorded during this period.

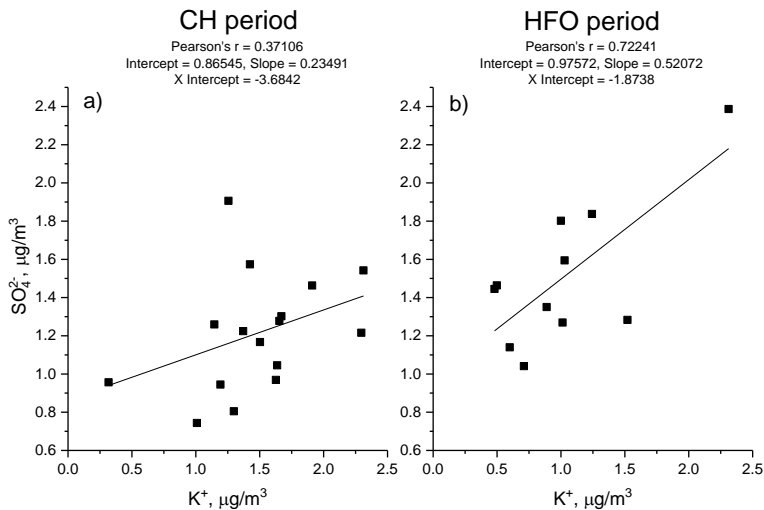


Figure S3. Correlation between of SO_4^{2-} and K^+ ion concentrations during a) the CH period ($p < 0.05$) and b) the HFO period ($p < 0.05$).

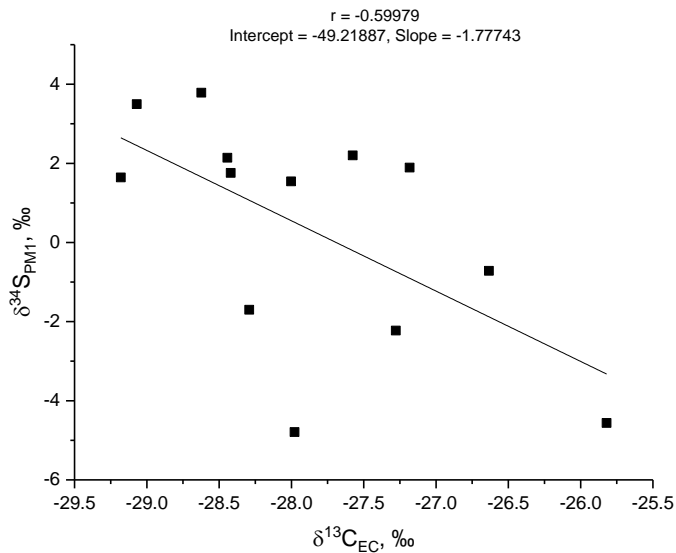


Fig. S4. Relationship between $\delta^{34}\text{S}$ of sulfate and $\delta^{13}\text{C}$ of elemental carbon fraction during the 2022 – 2023 season.

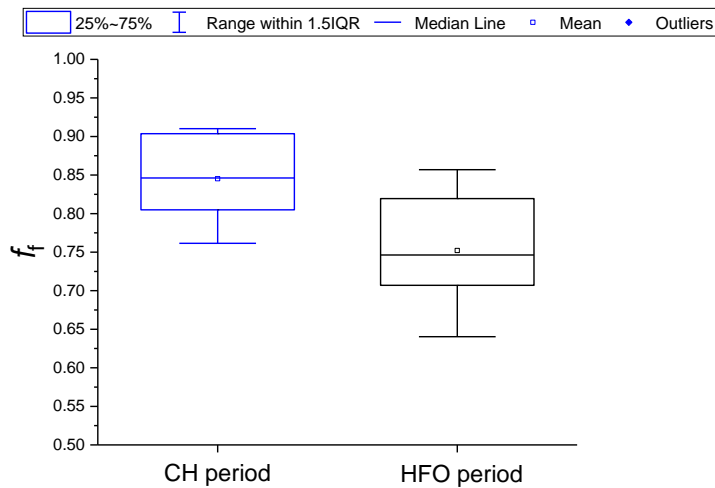


Fig. S5. Change in f_f values during the conventional heating (CH) period and during the period of increased heavy fuel oil (HFO) emissions.

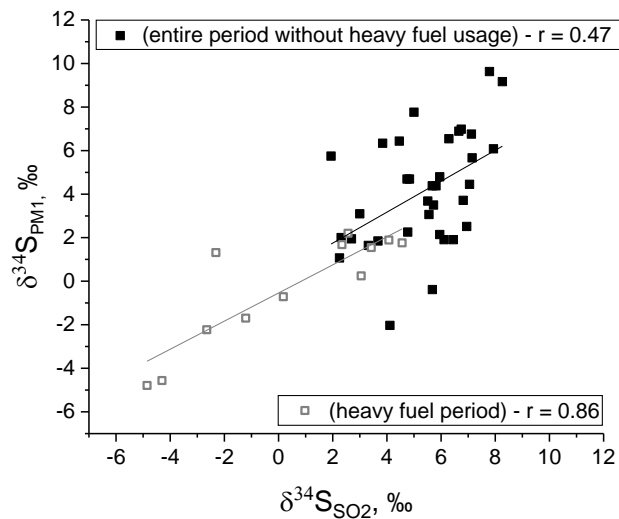


Fig. S6. Relationship between $\delta^{34}\text{S}$ values of $\text{PM}_1 \text{SO}_4^{2-}$ and of SO_2 , during the heavy fuel oil (HFO) usage period and the entire sampling period, excluding the HFO period.

SANTRAUKA

IVADAS

Aerozoliai yra mikroskopinė mažų skystų arba kietujų dalelių (angl. *particulate matter*, PM) suspensija ore. Smulkiosios aerozolio dalelės pasižymi įvairia sudėtimi ir gali būti sudarytos iš sulfatų (SO_4^{2-}), nitratų (NO_3^-), amonio (NH_4^+), organinių junginių (OC), juodosios anglies (BC) arba elementinės anglies (EC) ir pereinamųjų metalų jonų (TMI) (Pöschl, 2005; Seinfeld and Pandis, 2016). Sulfatiniai aerozoliai dažniausiai atmosferoje susidaro oksiduojantis SO_2 dujoms. Sulfatai yra ypač svarbus komponentas kietosiose dalelėse ir sudaro apie 12 – 44 % dalį dalelėse, kurių skersmuo mažesnis nei 1 μm (PM_1) (Bressi et al., 2021; Masalaite et al., 2022; Singh et al., 2019). Sieros junginiai atlieka svarbų vaidmenį atmosferos chemijoje, Žemės klimate ir daro žalingą poveikį žmonių sveikatai (Kiehl and Briegleb, 1993; Kreyling et al., 1999; Pope and Dockery, 2006). Istoriskai svarbus sieros taršos poveikio pavyzdys yra rūgštūs lietūs, kurie aštuntajame ir devintajame dešimtmeečiuose smarkiai pažeidė natūralias Europos ekosistemas (Menz and Seip, 2004; Worobiec et al., 2008). Taip pat sulfatiniai aerozoliai tiesiogiai sklaidydami krintančią saulės spinduliuotę arba netiesiogiai per įvairius debesyse vykstančius procesus, kurie keičia debesų albedo, jų gyvavimo trukmę bei kitas savybes, daro įtaką krintančios spinduliuotės balansui ir vésina atmosferą (Albrecht, 1989; Boucher and Lohmann, 1995; Kulmala et al., 2013, 2007; Ten Brink et al., 1997; Twomey, 1991). Tačiau sulfatų spinduliuotės sklaidos efektyvumas yra vis dar tiksliai neapibrėžtas (Bellouin et al., 2020; Myhre et al., 2004; Solomon, S. et al., 2007). Miesto aplinkoje nejūrinės druskos (angl. *non-sea salt*, nss) kilmės sulfatai yra daugiausia antrinės dalelės, susiformavusios SO_2 dujoms virstant kietosiomis dalelėmis cheminių reakcijų metu (Tomasi et al., 2017). Atmosferoje apie 50 % išmetamų SO_2 dujų yra oksiduojamos į sulfatinius junginius per įvairias reakcijas, vykstančias dujinėje arba skystojoje fazėje (Chin et al., 2000). Šiuo metu manoma, jog dominuojantys SO_2 oksidacijos keliai yra oksidacija OH radikalais dujinėje fazėje ir H_2O_2 , O_3 , O_2 katalizuojama pereinamųjų metalų jonų (angl. *transition metal catalysis*, TMI) skystojoje fazėje (Harris et al., 2012; Herrmann et al., 2000; Tanaka et al., 1994). Pasiskirstymas tarp skirtingų SO_2 oksidacijos kelių yra esminis parametras, leidžiantis įvertinti susidariusių sulfatų spinduliuotės sklaidos savybes, todėl tai yra ypač svarbi problema sieros ciklo tyrimuose (Alexander et al., 2009; Harris et al., 2013b; Hegg et al., 2004). Dėl šių priežasčių būtina

išsamiai suprasti išmetamos sieros šaltinius ir sulfato aerosolių susidarymo mechanizmus, kurie lemia tolesnes aerosolių savybes, tokias kaip jų dydžio pasiskirstymas, optinės charakteristikos ir pernaša, darančias didelį poveikį aplinkai ir žmonių sveikatai (Thiemens, 2006; Tomasi et al., 2017; Zhang et al., 2023).

Šiame kontekste stabiliųjų izotopų analizė yra metodas, leidžiantis identifikuoti sieros emisijos šaltinius ir tirti atmosferoje vykstančius dujų transformacijos procesus į kietąsias daleles (Dasari ir Widory, 2024; Kawamura ir kt., 2001; Mukai ir kt., 2001). Pastaruoju metu daugybėje tyrimų buvo analizuojami veiksniai, lemiantys PM sulfatų izotopinės sudėties ($\delta^{34}\text{S}$) vertes, įskaitant taršos šaltinių izotopines vertes, sulfatų susidarymo kelius, aplinkos temperatūrą ir sieros junginių oksidacijos spartą užterštuose regionuose Kinijoje (Guo et al., 2019; Han et al., 2016; Li et al., 2020; Wei et al., 2018; Zhou et al., 2019), Indijoje (Dasari et al., 2022b; Dasari and Widory, 2024; Rastogi et al., 2020; Sawlani et al., 2021) ir Korējoje (Kim et al., 2021; Lee et al., 2023). O Europoje atliekami izotopinės sudėties tyrimai taršos šaltinių identifikavimo ir sieros junginių dinamikos atmosferoje tematika šiuo metu yra reti ir menkai ištyrinėti (Górka et al., 2017; Novák et al., 2001; Sinha et al., 2008). Todėl šiame darbe stabiliųjų izotopų analizės metodai bus taikomi siekiant ištirti sezonię sieros emisijos šaltinių kaitą ir jų transformacijos mechanizmus atmosferoje, siekiant geriau suprasti atmosferinės sieros taršos priežastis ir jos poveikį aplinkai. Šiame tyime pateikiamas išsamus metodas atmosferinės taršos šaltiniams identifikuoti ir kiekybiškai įvertinti jų indėlius, pasitelkiant stabiliųjų sieros izotopų analizę su papildomais meteorologiniais duomenimis, vandenye tirpių neorganinių jonų (angl. *water-soluble inorganic ion*, WSII) ir radioanglies duomenimis.

Tyrimo tikslas ir uždaviniai

Šio darbo tikslas – ištirti ilgalaikę sezonię sieros junginių kaitą atmosferoje ir įvertinti jų emisijos šaltinius, taikant stabiliųjų sieros izotopų analizę. Šiam tikslui pasiekti buvo suformuoti šie uždaviniai:

- Ištirti sieros junginių dinamiką atmosferoje, naudojant kelių izotopų analizės metodą (^{34}S , ^{13}C ir ^{14}C).
- Nustatyti veiksnius, lemiančius sezoniškus SO_2 ir PM_1 sulfatų koncentracijų bei izotopinių sudėčių pokyčius.
- Identifikuoti ir kiekybiškai įvertinti sezoniškus sieros taršos šaltinius, darančius įtaką oro kokybei Vilniuje, pasitelkiant Bajeso

statistinį modelį, integruotą su regionui būdingomis izotopinėmis vertėmis.

- Ivertinti skirtinį SO₂ oksidacijos kelių santykinį indėlį į PM₁ sulfatų susidarymą.
- Ivertinti kintančių emisijos šaltinių poveikį oro kokybei ir PM₁ izotopinei sudėčiai neįprastais laikotarpiais (pvz., COVID-19 apribojimų metu ar padidėjus sunkiojo kuro emisijoms).

Mokslinio darbo naujumas

Šio darbo metu gauti rezultatai parodė atvirkštinę sezoninę sieros junginių izotopinės sudėties dinamiką atmosferoje; ji skiriasi nuo daugumos šia tema paskelbtų duomenų. Tai daugiausia lėmė kintantys vietinių ir tolimųjų taršos šaltinių indėliai skirtiniais metų laikais.

Pirmą kartą pritaikytas kompleksinis kelių stabiliųjų izotopų (³⁴S ir ¹³C) ir radioanglies (¹⁴C) analizės metodas, kuris leido charakterizuoti pagrindinius antropogeninius šaltinius, prisidedančius prie sulfatų ir anglies aerosolių susidarymo.

Sinchroniškai surinktų SO₂ ir sulfatinių aerosolių mėginių izotopų analizės duomenys leido kiekybiškai ivertinti dominuojančius atmosferinius SO₂ oksidacijos kelius. Šis tyrimas patvirtino, jog Vilniaus miesto aplinkoje žiemos metu pagrindinis SO₄²⁻ susidarymo mechanizmas buvo SO₂ oksidacija, katalizuojama pereinamųjų metalų jonų.

Mokslinio darbo aktualumas

Sieros junginiai turi didelę įtaką Žemės klimatui ir daro poveikį oro kokybei bei žmonių sveikatai. Sulfatiniai aerosoliai prisideda prie klimato vėsimo, sklaidydami Saulės spinduliuotę. Susidariusių sulfatų sklaidos savybės priklauso nuo SO₂ oksidacijos kelių, todėl tikslus sieros taršos šaltinių ir SO₂ oksidacijos kelių nustatymas yra būtinės siekiant ivertinti jų poveikį aplinkai ir klimatui.

Šioje disertacijoje pateikiami stabiliųjų izotopų (³⁴S ir ¹³C) bei radioanglies (¹⁴C) matavimais paremti metodai, skirti antropogeninių emisijų ir jų atmosferinės kaitos charakterizavimui. Atmosferinių sieros junginių izotopinių verčių matavimai gali būti pritaikyti aplinkos monitoringe, leidžiant nustatyti sezoninius taršos šaltinius, atskirti vietinės ir tolimosios kilmės emisijas bei aptikti naujo taršos šaltinio emisijas. Izotopiniai tyrimai pagrįstas taršos šaltinių charakterizavimas gali padėti aplinkosaugos agentūroms kurti tikslines strategijas mažinant emisijas bei veiksmingai

gerinant oro kokybę. Taip pat SO₂ oksidacijos kelių tyrimai gali būti pritaikyti klimato modelių tobulinimui, leidžiant tiksliau įvertinti atmosferinių sulfatų spindulinės sklaidos poveikį.

Autoriaus indėlis

Savaitinis SO₂ ir sulfatinių aerosolių mèginių rinkimas viso mèginių èmimo laikotarpiu (nuo 2020 m. lapkričio 11 d. iki 2023 m. birželio 30 d. Cheminio paruošimo metodų verifikacija ir jų pritaikymas sulfato išskyrimui iš SO₂ ir aerosolių mèginių. Mèginių paruošimas stabiliųjų izotopų santykiai, radioanglies ir vandenye tirpių neorganinių jonų koncentracijų matavimams. Aktyvus dalyvavimas rengiant, įgyvendinant ir validuojant metodikas sieros izotopų santykio matavimams. Sieros izotopinių santykiai matavimas izotopinio santykio masių spektrometru. Stabiliųjų izotopų santykio rezultatų korekcija ir normalizavimas. Meteorologinių duomenų rinkimas ir adaptavimas bei atgalinës oro masių pernašos trajektorijų modelių taikymas. Bajeso statistinių modelių taikymas. Duomenų interpretavimas ir analizë. Straipsnių rankraščių rengimas, išskaitant metodologijos, duomenų analizës ir skaičiavimų aprašymus, rezultatų interpretaciją, duomenų vizualizaciją ir išvadų formulavimą.

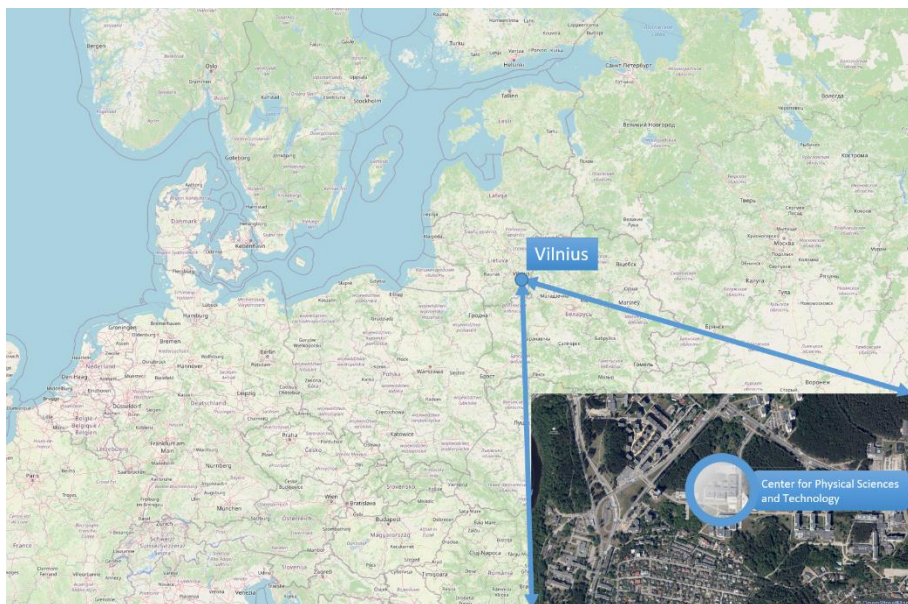
Ginamieji teiginiai

1. Sieros junginių izotopinė sudëtis rodo ryškius sezoninius svyravimus: su aukštësnëmis $\delta^{34}\text{S}$ vertëmis vasaros mënesiams ir žemesnëmis – žiemos mënesiams. Šiuos pokyčius lemia dominuojančių taršos šaltinių ir oksidacijos kelių kaita.
2. Pagrindiniai sieros taršos šaltiniai, darantys įtaką miesto oro kokybei Vilniuje, buvo biomasës deginimas, anglies degimo emisijos iš kaimyninių šalių, o 2022 – 2023 m. šildymo sezono metu reikšmingu taršos šaltiniu tapo sunkiojo kuro deginimo emisijos.
3. Padidėjusių sunkiojo kuro deginimo emisijų laikotarpiu pagrindinis sulfatų susidarymo kelias buvo SO₂ oksidacija deguonimi (O₂), katalizuojama pereinamujų metalų ionų. Tuo metu oksidacija per vandenilio peroksidą (H₂O₂) ir hidroksilo radikalus (OH) sudarë mažesnį indėlį i sulfatų susidarymą.

TYRIMO OBJEKTAS IR METODIKA

Bandinių rinkimas

Tyrimo metu, nuo 2020 m. lapkričio 11 d. iki 2023 m. birželio 30 d., buvo surinkti 92 PM₁ dalelių mèginiai Vilniuje, Lietuvoje. Nuo 2021 m. gruodžio 10 d. kartu su PM₁ mèginiais buvo pradèti rinkti ir SO₂ dujų mèginiai (iš viso surinkti 48 SO₂ bandiniai). PM₁ ir SO₂ mèginiai buvo renkami ant Fizinių ir technologijos mokslų centro pastato stogo (158 m virš jūros lygio) (1 pav.). Ši vietovè yra apsupta įvairaus tipo gyvenamujų pastatų, išskaitant privačius namus. Artimiausia intensyvaus eismo gatvè yra nutolusi 1 km atstumu. Ši bandinių rinkimo vietovè reprezentuoja tipinę miesto foninę aplinką Lietuvoje.



1 pav. Bandinių rinkimo vietovè (pažymèta melynu tašku; 54.72°N, 25.32°E) Fizinių ir technologijos mokslų centre, Vilniuje, Lietuvoje.

PM₁ mèginiai buvo renkami ant išskaitintų (500 °C) kvarco pluošto filtrų (150 mm skersmens, Whatman, QM-A), o SO₂ bandiniai buvo renkami ant stiklo pluošto filtrų (Munktell and Filtrak, Gf-Microfilter), impregnuotų K₂CO₃ glicerolio tirpale pagal Amiri et al. (2018) naudotą metodiką. PM₁ ir SO₂ mèginiai buvo renkami vienu metu su didelio tūrio aerozolių rinkimo įranga (DIGITEL DH-77), veikiančia 500 l/min greičiu. Vidutinė mèginio èmimo

trukmė vienam filtrui buvo 191 val. Surinkti bandiniai buvo apvelkami iškaitinta aluminio folija ir dedami laikyti šaldiklyje -20 °C temperatūroje iki tolimesnių matavimų.

Bandinių cheminis paruošimas

Prieš izotopinių verčių matavimus siera turėjo būti išskirta iš surinktų PM₁ ir SO₂ filtru. Cheminio paruošimo metu vandenye tirpūs sulfatai nusodinami BaSO₄ pavidalu, pridėjus BaCl₂. Šis metodas nesukelia izotopinio frakcionavimo (Claypool et al., 1980; Fan et al., 2020), todėl yra plačiai taikomas atmosferinių sieros junginių stabiliųjų izotopų tyrimuose (Mayer and Krouse, 2004; Mukai et al., 2001; Zhang et al., 2010).

Pirmiausia pusė PM₁ kvarcinio filtro (~ 77 cm²) supjaustoma, įdedama į 100 ml aukštous grynumo (angl. *ultrapure*) vandens ir mėgintuvėliai 30 minučių patalpinami į ultragarsinę vonelę. Kitą dieną mėginiai yra prafiltruojami per švirkštinius filtrus (0,22 µm), o prafiltruotas tirpalas tada yra parūgštinamas su HCl iki 2 – 3 pH. Toliau į tirpalą pridedama 5 ml 1 mol/l BaCl₂, kad sulfatas būtų nusodintas kaip BaSO₄ nuosėdos. Kitą dieną nuosėdos surenkamos ant 47 mm celiuliozės acetatinių filtrų (0,2 µm, Sartorius CA), kurie vėliau išplaunami su 150 ml aukštaus grynumo vandeniu ir dedami džiovinti 6 val. 60 °C temperatūroje. Vėliau filtrais deginami 500 °C temperatūroje, kad liktų tik BaSO₄.

Surinktų SO₂ filtru cheminio paruošimo procedūra yra beveik vienoda, tačiau papildomai filtrai iš pradžių yra apdorojami 1 ml 30 % w/w vandenilio peroksoido tirpalu. Po to atliekami anksčiau aprašyti veiksmai: patalpinimas ultragarsinėje vonelėje, filtravimas, rūgštinimas, BaSO₄ nusodinimas ir susidariusių nuosėdų surinkimas.

Izotopų santykio masių spektrometrija

Šiame darbe anglies ir sieros izotopinės vertės buvo nustatytos, naudojant elementinį analizatorių (angl. *elemental analyzer*, EA), prijungtą prie izotopų santykio masių spektromетro (angl. *isotope ratio mass spectrometer*, IRMS). IRMS prietaisas yra skirtas matuoti nedidelius lengvujų elementų, tokius kaip ³⁴S/³²S ir ¹³C/¹²C, izotopinių santykijų skirtumus. Šiame darbe naudota sistema („Thermo Fisher Scientific“) sudaryta iš Flash EA1112 elementinio analizatoriaus, sujungto su Delta V Advantage masių spektrometru per ConFlow III sasają.

Sieros matavimams apie 0,50 mg BaSO₄ mèginio yra sumaišoma su V₂O₅ ir dedama į alavo kapsules. Taip supakuoti bandiniai patenka į oksidacinę/redukcinę kolonélę, įkaitintą iki 1050 °C, kurioje jie termiskai suskyla iki SO₂ dujų. Sieros matavimams pritaikyta kolonélė yra užpildyta WO₃ granulémis ir Cu vielomis. Tada iš kolonės išėjusių dujų yra pašalinamas vanduo su Mg(ClO₄)₂ sorbentu. Vėliau išeinančios SO₂, CO₂ ir N₂ dujos atskiriamos dujų chromatografinėje kolonélėje (2 m, PTFE) ir tada yra detektuoamos šiluminio laidumo detektoriumi (angl. *thermal conductivity detector*, TCD).

Dėl srautų skirtumų, esančių tarp iš EA išeinančio srauto (80 – 120 ml/min) ir aukšto vakuumo sąlygų IRMS sistemoje, būtina sumažinti dujų srautą. Tai atliekama per ConFlo III sasają ir srautas sumažinamas iki 0,3 ml/min. ConFlo III sasaja taip pat yra atsakinga už palyginamujų dujų padavimą į IRMS prietaisą.

Praskiestos dujos, patekusios į IRMS šaltinį, yra jonizuojamos jas bombarduojant elektronais (angl. *electron ionization*, EI), taip sukuriant teigiamus jonus. Tada jonai iš šaltinio pagreitinami ekstrakcijos plokšteliemis ir sufokusuojami lėšių sistema, ir suformuotas jonų pluoštelis tada keliauja per magnetinį lauką, kur pagal skirtingus m/z santykius atskiriamos norimos masës ir detektuoamos Faradéjaus detektoriais. Sieros matavimams naudojami du detektoriai, sukonfiguruoti m/z: 66 ir 64, kurie atitinka ³⁴S¹⁶O₂ ir ³²S¹⁶O₂. Anglies matavimams naudojami trys detektoriai (m/z: 44, 45 ir 46), atitinkantys ¹²C¹⁶O₂, ¹³C¹⁶O₂ ir ¹³C¹⁷O¹⁶O. Naudojant trijų detektorių konfiguraciją įvertinama ¹⁷O įtaka, kuri yra automatiškai pakoreguojama pagal iš anksto nustatytus algoritmus (Assonov and Brenninkmeijer, 2003; Brand et al., 2010). Taip sukuriamas chromatograma, rodanti užfiksotą intensyvumą pagal laiką specifinëms m/z vertëms, proporcinq aptiktų jonų skaičiui (Dunn and Carter, 2018).

Stabiliųjų izotopų santykijų matavimų duomenų korekcijos

Iš pradžių IRMS matavimai suteikia neapdorotas izotopinių santykijų δ vertes, kurios yra susietos su žinomu izotopinių verčių palyginamosiomis dujomis. Siekiant užtikrinti laboratorijų rezultatų palyginamumą ir atsekamumą, išmatuotos δ reikšmës turi būti susietos su skalëmis, paremtomis tarptautiniais standartais (V-CDT – δ³⁴S matavimams ar V-PDB – δ¹³C matavimams) per kalibravimo (normalizavimo) procesą (Assonov, 2018; Ding et al., 2001). Šiame darbe visi izotopinių δ verčių rezultatai yra susieti su šiomis skalëmis. Sieros mèginiai buvo analizuojami kartu su etaloninëmis medžiagomis IAEA-

SO-5 ($\delta^{34}\text{S} = 0,5 \pm 0,2 \text{ ‰}$) ir NBS-127 ($\delta^{34}\text{S} = 20,3 \pm 0,4 \text{ ‰}$) bei darbiniais BaSO_4 standartais. Izotopinių $\delta^{13}\text{C}$ verčių matavimams buvo naudojamos etaloninės medžiagos IAEA-600 ($\delta^{13}\text{C} = -27,771 \pm 0,043 \text{ ‰}$) ir USGS24 ($\delta^{13}\text{C} = -16,05 \pm 0,04 \text{ ‰}$). Tokiu būdu, matuojant mèginius kartu su dviem etaloninėmis medžiagomis vienoje sekoje, δ skalës realizavimui galima taikyti dviejų taškų tiesinę normalizaciją (angl. *two-point linear normalization*), pagal metodiką aprašytą Dunn and Carter (2018).

Tačiau prieš atliekant δ verčių normalizaciją, būtina įsitikinti, ar pradiniam rezultatams korekтиška pritaikyti duomenų pataisas. Jei matavimų sekoje pastebimi padidėję tuščių bandinių signalai, duomenų dreifas, prasta tiesiskumas ar liekamieji atminties efektai, tuomet būtina priktaikyti duomenų korekcijas. Šios pataisos atliekamos prieš normalizaciją ir turi būti nuosekliai taikomos visoje mèginų sekoje pagal PIT (angl. *principle of identical treatment*, PIT) (Carter and Fry, 2013). Šiame tyrime buvo pastebėtas nedidelis $\delta^{34}\text{S}$ reikšmių dreifas ir, siekiant jį kompensuoti, viso sekos metu buvo reguliarais intervalais matuojamos darbinės laboratorinės BaSO_4 medžiagos.

Radioanglies matavimai

Prieš radioanglies matavimus mèginiai turi būti sugrafitizuojami. Grafitizacija atliekama naudojant automatizuotą grafitizacijos sistemą, sujungtą su elementiniu analizatoriumi (EA-AGE-3, Ionplus AG). Naudojantis metodika, aprašyta Butkus et al. (2022), su AGE-3 sistema įmanoma grafitizuoti mèginius, kurių anglies kiekis siekia vos 40 μg . EA-AGE-3 sistema leidžia atskirai sudeginti kelis vieno filtro gabalėlius, o išsiskyrusios CO_2 dujos yra surenkomos vienoje bendroje ceolito gaudyklėje. Tokiu būdu galima sudeginti mažą anglies kiekį turinčius filtro mèginius, o papildomas anglies kiekis, reikalingas grafitizacijai, pridedamas iš ^{14}C , neturinčios etaloninės medžiagos (ftalio anhidridas, PhA).

Radioanglies matavimai buvo atlikti naudojant vienos pakopos greitintuvu masių spektrometrą. Šiame darbe ^{14}C matavimai išreiškiami moderniosios anglies frakcija (f_M), kuri yra plačiai naudojama aplinkos tyrimuose (Stuiver and Polach, 1977).

Jonų koncentracijų matavimai

Vandenye tirpių sulfatų koncentracija buvo kiekybiškai įvertinta naudojant jonų chromatografinę sistemą (Dionex 2010i). Chromatografinė sistema

naudojo Ion Pac AS4A-SC kolonėlę neorganiniams anijonams atskirti. Analizės metu buvo naudojamas eluentas, sudarytas iš 1,8 mM Na₂CO₃ ir 1,7 mM NaHCO₃, ir 20 mM H₂SO₄ regenerantas. Kai kuriems bandiniams buvo taip pat išmatuotos ir jonų Mg²⁺, Ca²⁺, K⁺, NH₄⁺, Na⁺, SO₄²⁻, NO₃⁻ ir Cl⁻ koncentracijos.

Oro masių pernašos trajektorijos ir meteorologiniai parametrai

Atgalinių oro masių pernašos trajektorijos kiekvienam mēginių ēmimo laikotarpiui buvo sugeneruotos naudojant hibridinį vienos dalelės modelį HYSPLIT (NOAA) (Stein et al., 2015). Modelyje buvo taikomi šie parametrai: trajektorijos trukmė 48 val., naujos trajektorijos modeliuotos apytiksliai kas 8 val., 50, 500 ir 1500 metrų virš žemės lygio.

Skirtingų krypčių oro masės pasižymi skirtingais užterštumo lygiais ir šiame darbe šios kryptys buvo apibūdintos pagal Davulienė et al. (2021). Šiaurės vakarų oro masės, atkeliaujančios iš Skandinavijos šalių, laikomos santykinai švariomis. Vakarinės krypties oro masės (iš Šiaurės Lenkijos, Vokietijos) laikomos vidutiniškai užterštomis, o pietvakarių (Pietų Lenkija) ir pietų (Baltarusija, Ukraina) krypties oro masės yra labiau užterštos. Šiaurės (Latvija, Estija) ir rytų (Baltarusija, Rusija) krypties oro masės laikomos kaip vidutiniškai užterštos.

Meteorologiniai parametrai, kaip maišymosi sluoksnio aukštis, vėjo greitis, santykinė drėgmė ir aplinkos temperatūra, buvo paimti iš viešai pasiekiamos NOAA duomenų bazės (“NOAA Climate Data Online (CDO),” 2021).

Sieros oksidacijos kelių indėlių vertinimas

Naudojant stabiliųjų izotopų analizės metodus galima įvertinti skirtingų SO₂ oksidacijos kelių indėli, pasinaudojant surinktu PM₁ ir SO₂ mēginių matavimais. Skirtingų SO₂ oksidacijos kelių indėlis gali būti įvertintas analizuojant oksidacijos sukeliamą frakcionaciją, nes skirtingi oksidacijos keliai nulemia specifines δ³⁴S vertes PM₁ sulfatuose. Taip pat svarbu įvertinti SO₂ į SO₄²⁻ formacijos spartą arba sieros oksidacijos santykį (ang. *sulfur oxidation ratio*, SOR) (Mukai et al., 2001):

$$SOR = \frac{[SO_4^{2-}]}{[SO_4^{2-}] + [SO_2]} \quad (4)$$

kur $[SO_4^{2-}]$ yra sulfatų jonų molinė koncentracija, o $[SO_2]$ sieros dioksido molinė koncentracija.

Siekiant įvertinti skirtinį SO_2 oksidacijos kelių indėlių, pirmiausia reikia nustatyti $\delta^{34}S_{\text{emission}}$ reikšmes, kurios atspindi pradines vietinių taršos šaltinių emijos $\delta^{34}S$ reikšmes ($SOR = 0$). Naudojant išmatuotomos $\delta^{34}S_{SO_2}$ vertėmis, galime taip įvertinti $\delta^{34}S_{\text{emission}}$ reikšmes (Fan et al., 2020; Li et al., 2020):

$$\delta^{34}S_{\text{emission}} = \delta^{34}S_{SO_2} \times (1 - SOR) + \delta^{34}S_{PM1} \times SOR \quad (5)$$

kur $\delta^{34}S_{SO_2}$ ir $\delta^{34}S_{PM1}$ yra surinktų SO_2 ir PM_1 sulfatų izotopinės vertės.

Toliau turime įverinti frakcionacijos faktorių $\varepsilon_{g \rightarrow p}$:

$$\delta^{34}S_{SO_2} = \delta^{34}S_{\text{emission}} + \ln(1 - SOR) \times \varepsilon_{g \rightarrow p} \quad (6)$$

Ir galiausiai galime įvertinti skirtinį SO_2 oksidacijos kelių indėlių, naudojant šią maišymosi lygtį:

$$\varepsilon_{g \rightarrow p} = \varepsilon_{OH} \times f_{OH} + \varepsilon_{TMI} \times f_{TMI} + \varepsilon_{H_2O_2} \times f_{H_2O_2} \quad (7)$$

kur ε_{OH} , ε_{TMI} ir $\varepsilon_{H_2O_2}$ yra atitinkami OH, TMI ir H_2O_2 oksidacijos kelių frakcionacijos faktoriai. O f_{OH} , f_{TMI} ir $f_{H_2O_2}$ yra skirtinį OH, TMI ir H_2O_2 oksidacijos kelių indėliai.

Tačiau, f_{OH} indėlis buvo įvertintas atskirai naudojant šia formule (Harris et al., 2013a):

$$f_{OH} = SOR \times 0.27 \times \frac{[OH]}{[OH]_m} \times \frac{24}{HL} \quad (8)$$

kur 0.27 vidutinis metinis sulfatų produkcijos indėlis per OH oksidaciją (Sofen et al., 2011). $[OH]/[OH]_m$ santykis apibūdina sezoniinius OH koncentracijos svyrapimius pagal pasaulinį troposferinį OH koncentracijos paskirstymo modelį ACM (angl. *Global Change Research Program Atmospheric Chemistry Model* (Bahm and Khalil, 2004)), naudojant Lietuvai tinkančias vidutines metines koncentracijų vertes. Santykis 24/HL atspindi saulės šviesos valandas dienoje kaip santykį. Taigi, naudojantis 8 lygtimi, OH oksidacijos kelio indėlis buvo pašalintas iš 7 lygties atėmus $\varepsilon_{OH} \times f_{OH}$ narį.

Ivykių aprašymas

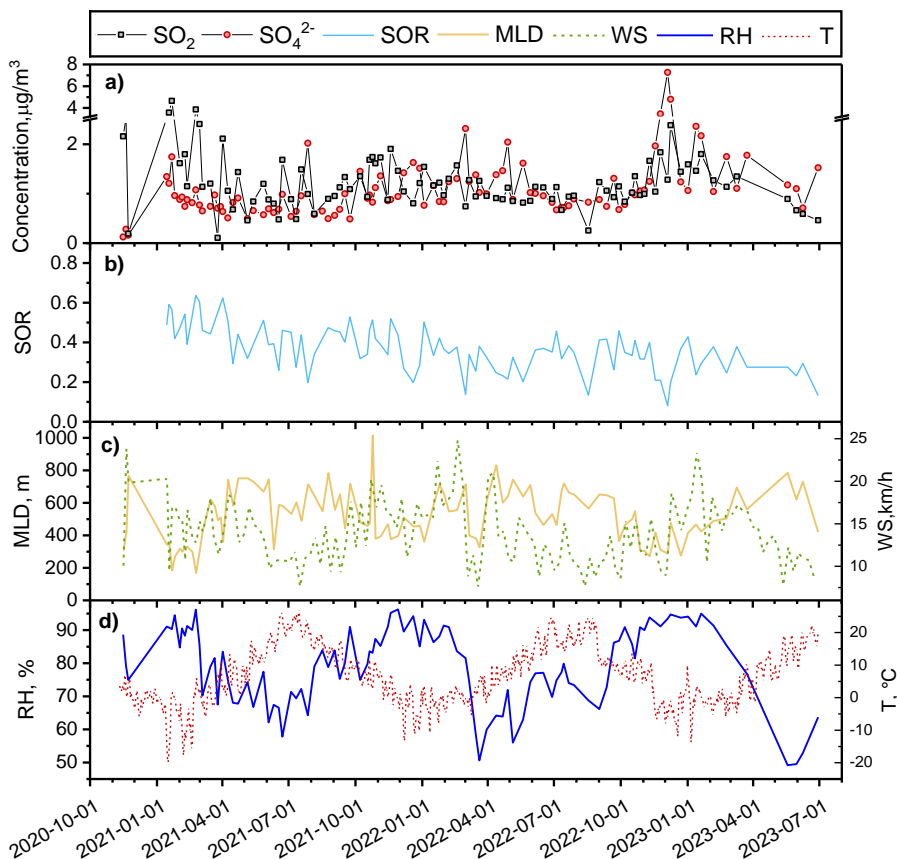
Mėginių ėmimo laikotarpis (nuo 2020 m. lapkričio 11 d. iki 2023 m. birželio 30 d.) apėmė kelis reikšmingus įvykius, kurie galėjo daryti įtaką vietiniams oro taršos lygiams Vilniuje. Vienas iš tokų įvykių buvo koronaviruso ligos (COVID-19) protrūkis. Lietuvoje pirmasis COVID-19 atvejis oficialiai užfiksuotas 2020 m. vasario 28 d. Atsižvelgiant į sparčiai augantį uzsikrėtusiuju žmonių skaičių, pirmasis karantinas buvo paskelbtas 2020 m. kovo 16 d. ir tęsėsi iki birželio 17 d. Tačiau vasarą COVID-19 atvejų skaičiaus vėl pradėjo augti ir 2020 m. lapkričio 4 d. buvo įvestas antrasis karantinas. Jo metu Lietuvoje buvo taikomos įvairios priemonės siekiant sulėtinti viruso plitimą. Buvo uždaryta daugelis viešųjų vietų (pvz., restoranai, kavinės, barai), uždrausti susibūrimai ir buvo rekomenduojama vengti nebūtinų kelionių. Mažėjant atvejų skaičiui, karantinas buvo atšauktas 2021 m. liepos 1 d. Pasauliniu mastu COVID-19 visuotiniai karantinai reikšmingai paveikė aerozolių koncentracijas ir jų taršos šaltinius, tačiau šių pokyčių mastas skyrėsi skirtinguose pasaulio regionuose (Rodríguez-Urrego and Rodríguez-Urrego, 2020).

Antrasis reikšmingas įvykis bandinių rinkimo laikotarpiu buvo mažasiero (0,9 %) mazuto (angl. *heavy fuel oil*, HFO) naudojimas Vilniaus šiluminėje elektrinėje (angl. *thermal power station*, TPS) šaltojo sezono metu 2022–2023 metais. Sunkusis mazutas buvo naudojamas nuo 2022 m. lapkričio 9 d. iki 2023 m. kovo pabaigos, didžiąja dalimi pakeitęs prieš tai naudotas gamtines dujas. 2022 – 2023 metų laikotarpiu mazutas sudarė 36 % Vilniaus TPS viso naudojamo kuro, o biokuras (biomasė), gamtinės dujos ir dyzelinas atitinkamai sudarė 56 %, 7 % ir 1 % (AB Vilniaus šilumos tinklai, 2023). Ankstesniu 2021 – 2022 metų laikotarpiu kuro mišinį elektrinėje sudarė tik biokuras (61 %) ir gamtinės dujos (39 %) (AB Vilniaus šilumos tinklai, 2021).

REZULTATAI

Viso bandinių émimo laiktorapio rezultatai

Sezoninė variacija savaitinių SO_2 ir sulfatų jonų koncentracijų vidurkių pateikta 2 pav.(a), apimanti visą 2020 – 2023 m. mëginių émimo laikotarpi. 2 pav.(b) taip pat parodytas sieros oksidacijos santykis (SOR). Véjo greičio (WS) savaitiniai vidurkiai ir maišymosi sluoksnio aukštis (MLD) pateikti 2 pav.(c). Santykiné drégmë (RH) ir temperatûros (T) kaita pavaizduota 2 pav.(d).

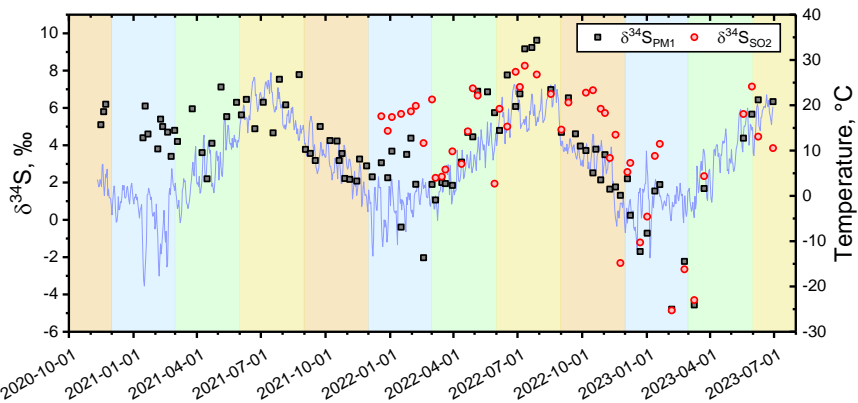


2 pav. Išmatuotos SO_4^{2-} koncentracijos ir monitoring duomenys periodo nuo 2020 m. lapkričio 11 d. iki 2023 m. birželio 30 d. Grafike pateikta: a) SO_2 and SO_4^{2-} koncentracijos; b) sieros oksidacijos santykis (SOR); c) véjo greitis (WS) ir maišymosi sluoksnio aukštis (MLD); d) santykiné drégmë (RH) ir aplinkos temperatûra (T).

Per visą matavimų laikotarpį SO₂ koncentracijos svyravo nuo 0,49 iki 7,27 µg/m³ su vidutine $1,16 \pm 0,85$ µg/m³ verte. Tuo pačiu metu SO₄²⁻ koncentracijos svyravo nuo 0,11 iki 2,39 µg/m³ su $1,19 \pm 0,52$ µg/m³ vidurkiu. Silpna, bet statistiškai reikšminga koreliacija tarp SO₂ ir SO₄²⁻ ($r = 0,25$, $p < 0,05$) rodo, kad SO₄²⁻ koncentracijų pokyčiai negali būti paaškinti vien tik SO₂ koncentracijų svyravimais atmosferoje. Tai rodo, jog SO₂ ir sulfatų šaltiniai atmosferoje yra skirtingi. Todėl yra vertinga šiam laikotarpui taikyti izotopinę analizę šių šaltinių atskyrimui ir identifikavimui.

Sulfatų jonų koncentracijos pasižymėjo vidutine koreliacija su temperatūra ($r = -0,46$, $p < 0,05$), nurodant galimą cheminių reakcijų priklausomybę nuo temperatūros arba vyraujančių šaltinių emisijų pokyčius. Per visą tyrimo laikotarpį vėjo greitis svyravo nuo 7,5 km/h iki 24,8 km/h (vidurukis – 14,0 km/h). Žiemos mėnesiais vėjo greitis buvo didesnis – vidutiniškai 16,6 km/h, o vasarą mažesnis – vidutiniškai 11,1 km/h. Tačiau vėjo greičio kaita neturėjo reikšmingo poveikio nei SO₂, nei SO₄²⁻ koncentracijoms. Taip pat šio tyrimo metu MLD svyravo nuo 167,2 m iki 1015,2 m, vidutiniškai siekdamas 519,5 m. MLD silpnai koreliavo su SO₂ koncentracijomis ($r = -0,22$, $p < 0,05$), o SO₄²⁻ koncentracijos parodė stipresnę priklausomybę nuo MLD ($r = -0,52$, $p < 0,05$), rodydamos didesnį MLD poveikį dalelių kaupimuisi. Galiausiai, RH parodė vidutinę koreliaciją su SO₄²⁻ koncentracijomis ($r = 0,45$, $p < 0,05$), kadangi aukštėsnė santykinė drėgmė skatina antrinių dalelių formavimąsi, jų higroskopinį augimą ir skystojoje fazėje vykstančių reakcijų spartos didėjimą.

Išmatuotų izotopinių verčių kitimas SO₂ ir PM₁ sulfatuose yra pavaizduota 3 pav., kartu su vidutinių (24 val. vidurkis) temperatūrų kitimu.



3 pav. Išmatuotų SO₂ dujų ($\delta^{34}\text{S}_{\text{SO}_2}$) ir PM₁ sulfatų ($\delta^{34}\text{S}_{\text{PM}1}$) $\delta^{34}\text{S}$ vertės visu bandinių įmimo laikotarpiu nuo 2020 m. lapkričio 11 d. iki 2023 m. birželio 30 d. Dienos vidutinė temperatūra yra pavaizduota kaip mėlyna ištisinė linija. Duomenys pateikiami skirtingais metų laikais: mėlyna dalis žymi žiemą, žalia – pavasarį, geltona – vasarą, o ruda – rudenį.

Izotopinės SO₂ vertės kito plačiame intervale nuo -4,85 ‰ iki 9,41 ‰ (vidurkis $-4,38 \pm 3,12 \text{ ‰}$). Tuo metu PM₁ sulfatų $\delta^{34}\text{S}_{\text{PM}1}$ vertės svyraavo nuo -4,79 ‰ iki 9,63 ‰, (vidurkis $-3,88 \pm 2,62 \text{ ‰}$). Išmatuotos ribinės $\delta^{34}\text{S}_{\text{SO}_2}$ ir $\delta^{34}\text{S}_{\text{PM}1}$ yra labai artimos ir patenka į tipinio $\delta^{34}\text{S}$ matavimų tikslumo ribas ($<0,10 \text{ ‰}$), kas rodo, jog šios ekstremumų vertės atspindi skirtingų dominuojančių sieros taršos šaltinių įtaką skirtingais metų laikas (žiemą – vasarą). Be to, $\delta^{34}\text{S}$ vertės tarp SO₂ ir PM₁ sulfatų pasižymėjo reikšminga teigama koreliacija ($r = 0,77$, $p < 0,05$), rodančia, jog SO₂ emisijos ir sulfatų formavimosi procesai yra glaudžiai tarpusavyje susiję.

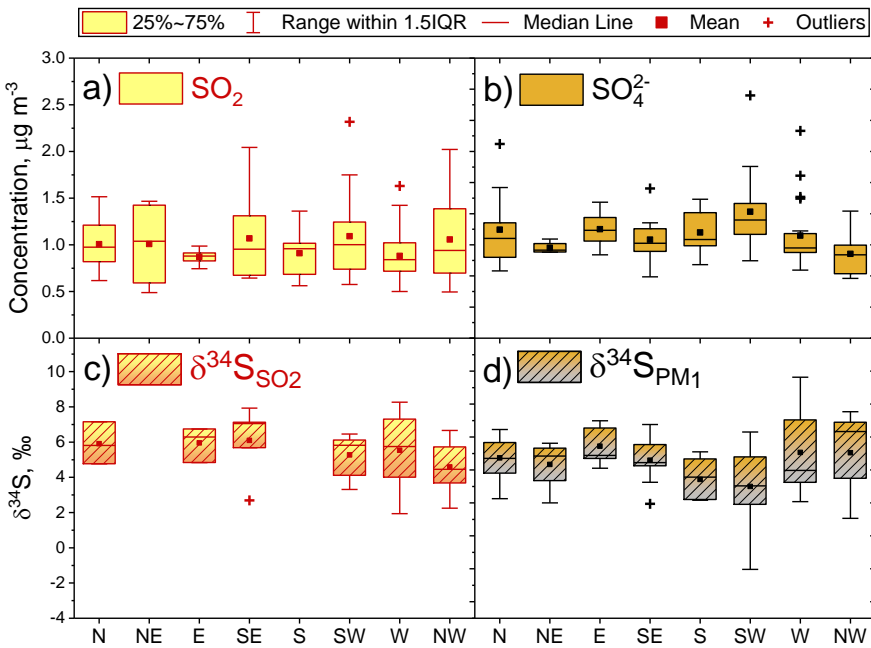
Vis dėlto $\delta^{34}\text{S}$ vertės rodė statistiškai prasmingas, tačiau žemos koreliacijas su daugeliu meteorologinių parametrų. Vidutiniškai aukšta teigama koreliacija buvo užfiksuota tik su aplinkos temperatūra (SO₂: $r = 0,57$, $p < 0,05$; SO₄²⁻: $r = 0,51$, $p < 0,05$). SOR pasižymėjo silpnomis koreliacijomis su $\delta^{34}\text{S}_{\text{SO}_2}$ ir $\delta^{34}\text{S}_{\text{PM}1}$ vertėmis (SO₂: $r = 0,06$, $p < 0,05$; SO₄²⁻: $r = 0,08$, $p < 0,05$), kas rodo, jog vietiniai taršos šaltiniai turėjo mažesnę įtaką išmatuotoms $\delta^{34}\text{S}_{\text{PM}1}$ vertėms ir jos labiau priklausė nuo tolimųjų taršos šaltinių. Taip pat santykini drėgmė rodė aukštesnę koreliaciją su $\delta^{34}\text{S}_{\text{PM}1}$ vertėmis (SO₄²⁻: $r = 0,41$, $p < 0,05$), pabrėžiant skystosios fazės reakcijų svarbą sulfatų formacijai aerosoliuose.

Tolimosios oro masių pernašos įtaka

Nuo 1980-ųjų Lietuvoje SO₂ koncentracijos rodo pastovų mažėjimą, o 2008 metais atmosferinių PM SO₄²⁻ koncentracijos viršijo SO₂ emisijų lygius, nurodydamos didėjančią tolimųjų sieros taršos šaltinių įtaką (Davuliene et al., 2021). Todėl būtina įvertinti tolimųjų sieros šaltinių emisijų pernašos poveikį oro kokybei Vilniuje.

SO₂ ir SO₄²⁻ koncentracijų priklausomybė nuo skirtingų oro masių pernašos kilmės krypcijų pavaizduota 4 pav.(a, b). Mėginiai, surinkti mazuto naudojimo laikotarpiu, buvo neįtraukti į oro masių analizę dėl tikėtinos išaugusios vietinių taršos šaltinių įtakos. Šio tyrimo metu SO₂ koncentracijos, susijusios su skirtingomis oro masių kryptimis, išliko santykinai stabilios ir kito siaurame intervale nuo $0,87 \pm 0,07 \text{ } \mu\text{g}/\text{m}^3$ iki $1,08 \pm 0,42 \text{ } \mu\text{g}/\text{m}^3$ (4 pav.(a)). Pažymėtina, jog nebuvo užfiksotas pastebimas SO₂ koncentracijų padidėjimas iš šiaurės vakarų krypties, kur yra pagrindiniai sieros taršos šaltiniai Lietuvoje, išskaitant trąšų gamyklą Kėdainiuose (~100 km atstumu) ir naftos perdirlimo gamyklą Mažeikiuose (~270 km atstumu) (European Environment Agency, 2023). Taip pat, atsižvelgiant į trumpą SO₂ atmosferinį gyvavimo laiką (apie 12 valandų) (Lee ir kt., 2011), galime teigti, jog šiaurės vakarų krypties emisijų poveikis buvo minimalus, o Vilniuje surinkti SO₂ mėginiai daugiausia atspindėjo vietinių šaltinių emisijas.

Tuo metu SO₄²⁻ koncentracijos kito platesniame intervale – nuo $0,86 \pm 0,32 \text{ } \mu\text{g}/\text{m}^3$ iki $1,53 \pm 0,63 \text{ } \mu\text{g}/\text{m}^3$, o aukščiausios koncentracijos buvo užfiksuotos pietvakarių kryptimi (4 pav.(b)). Oro masės, atkeliaujančios iš pietvakarių, dažnai keliauja pro pietinę Lenkijos dalį, kur akmens anglis yra plačiai naudojama energijos gamybai ir šildymui (Bertelsen and Mathiesen, 2020; Igliński et al., 2015). Taip pat SO₄²⁻ koncentracijų padidėjimas nebuvo stebimas oro masėse iš šiaurės vakarų krypties, kas leidžia teigti, jog sieros emisijos iš šių pramoninių šaltinių turėjo minimalų poveikį oro kokybei Vilniuje.



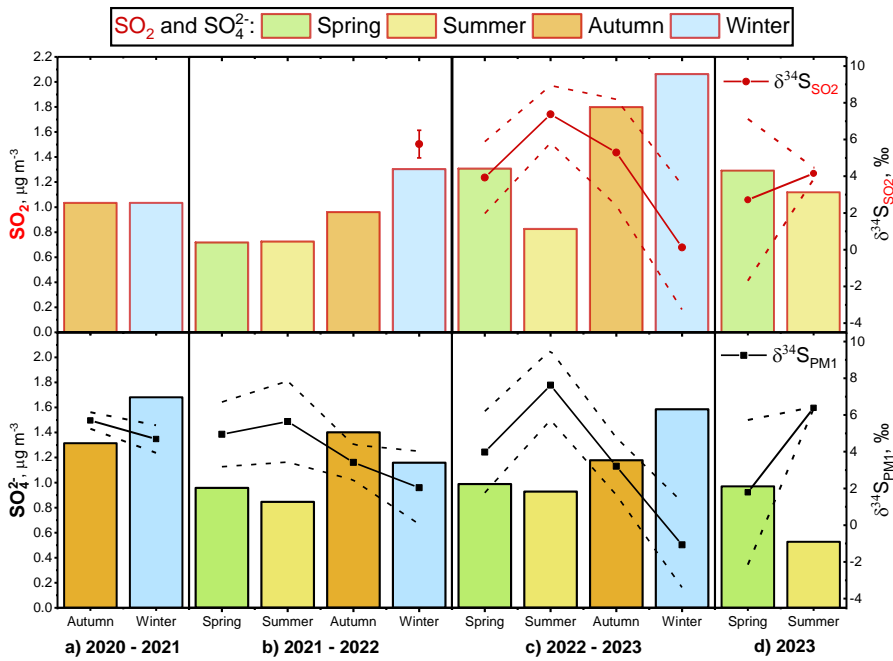
4 pav. SO_2 (a) ir SO_4^{2-} (b) koncentracijų pasiskirstymas pagal skirtinges oro masių kilmes kartu su atitinkamomis $\delta^{34}\text{S}_{\text{SO}_2}$ (c) ir $\delta^{34}\text{S}_{\text{PM}1}$ (d) vertėmis.

$\delta^{34}\text{S}_{\text{SO}_2}$ vertės skirtiniose oro masių kryptyse svyravo nuo $3,5 \pm 1,2 \text{ ‰}$ iki $6,1 \pm 1,7 \text{ ‰}$ (4 pav.(c)). Tačiau $\delta^{34}\text{S}_{\text{SO}_2}$ vertės nepasižėmėjo aiškia priklausomybe nuo oro masių krypčių ir tai byloja, jog SO_2 labiau atspindi vietinių taršos šaltinių emisijų vertes. Priešingai, $\delta^{34}\text{S}_{\text{PM}1}$ vertės pasižymėjo didesne izotopinių verčių kaita priklausomai nuo oro masių kilmės, ir $\delta^{34}\text{S}_{\text{PM}1}$ vertės svyravo nuo $3,0 \pm 2,2 \text{ ‰}$ iki $5,4 \pm 1,0 \text{ ‰}$ (4 pav.(d)). Pietų ir pietvakarių kryptys pasižymėjo žemiausiomis vidutinėmis $\delta^{34}\text{S}_{\text{PM}1}$ vertėmis – atitinkamai $3,4 \pm 1,1 \text{ ‰}$ ir $3,0 \pm 2,2 \text{ ‰}$. Būtent pietvakarių kryptyje buvo užfiksuotos žemiausios $\delta^{34}\text{S}_{\text{PM}1}$ vertės viso eksperimento metu (neįtraukiant HFO naudojimo laikotarpio) ir tai nurodo oro masių, atkeliaujančių iš pietų Lenkijos, reikšmingą įtaką oro taršai Vilniuje. Taigi išmatuotos $\delta^{34}\text{S}_{\text{SO}_2}$ vertės labiau atspindėjo vietinių taršos šaltinių SO_2 emisijas, o $\delta^{34}\text{S}_{\text{PM}1}$ vertės buvo glaudžiau susijusios su tolimaja sulfatinių aerozolių pernaša.

Koncentracijų ir izotopinių verčių sezoniškumas

Sezoninė SO₂ ir SO₄²⁻ koncentracijų kaita su atitinkamais δ³⁴S_{SO₂} ir δ³⁴S_{PM₁} verčių pasiskirstymais pateikiama 5 pav. Pirmojo segmento metu (5 pav.(a)) Lietuvoje nuo 2020 m. lapkričio 7 d. buvo įvestas antrasis nacionalinis karantinas. Kitas laikotarpis, apimantis 2021 – 2022 metus (5 pav.(b)), pasižymėjo karantino apribojimų švelninimu, kurie buvo visiškai panaikinti 2021 m. liepos 1 d. Kitas 2022 – 2023 m. laikotarpis (5 pav.(c)) yra išskirtinis dėl mazuto naudojimo Vilniaus TPS šildymo sezono metu. HFO buvo naudojamas nuo 2022 m. lapkričio 9 d. iki 2023 m. kovo 31 d. O paskutinis 2023 m. segmentas (5 pav.(d)) žymi HFO naudojimo pabaigą Vilniaus TPS.

Eksperimento metu buvo pastebėta ryški SO₂ ir SO₄²⁻ koncentracijų variacija skirtingais metų laikais. Vasaros mėnesiais (birželis, liepa, rugpjūtis) buvo stebima sumažėję koncentracijų lygai ir SO₂ koncentracijų vidurkis buvo lygus $0.83 \pm 0.33 \mu\text{g}/\text{m}^3$, o SO₄²⁻ – $0.89 \pm 0.33 \mu\text{g}/\text{m}^3$. Žiemos mėnesiais (gruodis, sausis, vasaris) buvo stebimos išaugusios koncentracijų vertės, vidutiniškai siekiančios $1.35 \pm 0.80 \mu\text{g}/\text{m}^3$ (SO₂) ir $1.50 \pm 0.65 \mu\text{g}/\text{m}^3$ (SO₄²⁻). Svarbi tendencija buvo stebima per 2022 – 2023 metų laikotarpį (5 pav.(c)), kuomet SO₂ koncentracijos žymiai išaugo rudens (vidurkis – $1.80 \mu\text{g}/\text{m}^3$) ir žiemos (vidurkis – $2.06 \mu\text{g}/\text{m}^3$) mėnesiais, viršydamos SO₄²⁻ koncentracijas, kurios rudens metu siekė $1.18 \mu\text{g}/\text{m}^3$, o žiemą – $1.59 \mu\text{g}/\text{m}^3$. Nors SO₄²⁻ koncentracijos buvo žemesnės nei SO₂, jos 2022 – 2023 m. žiemą padidėjo 37 % lyginant su ankstesne 2021 – 2022 m. žiema. PM₁ sulfatų taršos padidėjimą, tikėtina, lėmė SO₂ emisijų augimas, susijęs su mazuto naudojimu Vilniaus TPS.



5 pav. Sezoninė SO_2 , SO_4^{2-} koncentracijų ir $\delta^{34}\text{S}_{\text{SO}2}$, $\delta^{34}\text{S}_{\text{PM}1}$ verčių kaita skirtinių laikotarpiais: a) 2020 – 2021; b) 2021 – 2022; c) 2022 – 2023 ir d) 2023.

Ekperimento metu SO_2 ir PM_1 sulfatų izotopinės vertės taip pat pasižymėjo ryškiomis sezoniškėmis tendencijomis (5 pav.), kas rodo, jog sieros taršos šaltinių indėliai keičiasi skirtinių metų laikais. Tačiau sulfate $\delta^{34}\text{S}$ vertėms įtaką daro ir SO_2 oksidacijos kelių pasiskirstymo kaita (Harris et al., 2013a; Mukai et al., 2001; Novák et al., 2001), frakcionacijos faktorių temperatūrinę priklausomybę (Caron et al., 1986; Harris et al., 2013a) ir tolimuju taršos šaltinių emisijų pernaša. Šiame tyrime sezoniiniai $\delta^{34}\text{S}$ verčių pokyčiai skiriasi nuo kitų tyrimų, atliktų kituose pasaulyje regionuose, išskaitant Rytų Aziją (Han et al., 2016; Kawamura et al., 2001; Lin et al., 2022; Mukai et al., 2001), Šiaurės Ameriką (Nriagu and Coker, 1978; Saltzman et al., 1983) ir kitus Europos regionus (Mayer et al., 1995), kur paprastai fiksuojama aukštos $\delta^{34}\text{S}$ vertės žiemą ir žemos vasarą. Šiame tyrime sieros junginiai buvo labiau izotopiškai praturtinti vasaros mėnesiais ($\delta^{34}\text{S}_{\text{SO}2} = 6.5 \pm 1.7 \text{ ‰}$; $\delta^{34}\text{S}_{\text{PM}1} = 6.5 \pm 1.5 \text{ ‰}$), o izotopiškai lengvesnės frakcijos buvo sutinkamos žiemą ($\delta^{34}\text{S}_{\text{SO}2} = 3.1 \pm 3.4 \text{ ‰}$; $\delta^{34}\text{S}_{\text{PM}1} = 2.3 \pm 2.7 \text{ ‰}$). Panašios $\delta^{34}\text{S}$ verčių sezoniškės tendencijos (žemos $\delta^{34}\text{S}$ vertės žiemą, aukštos $\delta^{34}\text{S}$ vertės vasarą) buvo anksčiau užfiksuotos tik viename tyrime Čekijoje (Novák et al., 2001). Tai

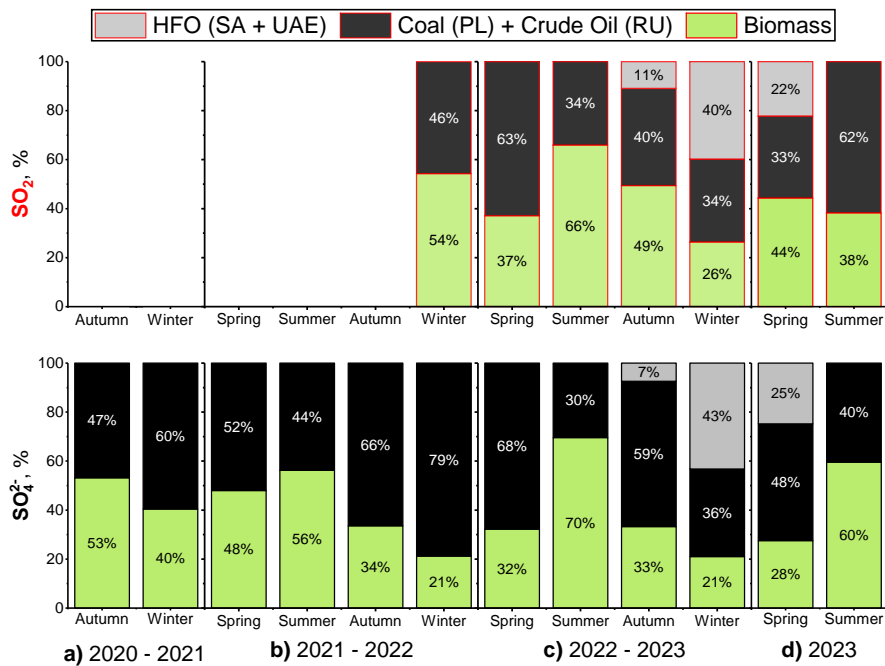
rodo, jog atmosferinių sieros junginių dinamika Vilniaus miesto aplinkoje yra kompleksinė ir papildomai priklauso nuo vietinių ir kaimyninių šalių emisijų, kurių santykinis indėlis keičiasi per metus.

Per visa eksperimento laikotarpį keli periodai buvo išskirtiniai. Vienas iš jų buvo stebimas 2021 – 2022 metais, kuomet žiemos metu buvo fiksuoamos pastebimai žemos vidutinės $\delta^{34}\text{S}_{\text{PM}1}$ vertės (2.1 ‰), o $\delta^{34}\text{S}_{\text{SO}_2}$ vertės vidutiniškai buvo žymiai aukštesnės (5.5 ‰). Tai rodo skirtingus sieros taršos šaltinių indėlius SO_2 ir PM_1 sulfatams galimai dėl santykinio skirtumo tarp vietinių ir tolimosios pernašos šaltinių.

Kitas svarbus periodas buvo stebimas 2022 – 2023 m. laikotarpiu, kuomet vidutinės žiemos $\delta^{34}\text{S}_{\text{PM}1}$ vertės buvo 2.9 ‰ žemesnės (lygios 0.8 ‰), lyginant su 2021 – 2022 m. laikotarpiu, o $\delta^{34}\text{S}_{\text{SO}_2}$ vertės buvo 5.2 ‰ žemesnės (lygios 0.3 ‰). Taip pat laikotarpiu nuo 2023 m. sausio 20 d. iki 2023 m. vasario 6 d. buvo užfiksuotos išskirtinai žemos vidutinės izotopinės SO_2 ir PM_1 sulfatų vertės, siekiančios net $\delta^{34}\text{S}_{\text{SO}_2} = -4.85 \text{ ‰}$ ir $\delta^{34}\text{S}_{\text{PM}1} = -4.79 \text{ ‰}$. Šios užfiksuotos vertės negali būti paaškinamos įprastų sieros taršos šaltinių (biomasės ir akmens anglies deginimo) Lietuvoje $\delta^{34}\text{S}$ vertėmis. Remiantis įvairių natūralių ir antropogeninių šaltinių $\delta^{34}\text{S}$ vertėmis, tai galėjo sukelti tik antropogeninės naftos produktų SO_2 emisijos, būtent mazuto iš Saudo Arabijos ($\delta^{34}\text{S}_{\text{SO}_2}$: -8.8 iki -0.7 ‰) arba Jungtinių Arabų Emiratų ($\delta^{34}\text{S}_{\text{SO}_2}$: -10.3 iki -4.3 ‰) (Becker and Hirner, 1998; Dasari and Widory, 2024). Šiuo laikotarpiu išmatuotos ypač žemos $\delta^{34}\text{S}_{\text{SO}_2}$ ir $\delta^{34}\text{S}_{\text{PM}1}$ vertės ir kartu užfiksuotos išaugusios SO_2 ir SO_4^{2-} koncentracijos rodo sustiprėjusią vietinių šaltinių įtaką, kai mazuto emisijos iš Vilniaus TPS galimai nusvėrė akmens anglies deginimo emisijų įtaką.

Sieros šaltinių skirstymas

Siekiant įvertinti besikeičiančių sieros taršos šaltinių įtaką, buvo kiekybiškai apskaičiuoti santykiniai indėliai tiek SO_2 , tiek PM_1 sulfatų frakcijų, pritaikant Bajeso statistinį modelį FRUITS. Viso bandinių rinkimo laikotarpio sezoniinė šaltinių indėlių kaita pateikta 6 pav.



6 pav. Sezoninė SO_2 and $\text{PM}_1 \text{SO}_4^{2-}$ taršos šaltinių indelių kaita: a) 2020 – 2021 m.; b) 2021 – 2022 m.; c) 2022 – 2023 m. ir d) 2023 m. laikotarpiais. Žalia spalva žymi biomasės deginimo indelius, juoda – lenkiškos (PL) akmens anglies deginimo emisijas ir rusiškos kilmės (RU) naftos deginimo emisijų indelius, pilka – Saudo Arabijos (SA) ir/arba Jungtinių Arabų Emyratų (UAE) kilmės mazuto emisijų indelius.

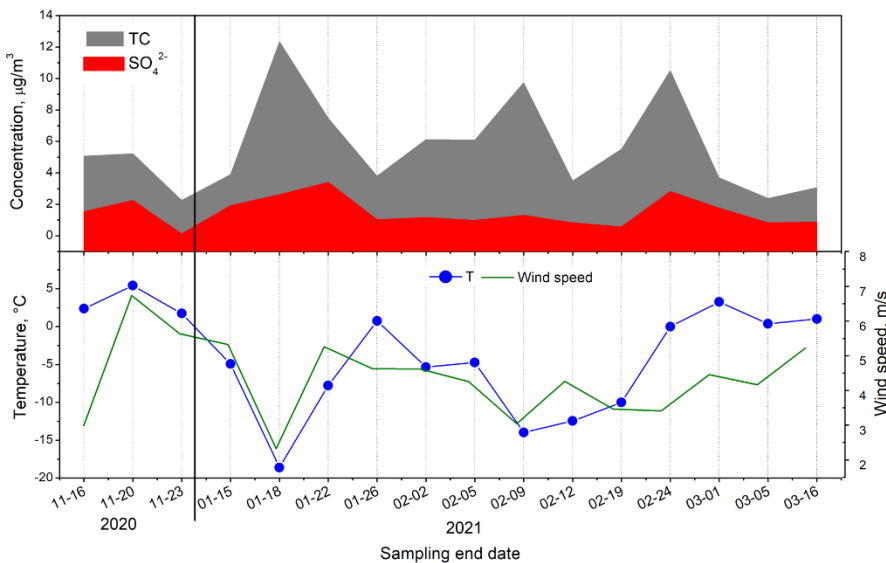
6 pv. matome, jog tiek SO_2 ir PM_1 sulfatų šaltinių indeliai rodė panašią sezonišką kaitą. Biomasės deginimo emisijų indėlis žiemą buvo mažesnis (vidutiniškai $28 \pm 14\%$), o akmens anglies deginimo produktų – didesnis (vidutiniškai $61 \pm 20\%$). Šaltuoju metų laikotarpiu tiek biomasės deginimo emisijos, susijusios su buitiniu šildymu, tiek ir elektros energijos gamybos emisijos padidėja. Tai lemia aukštėnės SO_2 emisijas žiemą, lyginant su vasara. Iprastai akmens anglies deginimo emisijos yra vyraujantis sieros taršos šaltinis žiemos metu Vilniuje (vidurkis $61 \pm 20\%$), pranokstantis vietinių biomasės deginimo šaltinių emisijas. Tai daugiausia lemia didelės sieros emisijos iš kaimyninių šalių, pvz., Lenkijos (2021 m. Lenkijos SO_2 emisijos buvo 35 kartus aukštėnės Lietuvos (European Environment Agency, 2023)). Vasaros mėnesiais, kai bendras sieros emisijų kiekis sumažėja, biomasės deginimo emisijos tampa dominuojančiu atmosferinės sieros šaltiniu, sudarančiu vidutiniškai $63 \pm 16\%$, o akmens anglies deginimo emisijų dalis

sumažėja iki $37 \pm 16\%$. Nors gyvenamųjų būstų šildymo emisijos vasarą yra žemos, kiti šaltiniai, tokie kaip ūkinės paskirties žemų deginimai ir miškų gaisrai, tampa svarbiu sieros šaltiniu (Rickly et al., 2022). Taip pat Vilniaus šiluminė elektrinė ir vasaros mėnesiais toliau naudoja biomasę, taip sudarydamą stabilų biomasės deginimo emisijų foną visus metus (Vilniaus šilumos tinklai, 2021; Vilniaus šilumos tinklai, 2022). Per visą bandinių rinkimo laikotarpį biomasės deginimo emisijų indėlis dujiname SO₂ buvo didesnis (vidutiniškai 11 % daugiau) nei sulfatų frakcijoje ir tai atspindi vietinių taršos šaltinių įtaką.

Matome, jog iki 2022 metų biomasės deginimas bei anglies deginimo ir naftos produktų emisijos buvo pagrindiniai sieros taršos šaltiniai Vilniuje žiemos mėnesiais, sudarantys atitinkamai $30 \pm 16\%$ ir $70 \pm 16\%$. Tačiau nuo 2022 m. lapkričio 9 d. Vilniaus šiluminėje elektrinėje buvo pradėta naudoti mazutras. 2022 – 2023 m. žiemą HFO emisijos reikšmingai paveikė Vilniaus miesto oro kokybę ir sudarė $40 \pm 17\%$ SO₂ bei $40 \pm 13\%$ PM₁ sulfatų frakcijose. Šiuo laikotarpiu vietinės emisijos tapo vyraujančios tiek dujinės, tiek dalelinės sieros taršos šaltiniai Vilniuje.

Karantino sąlygų poveikis PM₁ emisijoms

Šiame skyriuje pateikiama PM₁ bandinių kompleksinė anglies ir sieros izotopų analizė (¹⁴C, ¹³C ir ³⁴S). Bandiniai rinkti nuo 2020 m. sausio 11 d. iki 2021 m. kovo 16 d, siekiant atskleisti antrojo COVID-19 karantino poveikį Lietuvos taršos šaltinių emisijoms. Šio periodo metu visos anglies (angl. *total carbon*, TC) koncentracijos svyrravo plačiame intervale nuo 2.4 µg/m³ iki 12.4 µg/m³, su vidutine $5.7 \pm 3.0\text{ }\mu\text{g}/\text{m}^3$ verte (7 pav.). Buvo pastebėta reikšminga atvirkštinė koreliacija tarp TC koncentracijų ir aplinkos temperatūros ($r = -0.60$, $p < 0.05$). Tyrimas, atliktas Vilniuje 2014 – 2015 m., parodė šiek tiek mažesnes TC koncentracijas, kurios vidutiniškai siekė $4.5\text{ }\mu\text{g}/\text{m}^3$ (Garbarienė et al., 2016). Pandemijos metu sumažėjusias transporto emisijas galėjo nusverti suintensyvėjusios emisijos iš elektros/šilumos gamybos ir namų šildymo emisijos.



7 pav. TC (pilka sritis) ir SO_4^{2-} (raudona sritis) koncentracijos PM_1 dalelėse, surinktose nuo 2020 m. lapkričio 11 d. iki 2021 m. kovo 16 d. Taip pat paveikslėlyje pateikta vidutinė temperatūra (mėlyna linija) ir vėjo greitis (žalia linija).

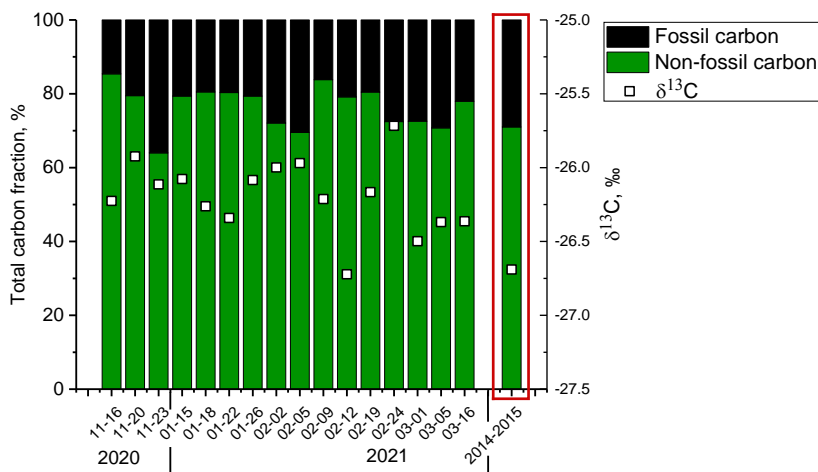
Šiuo laikotarpiu sulfatų jonų koncentracijos svyravo nuo $0,1 \mu\text{g}/\text{m}^3$ iki $3,4 \mu\text{g}/\text{m}^3$, o vidurkis siekė $1,5 \pm 0,9 \mu\text{g}/\text{m}^3$. Silpna koreliacija tarp SO_4^{2-} koncentracijų ir temperatūros ($r = -0,12$, $p < 0,05$) rodo minimalų vietinių šaltinių, tokiai kaip namų šildymo emisijų, indėlių į PM_1 sulfatinę dalį. Tačiau buvo pastebėta stipri koreliacija tarp TC ir SO_4^{2-} koncentracijų ($r = 0,66$, $p < 0,05$). Tai rodo, jog tiek anglingojai, tiek sulfatinė PM_1 dalys yra susijusios su bendrais antropogeniniaisiais šaltiniais.

Laikotarpis nuo sausio 15 d. iki sausio 18 d. yra išskirtinis dėl padidėjusių tiek TC, tiek SO_4^{2-} koncentracijų. Šis laikotarpis išsiskyrė užfiksuota žemiausia vidutinė temperatūra ($-17,2^\circ\text{C}$) per visą tyrimą, kartu su mažu vidutiniu vėjo greičiu ($2,6 \text{ m/s}$) ir žemu maišymosi sluoksnio aukščiu (352 m). Taigi, tikėtina, kad itin žemų temperatūrų laikotarpiu padidėjęs emisijų kiekis iš namų šildymo, kartu su nepalankiomis atmosferinėmis salygomis, lėmė PM_1 kaupimąsi. Todėl šiuo periodu buvo užfiksuotos neįprastai aukštos TC ir SO_4^{2-} koncentracijos.

Stipri koreliacija tarp TC ir SO_4^{2-} koncentracijų davė pagrindą pritaikyti kompleksinę $\delta^{13}\text{C}$ ir $\delta^{34}\text{S}$ analizę šiam periodui. 2020 – 2021 m. laikotarpiu TC izotopinė sudėtis anglingajame aerosolyje kito siaurame ruože, nuo $-26,7\text{ ‰}$ iki $-25,7\text{ ‰}$ (vidurkis: $-26,2 \pm 0,2\text{ ‰}$). $\delta^{13}\text{C}$ vertės silpnai

koreliavo su TC koncentracijomis ($r = 0,34$, $p < 0,05$). Tuo pačiu metu PM₁ sulfatų $\delta^{34}\text{S}$ vertės svyravo nuo 3,4 ‰ iki 6,1 ‰ (vidurkis: $4,8 \pm 0,8$ ‰). $\delta_{34}\text{S}$ vertės taip pat rodė mažą koreliaciją su SO₄²⁻ koncentracijomis ($r = 0,13$, $p < 0,05$). Užfiksuotos silpnos koreliacijos tarp izotopinių verčių ir koncentracijų rodo, jog keli skirtinai šaltiniai su savitomis izotopinėmis vertėmis galėjo daryti įtaką. Sieros taršos šaltiniai ženkliai skiriasi sieros kiekiu, todėl padidėjusių mažai sieros turinčių šaltinių emisjos (pvz., biomasės deginimo) poveikis gali nebūtinai padidinti atmosferines SO₄²⁻ koncentracijas, bet gali sukelti pastebimus $\delta^{34}\text{S}$ reikšmių pokyčius. Taip pat oro masių pernašos analizė parodė, jog anglingujų aerosolio taršos koncentracijos ir izotopinės vertės labiau atspindėjo vietinių šaltinių įtaką. O sulfatinių aerosolių rezultatai atspindėjo teršalų tolimosios pernašos įtaką iš kaimyninių regionų.

Toliau, pritaikant radiokaanglies matavimus, galime tiksliai nustatyti iškastinio ir neiškastinio kuro šaltinių indėlius šiuo laikotarpiu (8 pav.).

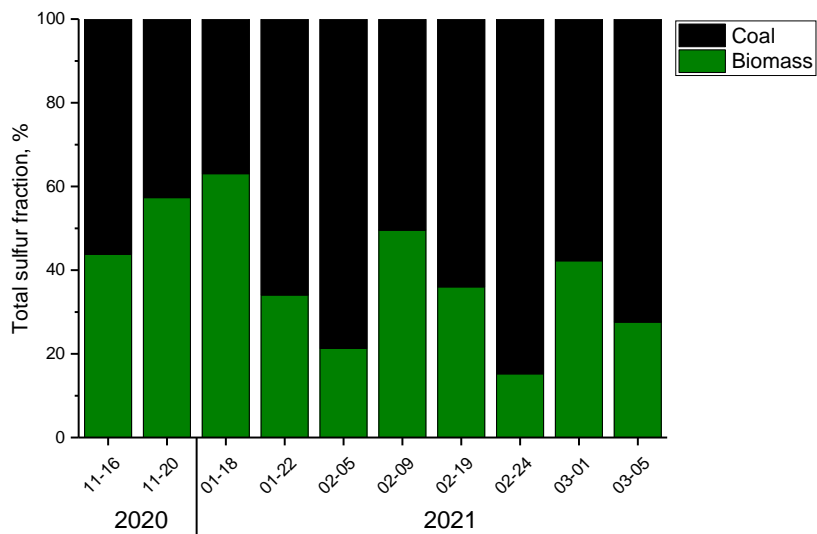


8 pav. Iškastinio ir neiškastinio kuro šaltinių indėliai į anglingujų aerosolių frakciją 2020 – 2021 m. laikotarpiu. Šis laikotarpis palygintas su tyrimu (pažymėta raudonai), atliktu 2014 – 2015 m. (Garbarienė et al., 2016). Be to, pateiktos $\delta^{13}\text{C}$ vertės (balti kvadrateliai).

2020–2021 m. laikotarpiu neiškastinis kuras buvo pagrindinis anglingujų aerosolių šaltininis dėl vietinių namų šildymo emisijų. Lietuvoje namų šildymui plačiai naudojamas biokuras, toks kaip kaip malkos, medžio granulės ir briketai (Lithuania's National Inventory Report, 2021.). Neiškastinio kuro emisijų indėlis svyravo nuo 64 % iki 85 % (vidurkis 77 ± 6 %), o iškastinio

kuro indėlis varijavo tarp 15 % ir 36 % (vidurkis $23 \pm 6\%$). 2020–2021 m. laikotarpiu iškastinio kuro indėlis buvo pastebimai mažesnis nei anksčiau, lyginant su 2014 – 2015 m. tyrimu (Garbarienė et al., 2016), kuriami iškastinio kuro indėlis vidutiniškai sudarė 30 %. Šis sumažėjimas greičiausiai atspindi sumažėjusias transporto emisijas COVID-19 karantino metu, o tuo metu biomasės deginimo emisijos suintensyvėjo. Šio tyrimo $\delta^{13}\text{C}$ vertės ($-26,2 \pm 0,2\%$) buvo teigiamesnės nei 2014 – 2015 m. ($-26,7 \pm 0,4\%$), kas patvirtina, jog transporto emisijos karantino metu sumažėjo, nes dalelių $\delta^{13}\text{C}$ vertės Lietuvoje paprastai svyruoja nuo -29 ‰ iki -28 ‰ (Garbarienė et al., 2016; Mašalaitė et al., 2012).

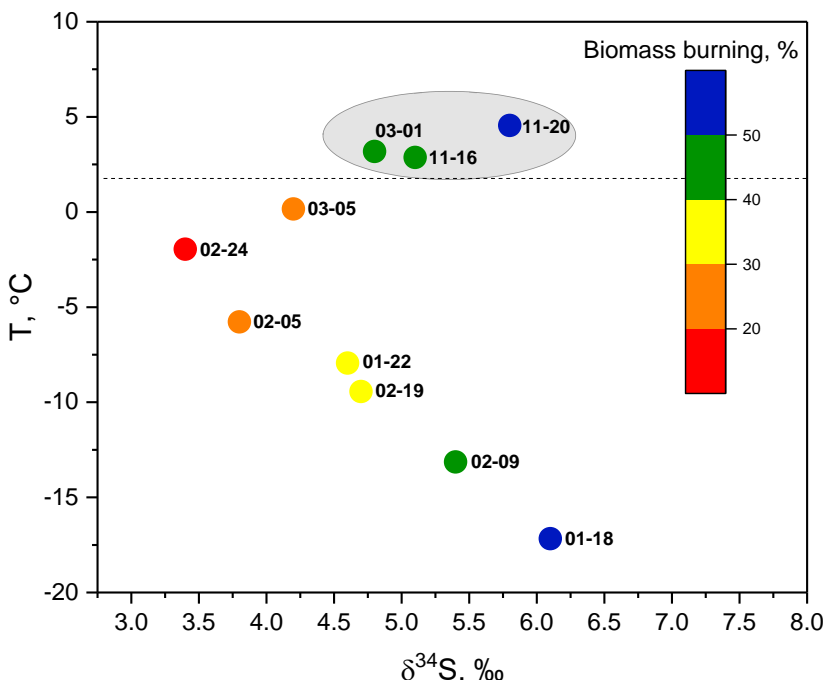
O sulfatinių aerosolių šaltinių skirstymas parodė, kad pagrindinis šaltinis buvo akmens anglies deginimo emisijos, kurios vidutiniškai sudarė $60 \pm 10\%$, svyruodamos nuo 40 % iki 80 % per visą 2020 – 2021 m. laikotarpi (9 pav.).



9 pav. Akmens anglies ir biomasės deginimo emisijų indėliai 2020 – 2021 m. laikotarpiu.

Biomasės deginimo emisijų indėlis sulfatų frakcijoje buvo gerokai mažesnis, siekė nuo 20 % iki 60 % (vidurkis: $60 \pm 10\%$). Tačiau biomasės deginimo emisijų indėlis buvo gerokai didesnis šiuo laikotarpiu, palyginti su kitais 2021 – 2022 ir 2022 – 2023 m. periodais, kai biomasės deginimo emisijos sudarė po 21 % kiekvienu laikotarpiu (6 pav.). Mažiausia akmens anglies dalis (40 %)

buvo užfiksuota anksčiau aptartu laikotarpiu 2021 m. sausio 15 – 18 d. Vilniuje. Taigi, žemos temperatūros laikotarpiai kartu su nepalankiomis atmosferos maišymosi sąlygomis gali nulemti vyraujantį vietinių taršos šaltinių indėlių tam tikrais laikotarpiais. Tai patvirtina $\delta^{34}\text{S}$ verčių priklausomybę nuo temperatūros, parodyta 10 pav.



10 pav. $\delta^{34}\text{S}$ verčių priklausomybę nuo vidutinių temperatūrų atskirais bandinių rinkimo laikotarpiais. Apskaičiuoti biomasės deginimo emisijų indėliai pažymėti kaip spalvų gradientas. Brūkšninė linija žymi ribą ties $2,9^\circ\text{C}$, žemiau kurios $\delta^{34}\text{S}$ vertės rodo stiprią atvirkštinę priklausomybę nuo užfiksuotų temperatūrų.

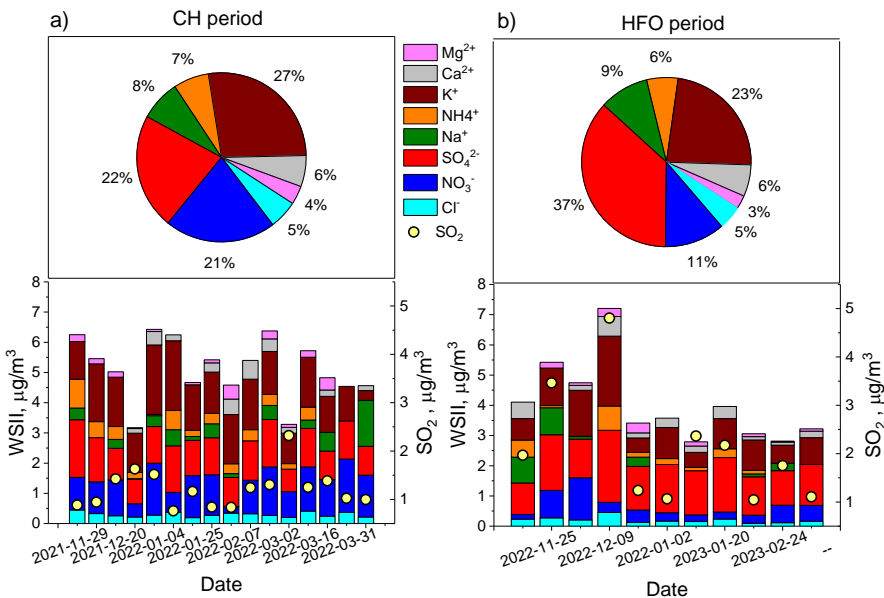
2020 – 2021 m. laikotarpiu PM₁ sulfatų $\delta^{34}\text{S}$ vertės stipriai koreliavo su temperatūra ($r = -0,90$, $p < 0,05$), kai temperatūra buvo žemesnė nei pasirinktas $\sim 2,9^\circ\text{C}$ slenkstis. Temperatūrai nukritus žemiau šios ribos, biomasės deginimo indėlis padidėjo nuo 20 % iki 60 %. Taigi, nors temperatūros sąlygoti sulfatų $\delta^{34}\text{S}$ verčių svyravimai gali būti siejami su besikeičiančiais SO₂ oksidacijos keliais arba frakcionavimo koeficientų pokyčiais, stebėtas $\delta^{34}\text{S}$ verčių kitimas šiuo laikotarpiu greičiausiai atspindi skirtingu sieros taršos šaltinių indėlių pokyčius. Be to, laikotarpiais, kai oro

masės atkeliaudavo iš mažiau užterštų šiaurės ir šiaurės vakarų sektorių, kuriuose SO_4^{2-} koncentracijos paprastai yra žemos (Davuliene et al., 2021), biomasės deginimo dalis sudarydavo 60 % indėlių ir vietinių šaltinių įtaka buvo vyraujanti. Todėl PM_1 bandiniai, surinkti 01-18, 02-05, 02-09 ir 02-19, galėtų būti laikomi atspindinčiais laikotarpis, kada vyrauja vietiniai taršos šaltiniai.

Sunkiojo kuro emisijų poveikis

Siekiant įvertinti sunkiojo kuro (mazuto, HFO) poveikį oro kokybei Vilniuje, buvo atlikta PM_1 dalelėlių vandenyeje tirpių neorganinių jonų koncentracijų palyginamoji analizė. Buvo palyginti du šildymo sezoni: įprastas šildymo laikotarpis (CH laikotarpis: 2021 – 2022), kai Vilniaus šiluminėje jégainėje buvo naudojama tik biomasė ir gamtinės dujos, ir HFO naudojimo laikotarpis (2022 – 2023), kai mažasieris (0,9 %) mazutas pradėtas naudoti Vilniaus TPS. Mazutas buvo naudojamas nuo 2022 m. lapkričio 9 d. iki 2023 m. kovo pabaigos. Meteorologinės sąlygos tiek CH laikotarpiu, tiek HFO naudojimo laikotarpiu buvo panašios.

CH ir HFO naudojimo laikotarpiais buvo išmatuotos koncentracijos šių WSII koncentracijos PM_1 frakcijoje: Mg^{2+} , Ca^{2+} , K^+ , NH_4^+ , Na^+ , SO_4^{2-} , NO_3^- ir Cl^- (11 pav.). Taip pat pateikiami SO_2 koncentracijų monitoringo duomenys. Dažniausiai pasitaikantys jonai buvo SO_4^{2-} , K^+ ir NO_3^- , sudarę apie 70 % visų WSII tiek CH, tiek HFO laikotarpiais. CH laikotarpio (11 pav.(a)) metu vidutinė SO_4^{2-} koncentracija buvo lygi $1,16 \pm 0,31 \mu\text{g}/\text{m}^3$, K^+ lygi $1,61 \pm 0,48 \mu\text{g}/\text{m}^3$ ir NO_3^- lygi $1,05 \pm 0,44 \mu\text{g}/\text{m}^3$. Kalio jonai sudarė 27 % nuo bendros WSII koncentracijos, rodančios reikšmingą biomasės deginimo emisijų įtaką CH periodu (Urban et al., 2012).



11 pav. CH (a) ir HFO (b) periodų WSII koncentracijų paskirstymas PM_1 - dalelėse ir jų santykiniai indėliai į bendras WSII koncentracijas.

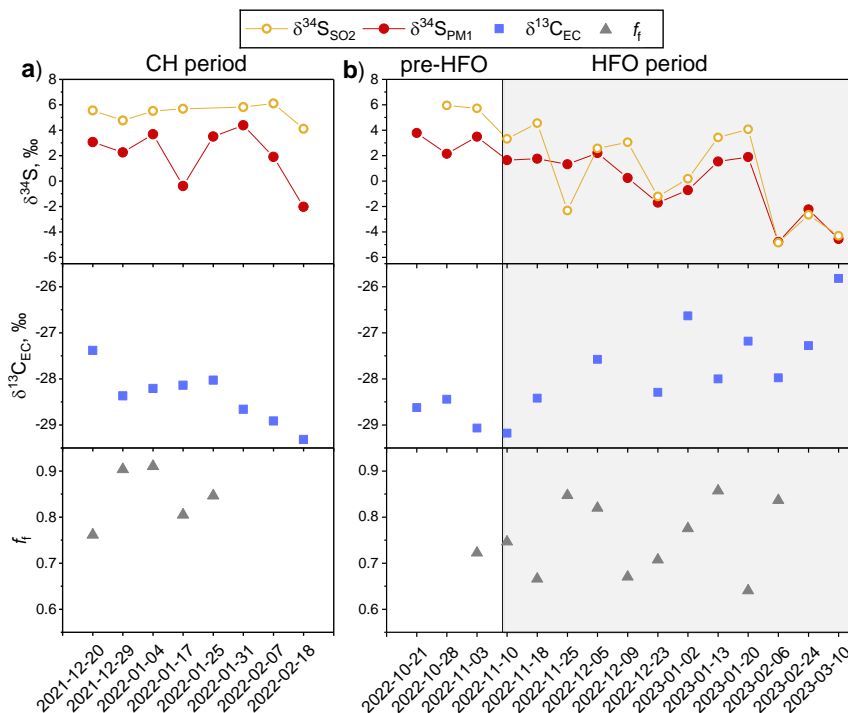
Per HFO naudojimo laikotarpi (11 pav.(b)) išaugo SO_4^{2-} koncentracijos, sudarydamos 37 % viso WSII, t.y. 15 % daugiau nei per CH laikotarpi. Sulfatų jonų koncentracijos padidėjo 1,3 karto ir pasiekė vidutinę $1,53 \pm 0,38 \mu\text{g}/\text{m}^3$ vertę. Tačiau K^+ ($1,04 \pm 0,58 \mu\text{g}/\text{m}^3$) ir NO_3^- ($0,47 \pm 0,37 \mu\text{g}/\text{m}^3$) koncentracijos sumažėjo. Be to, per HFO naudojimo laikotarpi užfiksuotas žymus SO_2 koncentracijų padidėjimas ir vidutinė vertė buvo lygi $2,54 \pm 2,13 \mu\text{g}/\text{m}^3$ – beveik dvigubai daugiau nei per CH laikotarpi ($1,30 \pm 0,39 \mu\text{g}/\text{m}^3$).

Toliau palyginome CH ir HFO periodus pasitelkiant kompleksinę izotopų analizę (^{13}C , ^{14}C ir ^{34}S), kaip parodyta 12 pav. CH laikotarpiu (12 pav.(a)) SO_2 $\delta^{34}\text{SSO}_2$ vertės išliko santykinai pastovios, svyrudamos siaurame intervale nuo 4,8 % iki 6,1 % (vidurkis: $5,4 \pm 0,6 \text{‰}$). O PM_1 sulfatų vertės kito plačiame intervale nuo -2,0 % iki 4,4 % (vidurkis: $2,0 \pm 2,1 \text{‰}$), atspindėdamos kintantį tolimąjį ir vietinių sieros taršos šaltinių santykinį poveikį.

CH laikotarpiu PM_1 frakcijos elementinės anglies (angl. *elemental carbon*, EC) $\delta^{13}\text{C}_{\text{EC}}$ vertės svyravo nuo -29,3 % iki -27,4 % su vidutine $-28,4 \pm 0,6 \text{‰}$ verte. Nors Lietuvoje vietinių taršos šaltinių $\delta^{13}\text{C}_{\text{EC}}$ vertės nėra žinomas, mūsų rezultatus galime palyginti su literatūroje pateikiamais skirtingu šaltinių izotopinių verčių intervalais. CH laikotrapio metu gautos $\delta^{13}\text{C}_{\text{EC}}$ gerai atitinka

biomasės deginimo šaltinius, kurių $\delta^{13}\text{C}_{\text{EC}}$ vertės svyruoja nuo -29,9 ‰ iki -25,4 ‰ (Aguilera and Whigham, 2018; Liu et al., 2014; C. Zhang et al., 2023) ir yra artimos transporto emisijų vertėms TC frakcijoje, kurios svyruoja nuo -31,6 iki -29,9 ‰ (Garbaras et al., 2023). Tačiau gautos izotopinės vertės nepatenka į tipinį akmens anglies deginimo emisijų EC frakcijoje ruožą, kuris svyruoja nuo -24,7 iki -23,3 ‰ (Kawashima and Haneishi, 2012; Yao et al., 2022; C. Zhang et al., 2023).

Tuo pačiu metu radioanglies analizė parodė, kad neiškastinio kuro frakcija sudarė 15 ± 6 %, kas atitinka ankstesnių tyrimų duomenis (Bernardoni et al., 2013; Dusek et al., 2017; Genberg et al., 2011; Szidat et al., 2004). O iškastinio kuro frakcija sudarė nuo 76 % iki 91 % indėlį su vidutine 85 ± 6 % verte. Tai rodo, jog, nepaisant reikšmingos biomasės deginimo įtakos $\delta^{13}\text{C}_{\text{EC}}$ vertėms, iškastinis kuras buvo pagrindinis EC šaltinis CH laikotarpiu.



12 pav. $\delta^{34}\text{S}_{\text{SO}_2}$, $\delta^{34}\text{S}_{\text{PM}_1}$, $\delta^{13}\text{C}_{\text{EC}}$ ir f_r vertės laikotarpiui nuo 2021 m. gruodžio 10 d. iki 2022 m. vasario 18 d. (b) yra priskiriamos įprastam šildymo laikotarpiui (CH). Laikotarpis nuo 2022 m. spalio 17 d. iki 2023 m. kovo 10 d. (b), kai buvo naudojamas mazutės (HFO) pažymėtas pilkai. Matavimai, atlikti iki HFO naudojimo pradžios (iki 2022 m. lapkričio 9 d.), klasifikuojami kaip laikotarpis prieš HFO (pre-HFO).

Mazuto naudojimo Vilniaus TPS laikotarpiu (12 pav.(b)) buvo pastebėti reikšmingi pokyčiai tiek SO₂ ir SO₄²⁻ δ³⁴S izotopinėse vertėse, tiek δ¹³C EC vertėse. Lyginant su CH periodu, HFO laikotarpiu δ³⁴S_{SO2} vertės buvo neigiamesnės ir pasižymėjo padidėjusia variacija su vidutine 0,4 ± 3,2 ‰ verte, o mažiausia užfiksuota vertė buvo lygi -4,9 ‰. Tuo metu δ³⁴S_{PM1} vertės vidutiniškai siekė -0,3 ± 2,4 ‰, su žemiausia -4,8 ‰ užfiksuota verte. Šios žemos δ³⁴S vertės rodo naujo šaltinio įtaką, greičiausiai susijusio su HFO deginimu, kurio kilmė galimai yra Jungtinių Arabų Emyratų arba Saudo Arabijos.

O PM₁ EC izotopinės vertės pasižymėjo priešinga tendencija ir HFO naudojimo metu tapo teigiamesnės. Prieš HFO naudojimo pradžią δ¹³C_{EC} vertės vidutiniškai siekė -28,8 ± 0,3 ‰. Pradėjus naudoti HFO, šių verčių vidurkis buvo lygus -27,5 ± 0,8 ‰ ir pasiekė teigiamiausią 25,8 ‰ reikšmę, kuri artima sunkiojo kuro dalelių vertėms (~ -26,0 ‰ – -25,5 ‰) pagal Widory (2006). HFO periodo metu stebimos tendencijos – neigiamesnės δ³⁴S_{SO2} ir δ³⁴S_{PM1} vertės kartu su labiau teigiamomis δ¹³C_{EC} vertėmis – byloja apie bendrą taršos šaltinį. Tai patvirtina ir reikšminga neigiamama koreliacija tarp δ³⁴S_{PM1} ir δ¹³C_{EC} verčių ($r = -0,6$, $p < 0,05$).

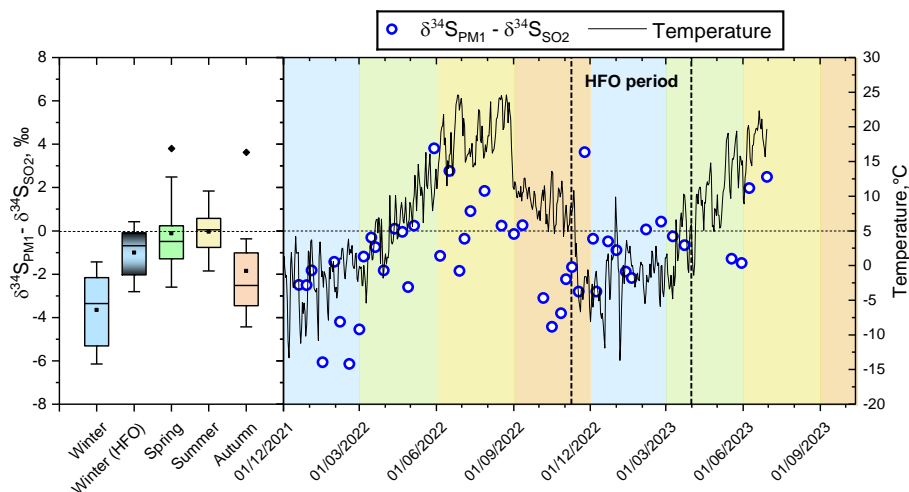
HFO naudojimo laikotarpiu EC iškastinio kuro emisijų frakcija f_f svyravo nuo 64 % iki 86 %. Tačiau, palyginus su CH laikotarpiu, vidutinė f_f vertė reikšmingai nepasikeitė ir siekė 75 ± 7 %. Iškastinio kuro frakcijos sumažėjimą galimai lėmė padidėjusios biomasės deginimo emisijos.

Faktoriai, lemiantys izotopinių verčių kaitą

Sezoniniai δ³⁴S_{SO2} ir δ³⁴S_{PM1} verčių pokyčiai, be anksčiau analizuotų šaltinių emisijų pokyčių, taip pat yra veikiami SO₂ oksidacijos kelių pokyčių ir temperatūros sukelty izotopinių frakcionavimo efektų. Bendrai surinktų SO₂ ir PM₁ sulfatų bandinių analizė gali suteikti informacijos apie veiksnius, lemiančius izotopinius verčių skirtumus tarp jų (δ³⁴S_{PM1} - δ³⁴S_{SO2}). Tokiu būdu galima neatsižvelgti į SO₂ taršos šaltinių emisijų kaitą. Toliau šiame skyriuje bus lyginami izotopiniai verčių skirtumai δ³⁴S_{PM1} - δ³⁴S_{SO2} skirtingais bandinių rinkimo laikotarpiais.

13 pav. pateikiami izotopinių verčių skirtumai δ³⁴S_{PM1} - δ³⁴S_{SO2}. Neigiamos δ³⁴S_{PM1} - δ³⁴S_{SO2} vertės buvo stebėtos žiemą (vidurkis $-2,0 \pm 1,7$ ‰), pavasarį (vidurkis $-0,5 \pm 1,4$ ‰) ir rudenį (vidurkis $-1,6 \pm 2,3$ ‰). Tačiau vasaros metu sulfatų dalelės buvo labiau izotopiškai praturtintos ³⁴S (vidurkis: δ³⁴S_{PM1} - δ³⁴S_{SO2} = $0,4 \pm 1,3$ ‰). 2021 – 2022 m. žiemą stebimi didžiausi δ³⁴S_{PM1} -

$\delta^{34}\text{S}_{\text{SO}_2}$ skirtumai, vidutiniškai atitinkantys $-3,6 \pm 1,7 \text{‰}$ skirtumą. Šis žiemos laikotarpis buvo aprašytas anksčiau kaip įprastas šildymo laikotarpis (CH), kuomet $\delta^{34}\text{S}_{\text{SO}_2}$ vertės atspindėjo vietinių biomasės deginimo emisijų įtaką, o $\delta^{34}\text{S}_{\text{PM}1}$ vertės rodė tolimųjų šaltinių, ypač akmens anglies deginimo, įtaką. Taip pat dideli $\delta^{34}\text{S}_{\text{PM}1} - \delta^{34}\text{S}_{\text{SO}_2}$ skirtumai buvo stebimi, kai oro masės atkeliaudavo iš pietinių–pietvakarinių kryptei (vidurkis $-5,2 \pm 0,9 \text{‰}$). Tai pabrėžia ryškius vietinių SO_2 ir tolimųjų sulfatinių aerozolių šaltinių skirtumus. Harris et al. (2013a) tyrime sezoniainiai $\delta^{34}\text{S}_{\text{PM}1} - \delta^{34}\text{S}_{\text{SO}_2}$ svyravimai buvo modeliuojami remiantis tik oksidacijos kelių pokyčiais ir frakcionavimo faktorių priklausomybe nuo temperatūros. Tyrimė vasarą buvo fiksuojami mažesni, o žiemą – didesni $\delta^{34}\text{S}_{\text{PM}1} - \delta^{34}\text{S}_{\text{SO}_2}$ skirtumai, kurie gerai sutapo su Novák et al. (2001) atlirkais matavimais. Tačiau matavimai, atlirkti santykinių švarioje Vilniaus aplinkoje, yra stipriai veikiami tolimųjų taršos šaltinių bei kintančių SO_2 emisijų lygių, kas galimai paaiškina pastebėtą neatitinkamą lyginant su Harris et al. (2013a) modeliu. Taip pat TMI katalizės kelias tiketinai buvo nepakankamai įvertintas modelyje, kuriame TMI kelias sudarė 35 % visos metinės SO_2 oksidacijos.



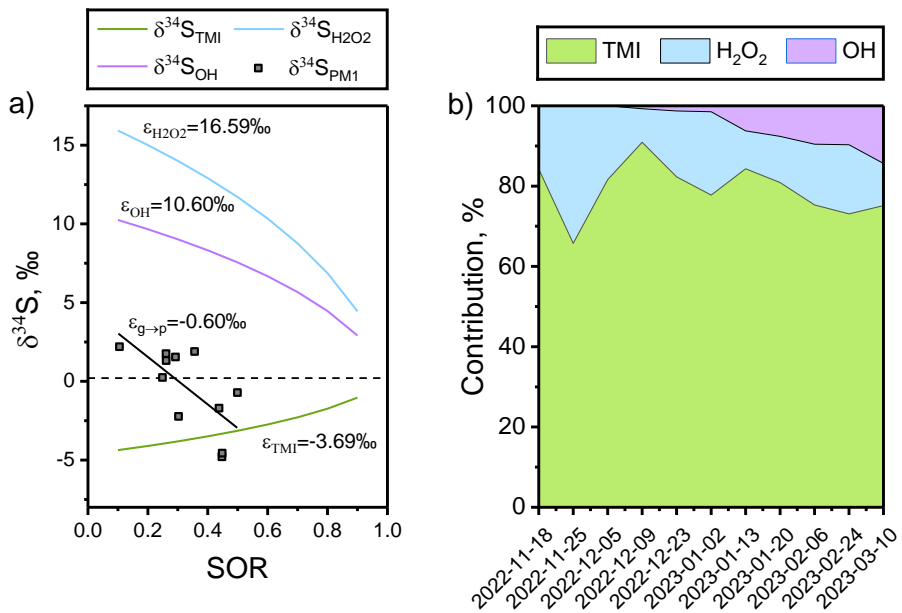
13 pav. Dešinėje paveikslėlio dalyje pateikiami $\delta^{34}\text{S}_{\text{PM}1} - \delta^{34}\text{S}_{\text{SO}_2}$ skirtumai laikotarpiui nuo 2021 m. gruodžio 10 d. iki 2023 m. birželio 30 d. HFO laikotarpis išskirtas punktyrinėmis linijomis. Kairėje paveikslėlio dalyje pateiktos *boxplot* $\delta^{34}\text{S}_{\text{PM}1} - \delta^{34}\text{S}_{\text{SO}_2}$ skirtumų diagramos atitinkamiams sezonams su HFO laikotarpiu, išskirtu juodos spalvos šešeliu.

Priešingai nei 2021 – 2022 m. žiemą, HFO naudojimo laikotarpiu $\delta^{34}\text{S}_{\text{PM}1} - \delta^{34}\text{S}_{\text{SO}_2}$ skirtumai tapo gerokai mažiau ryškūs, vidutiniškai siekdami $-0,7 \pm$

1,7 %. Taip pat šiuo laikotarpiu buvo pastebėta žymiai stipresnė $\delta^{34}\text{S}_{\text{PM}1}$ ir $\delta^{34}\text{S}_{\text{SO}_2}$ verčių koreliacija ($r = 0,86$, $p = 0,05$), lyginant su visais kitais laikotarpiais ($r = 0,47$, $p < 0,05$). Be to, $\delta^{34}\text{S}_{\text{PM}1}$ vertės pasižymėjo stipria koreliacija su SOR ($r = -0,69$, $p = 0,05$), priešingai nei kitaip periodais ($r = -0,06$, $p < 0,05$). Šie rezultatai rodo padidėjusį vietinių SO_2 taršos šaltinių poveikį, sie šaltiniai tiesiogiai prisdėjo prie tolimesnės PM_1 sulfatų gamybos atmosferoje per įvairias oksidajos reakcijas. Taigi HFO naudojimo laikotarpiu išmatuotos $\delta^{34}\text{S}_{\text{PM}1}$ vertės atspindėjo vietinius taršos šaltinius, o $\delta^{34}\text{S}_{\text{PM}1} - \delta^{34}\text{S}_{\text{SO}_2}$ skirtumai buvo nulemti sulfate formavimosi frakcionavimo efektu, o ne skirtumą tarp tolimųjų ir vietinių taršos šaltinių. Todėl šis laikotarpis buvo pasirinktas kaip tinkamas detaliau analizuoti SO_2 oksidacijos reakcijų frakcionavimo efektus ir kiekybiškai įvertinti skirtinį oksidacijos kelių indėlių. Atsižvelgiant į tai, jog HFO emisijos Vilniuje vyko tik šaltuoju metų laiku, buvo tikimasi, jog OH radikalų oksidacijos indėlis bus minimalus dėl mažos OH radikalų koncentracijos (Harris et al., 2013a). OH oksidacijos indėlis buvo įvertintas atskirai, remiantis ankstesnių tyrimų duomenimis (Harris et al., 2013a; Sofen et al., 2011). Be to, SO_2 oksidacija su O_3 nebuvo vertinama atskirai dėl jos nedidelio metinio indėlio ir panašaus frakcionavimo faktoriaus į H_2O_2 . NO_2 kelio indėlis taip pat nebuvo nagrinėjamas dėl mažų vietinių koncentracijų ir mažo frakcionavimo esant žemai temperatūrai (žemiau $\sim 8^\circ\text{C}$) (Au Yang et al., 2018). Todėl buvo pasirinkti trys pagrindiniai SO_2 oksidacijos keliai: OH, H_2O_2 ir O_2 katalizuojamai pereinamujų metalų jonų (TMI).

HFO laikotarpiu vidutinė $\delta^{34}\text{S}_{\text{emission}}$ vertė buvo lygi $0,2 \pm 2,9\text{‰}$. Bendro dujų virtimo į daleles frakcionavimo faktoriaus $\epsilon_{g \rightarrow p}$ vertė buvo vidutiniškai lygi $-0,6 \pm 1,5\text{‰}$. Šiuo laikotarpiu vidutinė aplinkos temperatūra svyravo nuo $-4,5^\circ\text{C}$ iki $3,7^\circ\text{C}$ ir atitinkamai ϵ_{OH} faktorius svyravo nuo $10,59\text{‰}$ iki $10,62\text{‰}$ (vidurkis $10,60 \pm 0,01\text{‰}$), $\epsilon_{\text{H}_2\text{O}_2}$ svyravo nuo $16,20\text{‰}$ iki $16,87\text{‰}$ (vidurkis $16,59 \pm 0,24\text{‰}$), o ϵ_{TMI} svyravo nuo $-4,36\text{‰}$ iki $-3,14\text{‰}$ (vidurkis $-3,69 \pm 0,35\text{‰}$). Frakcionavimo faktoriai priklauso ir nuo SOR ir jie pateikti 14 pav.(a), kuriami pavaizduota vidutinė $\delta^{34}\text{S}_{\text{emission}}$ reikšmė kartu su išmatuotais $\delta^{34}\text{S}_{\text{PM}1}$ duomenimis. Iš paveikslėlio matyti, jog skirtinį SO_2 oksidacijos kelių indelių vertinimas yra pagrįstas tik mažesnėse SOR vertėse, kuriose santykiniai frakcionavimo faktorių skirtumai yra didžiausi. HFO laikotarpio rezultatai patenka į šį mažesnių SOR verčių intervalą, todėl pavyko apskaičuoti oksidacijos kelių paskirstymą su neapibrėžtumais, daugeliu atvejų nesiekiančiais 10 \% (1σ).

14 pav.(b) matomas vyraujantis TMI oksidacijos kelio indėlis, kuris vidutiniškai sudarė $79 \pm 7\text{ \%}$ HFO laikotarpiu. H_2O_2 kelias vidutiniškai sudarė $16 \pm 7\text{ \%}$ indėlių. OH kelias vidutiniškai sudarė $5 \pm 5\text{ \%}$ indėlių.



14 pav. (a) $\delta^{34}\text{S}_{\text{PM}1}$ verčių priklausomybė nuo SOR pažymėta juoda linija, atspindinčia išmatuotas $\delta^{34}\text{S}_{\text{PM}1}$ reikšmes ($r = -0.69$, $p < 0.05$, $N = 11$). Palyginimui teorinės $\delta^{34}\text{S}_{\text{PM}1}$ verčių kreivės buvo apskaičiuotos kiekvienam SO_2 oksidacijos keliui, remiantis vidutine $\delta^{34}\text{S}_{\text{emission}} = 0.2 \text{ ‰}$ reikšme (žymima punktyrine linija). (b) Įvertintų SO_2 oksidacijos kelių indelių kaita HFO naudojimo laikotarpiu.

Anksčiau atlirk tieoriniai tyrimai įvertino, jog TMI katalizuojama SO_2 oksidacija su O_2 gali sudaryti iki 17 % pasaulinės sulfatų gamybos atmosferoje (Alexander et al., 2009). Tačiau naujesni tyrimai rodo, kad TMI katalizės kelias gali sudaryti didesnį nei 35 % indėlį (Harris et al., 2013a, 2013b). Taip pat šio kelio svarba išauga žiemos metu dėl padidėjusių antropogeninių emisijų iš energijos gamybos, ypač dėl akmens anglies deginimo emisijų (Jacob and Hoffmann, 1983; Luo et al., 2008; McCabe et al., 2006). Atsižvelgiant į tai, kad akmens anglies deginimas yra pagrindinis Fe ir Mn jonų šaltinis, TMI katalizė galimai atlieka ypač svarbų vaidmenį SO_2 oksidacijoje Centrinėje ir Rytų Europoje (Alexander et al., 2009). Be to, mazuto deginimo emisijos pasižymi aukštomis metalų jonų koncentracijomis, ypač Fe jonų (sudarantys ~34 % masės susidariusiose pirminėse PM dalelėse) (Allouis et al., 2003). Todėl padidėjusios metalų jonų emisijos iš anglies deginimo ir mazuto naudojimo Vilniaus TPS galimai padidino TMI oksidacijos kelio vyrovimą, stebėtą 2022 – 2023 m. žiemą.

IŠVADOS

1. Per daugiau nei dvejus metus buvo stebėta ryški sezoninė SO₂ ir sulfatų izotopinių verčių kaita ir izotopiškai praturtintos sieros rūšys buvo paplitusios vasaros mėnesiais ($\delta^{34}\text{S}_{\text{SO}_2} = 6,5 \pm 1,7 \text{ ‰}$; $\delta^{34}\text{S}_{\text{PM1}} = 6,5 \pm 1,5 \text{ ‰}$), o izotopiškai lengvesnės frakcijos – žiemos mėnesiais ($\delta^{34}\text{S}_{\text{SO}_2} = 3,1 \pm 3,4 \text{ ‰}$; $\delta^{34}\text{S}_{\text{PM1}} = 2,3 \pm 2,7 \text{ ‰}$). Sezonines $\delta^{34}\text{S}_{\text{SO}_2}$ ir $\delta^{34}\text{S}_{\text{PM1}}$ variacijas daugiausia lėmė sieros šaltinių emisijų pokyčiai ir SO₂ oksidacijos kelių persiskirstymas. Tuo metu temperatūros sukelta frakcionacija turėjo sėlyginai mažesnę reikšmę.
2. Iki 2022 metų pagrindiniai sieros taršos šaltiniai buvo vietinis biomasės deginimas ($30 \pm 16 \text{ %}$) ir tolimųjų akmens anglies degimo emisijų pernaša iš kaimyninių šalių ($70 \pm 16 \text{ %}$) žiemos metu Vilniuje. O vasaros sezona per visą mėginių rinkimo laikotarpį pasižymėjo sumažėjusiomis akmens anglies ir naftos deginimo emisijomis. Todėl vasaros laikotarpiu pagrindiniu sieros taršos šaltiniu tapo biomasės deginimas, kuris sudarė $60 \pm 18 \text{ %}$ indėlių SO₂ emisijoje ir $63 \pm 16 \text{ %}$ PM₁ frakcijoje.
3. 2022 – 2023 metų žiemos laikotarpiu sunkiojo kuro naudojimas Vilniaus šiluminėje elektrinėje lėmė reikšmingus sieros junginių ir anglingujų PM₁ izotopinių verčių pokyčius. Šiuo laikotarpiu buvo užfiksuotos ypač neigiamios $\delta^{34}\text{S}$ reikšmės ($\delta^{34}\text{S}_{\text{SO}_2} = 0,4 \text{ ‰}$, $\delta^{34}\text{S}_{\text{PM1}} = -0,3 \text{ ‰}$) ir labiau teigiamos $\delta^{13}\text{C}$ vertės ($-27,5 \pm 0,8 \text{ ‰}$). Taip pat šiuo laikotarpiu sunkiojo kuro emisijos sudarė apie 40 % tiek SO₂, tiek sulfatų frakcijose. O akmens anglies deginimo emisijų indėlis sumažėjo iki $34 \pm 6 \text{ %}$ SO₂ ir $36 \pm 8 \text{ %}$ sulfatų frakcijose.
4. Sunkiojo kuro naudojimo Vilniaus šiluminėje elektrinėje metu vietinių taršos šaltinių sieros emisijos buvo vyraujančios lyginant su tolimųjų šaltinių emisijomis, todėl buvo įmanoma įvertinti frakcionavimo faktorius bei apskaičiuoti skirtingų SO₂ oksidacijos kelių santykinius indėlius. Buvo nustatyta, jog pagrindinis SO₂ oksidacijos kelias buvo O₂ oksidacija, katalizuojama pereinamujų metalų ionų, ir sudarė $79 \pm 7 \text{ %}$ indėlių sulfatų aerosoliuose. Kiti oksidantai buvo mažiau efektyvūs ir H₂O₂ oksidacija sudarė $16 \pm 7 \text{ %}$, o OH kelias sudarė $5 \pm 5 \text{ %}$.

ACKNOWLEDGEMENT

First and foremost, I am immensely grateful to my supervisor, dr. Andrius Garbaras, under whose guidance I completed my bachelor's, master's works, and ultimately this dissertation. Dr. Andrius Garbaras introduced me to the stable isotope world and equipped me with skills ranging from the principles of spectrometer operation to the scientific interpretation of results. His support and constant consultations on all matters related to the scientific and formal aspects of the work allowed me to successfully accomplish all the tasks of the doctoral program and overcome the challenges associated with them.

I would like to thank dr. Inga Garbarienė and dr. Agnė Mašalaitė for truly helpful consultations with them, their valuable inputs and for enduring the challenges of writing articles with me. Additionally, I am very grateful to dr. Inga Garbarienė for the insights provided on numerous scientific questions and conundrums I was plagued by.

I am very thankful to dr. Justina Šapolaitė and dr. Žilvinas Ežerinskis for providing help in radiocarbon-related questions, discussions, and analyses. I am also deeply grateful to them for warmly welcoming me into their group and creating a pleasant work atmosphere.

I would also like to thank dr. Dalia Jasinevičienė for the WSII concentration measurements and their valuable contributions to the written articles.

Lastly, I am immensely grateful to prof. habil. dr. Vidmantas Remeikis for his initial lectures that sparked my interest in this field and for providing me with the opportunity to pursue my further studies.

The dissertation would not have been possible without the many people mentioned here, as well as countless others too numerous to name, to whom I also extend my gratitude.

PUBLICATIONS AND CONFERENCES

Scientific publications on the topic of thesis:

1. **Bučinskas, L.**, Garbarienė, I., Mašalaitė, A., Šapolaitė, J., Ežerinskis, Ž., Jasinevičienė, D., Remeikis, V. and Garbaras, A., 2024. Dual carbon and sulfur isotopes as tracers of PM₁ pollution sources after COVID-19 confinement in Vilnius, Lithuania. *Urban Climate*, 55, p.101894. <https://doi.org/10.1016/j.uclim.2024.101894>
2. **Bučinskas, L.**, Garbarienė, I., Mašalaitė, A., Šapolaitė, J., Ežerinskis, Ž., Jasinevičienė, D. and Garbaras, A., 2024. Evaluating the impact of increased heavy oil consumption on urban pollution levels through isotope ($\delta^{13}\text{C}$, $\delta^{34}\text{S}$, ^{14}C) composition. *Atmosphere.*, 15(8), pp.1-15. <https://doi.org/10.3390/atmos15080883>
3. **Bučinskas, L.**, Garbarienė, I., Mašalaitė, A., Jasinevičienė, D., Remeikis, V. and Garbaras, A. Variability in Stable Sulfur Isotope Composition of PM₁ and SO₂: Insights from a 2-year Investigation into Seasonal Dynamics. *Aerosol and Air Quality Research*, 24, 240142. <https://doi.org/10.4209/aaqr.240142>

Other scientific publications:

1. Šapolaitė, J., Ežerinskis, Ž., Butkus, L., Garbarienė, I., Garbaras, A., Kurila, L., **Bučinskas, L.**, Pabedinskas, A. and Remeikis, V., 2021. Development of an online sulfur trapping system for graphitization of cremated bones with automated graphitization system AGE-3. *Nuclear Instruments and Methods in Physics Research Section B: Beam Interactions with Materials and Atoms*, 505, pp.17-23. <https://doi.org/10.1016/j.nimb.2021.08.006>
2. Garbarienė, I., Pauraitė, J., Pashneva, D., Minderytė, A., Sarka, K., Dudoitis, V., Davulienė, L., Gaspariūnas, M., Kovalevskij, V., Lingis, D. and **Bučinskas, L.**, Šapolaitė, J., Ežerinskis, Ž., Mainelis, Gediminas, Ovadnevaitė, J., Kecorius, S., Plauškaitė-Šukienė, K. and Byčenkiene, S., 2022. Indoor-outdoor relationship of submicron particulate matter in mechanically ventilated building: chemical composition, sources and infiltration factor. *Building and Environment*, 222, p.109429. <https://doi.org/10.1016/j.buildenv.2022.109429>

3. Butkus, L., Šapolaitė, J., Garbarienė, I., Garbaras, A., **Bučinskas, L.**, Pabedinskas, A., Remeikis, V. and Ežerinskis, Ž., 2022. Development of graphitization method for low carbon aerosol filter samples with Automated Graphitization System AGE-3. *Applied Radiation and Isotopes*, 190, p.110461. <https://doi.org/10.1016/j.apradiso.2022.110461>
4. Cappelletti, D., Ežerinskis, Ž., Šapolaitė, J., **Bučinskas, L.**, Luks, B., Nawrot, A., Larose, C., Tuccella, P., Gallet, J.C., Crocchianti, S., Bruschi, F., Moroni, B. and Spolaor, A., 2023. Long-range transport and deposition on the Arctic snowpack of nuclear contaminated particulate matter. *Journal of Hazardous Materials*, 452, p.131317. <https://doi.org/10.1016/j.jhazmat.2023.131317>
5. Garbaras, A., Garbarienė, I., **Bučinskas, L.**, Šapolaitė, J., Ežerinskis, Ž., Matijošius, J., Rimkus, A. and Remeikis, V., 2023. Characterization of particulate matter emissions from internal combustion engines using $\delta^{13}\text{C}$ values: Impact of engine operation conditions and fuel type on PM_{10} isotopic composition. *Atmospheric Pollution Research*, 14(9), p.101868. <https://doi.org/10.1016/j.apr.2023.101868>
6. Mašalaitė, A., Garbarienė, I., Garbaras, A., Šapolaitė, J., Ežerinskis, Ž., **Bučinskas, L.**, Dudoitis, V., Kalinauskaitė, A., Pashneva, D., Minderytė, A. Remeikis, V. and Byčenkienė, S., 2024. Dual-isotope ratios of carbonaceous aerosols for seasonal observation and their assessment as source indicators. *Science of The Total Environment*, 949, p.175094. <https://doi.org/10.1016/j.scitotenv.2024.175094>

Presentations at scientific conferences:

1. Open Readings. **Bučinskas, L.**, Garbaras, A. Poster presentation: Stable sulfur isotope ratio variation of atmospheric particulate matter in Vilnius, Lithuania. March 15 –18, 2021, Vilnius, Lithuania.
2. European Geosciences Union General Assembly. **Bučinskas, L.**, Garbaras, A. Oral presentation: Stable sulfur isotope analysis of aerosol in Vilnius, Lithuania. April 19 – 30, 2021, Vienna, Austria.
3. International Conference on the Sustainable Energy and Environmental Development. **Bučinskas, L.**, Garbarienė, I., Šapolaitė, J., Ežerinskis, Ž., Garbaras, A. Oral presentation:

- Aerosol source apportionment using stable sulfur and radiocarbon isotope analysis. October 14 – 15, 2021, Krakow, Poland.
4. FizTeCh2021. **Bučinskas, L.**, Garbarienė, I., Šapolaitė, J., Ežerinskis, Ž., Garbaras, A. Poster presentation: Stabiliųjų sieros izotopų santykio ir radioanglies metodų taikymai aerozolių šaltinių charakterizavimui. October 20 – 21, 2021, Vilnius, Lithuania.
 5. European Geosciences Union General Assembly. **Bučinskas, L.**, Garbarienė, I., Šapolaitė, J., Ežerinskis, Ž., Garbaras, A. Oral presentation: A dual stable isotope and radiocarbon approach for apportionment of aerosol sources. May 23 – 27, 2022, Vienna, Austria.
 6. Joint European Stable Isotope Users group Meeting. **Bučinskas, L.**, Garbarienė, I., Šapolaitė, J., Ežerinskis, Ž., Garbaras, A. Poster presentation: Characterization of urban aerosol pollution sources by sulfur and carbon isotope analysis. October 10 – 14, 2022, Kuopio, Finland.
 7. FizTeCh2022. **Bučinskas, L.**, Garbarienė, I., Šapolaitė, J., Ežerinskis, Ž., Jasinevičienė, D., Garbaras, A. Oral presentation: Stabiliųjų anglies ir sieros izotopų santykio ir radioanglies metodų taikymai aerozolių taršos šaltinių charakterizavimui. October 19 – 20, 2022, Vilnius, Lithuania.
 8. German Association for Stable Isotope Research. **Bučinskas, L.**, Garbarienė, I., Mašalaitė, A., Šapolaitė, J., Ežerinskis, Ž., Jasinevičienė, D., Remeikis, V., Garbaras, A. Poster presentation: Application of dual carbon and sulfur isotopes as tracers of PM₁ pollution sources. September 27 – 29, 2023, Bayreuth, Germany.
 9. FizTeCh2023. **Bučinskas, L.**, Garbarienė, I., Mašalaitė, A., Šapolaitė, J., Ežerinskis, Ž., Jasinevičienė, D., Remeikis, V., Garbaras, A. Oral presentation: Stabiliųjų izotopų santykio ir radioanglies metodų pritaikymas kietujų dalelių taršos šaltinių charakterizavimui. October 18 – 19, 2023, Vilnius, Lithuania.
 10. Lietuvos Nacionalinė Fizikos Konferencija. **Bučinskas, L.**, Garbarienė, I., Mašalaitė, A., Šapolaitė, J., Ežerinskis, Ž., Jasinevičienė, D., Remeikis, V., Garbaras, A. Poster presentation: Stabiliųjų anglies ir sieros izotopų pritaikymas KD₁ šaltinių identifikacijai ir atskyrimui COVID-19 pandemijos metu. October 25 – 27, 2023, Vilnius, Lithuania.

Training courses and student workshops:

1. Stable Isotope Summer School GASIR 2023. September 24 – 26, 2023, University of Bayreuth, Bayreuth, Germany.
2. Training Course on Data Quality Assurance in Stable Isotope Laboratories. November 18 – 22, 2024, International Atomic Energy Agency, Vienna, Austria.

CURRICULUM VITAE

Laurynas Bučinskas

17 March, 1995, Marijampolė, Lithuania

Education:

- 2020-2024 PhD studies in Physics (Center for Physical Sciences and Technology, Lithuania).
- 2018-2020 Master's degree in Physics (Vilnius University, Lithuania).
- 2014-2018 Bachelor's degree in Physics (Vilnius University, Lithuania).

Work experience:

- 2024-now Junior Scientific Researcher, Isotopic Research Laboratory, Center for Physical Sciences and Technology.
- 2023-2024 Senior Engineer, Isotopic Research Laboratory, Center for Physical Sciences and Technology.
- 2018-2023 Engineer, Department of Nuclear Research, Center for Physical Sciences and Technology.
- 2016-2018 Technician, Department of Nuclear Research, Center for Physical Sciences and Technology.

Links to personal profiles:

<https://orcid.org/0000-0001-7133-7864>

<https://www.researchgate.net/profile/Laurynas-Bucinskas>

-NOTES-

-NOTES-

-NOTES-

Vilniaus universiteto leidykla
Saulėtekio al. 9, III rūmai, LT-10222 Vilnius
El. p. info@leidykla.vu.lt, www.leidykla.vu.lt
bookshop.vu.lt, journals.vu.lt
Tiražas 15 egz.